Investigations of Solar Thermochemical Splitting of CO_2 and H_2O to Generate CO and H_2 and of Physiochemical Aspects of Inorganic Nanomaterials

---

A THESIS SUBMITTED FOR DEGREE OF
Doctor of Philosophy

By

Sunita Dey

Chemistry and Physics of Materials Unit
Jawaharlal Nehru Centre for Advanced Scientific Research
(*A Deemed University*)
Bangalore, India.

October 2016

Dedicated to my ma

Declaration

I hereby declare that the matter embodied in this thesis entitled "**Investigations of Solar Thermochemical Splitting of CO_2 and H_2O to Generate CO and H_2 and of Physiochemical Aspects of Inorganic Nanomaterials"** is the result of investigations carried out by me under the supervision of Prof. C. N. R. Rao, FRS at the Chemistry and Physics of Materials Unit, Jawaharlal Nehru Centre for Advanced Scientific Research, Bangalore, India and that it has not been submitted elsewhere for the award of any degree or diploma. In keeping with the general practice in reporting scientific observations, due acknowledgement has been made whenever the work described is based on the findings of other investigators.

(Sunita Dey)

Certificate

I hereby certify that the matter embodied in this thesis entitled "**Investigations of Solar Thermochemical Splitting of CO_2 and H_2O to Generate CO and H_2 and of Physiochemical Aspects of Inorganic Nanomaterials"** has been carried out by Ms. Sunita Dey at the Chemistry and Physics of Materials Unit, Jawaharlal Nehru Centre for Advanced Scientific Research, Bangalore, India under my supervision and it has not been submitted elsewhere for the award of any degree or diploma.

(Prof. C. N. R. Rao)
(Research Supervisor)

Acknowledgements

I take this opportunity to express my gratitude to my research supervisor, **Prof. C. N. R. Rao, FRS, ,** for giving me an opportunity to work under him and guiding me throughout. He has always encouraged me to pursue science, to have an innovative outlook while solving challenging problems in science. I am grateful to him for introducing me to the fascinating field of energy production. His compassion towards science, comprehension, dedication, discipline and punctuality towards work have influenced in my career. His great persona has motivated me for changing my outlook towards life. Not only has he been a great teacher, but also a valuable moral support on the personal front. It has been a fulfilling experience, a lifetime opportunity for me to work under his full spirited guidance.

I sincerely thank my collaborators Prof U. V. Waghmare, Prof. D. D. Sarma, Dr. Kanishka Biswas and Dr. Angshuman Nag for the their invaluable discussions and timely guidance.

I am grateful to Dr. A. Govindaraj for helping me in various experimental aspects during my Ph.D.

Most of my research problems would have been incomplete without the help of my co-workers – Dr. Barun Das, Dr. Rakesh Voggu, Dr. H. S. S. R. Matte, Dr. P. Chithaiah, Dr. Urmimala Maitra, Dr. Sharmila N. Shirodkar, Mr. Metikoti Jagadeeswararao, Mr. S. Rajesh, Ms. Sunita Belawadi, Mr. Madhu Mohan Saga, Mr. Manjeet Chhetri, Mr. S. R. Lingampalli, Mr. Uttam Gupta and Mr. Anand Roy.

I would like to thank specially to Dr. B. S. Naidu for helping me in various experimental aspects and for the valuable discussions. It has been a wonderful learning experience working with you. I count myself fortunate to have a caring senior like you.

I shall remain ever thankful to all my past and present labmates especially Dr. Nitesh Kumar, Dr. Urmimala Maitra, Dr. Moses Kota, Dr. K. Vasu, Dr. Basant, Gopalakrishnan, Rana, Pramoda, Ram, Srinivas, Sreedhara, Uttam, Anand, Manjeet, Bollagovind, Sreekanth, Dr. Anupama Ghosh, Dr. Krishnendu Biswas, Dr. Prasad, Dr. Deepa, Dr. Vishnoi, Dr. Magesh, Manjunath and many more for their help in various occasions and for always keeping an amicable and enjoyable atmosphere in lab.

I enjoyed attending courses provided by Prof. S. M. Shivaprasad, Prof. G. U. Kulkarni, Prof. A. Sundaresan, Dr. R. Viswanatha, Dr. T. Govindaraju, Dr. S. J. George and Dr. U. K. Gautam.

I am thankful to past and present chairmen of CPMU for allowing me to use the various departmental facilities.

I highly appreciate technical help from Ms. N. R. Selvi, Mrs. T. Usha, Dr. J. Ghatak, Mr. Anil, Mr Mahesh, Mr. A. Srinivas and Mr. Kishor. Special thanks to Mr. Vasu (for TGA, UV, PL, IR) and Mr. Srinath for their assistance in various projects. Without their help, completion of various projects would not have been possible. I thank Mrs. Shashi, Mrs. Sudha, Mr. Gowda and Mr. Victor for their help in various aspects.

I thank CSIR and Sheik Saqr laboratory for providing fellowships. I thank JNCASR and IISc for research facilities. The hostel, admin staff, academic staff, complab staff and Dhanvantari for all their help during my stay in JNCASR.

My deepest thanks to Mrs. Indumati Rao and Mr. Sanjay for their love, affection and hospitality extended to me during the course of my association with them. I can never forget those wonderful dinners at Prof.'s house every now and then.

Thanks to all my PhD. batch mates with whom I started my life at this centre and whose cheerful company made these five years of life so memorable. I specially thank to Piyush, Amrit da, Sudip da, Jia da, Shiva, Somnath, Arpan, Avijit, Anindita, Papri, Deboshree, Nivedita, Tarak, Moumita, Chandan and Sisir for discussions on various aspects of science and beyond. I thank all my friends for the wonderful time and their help and support at various times during my stay at JNCASR.

I take this opportunity to thank Suryoday, Amit, Bratati and Nabadyuti for bearing with me during my ups and down. I consider myself blessed to have received all the care, affection, suggestions and advice. You all stood by me whenever I felt depressed and led me to find the correct way. You guys are no less than family members to me.

I express my deep gratitude to all my teachers from IITR and my native place for their helps and support.

Above all I would like to thank my family. It was my mother who induces in me the enthusiasm for my work, dedication and the spirit of fighting against all odds. This thesis is a humble offering to my mother without whom I would not have been here. I am also indebted to my grandmother, Tinku aunti and choto pisi who have been there like a guardian to me. Thanks to my baba, brother, aunt and my late uncle for their love and support.

Contents

Part 3. Investigations of carbon quantum dots 165

Part 4. Interaction of electron donor and acceptor molecules with inorganic nanostructures 219

List of Abbreviations

Abbreviations	Full form/formula
LSM50	Lanthanum Strontium Manganite perovskite of composition $La_{0.5}Sr_{0.5}MnO_3$
LCM50	Lanthanum Calcium Manganite perovskite of composition $La_{0.5}Ca_{0.5}MnO_3$
YSM50	Yttrium Strontium Manganite perovskite of composition $Y_{0.5}Sr_{0.5}MnO_3$
CDs	Carbon Dots
CQDs	Carbon Quantum Dots
GQDs	Graphene Quantum Dots
B-GQDs	Boron doped Graphene Quantum Dots
N-GQDs	Nitrogen doped Graphene Quantum Dots
NCs	Nanocrystals
QY	Quantum yield
PL	Photoluminescence
TTF	Tetrathiafulvalene
TCNE	Tetracyanoethylene
ITC	Isothermal titration calorimetry

Prologue

Generation of H_2 and CO by splitting H_2O and CO_2 respectively constitutes an important aspect of the present-day concerns with energy and environment. The solar thermochemical route making use of metal oxides is a viable means of accomplishing these reduction reactions. The method essentially involves reducing a metal oxide by heating and passing H_2O or CO_2 over the nonstoichiometric oxide to cause reverse oxidation by abstracting oxygen from H_2O or CO_2. While ceria, perovskites and other oxides have been investigated for this purpose, recent studies have demonstrated the superior performance of perovskites of the type $Ln_{1-x}A_xMn_{1-y}M_yO_3$ (Ln=rare earth, A= alkaline earth, M=various +2 and +3 metal ions), in the thermochemical generation of H_2 and CO. We present the important results obtained hitherto to point out how the alkaine earth and the Ln ions, specially the radius of the latter, determine the performance of the perovskites.

The thesis contains four parts of which **Part 1** presents the results of investigations of thermochemical splitting of H_2O or CO_2 by employing manganite perovskites in two-temperature as well as isothermal processes. This part consists of four sections along with an introduction and concluding remarks. In **section 1.4.1** the performances of $La_{1-x}Ca_xMnO_3$ (x=0.25, 0.5 and 0.65) family of perovskite oxides have been investigated for the thermochemical splitting of H_2O and CO_2 to produce H_2 and CO respectively. The study was carried out in comparison with $La_{1-x}Sr_xMnO_3$ and the state of the art material, CeO_2. The $La_{1-x}Ca_xMnO_3$ system exhibits superior characteristics in evolution of oxygen at 1400°C, and in reducing CO_2 to CO and H_2O to H_2 at 1100°C. The production of O_2 as well as CO of $La_{0.5}Ca_{0.5}MnO_3$ is significantly higher than $La_{0.5}Sr_{0.5}MnO_3$ although the amount of substituent and the reaction temperature is similar in both the cases. The production of both O_2 and CO by $La_{0.5}Ca_{0.5}MnO_3$ is extremely high in comparison with CeO_2. The structure property relationship has been investigated in detail and found the orthorhombic structure of $La_{0.5}Ca_{0.5}MnO_3$ which induces more structural distortion is the crucial factor to generate higher oxygen nonstoichiometry during reduction. Perovskite with similar extent of structural distortion as of $La_{0.5}Ca_{0.5}MnO_3$ has been synthesized to prove this assumption further. The thermochemical fuel production is also investigated using $La_{1-x}MnO_3$ (x=0.1, 0.2) and $La_{0.7}Sr_{0.3}FeO_3$ oxides.

Motivated by the finding, that structural distortion has a role to play on the reduction extent of perovskites, we have investigated the thermochemical splitting of H_2O and CO_2 by $Ln_{0.5}A_{0.5}MnO_3$ (Ln= lanthanide, A=Sr, Ca) family of perovskites and described in **section 1.4.2.** Lanthanides with decreasing order of ionic radii, La>Nd>Sm>Gd>Dy>Y, have been used for synthesizing perovskites with both Sr and Ca alkaline earth ions. The amounts of O_2 and CO produced are found to increase with the decreasing the size of the rare earth ions. Y based manganites give out the maximum amount of O_2, and hence the maximum amount of CO. The structure-property relationship has been investigated in detail and confirmed further that the manganite with the smallest rare earth possessing the highest distortion due to smallest tolerance factor and hence creates maximum oxygen nonstoichiometry. $Y_{0.5}Ca_{0.5}MnO_3$ with the lowest tolerance factor, releases more $CO(O_2)$ than $Y_{0.5}Sr_{0.5}MnO_3$ during 1400°C-1100°C redox cycle. The reduction of $Y_{0.5}Sr_{0.5}MnO_3$ has, however been observed to start at a signicantly lower temperature than $Y_{0.5}Ca_{0.5}MnO_3$. Size disorder factor appears to be a crucial factor in this purpose. The difference in the ionic radii of Y^{3+} and A^{2+} is found to be higher for $Y_{0.5}Sr_{0.5}MnO_3$, causes more tilting of octahedra and gives out more O_2. This phenomenon is discussed in detail in this section. The best results are found with $Y_{0.5}Sr_{0.5}MnO_3$ which possesses the highest distortion and size disorder. $Y_{0.5}Sr_{0.5}MnO_3$ shows remarkable fuel production activity even at the reduction and oxidation temperatures as low as 1200°C and 900°C respectively and produces the highest amount of O_2 and CO, which is superior to all other perovskite oxides reported so far. The extraordinary activity of $ABO_{3-\delta}$ perovskites in thermochemical CO_2 and H_2O splitting opens up the possibility of investigation of numerous combinations of A and B metal ions for the same purpose.

The partial or complete substitution of B site ion by aliovalent transition metal cations is known to show the enhance catalytic activity due to synergistic valence changes and for the incorporation of oxygen vacancy related microstructural defects in the oxide lattice. In **section 1.4.3**, we demonstrate the effect of substitution of various amounts of Al^{3+}, Ga^{3+} and Sc^{3+} ions on the Mn^{3+} site of $La_{0.5}Sr_{0.5}MnO_3$ perovskite on the thermochemical splitting of CO_2 to generate CO in detail. Increasing Al^{3+}, Ga^{3+} and Sc^{3+} concentration has found to increase the fuel yield than the unsubstituted one. The structural stability of substituted perovskites has been studied throughly and found the Ga^{3+} and Sc^{3+} doping is limited upto 35% and 10% respectively bescause of the secondary phase segregation on over doping. The best performnace is obtained with 5% Sc^{3+} substitution which gives yield of twice than $La_{0.5}Sr_{0.5}MnO_3$. This manganite has also employed for the generation of H_2 by the thermochemical splitting of H_2O. Moreover multiple cyclabilty and microstructural stability of these materials has been tested for long time use. Furthermore experiments have been conducted to investigated any involvement of carbonate formation during CO_2 splitting is presented in detail in this chapter. Thermodynamic considerations demand $T_{red} > T_{oxd}$ to split CO_2 in the above two steps. Such cyclic rotation between T_{red} and T_{oxd} causes irreversible heat losses (reduces thermodynamic efficiency), time loss to shuttle between T_{red} and T_{oxd} and creates thermal stress on the reactive substrate as well as on system components. Thus, it is found desirable to split CO_2 isothermally. Although the large pressure swing in the gas composition in between the reduction and oxidation steps act as a thermodynamic driving force.

Considering the extraordinary properties of perovskite manganites in the two-step process, we have employed $La_{1-x}Sr_xMnO_3$ (x=0.3, 0.4 and 0.5) for solar isothermal CO production as discussed in **section 1.4.4**. Initially thermodynamic calculations are performed to predict the maximum yield of O_2 and CO under equilibrium conditions in accordance with our experimental conditions. The CO yield in isothermal condition is predicted to be increase with increasing Sr^{2+} substitution. Experiments performed using the thermogravimetric technique show the increase in fuel yield with increasing +2 ion substitution although the overall yield is found to be lesser than the theoretical predictions. We have further investigated the reasons behind this discrepancy and improvement has been found with altering the reduction time and changing the gas flow rates. The global CO production rate and total CO yield by $La_{0.5}Sr_{0.5}MnO_3$ is found to be far superior to the reported values of CeO_2 in literature. Notably CeO_2 performs only at or above 1773K while these perovskites show superior activity even at 1673K. While the two-step cycles are thermodynamically restricted to being performed at high temperatures, multi-step cycles are popular due to their reactivity at temperatures lower than 1200K. Although most of these multi-step cycles suffers due to the involvement of corrosive intermediates, loss of products and many more. Mn-oxide based cycles are interesting due to the thermodynamically predicted high solar-to-fuel conversion efficiency and absence of any toxic materials. Davis and Co-workers employed the Mn_3O_4-Na_2CO_3 cycle at 850°C to obtain stoichiometric amounts of O_2 and H_2. Although the rate of H_2 production was found to be slow and we have attempted to improve this further in **Part 2**. Thus, in an effort to bring down the temperature of this cycle, we have used the nanoparticles of Mn_3O_4 and Na_2CO_3 and found the use of nanoparticles of Mn_3O_4 is to be particularly effective. Notably, Davis and co-workers did not observe any H_2 evolution below 850°C. We considered it purposeful to bring down the operating temperature further by using nanomaterial reactants. The temperature of the solid state reaction between nanoparticles of Na_2CO_3 and Mn_3O_4 occurs at a temperature 200°C lower than with bulk samples. It has been possible to operate this cycle and generate H_2 at much faster rates at 750°C and even at 700°C by this means. Furthermore, various hydrolysis conditions has been investigated in detail in order to reduce its energy and material consumption.

Semiconductor quantum dots are of great interest in the fields of bioimaging because of their novel optical properties. However, disadvantages such as low biocompatibility, poor aqueous solubility, high toxicity and high cost limit their applications. Carbon quantum dots (CQDs), have been found to be superior to the traditional semiconductor quantum dots in terms of low toxicity, good solubility and high biocompatibility. Furthermore, their excellent photo and electro-catalytic performances has enriched their applications in the field of energy conservation. Hetero atoms such as nitrogen and boron incorporation on carbon materials like carbon nanotube, graphene is always a fascinating field of research because of its outstanding contribution in changing the band structure, electronic properties of these materials and which also contributes multitudinous ways in the energy research. Attempts to dope N and B in carbon quantum dots have been presented in **Part 3** of this thesis. In **section 3.4.1** we present the simple, easy and rapid methods to synthesize carbon quantum dots with high nitrogen doping which involves the reaction of glucose in presence of urea. Doping is performed by hydrothermal route and under microwave irradiation. The N-doped carbon quantum dots (N-CQDs) show high aqueous solubility and tunable photoluminescence. Interaction of N-CQDs with exfoliated graphene or dimethylaniline quenches the photoluminescence. Interaction of N-doped as well as undoped C-dots with electron-donating tetrathiafulvalene and electron-withdrawing tetracyanoethylene has also been examined. Blue photoluminescence of carbon quantum quantum dots (CQDs) has been exploited to produce white light by mixing the CQDs with yellow light emitting ZnO nanoparticles or graphene oxide. The N-doped CQDs exhibit superior photocatalytic activity compare to pristine carbon quantum dots. Doping B in carbon matrix at low temperature is a bit tricky as the decomposition of boron-based compounds happens at high temperature. The carbon dots don't retain their small sizes and related properties while annealing at high temperature. We present a route to synthesize B doped graphene quantum dots in **section 3.4.2.** Initially B doped graphene is synthesized by the arc-discharge route, following which oxidative cutting under strong acid gives B-GQDs. B-GQDs are prepared by starting with two different B- precursors. N doped GQDs have been prepared for comparison. Significant shift in the PL band and change in quantum yield are observed due to B and N doping. Radiative recombination has been found to increase or decrease as a result of N or B doping respectively. Interestingly, up-conversion PL emission is observed, which enables emission at visible wavelengths upon excitation at near-IR. Few other interesting properties including wavelength-independent emission are reported.

Part 4 deals with the interaction of electron donor and acceptor molecules with inorganic nanostructures such as CdSe and ZnO nanocrystals and with few-layer MoS_2. Tetrathiafulvalene (TTF) and Tetracyanoethylene (TCNE) which are well-known as organic electron donor and acceptor respectively have been employed for this purpose (**section 4.4.1**). Various spectroscopic and physical property measurement techniques such as UV, PL, Raman and ITC were employed to trace the interaction. Interaction of larger CdSe nanocrystals with TCNE causes a red-shift in the band-edge emission because of agglomeration, while the smaller CdSe nanocrystals, exhibiting stronger interaction with TCNE modify the optical gap of the nanocrystals. Isothermal Calorimetry shows CdSe nanocrystals interact more strongly with TCNE than TTF and the interaction energy is higher for small size CdSe nanocrystals. Luminescence of CdSe gets quenched sharply after addition of both TTF and TCNE confirms the interaction between them. ZnO nanocrystals also exhibit luminescence quenching but to a lesser extent. The interaction of TTF and TCNE molecules with the two-dimensional layered material MoS_2 has been presented in **section 4.4.2**. We have observed the occurrence of charge-transfer between few-layer MoS_2 material with TTF, but not with TCNE. Electronic absortion spectroscopic measurements indicate formation of the TTF radical cation by the interaction of TTF with few-layer MoS_2, accompanied by the stiffening of the A_{1g} mode of MoS_2 in the Raman spectrum. We have carried out first-principles calculations to understand the results.

Part 1

Solar thermochemical splitting of CO_2 and H_2O to generate CO and H_2 based on perovskite manganites

Part 1

Solar thermochemical splitting of CO_2 and H_2O to generate CO and H_2 based on perovskite manganites[*]

Summary

Perovskite oxides of the composition $La_{1-x}Ca_xMnO_3$ (LCM) have been investigated for the thermochemical splitting of H_2O and CO_2 to produce H_2 and CO respectively. The study was carried out in comparison with $La_{1-x}Sr_xMnO_3$, state of art material CeO_2 and other oxides. The LCM system exhibits superior characteristics in high-temperature evolution of oxygen, and in reducing CO_2 to CO and H_2O to H_2. The production of O_2 as well as CO of LCM is significantly higher than $La_{1-x}Sr_xMnO_3$ (LSM) and CeO_2 too. Notably the best results are found with $La_{0.5}Ca_{0.5}MnO_3$ which produces ~5 times more CO than CeO_2. The orthorhombic structure of LCM seems to be a crucial factor which induces more structural distortion and helps to generate higher oxygen nonstoichiometry during reduction.

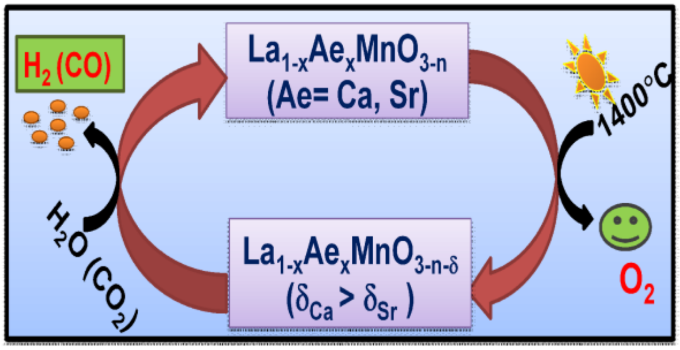

Perovskite oxides of the $Ln_{0.5}A_{0.5}MnO_3$ (Ln= lanthanide, A=Sr, Ca) family have been investigated for the thermochemical splitting of H_2O and CO_2 to produce H_2 and CO respectively. The amounts of O_2 and CO produced strongly depend on the size of the rare earth ions and alkaline earth ions. The manganite with the smallest rare earth possessing the highest distortion and size disorder as well as the smallest tolerance factor, gives out the maximum amount of O_2, and hence the maximum amount of CO. Thus, the best results are found with $Y_{0.5}Sr_{0.5}MnO_3$ which possesses highest distortion and size disorder. $Y_{0.5}Sr_{0.5}MnO_3$ shows remarkable fuel production activity even at the reduction and oxidation temperatures as low as 1200°C and 900°C respectively.

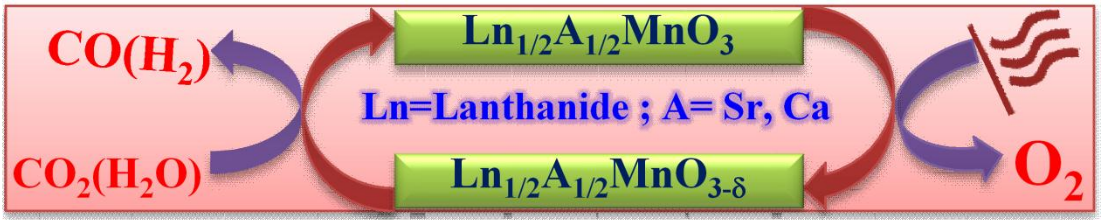

The effect of substitution of Al^{3+}, Ga^{3+} and Sc^{3+} ions in the Mn^{3+} site of $La_{0.5}Sr_{0.5}MnO_3$ on the thermochemical splitting of CO_2 to generate CO has been studied in detail. Both $La_{0.5}Sr_{0.5}Mn_{1-x}Ga_xO_3$ and $La_{0.5}Sr_{0.5}Mn_{1-x}Sc_xO_3$ give high yields of O_2 and generate CO more efficiently than $La_{0.5}Sr_{0.5}Mn_{1-x}Al_xO_3$ or the parent $La_{0.5}Sr_{0.5}MnO_3$. Substitution of even 5% Sc^{3+} (x=0.5) results in a remarkable improvement on performance. Thus $La_{0.5}Sr_{0.5}Mn_{0.95}Sc_{0.05}O_3$ produces 417 μmol/g of O_2 and 545 μmol/g of CO respectively, i.e. 2 and 1.7 times more O_2 and CO than $La_{0.5}Sr_{0.5}MnO_3$. This manganite also generates H_2 satisfactorily by the thermochemical splitting of H_2O.

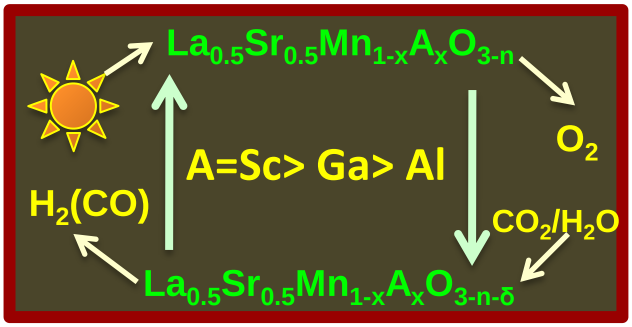

Solar isothermal thermochemical splitting of CO_2 to generate CO has been reported by oxides such as CeO_2 in the literature. With CeO_2, isothermal CO_2 splitting occurs at 1773K but the results are not satisfactory in terms of fuel yield. The limited reducibility and sublimation prevent the use of CeO_2. $La_{1-x}Sr_xMnO_3$ (LSM) based perovskites are recently being identified as a potential candidate of two-step process in view of the greater oxygen release at reduced temperature and greater fuel yield than CeO_2. Considering the extraordinary properties of perovskites manganites in the two-step process, we have employed $La_{1-x}Sr_xMnO_3$ (x=0.3, 0.4 and 0.5) for solar isothermal CO production and obtained CO yields of 133.9 µmol/g by $La_{0.5}Sr_{0.5}MnO_3$ as a temperature low as 1673K. The global CO production rate by $La_{0.5}Sr_{0.5}MnO_3$ (601.8 µmol/g/hr) is far superior (~3 times higher) than CeO_2 at 1773K. Further improvement is achieved by using $Y_{0.5}Sr_{0.5}MnO_3$, containing a very small rare earth ion. This perovskite produces 1.8 times more CO than $La_{0.5}Sr_{0.5}MnO_3$ at a record low temperature of 1573K.

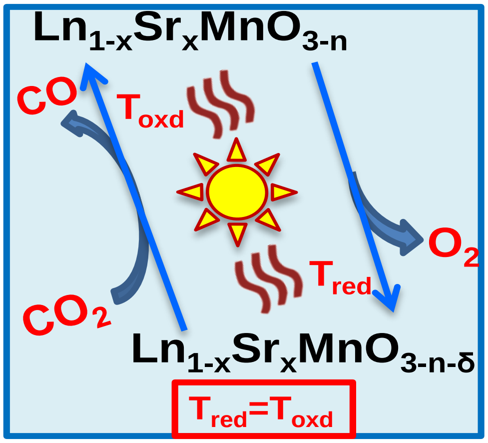

∗Papers based on this part of the thesis have been published in ***Phys. Chem. Chem. Phys.*** **(2015);** ***Chem. Eur. J.*** **(2015);** ***Dalton Trans.*** **(2015);** ***J. Solid State Chem.*** **(2016)** ***and ACS Energy Lett. (2016).***

1.1. Introduction

Increasing impact of global climate change and limited availability of fossil fuels in addition to worldwide increasing energy demand led to the artificial energy harvesting employing the renewable sources. Conversion of solar energy to H_2 and synfuels using H_2O and CO_2 is the potential route for future energy and environment solutions. Several pathways have been proposed for utilizing sunlight for fuel production, including electrochemical, photo-electrochemical, thermochemical, photo-catalytic processes, and their combinations.[1-3] Among these strategies, the solar-thermochemical process is promising in view of its high theoretical solar-to-fuel conversion efficiencies due to the utilization of the entire solar spectrum besides the thermal energy.[2] However, single step thermochemical water splitting appears to be the simplest pathway but the associated Gibbs free energy change found to be positive below 4300K at 1 bar, which makes it technically unprofitable in consideration of its large energy penalty and unavoidable mixing of explosive product gases at such high temperatures ($T > 2500K$).[4, 5] In search of an alternative, screening of few hundreds of thermochemical cycles were carried out and based on criteria related to feasible thermodynamics, theoretical efficiency calculations and cost, a few cycles have been identified by Abanades et al.[6], U.S. Department of Energy (DOE) Hydrogen Program [7] and Sandia National Laboratories[8]. Major contributors includes Japanese Atomic Energy Research Institute [9], Research Centre of the European Union in Ispra, Italy [10], General Atomics [11], and Westinghouse [12]. The potential cycles based on metal sulfates, sulfur-iodine, metal oxides, CuCl and few others are reviewed in the literature [13, 14].

Thermochemical cycles can be classified under two broad categories, namely high-temperature two-step processes and low-temperature multi-step processes. Correlation of maximum operating temperature with the number of steps undertaken to accomplish thermochemical splitting of H_2O (CO_2), is solely based on thermodynamic constraints (**Figure 1**). Multi-step processes with highest operating temperature below 1000°C, allow for the utilization of a broader spectrum of heat sources including waste heat of nuclear power sector and have attracted attention from early days [15]. There are, however, drawbacks such as efficiency loss, product separation and corrosive intermediates which make the implementation of multistep process become challenging in practice. But the two-step metal oxide process carried out with the aid of solar concentrators as the high density heat sources has various advantages [13, 14, 16-19].

The concept of the two-step thermochemical process based on stoichiometric metal oxides was first reported in the late 1970s [4, 20]. The basic reactions are,

$$\text{Endothermal Step: } \mathrm{MO_{oxd}} \rightarrow \mathrm{MO_{red}} + {}^{1}\!/_{2}\, \mathrm{O_2} ------(1)$$

$$\text{Exothermal step: } \mathrm{MO_{red}} + \mathrm{H_2O} \rightarrow \mathrm{MO_{oxd}} + \mathrm{H_2}$$

$$\mathrm{MO_{red}} + \mathrm{CO_2} \rightarrow \mathrm{MO_{oxd}} + \mathrm{CO} ----- (2)$$

Metal oxides (MO_{oxd}) undergo endothermic reduction (T_{red}) to metals or to lower valent metal oxides (MO_{red}) (eqn. 1) and reversibly get oxidized (T_{oxd}) to the higher valence metal oxides (MO_{oxd}) on reaction with H_2O or CO_2 (eqn. 2). Here, $T_{red} > T_{oxd}$ is the thermodynamic demand for this process to be attainable [21, 22], but a decrease or increase in the partial pressure of oxygen during the reduction and oxidation can render the process favorable. Besides, the kinetics of the reactions can also contribute to the overall efficiency.

1.1.1. Thermodynamic criteria

An analysis of the equilibrium thermodynamics of two-step metal oxide based H_2O and/or CO_2 splitting cycles determines the pressure and temperature region in which the reduction and gas-splitting are favorable (Figure 1) in terms of entropy and enthalpy change of reaction.[21, 22] Considering the minimum requirement of the Gibbs free energy change of reaction ($\Delta G_{RED,T_{RED}}, \Delta G_{GS,T_{GS}}$) equals to zero, Meredig and Wolverton[21] has derived the following equation,

$$\Delta T = -2\Delta G^{H_2O}_{f,T_{GS}} / (S^{O_2}_{T_{RED}}) = -2\Delta G^{CO_2}_{f,T_{GS}} / (S^{O_2}_{T_{RED}}) --- (3)$$

Here, $\Delta T = T_{RED} - T_{GS}$ and $2\Delta G^{H_2O,\, CO_2}_{f,T_{GS}}$ defines the free energy change of formation of H_2O and CO_2.

As shown in eqn. 3, the thermodynamic driving force is twice of $2\Delta G^{H_2O,\, CO_2}_{f,T_{GS}}$. Neglecting the solid state entropy dictates the product of the entropy of O_2 and temperature window (ΔT) must exceed or at least equal of it to proceed the reactions spontaneously. The $S^{O_2}_{T_{RED}}$ increases with temperature and so the decrease in ΔT window can be permitted at higher T_{RED}. Conversely, at lower T_{RED}, ΔT has to be higher. In Figure 1b, the variation of thermodynamically favorable T_{RED} and T_{GS} considering several constant values of $\Delta S_{REDUCTION}$ is plotted. The large positive values of $\Delta S_{\mathrm{REDUCTION}}$ improves the energetics, which is an important parameter and can be controlled by proper material design. In practice, most redox material systems exhibit negative entropy changes which give raises to an additional energy. Besides these thermodynamic considerations, the temperature ranges of two-step gas splitting reactor in real system are restricted due to material degradation at $T_{\mathrm{RED}} > 1873$ K and of very slow kinetics at low gas splitting temperatures ($T_{\mathrm{GS}} < 973$ K).

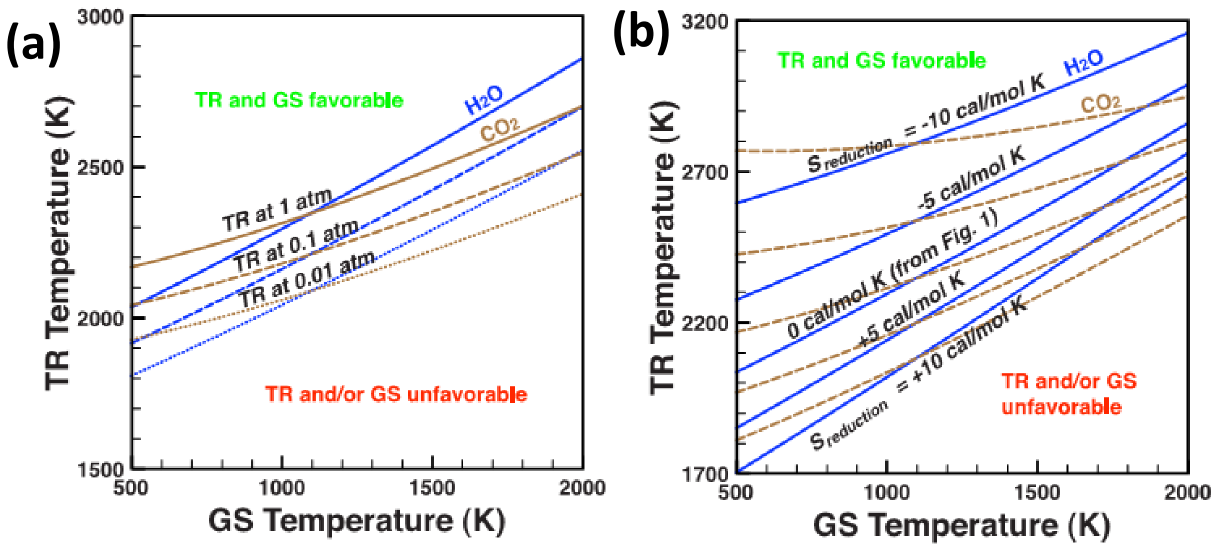

Figure 1. Temperature and pressure regime in which thermal reduction (TR) and gas splitting (GS) are energetically favorable are plotted with (a) neglecting and (b) considering a set of constant solid state entropy values. Reproduced by permission of American Physical Society from Ref.[21]

In **Figure 2**, Meredig and Wolverton[21] define the $\Delta H_{\mathrm{REDUCTION}}$ and $\Delta S_{\mathrm{REDUCTION}}$ regimes where both thermal reduction and gas splitting are thermodynamically favorable. The best known materials in water thermolysis framework tend to cluster near the reduction and gas splitting equilibrium lines but none of them fulfill the conditions to favor both the reactions in practical situation. Non-equilibrium conditions can push the reaction toward the desired direction. Thus an open challenge is to identify and develop the materials which possess large positive $\Delta S_{\mathrm{REDUCTION}}$ and required $\Delta H_{\mathrm{REDUCTION}}$.

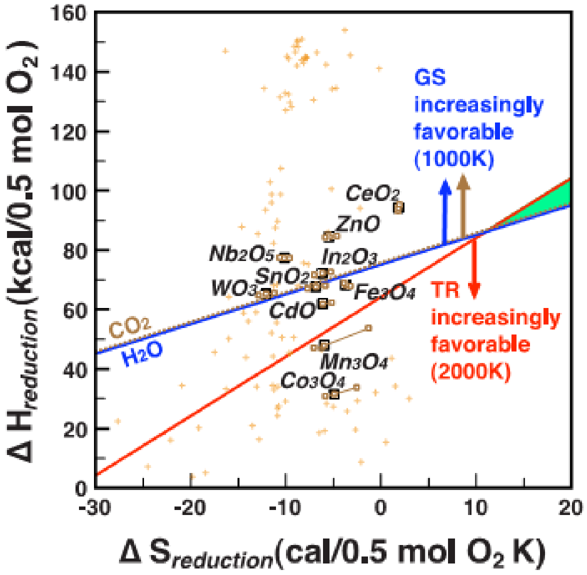

Figure 2. Thermodynamically favorable reduction and gas splitting region is plotted considering $\Delta S_{\mathrm{REDUCTION}}$ and $\Delta H_{\mathrm{REDUCTION}}$ which are actually material related properties. Materials are identified assuming T_{RED} and T_{GS} at 2000K and 1000K respectively. Reproduced by permission of American Physical Society from Ref.[21]

1.1.2. Determination of thermodynamic properties

To estimate the maximum possible oxygen nonstoichiometry(δ) of manganese based perovskites under thermodynamic equilibrium conditions at experimental temperature and oxygen partial pressure (pO_2), two approaches are known. As reported by Yang et. al,[23] a knowledge of partial molar enthalpy ΔH°(δ) and partial molar entropy ΔS°(δ) of oxygen vacancy formation as a function of δ, allows one to deduce the oxygen nonstoichiometry under any combinations of pO_2 and T as determined using eqn. 4.

$$\Delta G^{0}(\delta, T) = \Delta H^{0}(\delta)\text{-}T\Delta S^{0}(\delta) = -\frac{1}{2}RT\ \ln(p_{O_2}^{eq}(\delta, T)\ ---(4)$$

With the available experimental data of oxygen nonstoichiometry at various sets of pO_2 and T, the slope and intercept of the plots of $\ln p_{O_2}$vs T^{-1} gives the value of $\Delta H^0(\delta)$ and $\Delta S^0(\delta)$ respectively as a function of δ. ΔH^0 and ΔS^0 are independent of T and O_2 is behaving as an ideal gas are the considerations undertaken for the ease of calculation.

Another route is the defect modeling based calculations.[24, 25] Sr^{2+} doped $LaMnO_3$ is expressed as $La_{1-x}^{\times}Sr_{x}^{\prime}Mn_{1-x}^{\times}Mn_{x}^{\cdot}O_3$. The Kroger-Vink notation expresses the redox transition of tetravalent Mn ($Mn_{Mn}^{\cdot}$) to trivalent ($Mn_{Mn}^{\times}$) and then to divalent Mn ($Mn_{Mn}^{\prime}$) in terms of oxygen vacancy ($V_{O}^{\cdot\cdot}$) creation as follows,

$$2Mn_{Mn}^{\cdot} + O_{o}^{\times} = 2Mn_{Mn}^{\times} + V_{O}^{\cdot\cdot} + \frac{1}{2}O_2(g) ----(5)$$

$$\mathrm{Mn}_{\mathrm{Mn}}^{\cdot} + \mathrm{O}_{\mathrm{o}}^{\times} = \mathrm{Mn}_{\mathrm{Mn}}' + \mathrm{V}_{\mathrm{O}}^{\cdot\cdot} + \frac{1}{2}\mathrm{O}_2(\mathrm{g}) - - - - - (6)$$

The rate constant of reaction 5 (rate const. K_1) and reaction 6 (rate const. K_2) can be expressed as, $K_1 = \frac{[V_{O}^{\cdot\cdot}][Mn_{Mn}^{\times}]^2}{[O_{o}^{\times}][Mn_{Mn}^{\cdot}]^2}(p_{O_2}/p^0)^{1/2}$ and $K_2 = \frac{[V_{O}^{\cdot\cdot}]Mn_{Mn}']}{[O_{o}^{\times}]Mn_{Mn}^{\cdot}]}(p_{O_2}/p^0)^{1/2}$

Site and charge balances relate the K_1 with K_2 in terms of pO_2 and δ dependent linear function. The experimentally obtained pO_2 and δ values were used to obtain the K_1 with K_2 from the slope and intercept of those linear plots. However, the linear fitting of $\ln K_i$ (i=1, 2) vs T gives the ΔH_i^0 and ΔS_i^0 of the point defect reactions using eqn. (7).

$$-\ln K_i = \frac{\Delta H_i^0}{RT} - \frac{\Delta S_i^0}{R} - - - - (7)$$

ΔG^0 can be obtained using eqn. 4. The gibbs free energy of oxidation (ΔG_{oxd}) of the reduced oxides can be obtained using partial oxygen molar free energy (ΔG^0) as shown in eqn. 8. Oxidation is thermodynamically favorable only when, $\Delta G_{oxd} - \Delta G_{H_2O} < 0$ or $\Delta G_{oxd} - \Delta G_{CO_2} < 0$. ΔG_{H_2O} and ΔG_{CO_2} are the gibbs energy of oxidation of H_2 to H_2O and CO to CO_2 respectively.

$$\Delta G_{oxd} = \frac{\int_{\delta_i}^{\delta_f} \Delta G^0 d\delta}{\delta_i - \delta_f} - - - - (8)$$

Equilibrium H_2 yields and molar ratio of oxidant (n_{H_2O}) needed for that purpose can be obtained from the knowledge of ΔG^0 and ΔG_{H_2O} (it gives the equilibrium constant of H_2O dissociation, K_w) as shown below,

$$\Delta G^0(\delta_f, T) = RT\ln(\frac{n_{H_2O}K_w}{n_{H_2}}) - - - - (9)$$

1.1.3. Thermochemical cycles

Two step processes can be divided into two categories namely stoichiometric and nonstoichiometric cycles (**Table 1**). Stoichiometric oxides subcategorized in volatile and nonvolatile cycles depending on the chemical state of metal oxides during the course of reaction. A volatile redox cycle exhibits characteristic phase transitions, which includes ZnO/Zn, SnO/SnO_2, In_2O_3/In, CdO/Cd kind of redox pairs.[26, 27] High entropic gain due to the gaseous products formation during reduction makes volatile cycles thermodynamically more favorable, although solving the issue of recombination of product gases is a real technological challenge.[28] Nonvolatile cycles in which redox pairs remain in the condensed state, bypass the problem of product recombination and are more practical considering the reactor concept.

Table 1. Various categories of two-step redox pairs based on their chemical state. Adapted by permission of Elsevier from Ref.[16].

Category	**Cycle name**	**Redox pair**
Volatile	Zinc oxide Tin oxide	$ZnO(s) \leftrightarrow Zn(g)$ $SnO_2(s) \leftrightarrow SnO(g)$
Non-volatile (stoichiometric)	Iron oxide Ferrite Hercynite	$Fe_3O_4(s) \leftrightarrow FeO(s)$ $M_xFe_{3-x}O_4 \leftrightarrow xMO + (3-x)FeO$ $Fe_3O_4 + 3Al_2O_3 \rightarrow 3FeAl_2O_4$
Non-volatile (nonstoichiometric)	Ceria Doped Ceria Perovskite	$CeO_2(s) \leftrightarrow CeO_{2-\delta}(s)$ $M_XCe_{1-x}O_2(s) \leftrightarrow M_XCe_{1-x}O_{2-\delta}(s)$ $ABO_3(s) \leftrightarrow ABO_{3-\delta}(s)$

1.1.4. *Fe_3O_4 based cycles*

The first two step cycle was proposed by Nakamura et al[5] utilizing Fe_3O_4/FeO redox pair as shown in eqns.10 and 11.

$$\text{Thermal reduction: } Fe_3O_4 \rightarrow \text{ 3FeO} + {}^1\!/_2\,\mathrm{O_2} ------(10)$$

$$\text{Water Splitting: } \mathrm{3FeO + H_2O} \rightarrow \ Fe_3O_4 + \mathrm{H_2} ------(11)$$

The thermal reduction temperature in air (2573K) was found to exceed the melting point of Fe_3O_4 (1870 K) and FeO (1650 K).[5, 29] Alternating fusion and solidification of iron oxides results in coarsening of particles and deactivate the cycles with a rapid decrease in materials surface area. The iron-oxide phase diagram suggests the possibility of thermal reduction of Fe_3O_4 at lower temperature by reducing the oxygen partial pressure (< 10^{-7} atm), although the temperature is still high enough to melt the as formed FeO.[30-32] ZrO_2 or YSZ supports were used to dissolve Fe^{2+}, which prevent its melting. Interestingly, the oxidation rate of dissolved Fe^{2+} was found to be faster than undissolved one. This observation was attributed to the fact that the relatively slow diffusion of Fe^{2+} is the rate limiting step in undissolved ferrites while in dissolved sample the oxygen diffusion through the support-material lattice governs the rate.[33-36]

To reduce the reduction temperature further, various divalent metal ions (M= Zn, Ni, Co, Mg, and Mn) were incorporated in Fe_3O_4 lattice to form mixed ferrites ($M_xFe_{3-x}O_4$).[37-41] Notably, NiO (melting point= 2271 K) incorporation in iron oxide lattice solves the fusion problem and improved the performance, as well documented in literature.[13, 42, 43]

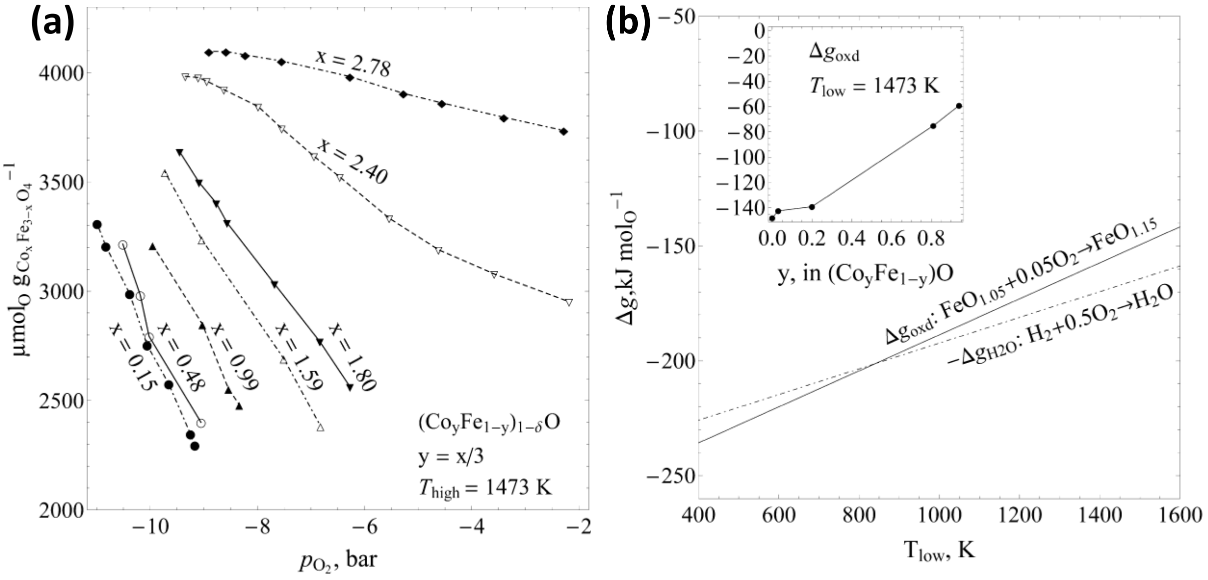

Figure 3. (a) Equilibrium O_2 yields due to the reduction of $Co_xFe_{3-x}O_4$ to $(Co_yFe_{1-y})_{1-\delta}O$. (b) Δg_{oxd} of wustite with temperature. Inset shows the effect on increasing Co concentration on Δg_{oxd}. Reproduced by permission of Elsevier from Ref.[16].

In $Co_xFe_{3-x}O_4$ spinel, increasing Co^{2+} content was found to increase the oxygen nonstoichiometry as shown in **Figure 3a**. Although with increasing reduction extent, the subsequent thermodynamic potential of oxidation has also decreased (Figure 3b). Complete removal of iron results in Co_3O_4 whose reduction product CoO is not capable of being reoxidized with CO_2 and H_2O.[13] Thus, thermodynamic calculation has concluded that intermediate composition of $M_xFe_{3-x}O_4$ (M=Ni, Co) with x=1, is the best one for maximizing fuel production.[40, 44] Addition of support (YSZ, ZrO_2, CaSZ etc.) with ferrite also improves the fuel production efficiency further.[39, 42, 43, 45, 46] Recent findings include improvement in reduction extent and reaction kinetics by atomic layer deposited $CoFe_2O_4$, $NiFe_2O_4$ on high surface area Al_2O_3 (hercynite cycle).[47, 48] Apart from Fe_3O_4/FeO, other spinel systems (M_3O_4/MO; M=Co, Mn) also have been investigated.[49] Thermodynamic calculation indicates MnO is not able the produce H_2 from H_2O more favorably like FeO in two step process.[13] However, Sturzenegger et al.[50] proposed Mn_2O_3/NaOH/MnO based cycle for H_2 production operating in three steps. $MnFe_2O_4$/Na_2CO_3/Fe_2O_3 multistep cycles were investigated by Kaneko et al.[51], but the cycle was not closed. Recently, Mn_3O_4/Na_2CO_3/MnO multistep cycle has been designed by Davis and coworkers,[22] obtained stoichiometric amount of H_2 and O_2 at significant low temperature (T_{max}=1123K), which is discussed in detail in Part 2 of present thesis. Nonstoichiometric cycles are found to be nonvolatile in general. The basic reaction of nonstoichiometric two-step process is explained exclusively in scheme 1. The fuel production and the solar-to-fuel conversion efficiency ($\eta_{solar\text{-}fuel}$) is directly dictated by the nonstoichiometry (δ). Tamura et al.[52] utilized the nonstoichiometry of Ni-Mn-ferrite system to produce H_2 by splitting H_2O at around 1073-1373 K. Unlike, Fe_3O_4/FeO phase transition, Ni-Mn-ferrite retains its spinel structure throughout.

1.1.5. CeO_2 cycles

CeO_2 is an old member in the field of automotive emission control catalysis and used extensively in surface oxidative catalysis, as an anode in SOFC. Otsuka et al first proposed application of δ phase of ceria for water decomposition in 1985.[53] In 2006, Abanades and Flamant demonstrated Ce_2O_3/CeO_2 based two-step thermochemical redox cycles (T_{RED} = 2273K) for H_2O splitting as shown in eqns.12 and 13.[54]

$$\text{Thermal reduction: } 2\mathrm{CeO_2} \rightarrow \mathrm{Ce_2O_3} + {}^{1}/_{2}\,\mathrm{O_2} ------(12)$$

$$\text{Water Splitting: } \mathrm{Ce_2O_3} + \mathrm{H_2O} \rightarrow 2\mathrm{CeO_2} + \mathrm{H_2} ------(13)$$

The high operating temperature (2273K), resulting in extensive sublimation and high energy losses due to reradiation, hinders the practical application of this cycle. However partial reduction of ceria ($CeO_2 \rightarrow CeO_{2-\delta}$) occurs at much lower temperature (T_{RED}= 1673K) under oxygen deficient atmosphere, recent studies are based on the change of oxidation state of a portion of CeO_2 as shown in eqn.14.[55]

$$\text{Thermal reduction: } \mathrm{CeO_2} \rightarrow \mathrm{CeO_{2-\delta}} + {}^{\delta}/_{2}\,\mathrm{O_2} ------(14)$$

CeO_2 can be stable in its fluorite structure upto δ of 0.35.[56] Thermodynamic analysis by Panlener et al.[57, 58] provide details of the oxygen nonstoichiometry of ceria at various temperatures and oxygen partial pressures. Thermal reduction of CeO_2 results in nonstoichiometry (δ) of 0.066 (T_{RED}= 1773K, pO_2 =10^{-5}atm) and further produces almost stoichiometric quantity of H_2.[19] Although the oxygen exchange capacity of CeO_2 is lower than iron oxide based cycles, but the sintering of CeO_2 is also less significant which avoid the requirements of various support.[59] Moreover diffusion of oxygen is found to be an order faster in CeO_2 than the diffusion of Fe^{2+} in ferrite cycles, rendering its faster kinetics.[46, 60-62]

1.1.6. Doped CeO_2 cycles

Oxidation kinetics of CeO_2 is quite favorable, but the drawback is the poor reduction ability despite the high reduction temperature. CeO_2 has been modified by several of metal ions and metal oxides to alter its thermodynamic and kinetic properties. Divalent (Ca, Sr, Mg)[63-67] and trivalent (La, Sc, Gd, Y, Cr, Sm)[68-70] cation dopants have been incorporated in the fluorite lattice to create intrinsic vacancies, which in turn promote the oxygen diffusion. In particular, La^{3+} is reported to improve the thermal stability during multiple cycling.[70] Addition of Cr^{3+} in CeO_2 observed to produce H_2 at a significantly low temperature while Ca^{2+} and Mg^{2+} improve the thermal reduction temperature and fuel productivity.[63, 69] Addition of tetravalent dopants (Zr, Ti, Hf, Sn)[68] is found to be more beneficial than di- and tri-valent dopants. As shown in **Figure 4a**, the reduction capability of CeO_2 increases significantly by the addition of the smaller Zr^{4+} ions (which promote lattice deformation of CeO_2). Thermodynamic evaluation shows the increase in reduction extent of Ce^{4+} increases with the introduction of Zr^{4+}, due to a decrease in partial oxygen molar enthalpy (Figure 4b).[68, 71-74] Thermodynamic calculations indicate that the Gibbs free energy of oxidation with H_2O ($\Delta G_{ox,water}$) becomes more positive with increasing Zr content [75] for all temperatures. As shown in Figure 4c, the quantity of H_2 reaches a maximum at $T \leq 900K$ and $T<400K$ for CeO_2 and $Zr_{0.2}Ce_{0.8}O_2$ respectively. Increase in water concentration can promote oxidation of $Zr_xCe_{1-x}O_2$ at higher temperature, but this results in an energy penalty. To further enhance the oxidation kinetics and heat transfer rate, various porus CeO_2 structures have been tested as described in later section.

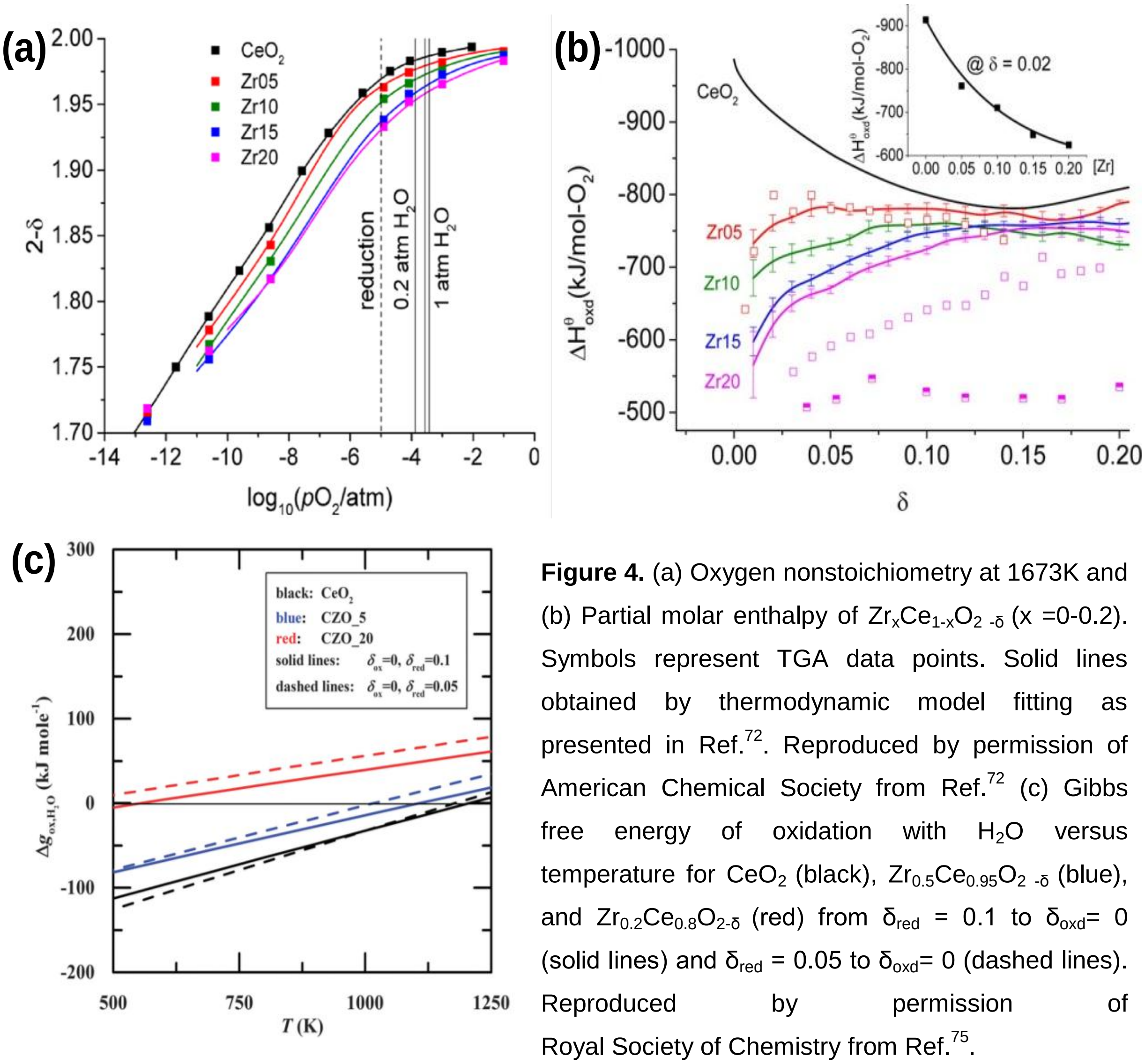

Figure 4. (a) Oxygen nonstoichiometry at 1673K and (b) Partial molar enthalpy of $Zr_xCe_{1-x}O_{2-\delta}$ (x =0-0.2). Symbols represent TGA data points. Solid lines obtained by thermodynamic model fitting as presented in Ref.[72]. Reproduced by permission of American Chemical Society from Ref.[72] (c) Gibbs free energy of oxidation with H_2O versus temperature for CeO_2 (black), $Zr_{0.5}Ce_{0.95}O_{2-\delta}$ (blue), and $Zr_{0.2}Ce_{0.8}O_{2-\delta}$ (red) from δ_{red} = 0.1 to δ_{oxd}= 0 (solid lines) and δ_{red} = 0.05 to δ_{oxd}= 0 (dashed lines). Reproduced by permission of Royal Society of Chemistry from Ref.[75].

1.1.7. Perovskites based thermochemical cycles

The mineral $CaTiO_3$ was discovered by Gustav Rose (1839) in Ural Mountain and named after a Russian mineralogist, Von Perovski. Since then immense investigations have been carried out on the perovskite family of materials due to the plethora of applications spanning energy production, solid oxide fuel cell electrode, high T_c superconductors to oxygen separation membranes, sensors, multiferroics and many more.[7, 76-78] Perovskite structure has the general stoichiometry of ABX_3 (A and B are the cations with $r_A > r_B$ and X is the anion). In $A^{3+}B^{3+}O_3$ type perovskite, with reducing A cation radii, a point will be reached when A will be too small to be in contact with the anions in the cubic structure resulting in the bending of

B-O-B links and tilting of the BO_6 octahedra to bring anions into contact with the A. The degree of distortion is expressed by tolerance factor (τ) as shown below,

$$\tau = \frac{r_A + r_O}{\sqrt{2}(r_B + r_O)} ----(15)$$

Lower the value of $\tau < 1$, more the structure is distorted from cubic. This distortion from cubic to orthorhombic is shown in **Figure 5**.

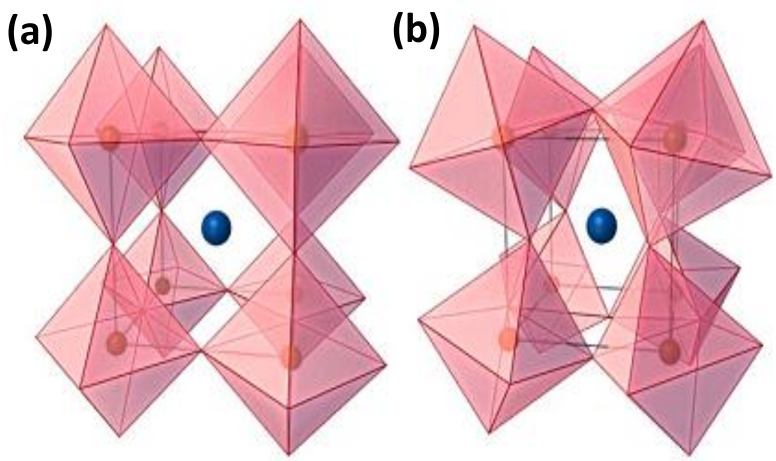

Figure 5. Distortion from (a) cubic to (b) orthorhombic perovskite.

For $Ln_{1-x}A_xMnO_3$ based perovskites four tilt systems are most common: $a^-a^-a^-$(rhombohedral, R-3c), $a^0a^0c^-$(tetragonal, I4/mcm), $a^-b^0a^-$(orthorhombic, Imma) and $a^-b^+a^-$(orthorhombic, Pnma). Lattice energy calculations which optimize the attractive columbic interaction between ions can predict the preferable tilt octahedra.[79, 80] However, these changes in tilt system are linked to the changes in various properties of perovskite materials. In addition to the tolerance factor the substantial difference between the ionic radii of Ln^{3+} and A^{2+} cations (defined by variance, σ^2)[81] are found to affect the curie temperature, magnetic phase transition temperature of $Ln_{1-x}A_xMnO_3$ perovskites significantly. The role of σ^2 is explained in brief in section 1.4.2.

$La_{1-x}Sr_xMO_3$ (M=Mn, Fe) perovskites were experimentally investigated by Nalbandian et al.[82-85] for syngas production using CH_4 and H_2O as reactants around 1273K. The partial oxidation of CH_4 was employed to create oxygen nonstoichiometry as shown in eqn. 16 followed by the isothermal oxidation with H_2O to produce H_2 with material regeneration.[82]

$$\mathrm{CH_4\ reduction: MO_{oxd} + CH_4 \rightarrow\ MO_{red} + \alpha CO + \beta CO_2 + \gamma H_2 + \varepsilon H_2O} ------(16)$$

Substitution of $La_{1-x}Sr_xFeO_3$ with transition metals (Cr, Co, Ni, Cu)[85] has improved the performance. $La_{0.7}Sr_{0.3}Cr_{0.1}Fe_{0.9}O_3$ is reported to show the highest production of H_2 on addition of 5% NiO[85], although significant coke formation has been observed. The oxidation and reduction steps were combined in a membrane reactor toward a continuous and isothermal production of H_2. These membranes are consisting of two compartments separated by dense membranes of these mixed ionic-electronic conductive perovskite. Through one compartment reducing gas (CH_4/CO) enters while H_2O(v) enters through another. Oxygen vacancy created on reductive site transfer to oxidative site through membranes and get annihilated up by the splitting of H_2O(v) and produces H_2. However, considering the environmental point of view thermochemical processes involving entirely water as oxidant instead of fossil fuel originated reactants such as methane or CO are the most acceptable.

Occurrence of the large degree of nonstoichiometry at elevated temperatures and reversible reoxidation incorporating oxygen from H_2O and/or CO_2 are the basic criteria for a material to be useful in this area and to further boost the solar to fuel conversion efficiency ($\eta_{solar\text{-}to\text{-}fuel}$). Nonstoichiometric $ABO_{3-\delta}$ family of perovskites is started to being explored very recently due to its higher reduction extent than CeO_2 even at considerably low temperature.[83]
Substitution can be done on both A and B sites, and immediate consideration of greater number of possible potential materials than ceria based oxides, encourage one to investigate them for further reoxidation thermodynamics.

i) Substitution of alkaline earth ions in the A site

$La_{1-x}Sr_xMnO_3$ family of perovskites has been investigated in the two-step thermochemical splitting of H_2O and CO_2 recently for H_2 and CO production respectively. In $La_{1-x}Sr_xMnO_3$ (LSM_x) oxides, substitution of trivalent La by divalent Sr creates Mn^{3+}/ Mn^{4+} redox active pairs. Scheffe et al.[83] have estimated the high-temperature nonstoichiometry of LSM perovskites, by extrapolating the low-temperature experimental nonstoichiometry data based on an appropriate defect model. Greater oxygen nonstoichiometry of LSM perovskites in comparison to ceria is thermodynamically predicted and proved subsequently by experiments. $La_{0.65}Sr_{0.35}MnO_3$ (LSM35) reduces to greater extent than CeO_2 under similar pO_2 and temperature (T_{red}=1773K). A experimental study of the thermochemical H_2O splitting of $La_{1-x}Sr_xMnO_3$ (x=0-0.5) by Yang et al.[23] gave a H_2/O_2 production ratio close to 2 even during multiple cycling. Yang et al.[23] have performed the thermodynamic evaluation of $La_{1-x}Sr_xMnO_3$ (x=0-0.5) by the method described in section 1.1.2 (eqn. 4). They reach a similar conclusion as Scheffe et al.[83], that increasing Sr^{2+} substitution decrease the partial molar enthalpy and entropy of reduction. This effect is greater in these perovskites than in CeO_2 for all the composition of x investigated (**Figure 6a**). Demont et al.[86] have reported a similar observation for CO_2 splitting. Although with increasing Sr^{2+} content the oxidation thermodynamics become growingly unfavorable. The Gibbs free energy of oxidation is more negative for CeO_2 than for LSM at all accessible temperatures. Applying little excess of H_2O than the molar nonstoichiometry oxidizes $CeO_{2-\delta}$ back CeO_2 in its starting composition, while for LSMs the amount of H_2O needed is largely excess and causes an energy penalty for heating this excess steam. Nevertheless, considering complete heat recovery from H_2O, the solar-to-fuel efficiency is thermodynamically predicted to be higher than CeO_2 because of the greater oxygen nonstoichiometry of LSM perovskites (Figure 6b).[67, 83]

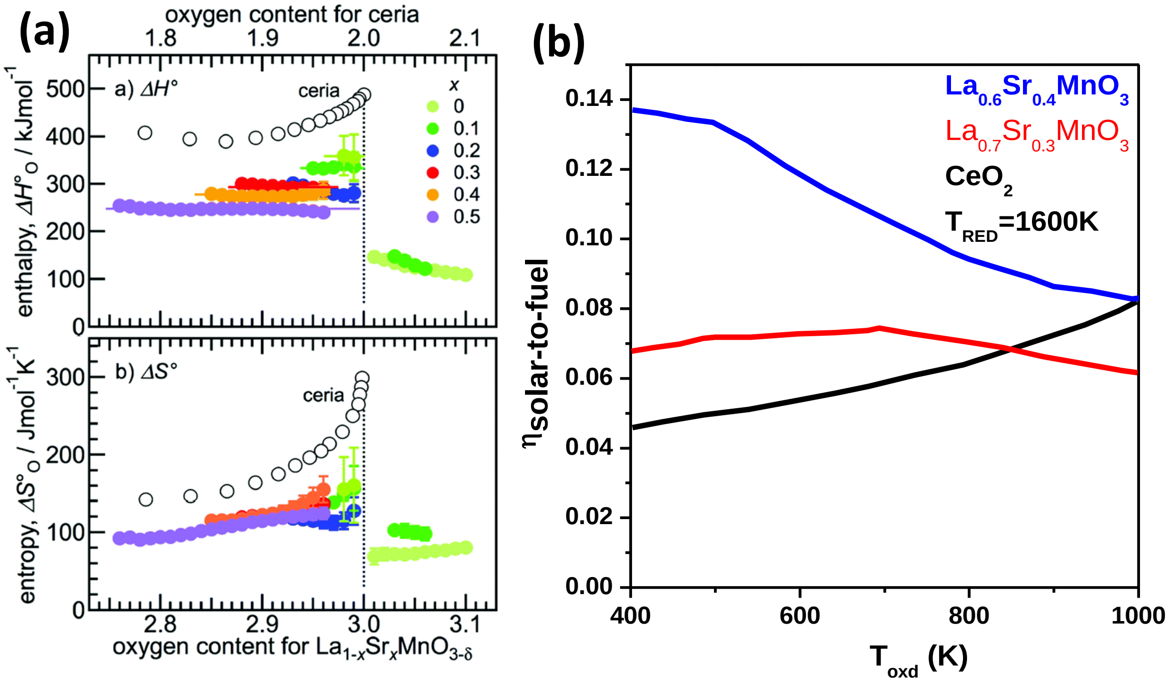

Figure 6. Partial molar (a) enthalpy and entropy of reduction as functions of oxygen non-stoichiometry of $La_{1-x}Sr_xMnO_3$ (x=0-0.5) perovskite. Reproduced by permission of Royal Society of Chemistry from Ref.[23]. (b) Solar−fuel energy conversion efficiency vs the oxidation temperature for $La_{1-x}Sr_xMnO_3$ (x=0.4, 0.3) and CeO_2 reduced at 1600 K. Adapted by permission of American Chemical Society from Ref.[83].

ii) B site substitution

Partial substitution of the catalytically active ‘B’ sites by some aliovalent transition metal cations can enhance the catalytic activity because of synergistic valence changes and micro-structural defects introduced into the lattice and are popular in areas such as oxygen separation membranes, sensors, multiferroics and colossal magnetoresistance.[76] Considering both A and B doping schemes in ABO_3 type perovskite, the number of possible combinations are quite large and out of them very few of B site dopants have been tried for the application in this field as explained below.

Al^{3+} Substitution : McDaniel et al.[87] first investigated Al substituted LSM_x (LSMA) for two-step H_2O and CO_2 splitting process. LSMA perovskites produces 9 times more H_2 and 6 times more CO than CeO_2, without altering the reaction kinetics significantly. Deml et al.[88] has performed DFT calculation to correlate the oxygen vacancy formation energy with solar to fuel production capacity of different LSMA composites. Recent investigation of Demont et al.[89] has found almost no increase in the performance of LSM_x due to Al doping whereas significant increment is reported by Cooper et al. in contrast.[24]

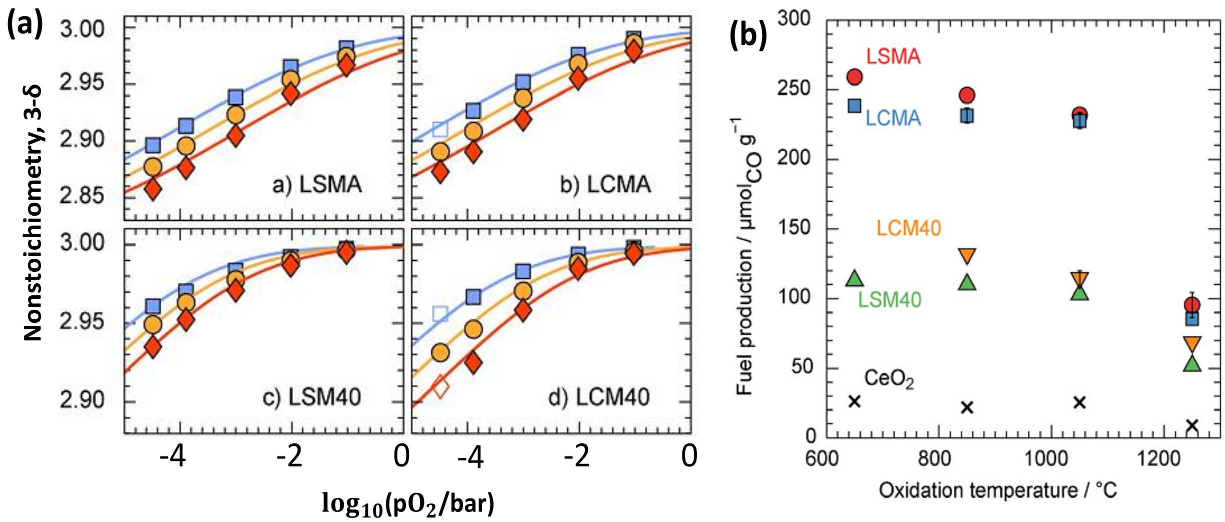

Figure 7. (a) Equilibrium oxygen nonstoichiometry as a function of oxygen partial pressure at three different reduction temperature as indicated by blue (1300°C), yellow (1350°C) and red (1400°C) colors and (b) Evolved CO yield (measurement time = 5 mins) as a function of CO_2 splitting temperature (T_{RED} is 1250°C) of $La_{1-x}A_xMn_{1-y}Al_yO_3$. Four different compositions of perovskites are used: $La_{0.6}Sr_{0.4}MnO_3$ (LSM40), $La_{0.6}Ca_{0.4}MnO_3$(LCM40), $La_{0.6}Sr_{0.4}Mn_{0.6}Al_{0.4}O_3$(LSMA) and $La_{0.6}Ca_{0.4}Mn_{0.6}Al_{0.4}O_3$(LCMA). Reproduced by permission of Wiley-VCH from Ref. [24].

Notably, Steinfeld and coworkers has found the beneficial role of Al doping in suppressing the carbonate formation through separate set of experiments.[90] Recently Steinfeld and co-workers[24, 25] have conducted detailed thermodynamic and experimental study to elucidate the effect of Al doping on perovskite lattice for thermochemical fuel CO production. Al doping leads to superior oxygen nonstoichiometry as well as decrease in partial molar enthalpy of vacancy formation (**Figure 7a**). $\Delta G_{oxd} - \Delta G_{CO_2} < 0$ has been observed for the LSMA and LCMA compositions at lower oxidation temperature, as reflected also in their CO production plot shown in Figure 7b.

Other metal ions substitution: Mg^{2+} incorporation in LSM_x shows greater resistance to sintering during two step cycles, however, fuel production is not found to improve in comparison of LSM_x.[89] Other than manganites combination of few other transition metal (Fe, Co, Cr) based perovskites have been reported in literature.[91-93]

1.1.8. Isothermal thermochemical fuel production

Thermodynamic considerations demand $T_{red} > T_{oxd}$ as the condition in the above two steps CO_2 splitting steps (TSCS). TSCS involving a temperature swing between T_{red} and T_{oxd}, has been studied with various oxides wherein large changes in stoichiometry are favored at higher T_{red} (low oxygen partial pressure) while reoxidation occurs at a lower T_{oxd}.[19, 68-70, 83, 94-97] Such cyclic rotation between T_{red} and T_{oxd} is accompanied by irreversible heat losses causing reduction in thermodynamic efficiency. Furthermore, time loss to shuttle between T_{red} and T_{oxd} is also an adverse factor. The efficiency penalty becomes more prominent in the case of metal oxides with a high specific heat,[83] continuous swing over a large temperature window creating thermal stress on the reactive substrate as well as on the system components.[98-100] In this context, it is found desirable to employ isothermal splitting of CO_2 (ITCS) which allows the two processes in the redox cycle to occur at the same temperature, since it depends on the large pressure swing in the gas composition between reduction and oxidation to produce nonstoichiometry. The driving force for oxidation at high temperature is lower, thus less amount of fuel/per cycle is expected in isothermal cycle than two- temperature one. The unshaded region in **Figure 8a** depicts the available operational region in isothermal cycle. In the shaded area the p_{O_2} during reduction is higher than the p_{O_2} established by H_2O decomposition, hence is not sufficient to produce H_2 at that temperature. Ermanoski et. al has derived a general formula which relates the isothermal temperature (T_{iso}) with p_{O_2}, and p_{H_2O}/p_{H_2} as shown in eqn. 17,

$$T_{iso} = \frac{-\Delta H^0}{R\left(\ln p_{O_2}^{1/2} - \ln \frac{p_{H_2O}}{p_{H_2}}\right) - \Delta S^0} ------ (17)$$

Figure 8b is plotted based on eqn. 17, which clearly conveys that decreasing T_{iso} either requires an increase in n_{water/H_2} or decrease in p_{O_2}.

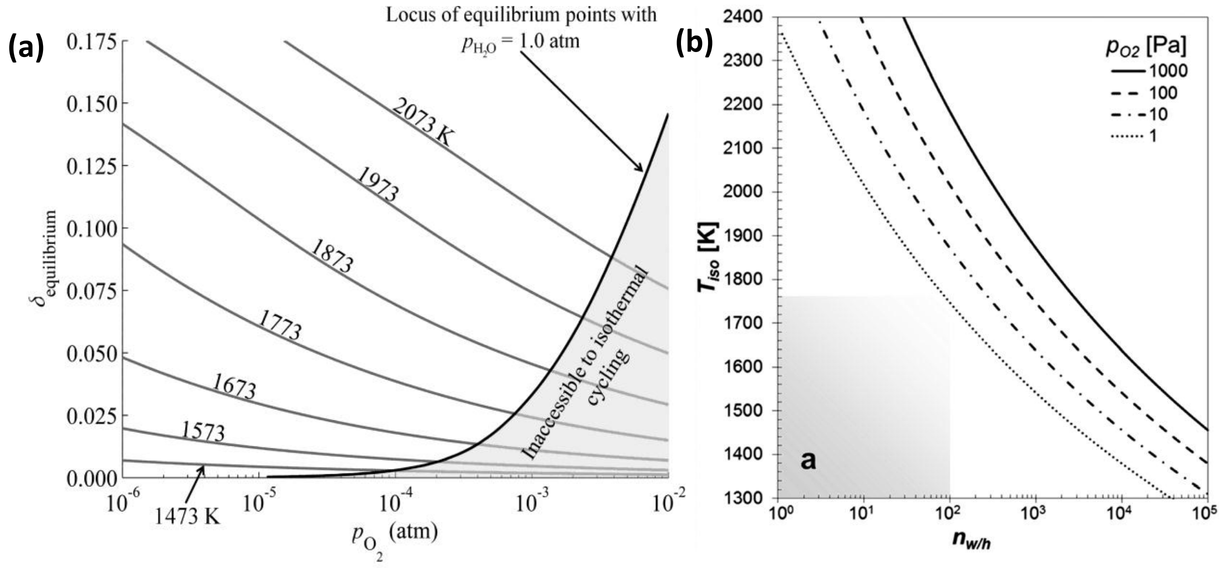

Figure 8. (a) δ-T-p_{O_2}state diagram of CeO_2. Reproduced by permission of American Chemical Society from Ref.[96] (b) Relationship of T_{iso} with n_{water/H_2}at different p_{O_2}. Constant value of $\Delta H^0(250.8\ \mathrm{kJ/mol})$ and $\Delta S^0(57.35\ \mathrm{J/mol/K})$ has been considered for derivation. Reproduced by permission of Royal Society of Chemistry from Ref.[101].

The major efficiency parameters are solid state heat recovery in TSCS and fluid phase heat recovery in ITCS.[99, 101, 102] CeO_2, which operates solely based on oxygen nonstoichiometry, is thermodynamically predicted to have conversion efficiencies of 18% during the isothermal splitting of CO_2 at 1773K.[96] Venstrom et. al[103] have shown the rate of ITCS to be comparable to that of TSCS. The CO production rate by CeO_2 is 284 µmol/g/hr, which is not very satisfactory considering the high temperature involved (1773K). The efficiency of CeO_2 based isothermal cycle is predicted to increase with increasing temperature,[98] but the oxide sublimes at high temperatures (>1773K)[70, 104]. In addition, CeO_2 has negligible reducibility at lower temperatures(T<1773K).[23, 98] The oxygen nonstoichiometry (δ_{red}) obtained at 1673K is ≤ 0.03,[57, 70] resulting lower yields of O_2 as well as CO.

1.1.9. Syngas production and role of porous morphology

Syngas ($CO+H_2$) a chemical feedstock that can be directly converted to liquid fuels, is an alternative route of transitioning away from a fossil-fuel-based system. The oxygen storage capacity of CeO_2 and $Sm_{0.15}Ce_{0.85}O_{1.925}$ have been explored for the production of syngas and CH_4 from the mixture of $CO_2 + H_2O$ with and without the presence of additional metal ion catalyst respectively.[55] Thermodynamic analysis by Krenzke et. al suggest that the CeO_2 –CH_4 based system can produce syngas even at 1223K with plausible solar-to-fuel efficiency of 40% without any heat recovery.[105] Furler et al.[104] have applied CeO_2 felt for syngas production in the solar cavity receiver via simultaneous splitting of H_2O and CO_2 in temperature range of 1800K-1100K. The optimum ratio of H_2: CO for the production of liquid hydrocarbon fuel is 1.7-2, generated by adjusting the CO_2/ H_2O molar feeding ratio. Multiple cycling for long duration yields a stable syngas composition, which demonstrates the feasibility of CeO_2-based redox cycles to produce constant amount of syngas in a solar reactor that closely replicates the practical solar fuel applications.[104] Deposition of CeO_2 due to high temperature sublimation hinders the entering of radiative power inside the reactor and causes a decrease in fuel production. However, a remarkable enhancement of $(\eta_{solar\text{-}to\text{-}fuel})_{peak}$ and $(\eta_{solar\text{-}to\text{-}fuel})_{average}$ to 3.53% and 1.73% respectively is obtained by engineering the porosity of ceria, which allows deeper penetration of solar radiation and higher mass loading.

As stated above efficient and uniform heat transfer during endothermal reduction and rapid oxidation kinetics are the most desirable characteristics needed to achieve higher solar to fuel conversion efficiency. Reticulated porous structure of CeO_2, composed of millimeter and micrometer scale pores together shown to be highly active and reaches ~10 times more CO production rate than non porus counterpart.[106, 107] While macropores enable the higher volumetric absorption of solar radiation, the micropores give high oxidation kinetics due to their high surface area. Different templates have been used for this purpose to give three dimensional porus structure.[108, 109]

1.1.10. Solar reactor

For all of the aforementioned processes, the heat to perform the chemical reaction can be supplied through the concentration of direct solar irradiation with optical systems like mirrors. Solar concentrating technologies working with a point focusing system is the only viable option which can provide the necessary high temperatures with high efficiency. Such systems are basically parabolic dish or central receiver systems as shown in **Figure 9**. The chemical reactor should be placed in the focus of the system and allows the radiation to enter the reactor either through a quartz window or it is absorbed on a black surface and channelized to the reactants by convection and conduction. There is a technological challenge in the development of an efficient solar energy collector and solar reactor. More than a decade of research has led to the development of DLR monolithic reactor (German Aerospace Centre), [110] foam reactor (Kodama et.al.), [111] rotary type reactor(Tokyo Institute of Technology) [112] and the CR5 (Sandia National Laboratories). [113]

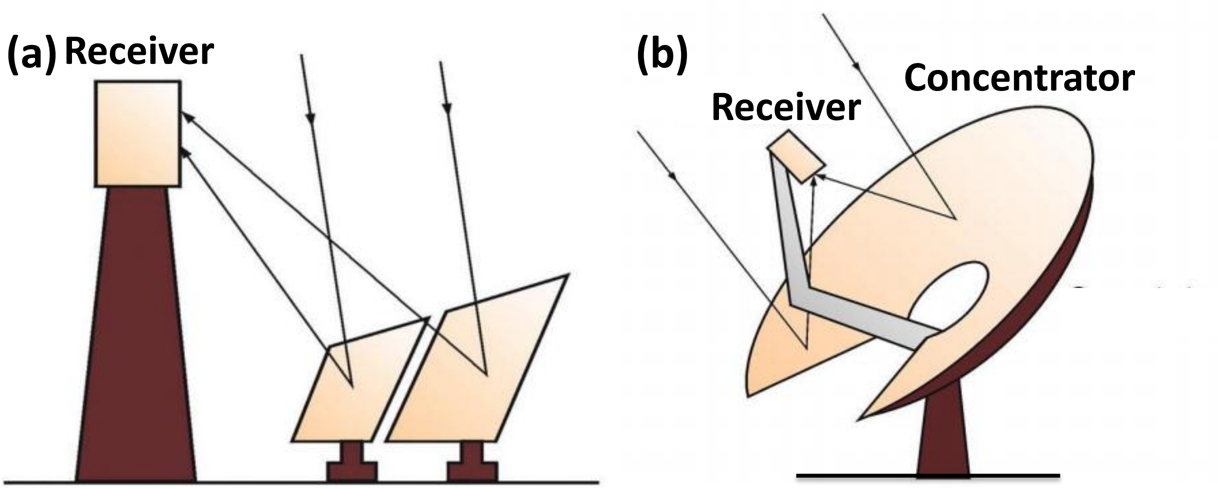

Figure 9. Schematic of (a) central receiver and (b) solar dish system. Reproduced by permission of Multidisciplinary Digital Publishing Institute from Ref.[14].

In 2010, porous monolithic CeO_2 was exploited for H_2 (CO) production by direct irradiation of solar cavity receiver by Chueh et al.[94] The experimental setup including a high flux solar simulator is presented in **Figure 10.** The solar reactor configuration in Figure 10b shows the entrance of solar radiation through a quartz windowed aperture. The outlet for product gases is axial to the inlet of reactant gases. O_2 production begins at 900°C, reaches the peak value, then dies down. The kinetics of O_2 production depends mainly on the heating rate and there is a heating gradient from the outer to inner shell of the cavity. The CO (H_2) production rate is much faster and unaffected due to isothermal heating temperature. Chueh et al. performed 23 cycles in the solar reactor, with a net solar to fuel conversion efficiency ($\eta_{\text{solar-to-fuel}}$) of 0.4% (without considering any heat recovery) and a peak efficiency of 0.7% and 0.8% for H_2O and CO_2 dissociation respectively.

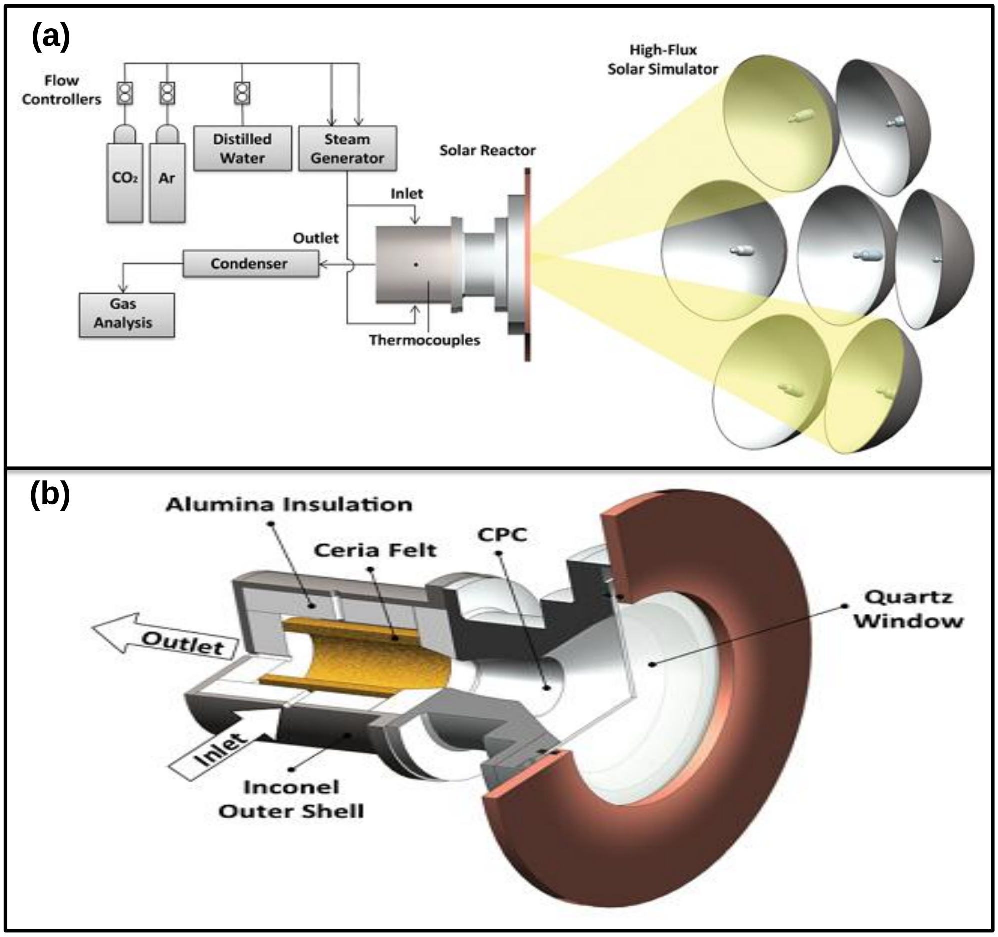

Figure 10. (a) Reaction set up of ETH's High flux solar simulator and (b) Schematic of solar reactor for performing two step thermochemical fuel production of CeO_2. Reproduced by permission of Royal Society of Chemistry from Ref.[104].

1.2. Scope of the present investigations

Nonvolatile nonstoichiometric oxide cycles are important in terms of easy separation of gaseous products, reactor integration and efficiency point of view. In this context, CeO_2 is established as a state of art material in the areas of thermochemical H_2, CO and syngas production mainly because of its reasonably good oxidation thermodynamics. Disadvantages, such as high T_{RED} and lower extent of reduction, however, limit its application. Interestingly, La-Sr-Mn oxide perovskites are promising candidates because of their superior reducibility even at lower T_{RED} than CeO_2. Mn based perovskites operate involving the Mn^{3+}/ Mn^{4+} redox pair created due to Sr^{2+} substitution, and increasing Sr^{2+} content increases its reducibility. Oxidation thermodynamics of these perovskites is somewhat unfavorable and further work is needed to find an alternative to oxide perovskites. With this purpose, we have employed La-Ca-Mn based perovskites (section 1.4.1). Increasing the Ca content increases the reduction extent. Notably $La_{0.5}Ca_{0.5}MnO_3$ evolves more amount of CO than $La_{0.5}Sr_{0.5}MnO_3$ as well as CeO_2. With in depth investigation we have established the structural relationship with this extraordinary property shown by Ca- family oxides.

$Ln_{0.5}A_{0.5}MnO_3$ (Ln= La, Nd, Sm, Gd, Dy and Y; A=Sr, Ca) family of perovskites show the good performances in various fields such as SOFC electrodes, catalysis, magnetism depending on the different sizes of Ln and A cations. We have employed the $Ln_{0.5}A_{0.5}MnO_3$ family of perovskites for investigating the thermochemical production of CO and H_2 from CO_2 and H_2O respectively. Our studies include the effect of decreasing the size of the rare earth ions to affect the O_2 and CO yields (section 1.4.2). Small rare earth ions cause a decrease in the tolerance factor (τ) and give rise to high O_2 and CO yields. Furthermore, the size difference between Ln^{3+} and A^{2+} cations acts as a crucial factor for controlling the reduction temperature. Thus the present study finds $Y_{0.5}Sr_{0.5}MnO_3$ to be an ideal material and yielding record amounts of O_2 and CO at as low as 1473K-1173K redox temperature range. Many possibilities with ABO_3 type perovskites are possible considering the various combinations of the A and B ions.

Replacement of Mn^{3+} with aliovalent ions is known to alter the properties because of synergistic valence change and local defect inducing properties. This motivated us to investigate the effect of partial substitution of Mn^{3+} with various other +3 ions such as Al, Ga and Sc and their high temperature fuel production capability (section 1.4.3). The performance is in the order of

Sc>Ga>Al. All these partially substituted perovskites showed far better performance than the undoped one.

Thermodynamic evaluation demands $T_{RED} > T_{OXD}$, but it is associated with the disadvantages like irreversible heat loss, material degradation and stress on the reactor components. Hence thermochemical fuel production using CeO_2 isothermally has been reported in literature at 1773K. So, CeO_2 suffers due to sublimation at 1773K. We have performed the isothermal thermochemical splitting of CO_2 using Ln-Sr-Mn based perovskites for the first time (section 1.4.4). Encouraging results are obtained with perovskites among which the performance of $Y_{0.5}Sr_{0.5}MnO_3$ is notable which gives higher amount of CO than CeO_2 even at 1573K isotherm.

1.3. Experimental Section

1.3.1. Materials:

La_2O_3 (Sigma-Aldrich, 99.9%), $SrCO_3$ (Merck, 99.9%), $CaCO_3$ (Sigma-Aldrich, ≥ 99.0%), MnO_2 (Sigma-Aldrich, ≥ 99.0%), Sc_2O_3 (Sigma-Aldrich, 99.9%), HNO_3(SD Fine, 70%), $La_{0.65}Sr_{0.35}MnO_3$ (Aldrich) and CeO_2 (Sigma-Aldrich, ≥ 99.9%) $La(NO_{3)3},6H_2O$ (Sigma-Aldrich, ≥ 99.0%)), $Sr(NO_3)_2$ (Fluka, 99.995%)), $Al(NO_{3)3},6H_2O$(Merck, 99.997%), $Ga(NO_{3)3},6H_2O$(Merck, 99.9%), $Mn(NO_3)_{3,}$ $9H_2O$(Merck), Ethylene diamine tetra acetic acid (EDTA, Aldrich, 99.995%) and Anhydrous Citric acid (Merck).

1.3.2. Synthesis

i) $La_{1-x}Ca_xMnO_3$ compositions were prepared by solid state reactions of stoichiometric amounts of La_2O_3, $CaCO_3$ and MnO_2. La_2O_3 was heated at 950°C for 12 hrs before weighing. Weighted precursors were mixed and ground well and the powders taken in a alumina crucible and fired at 1000°C for 2 hrs and 1450°C for 8hr. Intermediate grinding was carried out after every 4 hrs. For $La_{1-x}Sr_xMnO_3$ compounds, $SrCO_3$ was used as a precursor instead of $CaCO_3$, keeping all the other reaction procedures same. LSM 35 ($La_{0.65}Sr_{0.35}MnO_3$) and CeO_2 of commercial grade were purchased from Sigma-Aldrich. $Sm_{0.50}Sr_{0.50}MnO_3$ (SmSM 50) was prepared by the same solid state reaction procedures using stoichiometric amounts of Sm_2O_3, $SrCO_3$ and MnO_2. Sm_2O_3 was also preheated like La_2O_3 before weighing. $La_{1-x}MnO_3$ (x=0.1, 0.2) and $La_{0.7}Sr_{0.3}FeO_3$ was prepared by modified Pecini method. Stoichiometric amounts of metal nitrate precursors,

$M^x(NO_3)_x.yH_2O$ were dissolved in water in the presence of excess citric acid and ethylene glycol at room temperature. The gel was formed at 80°C, followed by drying at oven of 200°C for 12 hrs. The product was heated at 800°C for 6 hrs to remove the organics. Further heating at 1200°C for 6 hrs forms the final phase.

ii) $Ln_{0.5}Sr_{0.5}MnO_3$ (LnSM50) compositions were synthesized by solid state reactions of a mixture of stoichiometric quantities of Ln_2O_3, $SrCO_3$ and MnO_2. Ln_2O_3 (Ln= La, Nd, Sm, Gd, Dy and Y) was heated at 950°C for 12 hrs prior to weighing. These precursors were mixed, ground well and the powders transferred in an alumina crucible and heated at 1000°C for 2 hrs and 1450°C for 8hrs. Intermediate grinding was carried out after every 4 hrs of heating. $CaCO_3$ was used as a precursor instead of $SrCO_3$ to synthesize $Ln_{0.5}Ca_{0.5}MnO_3$ (LnCM50), keeping the other reaction conditions same.

iii) $La_{0.5}Sr_{0.5}Mn_{1-x}A_xO_3$ (A= Al, Ga and Sc) compositions were prepared by modified Pecini route. The synthetic methods specifically the heating conditions are summarized in **Table 2**.

Table 2. Summary of the synthesis conditions of perovskites.

Composition	x	Precursors	Synthesis method	Heating conditions
$La_{0.5}Sr_{0.5}Mn_{1-x}Al_xO_3$	0,0.25, 0.35,0.5	$La(NO_3)_3$,$6H_2O$ (Sigma-Aldrich),$Sr(NO_3)_2$(Fluka), $Al(NO_3)_3$,$6H_2O$(Merck),, $Mn(NO_3)_3$, $9H_2O$(Merck)	Sol-Gel	80°C for 8hrs, 200°C for 12hrs, 800°C for 10hrs, 1400°C for10hrs
$La_{0.5}Sr_{0.5}Mn_{1-x}Ga_xO_3$	0.25,0.35,0.5	$La(NO_3)_3$,$6H_2O$, $Sr(NO_3)_2$, $Ga(NO_3)_3$,$6H_2O$(Merck), $Mn(NO_3)_3$, $9H_2O$	Sol-Gel	80°C for 8hrs, 200°C for 12hrs,800°C for 10 hrs, 1400°C for10hrs
$La_{0.5}Sr_{0.5}Mn_{1-x}Sc_xO_3$	0.05,0.1, 0.15, 0.25	$La(NO_3)_3$,$6H_2O$, $Sr(NO_3)_2$,Sc_2O_3(Sigma-Aldrich), HNO_3(70%), $Mn(NO_3)_3$, $9H_2O$	Sol-Gel	80°C for 8hrs, 200°C for 12hrs,800°C for 6hrs, 1400°C for10hrs

Stoichiometric amounts of metal nitrate precursors were dissolved in water. Sc_2O_3 was converted to nitrate by heating in boiling HNO_3 at 150°C for 0.5 hrs. EDTA (EDTA: metal cations molar ratio= 1:1) dissolved in aqueous ammonia, slowly added to metal ions solution with stirring, combined with citric acid (citric acid: metal cations molar ratio= 1:2) followed by excess addition of aqueous ammonia to make the final solution become transparent (final pH=10). The gel was formed at 80°C, followed by drying at 200°C for 12 hrs. The product was heated at 800°C for 6 hrs to remove the organics. Further heating at 1400°C for 10 hrs forms the final phase.

iv) For isothermal thermochemical CO_2 splitting tests, reactive oxides were obtained by cutting porus monolith. Initially, $La_{1-x}Sr_xMnO_3$ (x=0.3-0.5), $Y_{0.5}Sr_{0.5}MnO_3$ (YSM50) and CeO_2 are prepared by modified Pecini route. Stoichiometric amounts of metal nitrate precursors were dissolved in water followed by slow addition of EDTA dissolved in NH_4OH and citric acid (EDTA: citric acid: metal cations molar ratio= 1:1:2). Excess NH_4OH was added to make the final solution become transparent (pH=10). The gel was formed at 80°C, followed by 12 hrs drying at 200°C. The product was heated at 800°C (5 hrs) under air to remove the organics. To obtain the porous monolith these powder particles were mixed with isopropanol and the thick paste was mounted on a cylindrical alumina crucible (diameter~10mm) and further heated at 1500°C (1773K) for 2 hrs under air.

1.3.3. Characterizations

Phase identification was performed by PXRD analysis with a Bruker D8 Advance diffractometer using Cu Kα radiation. The X-ray diffraction measurements were made in the range of 20-80°. Lebail fitting was carried out using Fullprof software in order to obtain the cell parameters of LCM 50, LSM 50, SmSM 50. FEI Nova Nanosem 600 was used to record the FESEM images and for Energy Dispersive X-Ray analysis (EDAX). X-ray photoelectron spectroscopy (XPS) was recorded with an Omicron nanotechnology spectrometer using Mg Kα (1253.6 eV) x-ray source. BET measurements were carried out in Quanta-chrome Autosorb instrument at 77K from N_2 absorption.

1.3.4. Reactivity Tests

i) CO_2 splitting test

Thermal reduction and CO_2 splitting experiments were carried out by thermo gravimetric analysis (TGA) using a Perkin-Elmer Pyris1 instrument (**Figure 11**). About 100 mg sample was introduced in a platinum crucible and placed inside the furnace chamber. The sample was heated to 1400°C with a heating rate of 20°C/min and maintained for 45 mins under continuous Ar

(99.9999% grade) flow of 40 ml/min. After cooling down to oxidation temperature (1100°C to 900°C), 40 % CO_2 mixed with Ar was injected to carry out the CO_2 splitting test. Quantification of O_2 and CO produced was done by calculating the change in mass.

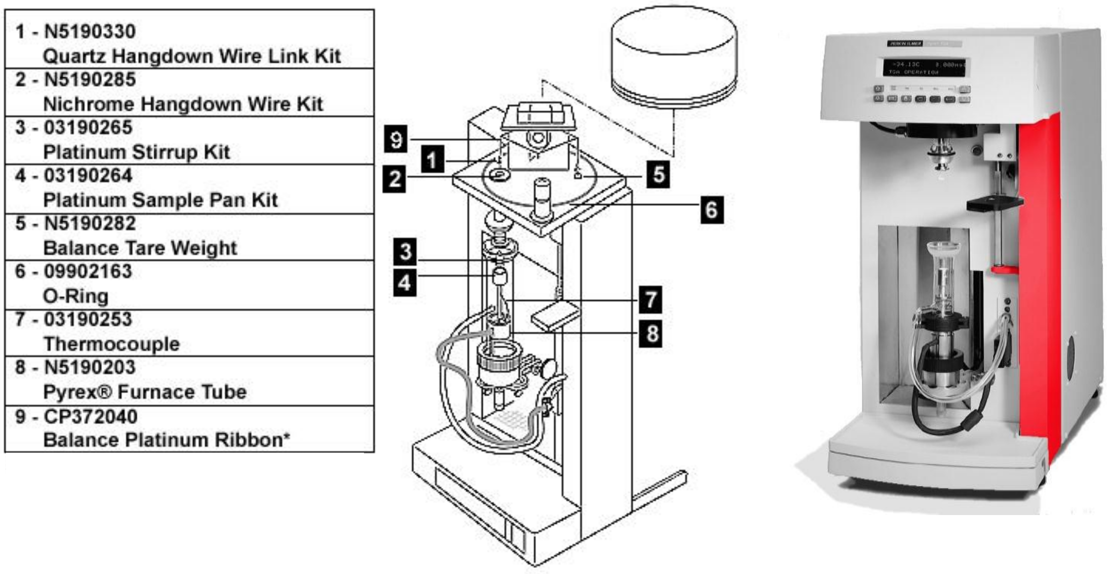

1 - N5190330	Quartz Hangdown Wire Link Kit
2 - N5190285	Nichrome Hangdown Wire Kit
3 - 03190265	Platinum Stirrup Kit
4 - 03190264	Platinum Sample Pan Kit
5 - N5190282	Balance Tare Weight
6 - 09902163	O-Ring
7 - 03190253	Thermocouple
8 - N5190203	Pyrex® Furnace Tube
9 - CP372040	Balance Platinum Ribbon*

Figure 11. Schematic and image of thermogravimetric instruments used in all our measurements. Model: Pyris 1, Supplier: Perkin Elmer.

ii) H_2O splitting test

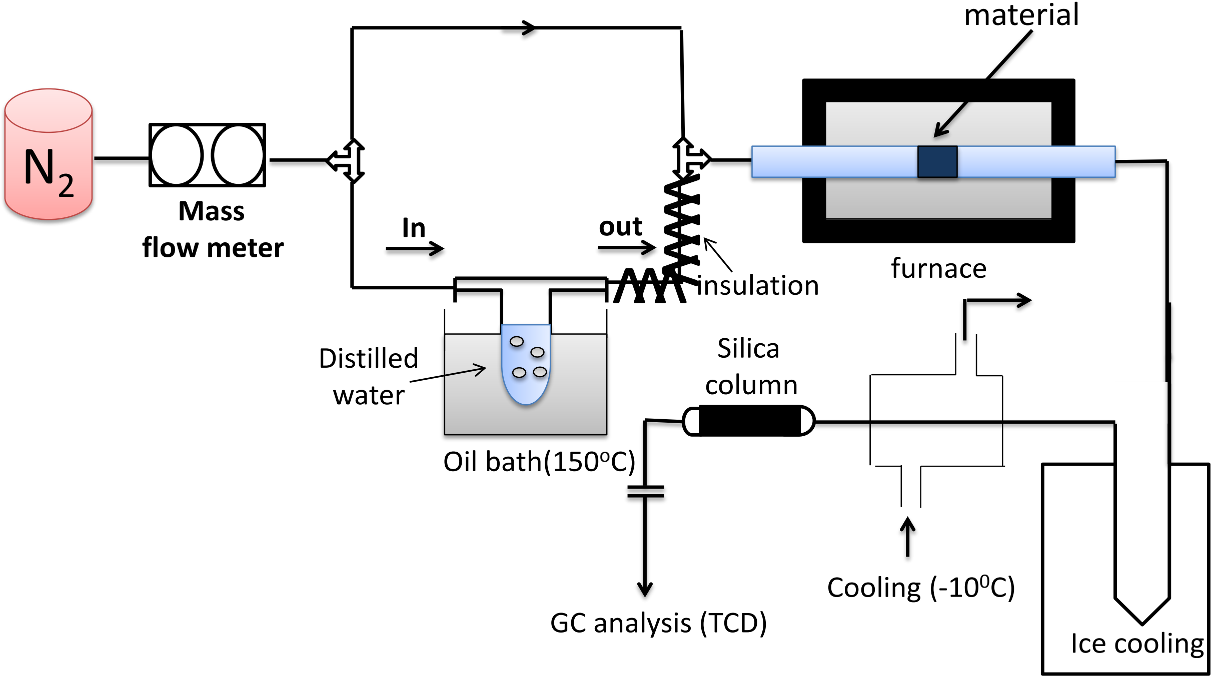

Figure 12. Experimental set-up for thermochemical H_2O splitting.

The water splitting activity of oxides was investigated using the experimental set up fabricated locally as shown in **Figure 12**. A known mass of the sample was kept in an alumina crucible and placed inside a tubular furnace. The sample temperature was ramped upto 1400 °C (rate 10°C/min) and maintained for 100 min under an inert atmosphere for complete reduction. The detection and measurement of O_2 released were carried out by a Gas chromatograph (PerkinElmer Clarus ARNEL 580) equipped with a Thermal conductivity detector (TCD). For the H_2 generation step, the furnace was cooled down to 1000°C and steam injected along with a continuous flow of inert gas. The sample was maintained at 1000°C for 100 min for complete oxidation. Numerical integration of molar flow rate-time curves gives the total amount of O_2 evolved whereas total amount of H_2 was calculated by water displacement method.

iii) Carbonate formation test

In order to examine the carbonate formation using TGA, two experiments were performed. In the first experiment, after reduction at 1400°C (for 45 mins) sample was cooled down to 700°C. At 700°C, CO_2 (40% v/v in Ar) was introduced in the sample chamber and immediately the temperature is further ramped up to 1200°C (heating rate of 10°C/min) in presence of CO_2. In the second experiment, after reduction at 1400°C (for 45 mins) sample was cooled down to 850°C. At 850°C, CO_2 (40% v/v in Ar) was introduced in the sample chamber to carry out the oxidation for 1 hour. The temperature is further ramped up to 1200°C with a heating rate of 10°C/min in presence of Ar.

iv) Isothermal thermochemical CO_2 splitting test

Isothermal CO_2 splitting experiments were performed by thermo gravimetric measurement (TGA) using a Mettler Toledo TGA 1 instrument. About 100 mg of porus body (obtained by cutting the porus monolith) was placed in a platinum crucible and kept inside the furnace chamber. The sample was heated to the reduction temperature (T_{red}) at a ramping rate of 25°C/min under continuous flow of 10^{-5} atm of O_2 premixed with N_2 (10 ppm of O_2 premixed with N_2, accuracy ± 2%, certified by Chemix gases pvt. ltd.) and maintained for 15 min. Gas switching was performed immediately by injecting 100% CO_2 (p_{CO_2}=1 atm) inside the furnace chamber at the same temperature and maintained for 15 min. Gas flow rate was 1000 ml/min/g.

v) Additional experiments of Isothermal thermochemical CO_2 splitting:

Reduction time variation: To check the role of reduction time on fuel productivity, the reduction duration (t_{red}) was increased as 15 min→20 min→25 under sweep gas (p_{O_2}=10^{-5} atm) flow of 1000 ml/min/g. The oxidation time (t_{oxd}) was 5 min under CO_2 (p_{CO_2}=1 atm) flow of 1000 ml/min/mg. T_I was 1773K.

Sweep gas flow rate variation during reduction: Sweep gas flow rate (p_{O_2}=10^{-5} atm) was varied as 1500ml/min/g→1000ml/min/g→600ml/min/g→200ml/min/g during reduction whereas CO_2 flow rate (p_{CO_2}=1 atm) was kept constant at 800 ml/min/g. t_{red} (15 min) was more than t_{oxd} (5 min). T_I was 1773K.

CO_2 flow rate variation during oxidation: CO_2 flow rate (p_{CO_2}=1 atm) was varied as 1400ml/min/g→1000ml/min/g→800ml/min/g→600ml/min/g→400ml/min/g→200ml/min/g during oxidation whereas sweep gas (p_{O_2}=10^{-5} atm) flow rate was kept constant at 1000ml/min/g. t_{oxd} (15 min) was more than t_{red} (10 min). T_I was 1773K.

Multiple cycling: During each cycle LSM50 was maintained at 1773K for t_{red} of 10 min during reduction (p_{O_2}=10^{-5} atm) and t_{oxd} of 5 min under oxidation (p_{CO_2}=1 atm) with flow rates of sweep gas and CO_2 are being 1000 and 400 ml/min/g respectively.

1.3.5. Activity Calculation

i) Moles of O_2 and CO evolved in TGA experiments

The weight loss in TGA measurements are converted to the mole amount of O_2 released per gram of composites by the following equation,

$$n_{O_2} = \Delta m_{loss} \ / \ [M_{O_2}.m_{material}] \quad \text{---------------------------} \ \text{(ES1)}$$

The amount of CO produced (mol/g) is calculated as follows,

$$n_{CO} = \Delta m_{gain} \ / \ [M_O.m_{material}] \quad \text{---------------------------} \ \text{(ES2)}$$

here, Δm_{loss} is the mass loss registered by TGA during reduction, M_{O_2} is the molecular weight of O_2 and $m_{material}$ the mass of compound during the TGA experiment. Δm_{gain} is the mass gain registered by TGA during CO_2 splitting, M_O is the atomic weight of O.

ii) Degree of Reduction and Oxidation

The extent of reduction can be expressed (% X_{red}) are as follows,

$\% X_{red} = n_{O_2}/n_{O_{2,max}} \times 100$ ------------------------------ (ES3)

Where $n_{O_{2,max}} = x/4. M_{material}$ ------------------------------ (ES4)

"x" denotes the stoichiometric coefficient of "A" in $Ln_{0.5}A_{0.5}MnO_3$ composition. $M_{material}$ is the molecular weight of specific $Ln_{0.5}A_{0.5}MnO_3$ composition.

The oxidation yield (α) is calculated as follows,

$$\alpha = \frac{n_{CO}}{X_{red} \times \frac{x}{2M_{material}}} = \frac{n_{CO}}{2 \times n_{O_2}} \text{ ------------------------------ (ES5)}$$

iii) Calculation of oxygen nonstoichiometry (δ)

The oxygen nonstoichiometry after reduction can be expressed as,

$\delta_{red} = 2 \times n_{O_2} \times M_{material}$------------------------------ (ES6)

Substituting n_{O_2} from eqn. (ES1) gives,

$$\delta_{red} = \frac{2 \times \Delta m_{loss} \times M_{material}}{M_{O_2} \times m_{material}} \text{ -------------------------- (ES7)}$$

The oxygen nonstoichiometry obtained after oxidation can be expressed as,

$\delta_{oxd} = 2 \times n_{CO} \times M_{material}$------------------------------ (ES8)

Substituting n_{CO} from eqn. (ES2) gives,

$$\delta_{oxd} = \frac{2 \times \Delta m_{gain} \times M_{material}}{M_O \times m_{material}} \text{-------------------------- (ES9)}$$

iv) Calculation of tolerance factor (τ)

In ABO_3 perovskite, the Goldsmith tolerance factor (τ) is calculated as,

$$\tau = \frac{(r_A + r_O)}{\sqrt{2}(r_B + r_O)} \text{-- (ES10)}$$

here r_A, r_B and r_O denotes the ionic radii of the constituent ions.In the present study "τ" is calculated considering 12 and 6 coordination no. of A and B site cations respctively.[114, 115]

v) Calculation of size variance (σ^2)

Statistical variance $\sigma^2(r_A)$ is used to represent the distribution of A cation radii in $Ln_{1-x}A_xMnO_3$ perovskites. In general variance is defined as,

$\sigma^2(r_A)$ = (standard deviation from mean $r_A)^2$ = $\sum_i y_i r_i^2 - \sum_i (y_i r_i)^2 = \langle {r_A}^2 \rangle - \langle r_A \rangle^2 - -$(ES11)

Here y_i is the proportion of each ion present. When only one ion is present $\sigma^2 = 0$ but for the mixture of two ions,

$$\sigma^2(r_A) = x(1-x)(\Delta_A)^2 \text{ -- (ES12)}$$

Δ_A is the difference between the Ln^{3+} and A^{2+} radii.

σ^2 is actually a function to define the total displacive disorder of the oxygen atoms due to A site cation size disparity in ABO_3 perovskite.

1.4. Results and discussion

1.4.1

$La_{1-x}A_xMnO_3$ (A=Ca, Sr; x=0-0.5) based perovskites for the two-step thermochemical splitting of CO_2 and H_2O

1.4.1. $La_{1-x}A_xMnO_3$ (A=Ca, Sr; x=0- 0.5) based perovskites for the two-step thermochemical splitting of CO_2 and H_2O

$La_{1-x}Ca_xMnO_3$ perovskites with x=0.35, 0.5, 0.65 (designated here as LCM 35, LCM 50 and LCM 65) possess an orthorhombic structure (**Figure 1**) with the lattice parameters decreasing slightly with increasing Ca content. This is because, as the content of the smaller Mn^{4+} (ionic radius 0.54 Å) increases over Mn^{3+} (ionic radius 0.65 Å) with the substitution of trivalent La with bivalent Ca. As synthesized $La_{0.5}Sr_{0.5}MnO_3$ (LSM 50) and CeO_2 (Sigma aldrich) was also used for comparison.

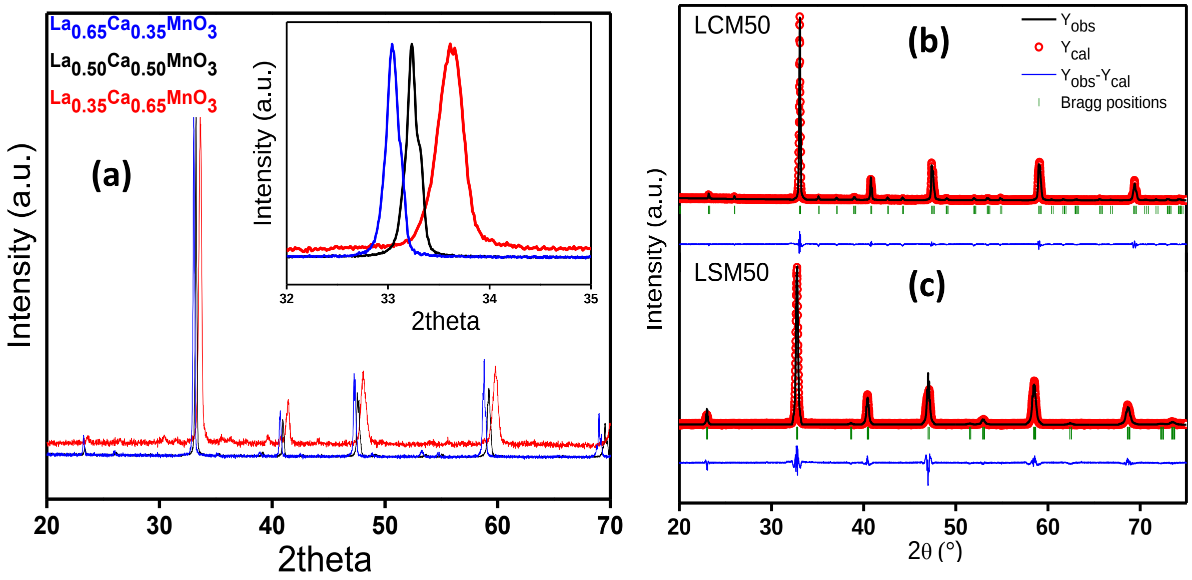

Figure 1. (a) Powder XRD of $La_{1-x}Ca_xMnO_3$ (x= 0.35, 0.5, 0.65) perovskites phases. Inset highlights magnified view of the (200) reflections. Rietveld refined XRD patterns of (b) $La_{0.5}Ca_{0.5}MnO_3$ (LCM 50) and (c) $La_{0.5}Sr_{0.5}MnO_3$ (LSM 50). The cell parameters obtained by fitting the Powder XRD patterns of LCM50 (space group Pnma) and LSM50 (space group R-3c) are a= 5.4228(2) Å, c= 7.6424(3) Å and a= 5.4683(3) Å, c= 13.3773 (9) Å respectively.

We have calculated the atomic % of La, Ca and Mn present in LCMs (**Table 1, Figure 2**) from EDS analysis. The composition of LCMs was established from the background corrected La3d (~ 836 eV), Ca2p (~ 286 eV) and Mn2p (~ 642 eV) XP survey scan spectra (eqn. 1, **Figure 3**). The calculated ratio among La, Ca and Mn in LCM 35, LCM 50 are0.66/0.37/1, 0.5/0.5/1 respectively (**Table 2**).

The intensity ratio of La, Ca and Mn was calculated as,

$$R_{1,2} = \frac{I_1/A_1}{I_2/A_2} - - - - - - - - - (1),$$

where I is the intensity obtained from the XPS spectrum after background correction and A is the atomic sensitivity factors.

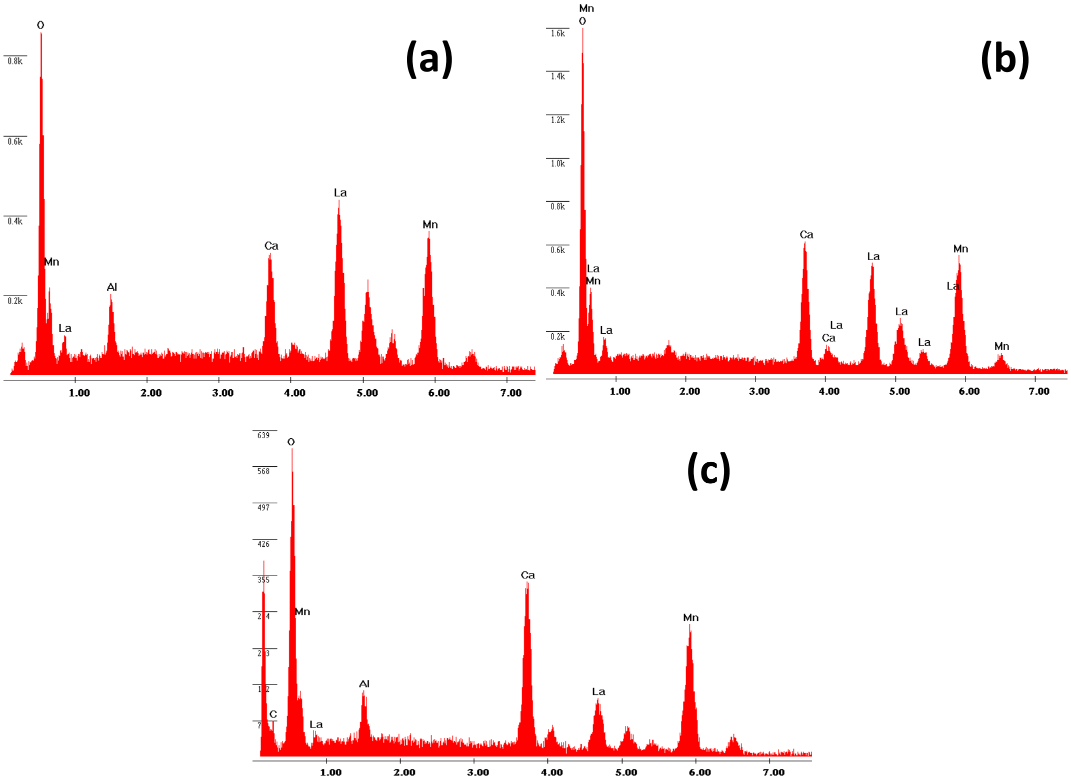

Figure 2. EDS (X and Y axis are Energy in KeV and counts respectively) of (a) LCM 35, (b) LCM 50 and (c) LCM 65.

Table 1. Atomic % of La, Ca and Mn present in LCMs as calculated from EDS analysis.

Materials	LCM 35	LCM 50	LCM 65
Element	**Atomic %**	**Atomic %**	**Atomic %**
O K	52.06	58.44	57.89
Ca K	8.25	9.97	13.63
La L	17.02	11.76	5.86
Mn K	22.66	19.84	22.62

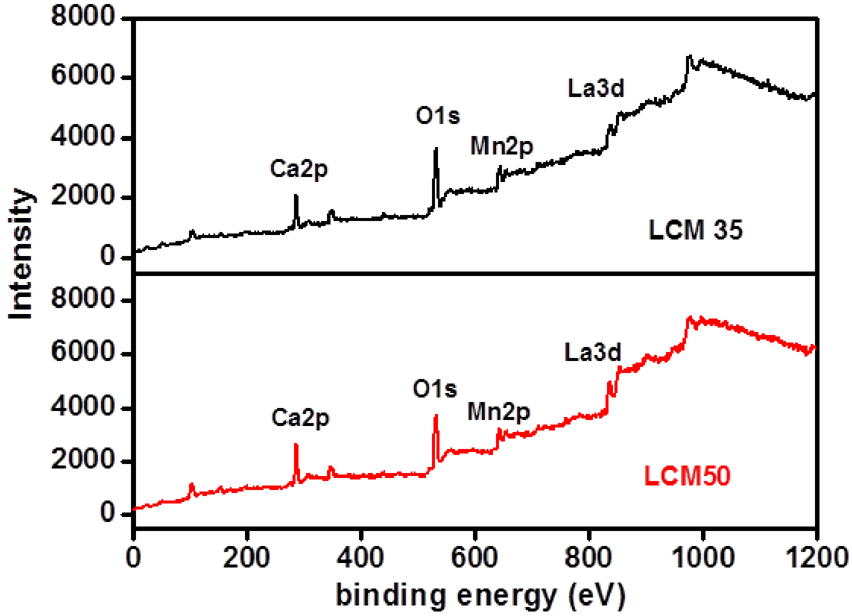

Figure 3. X- Ray photoelectron survey spectra of LCMs.

Table 2. The cation ratio of La, Ca and Mn in LCMs as calculated from XPS survey scan.

Materials	I_{La}/A_{La}	I_{Ca}/A_{Ca}	I_{Mn}/A_{Mn}	$R_{La/Ca/Mn}$
LCM 35	448	255	680	0.66/0.37/1
LCM 50	407	409	815	0.5/0.5/1

Thermogravimetric analysis (TGA) of the three LCM compositions shows that O_2 production on heating above 1000°C increases with the Ca^{2+} or Mn^{4+} content. The mass loss due to reduction starts around 1000°C and reaches a plateau after 1400°C.

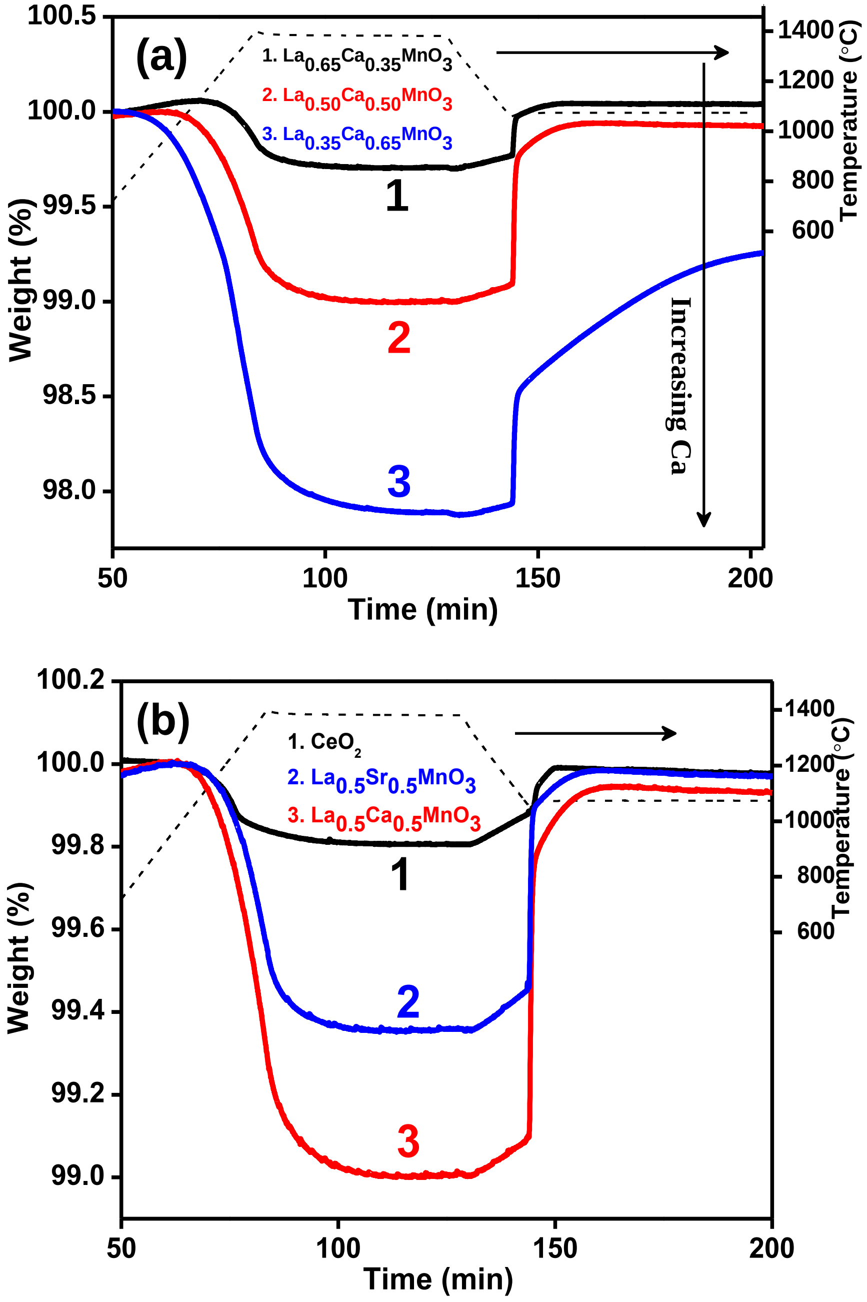

Figure 4. Representative TGA of thermochemical CO_2 splitting of (a) $La_{1-x}Ca_xMnO_3$ (x=0.35, 0.5, 0.65); (b) $La_{0.5}Ca_{0.5}MnO_3$ (LCM 50) and $La_{0.5}Sr_{0.5}MnO_3$ (LSM 50) in comparison with CeO_2. Reduction and oxidation temperatures are 1400 °C and 1100 °C respectively.

The O_2 released from LCM 35, LCM 50 and LCM 65 is 109, 316 and 653 µmol/g respectively (**Figure 4a**). It is to be noted that O_2 evolved by LCM 50 is greater than by $La_{0.5}Sr_{0.5}MnO_3$ (LSM 50), the value in the case of the latter being 201 µmol/g. Ceria evolves only 63 µmol/g of O_2 (Figure 4b). Thus, the O_2 evolved by LCM 50 is 1.6 times that of LSM 50 and five times that of ceria.

We have studied the splitting of CO_2 by the LCM compositions. A reversible mass gain is observed in all the compounds during the CO_2 injection at 1100°C (Figure 4a). A detailed study was carried out by changing the calcium content systematically. CO produced by LCM 35, LCM 50 and LCM 65 is 175, 525 and 810 µmol/g respectively over the same time scale (Figure 4b). The CO production activity of LCM50 is also about 1.6 times and 5 times more than LSM 50 and ceria respectively (**Table 3**).

Table 3. TGA results for O_2 and CO yield of associated samples

Materials	**O_2 released (µmol/g)**	**CO produced (µmol/g)**
$La_{0.65}Sr_{0.35}MnO_3$	100	137.5
$La_{0.5}Sr_{0.5}MnO_3$	**201.3**	**325**
$La_{0.65}Ca_{0.35}MnO_3$	109.4	175
$La_{0.5}Ca_{0.5}MnO_3$	**315.6**	**525**
$La_{0.35}Ca_{0.65}MnO_3$	653.1	350
Ceria	**62.5**	**112**

The kinetics of CO production appears to become sluggish at high Ca Content. The reoxidation peak of LCM 65 can be deconvoluted in two parts depending on its shape. The initial straight increase in mass (394 µmol/g) corresponds to the reaction-controlled regime followed by the slower constant gain (450 μmol/g) corresponds to diffusion controlled regime (Figure 4a).

The fuel production activity of LCM50 was tested during three successive cycles (**Figure 5**) in the temperature regime 1400-1000°C. This study has revealed reversibility in both O_2 evolution and CO production, though the kinetics of reoxidation appears to become slow on repeated cycling. We have carried out the reduction of LCM 50 compound at 1350°C followed by reoxidation at 1000°C (Figure 5 and **Table 4;** cycle 3). We found that the amount of O_2 evolved (237 μmol /g) and CO produced (481 μmol /g) over the 1350-1000°C range is more than the activity of Sr, Mn doped $LaAlO_3$ although the experimental set-up in the two cases is not identical.[87]

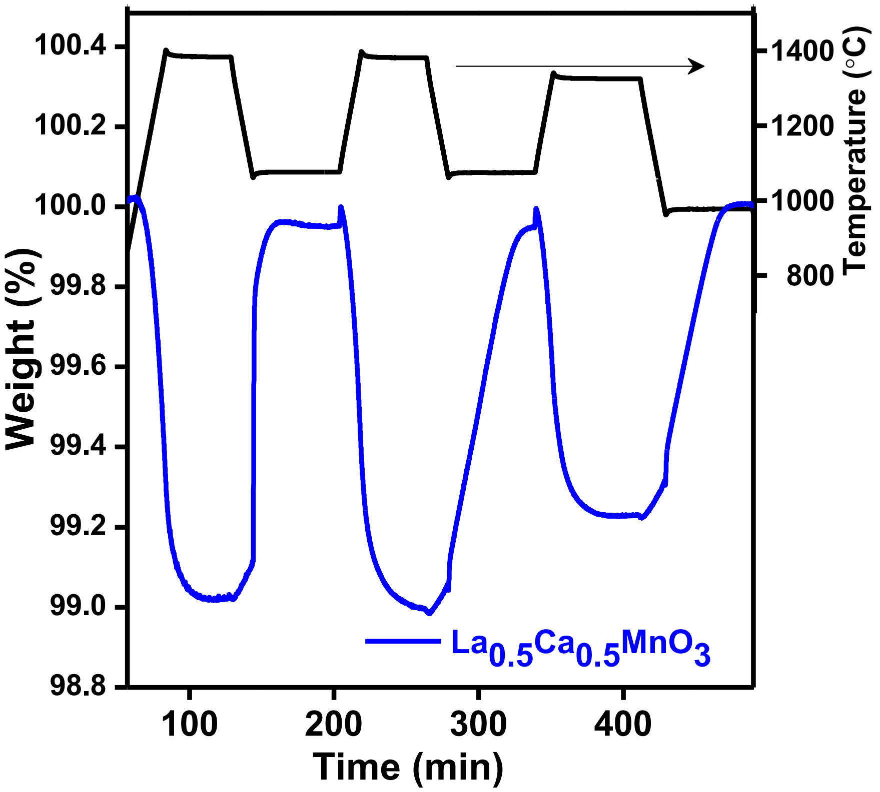

Figure 5. TGA of three consecutive thermochemical CO_2 splitting cycles with $La_{0.5}Ca_{0.5}MnO_3$ (LCM 50) performed in the range of 1400-1000°C.

As- synthesized LCM 50 is composed of few micron size particles as observed from FESEM images. No significant change in morphology of LCM 50 has been observed after TGA analysis (**Figure 6**).

Table 4. Quantity of O_2 released and CO produced during three consecutive thermochemical cycles of LCM 50.

Cycle No.	Reduction temperature (°C)	O_2 released (μmol/g)	CO_2 splitting temperature (°C)	CO produced (μmol/g)
Cycle 1	1400	309	1100	631
Cycle 2	1400	300	1100	600
Cycle 3	**1350**	**237**	**1000**	**481**

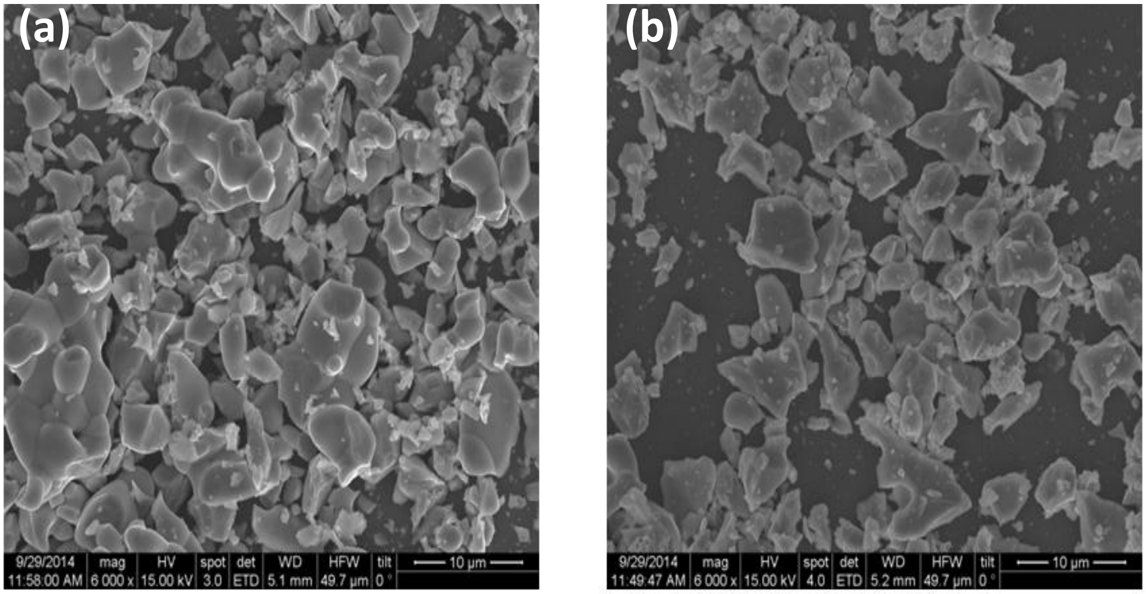

Figure 6. FESEM images of LCM 50 (a) before and (b) after TG analysis.

Inspite of having equal content of +2 ions (Sr or Ca) substitution on both LSM 50 and LCM 50 sites they behave entirely different than each other. The structure of LSM 50 is entirely different than LCM 50. LCM 50 crystallizes as orthorhombic space group whereas the LSM 50 forms rhombohedral structure. It related to their diffence in tolerance factor (τ) due to the size difference between Sr and Ca ions. The τ of LCM 50 (τ=0.982) is smaller than LSM 50. Lower the τ results in higher structural distortion. It is speculated the higher activity is due to the more distortion in MnO_6 octahedra in orthorhombic perovskites compare to the rhombohedral one. In order to understand the superior performance of LCM 50, we have prepared perovskite composition of $Sm_{0.5}Sr_{0.5}MnO_3$ (SmSM50) and carried out TG analysis.

SmSM 50 is as also an orthorhombic perovskite (**Figure** 7) with the tolerance factor (τ=0.982) comparable with orthorhombic LCM 50 (τ= 0.985), is the reason behind opting for it.[79]

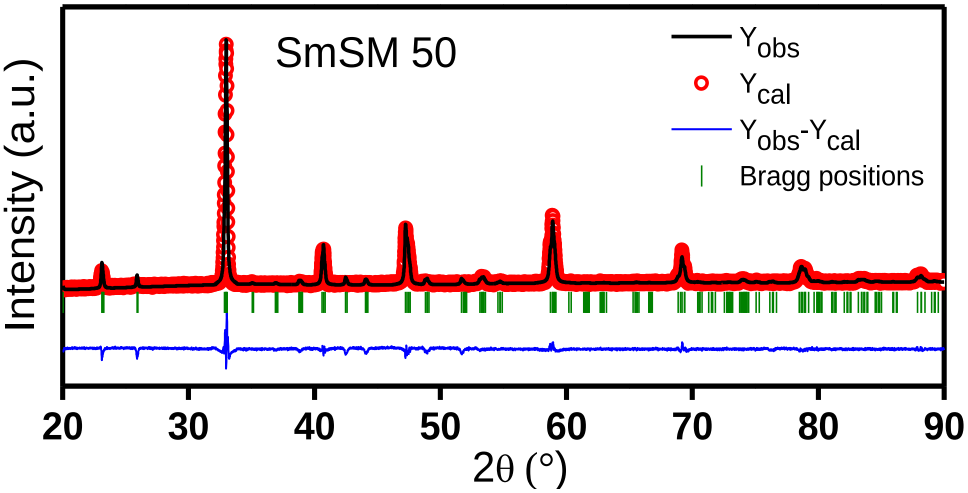

Figure 7. XRD patterns of $Sm_{0.5}Sr_{0.5}MnO_3$ (SmSM 50). The cell parameters obtained by fitting the Powder XRD patterns of SmSM50 (space group Pnma) is a= 5.4273 (3) Å, b= 7.6562(4) Å, c= 5.4494 (2) Å.

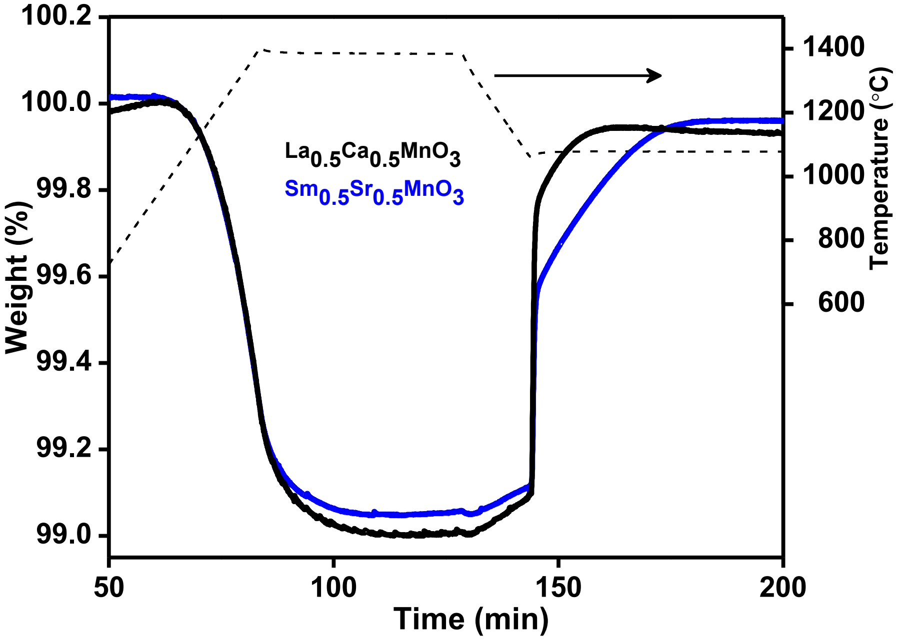

Figure 8. Representative TGA of thermochemical CO_2 splitting of $Sm_{0.5}Sr_{0.5}MnO_3$ (SmSM 50) in comparison with $La_{0.5}Ca_{0.5}MnO_3$ (LCM 50). Reduction and oxidation temperatures are 1400°C and 1100°C respectively.

Interestingly, both LCM 50 and SmSM50 produce comparable amounts of O_2 and CO during TG analysis in the temp range of 1400-1100° C unlike LSM 50 (**Figure 8**). This indicates that the orthorhombic perovskites show superior activity than the rhombohedral perovskites. This could be due to the distortion in MnO_6 octahedra in orthorhombic perovskites compare to the rhombohedral one.[79]

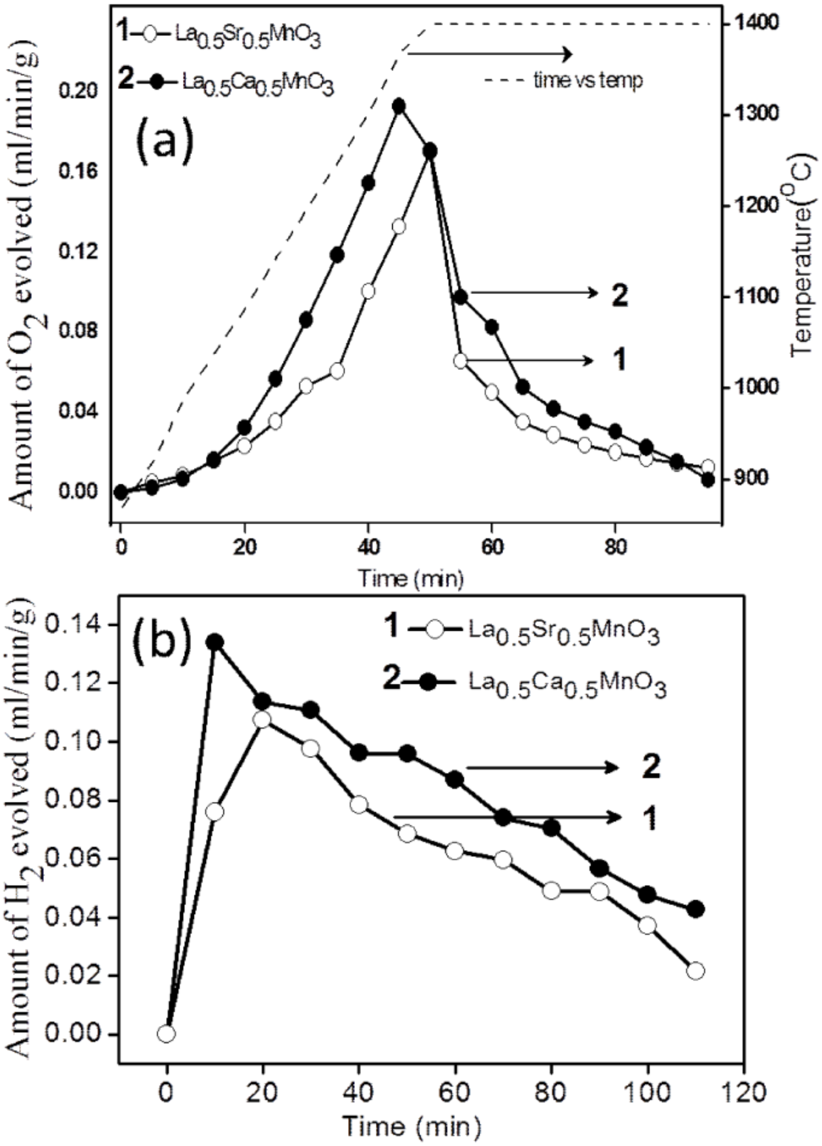

Figure 9. (a) Oxygen and (b) Hydrogen evolution profiles of $La_{0.5}A_{0.5}MnO_3$ (A= Sr, Ca). Reduction and oxidation temperatures are 1400°C and 1000°C respectively.

The H_2O splitting activity of LCM 50 was tested in comparison with LSM50 with the help of set up presented in in the reactivity test section. The sample was placed inside the tubular furnace and heated upto 1400°C under a constant N_2 flow. As shown in **Figure 9a,** O_2 evolution starts around 1000°C, and approaches the plateau region at 1400°C. Both LCM50 and LSM50 show the complete O_2 production within 30 mins after reaching 1400°C. The amount of O_2 produced in the case of LCM50 and LSM 50 are 272 and 193 µmol /g respectively, close to the values obtained from TGA measurements discussed earlier. The H_2O splitting activity was tested by introducing steam in a continuous N_2 flow. The splitting temperature of H_2O is 1000°C. Figure 9b shows the rate of H_2 production. Production of H_2 starts immediately after entry of H_2O in the gas stream. The amount of H_2 produced in a span of 100 mins is 407 and 308 µmol/g for LCM 50 and LSM 50 respectively. Notably, H_2 production is not complete even after 100 mins and exhibits an extended tail over a long duration. The slow kinetics of H_2 evolution can arise from causes such as decrease in chemical diffusivity, changes in surface reaction constant, steam concentrations as well as the intrinsic thermodynamic driving forces.[23]

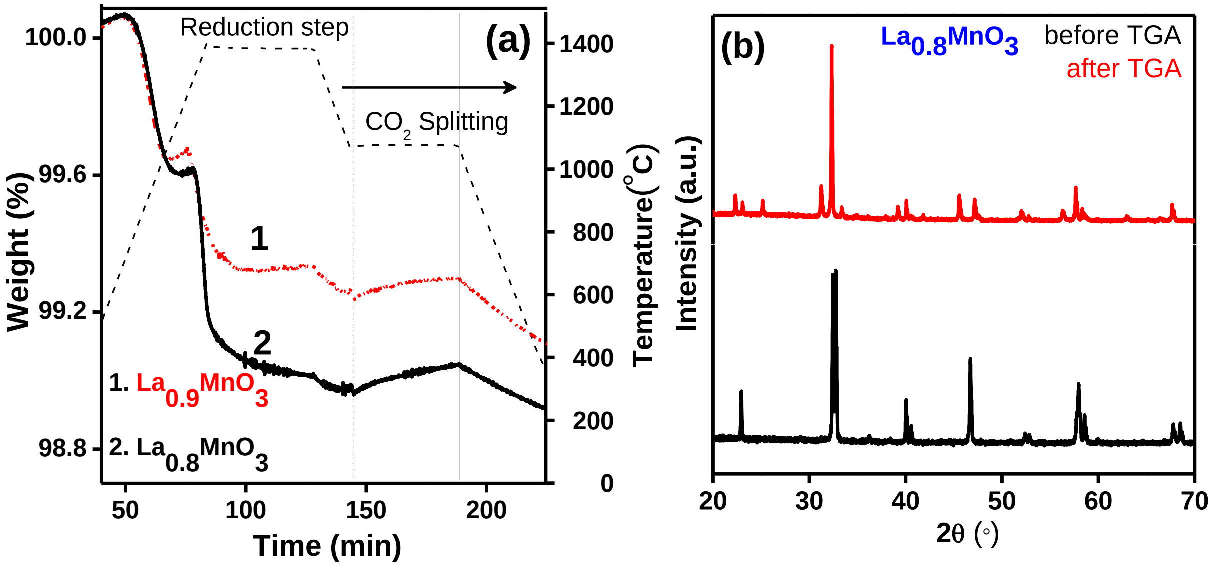

Figure 10. (a) Representative TGA of thermochemical CO_2 splitting of $La_{1-x}MnO_3$ (x=0.1, 0.2). Reduction and oxidation temperatures are 1400°C and 1100°C respectively. (b) PXRD patterns of $La_{0.8}MnO_3$ before and after TGA experiment.

We tested the CO_2 splitting activity of $La_{1-x}MnO_3$ (x=0.1, 0.2) as it contains a high concentration of Mn^{4+} (**Figure 10**).[116] But phase transformation from the rhombohedral to the orthorhombic structure takes place under the high temperature reaction conditions (Figure 10). $La_{1-x}MnO_3$ cannot therefore be used for this purpose.

We have also investigated the activity of $La_{1-x}Sr_xFeO_3$ (x=0.3) inspired by the literature data available for its H_2 production activity in membrane reactors.[84, 91] The O_2 evolution of $La_{0.7}Sr_{0.3}FeO_3$ starts at a low temperature, with the total amount of O_2 produced being 360 μmol/g at 1300°C (**Figure 11**). Unfortunately, the CO production yield is low (20% of reduction yield).

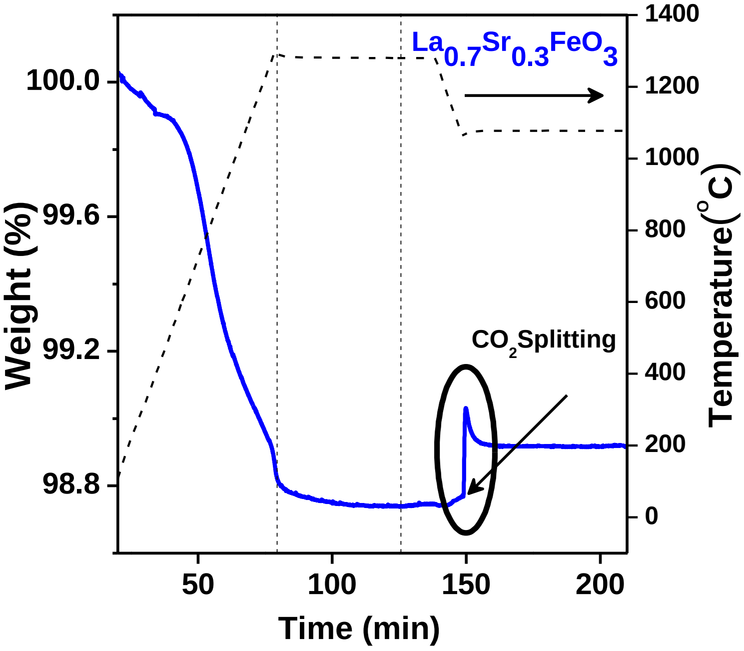

Figure 11. Representative TGA of thermochemical CO_2 splitting of $La_{0.7}Sr_{0.3}FeO_3$. Reduction and oxidation temperatures are 1400°C and 1100°C respectively.

Besides having different structures, LCM and LSM compositions possess Mn^{3+} and Mn^{4+} ions in different electronic states. While two Mn ions with distinctly different charges are present in LCMs, there is fast electron transfer from Mn^{3+} to Mn^{4+} in LSMs giving rise to magnetism and metalicity.[76]

1.4.2

$Ln_{0.5}A_{0.5}MnO_3$ (Ln=lanthanide, A= Ca, Sr) family of perovskites in the thermochemical generation of CO and H_2 from CO_2 and H_2O

1.4.2. $Ln_{0.5}A_{0.5}MnO_3$ (Ln=lanthanide, A= Ca, Sr) family of perovskites in the thermochemical generation of CO and H_2 from CO_2 and H_2O

$Ln_{0.5}Sr_{0.5}MnO_3$ and $Ln_{0.5}Ca_{0.5}MnO_3$ perovskites are designated throughout the manuscript as LnSM50 and LnCM50 respectively where Ln represents La, Nd, Sm, Gd, Dy and Y. $Ln_{0.5}Sr_{0.5}MnO_3$ (LnSM50) and $Ln_{0.5}Ca_{0.5}MnO_3$ (LnCM50) perovskites crystallize in the orthorhombic structure except LaSM50 which adopts the rhombohedral structure (**Figure 1**). The structural parameters of these perovskites are investigated in detail using Rietveld refinement (**Table 1**).

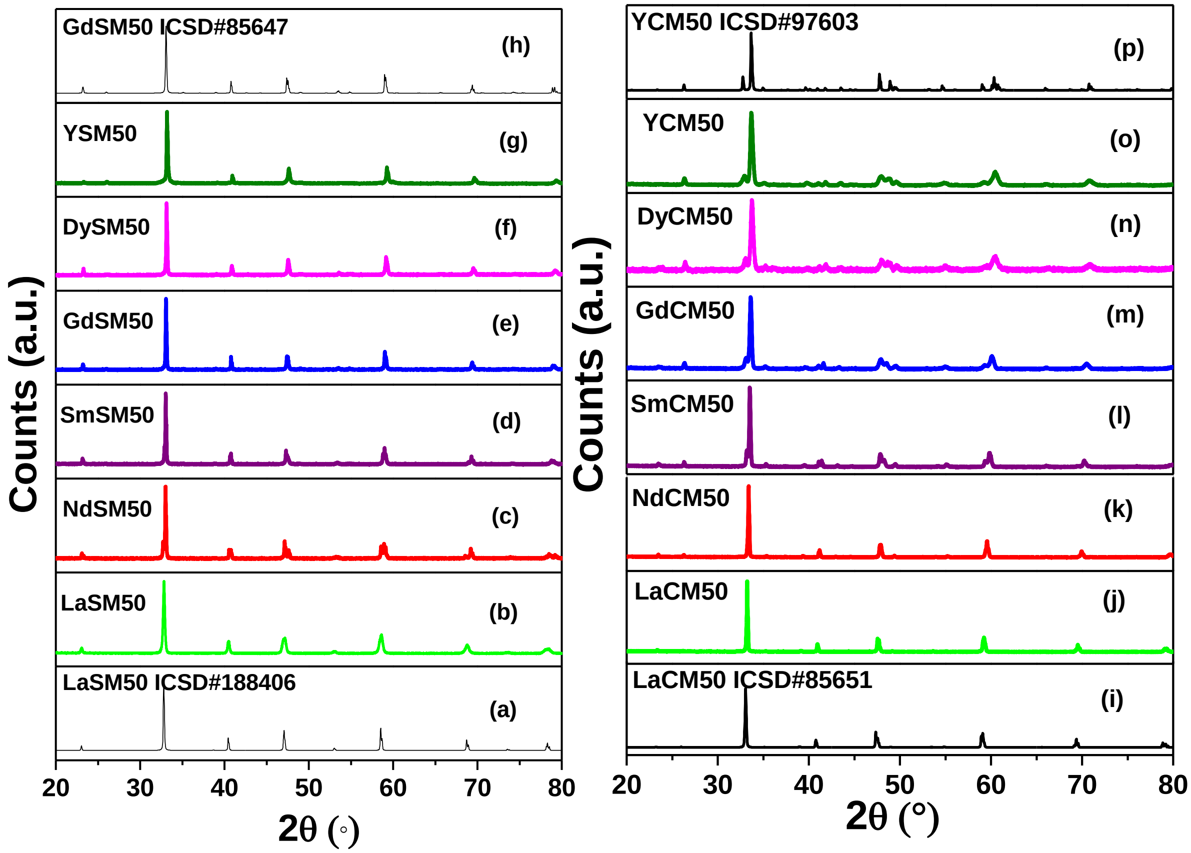

Figure 1. PXRD patterns of (b-g) $Ln_{0.5}Sr_{0.5}MnO_3$ (LnSM50) and (j-o) $Ln_{0.5}Ca_{0.5}MnO_3$ (LnCM 50); where Ln=La, Nd, Sm, Gd, Dy and Y. ICSD patterns corresponds to (a) LaSM50, (h) GdSM50, (i) LaCM50 and (p) YCM50 are marked in the graphs as reference. LaSM50 and NdSM50 crystallize in rhombohedral (R-3c space group) and orthorhombic (Imma space group) structure respectively. All others are crystallizes in orthorhombic structure having Pnma space group.

Table 1. Structural parameters of $Ln_{0.5}A_{0.5}MnO_3$ (Ln= La, Nd, Sm, Gd, Dy and Y; A=Sr and Ca) based perovskites obtained from Rietveld refined PXRD.

Materials	a (Å)	b (Å)	c (Å)	Crystal structure	Space group
LaSM 50	5.4683(3)	13.3773(9)	5.4683(3)	Rhombohedral	R-3c
NdSM 50	5.4302 (2)	7.6381(2)	5.4725(1)	Orthorhombic	Pnma
SmSM 50	5.4273 (2)	7.6562(3)	5.4494(2)	Orthorhombic	Pnma
GdSM 50	5.4169(2)	7.6447(3)	5.4235(2)	Orthorhombic	Pnma
DySM 50	5.4040(3)	7.6421(4)	5.4516(5)	Orthorhombic	Pnma
YSM 50	5.4058(2)	7.6404(2)	5.3992(2)	Orthorhombic	Pnma
LaCM 50	5.4228(2)	7.6424(3)	5.4127(2)	Orthorhombic	Pnma
NdCM 50	5.3796(2)	7.6011(3)	5.3993(2)	Orthorhombic	Pnma
SmCM 50	5.3511(2)	7.5519(3)	5.4071(2)	Orthorhombic	Pnma
GdCM 50	5.3228(4)	7.5093(8)	5.4256(5)	Orthorhombic	Pnma
DyCM 50	5.2978(4)	7.5362(7)	5.4313(2)	Orthorhombic	Pnma
YCM 50	5.2793(3)	7.4507(6)	5.4346(5)	Orthorhombic	Pnma

The Bragg peaks shift to higher angles as the size of the rare earth ion decreases (**Figure 2**) while moving from La to Y. The morphology and compositions of the manganites were also checked by FESEM and EDS analysis respectively, as shown in the case of YSM50 and YCM50 in **Figure 3** and **Table 2**. The as-synthesized materials are composed of micron size particles as observed from FESEM images. The BET surface areas of the samples are less than 1 m^2g^{-1}.

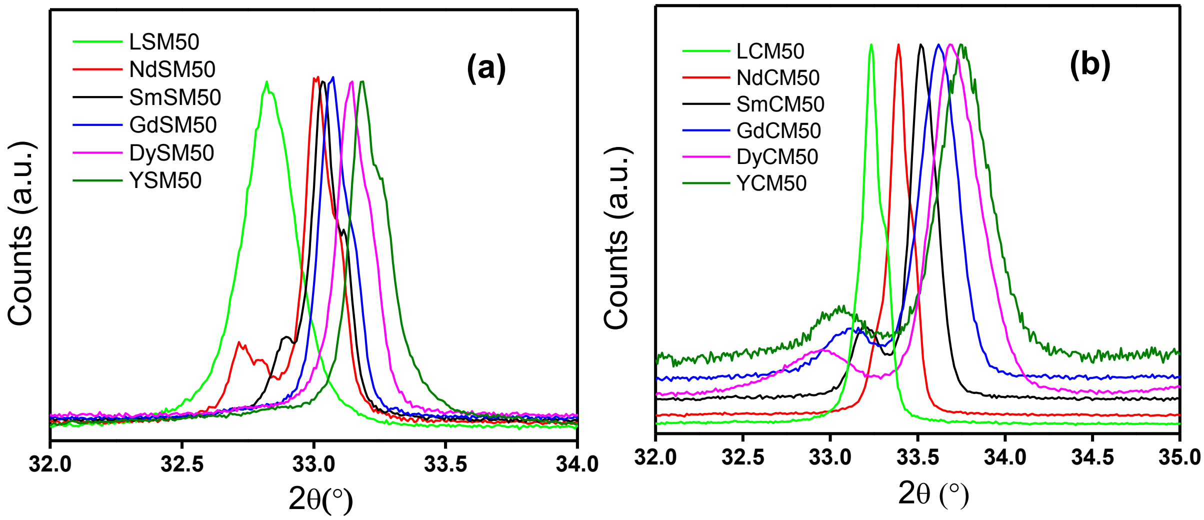

Figure 2. Magnified view of the (200) reflections of PXRD pattern of (a) LnSM50 and (b) LnCM50 series.

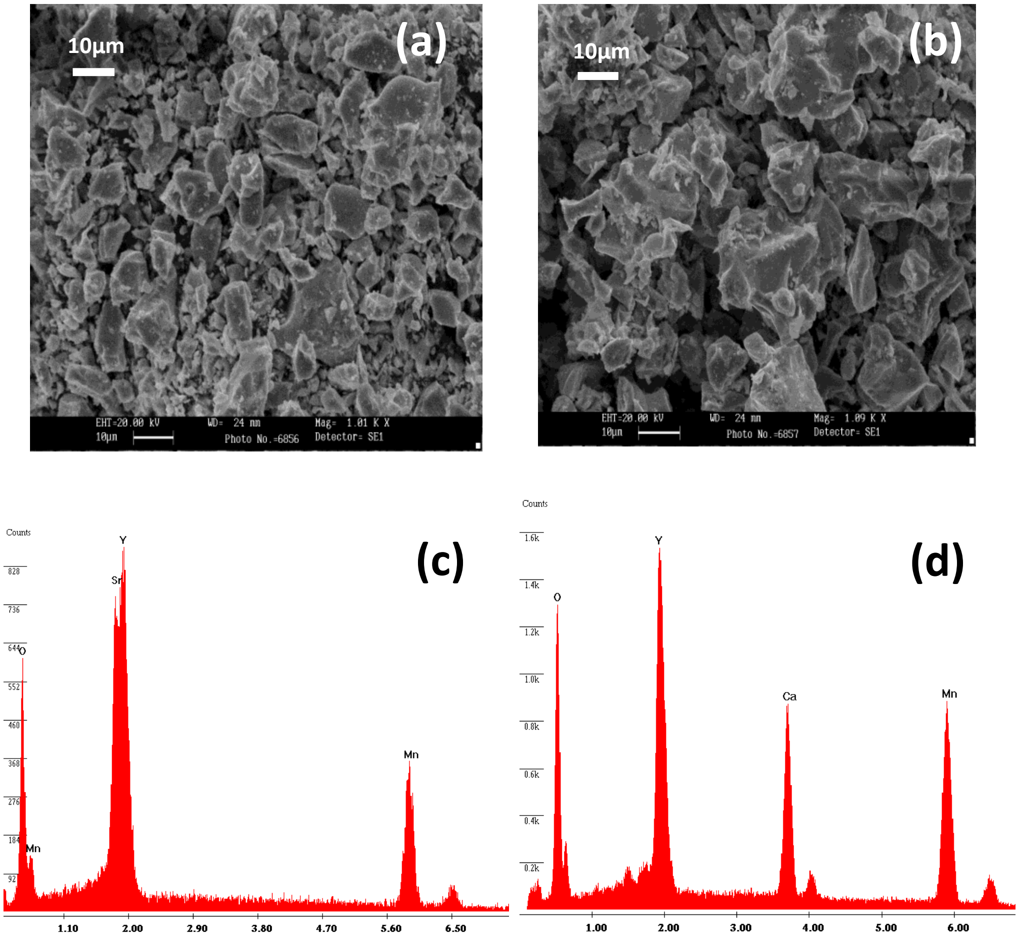

Figure 3. FESEM images (a) YSM 50 and (b) YCM 50. EDS (X and Y axis are Energy in KeV and counts respectively) of (c) YSM 50 and (d) YCM 50 respectively.

Table 2. Atomic % of Y, Sr, Ca and Mn present in YSM50 and YCM50 as calculated from EDS analysis.

	Y L	Sr L	Ca K	Mn K	O K
Materials	**Atomic %**	**Atomic %**	**Atomic %**	**Atomic %**	**Atomic %**
YSM50	11.6	12.2	--------	22.1	54.1
YCM50	10.5	--------	10.6	22.9	55.9

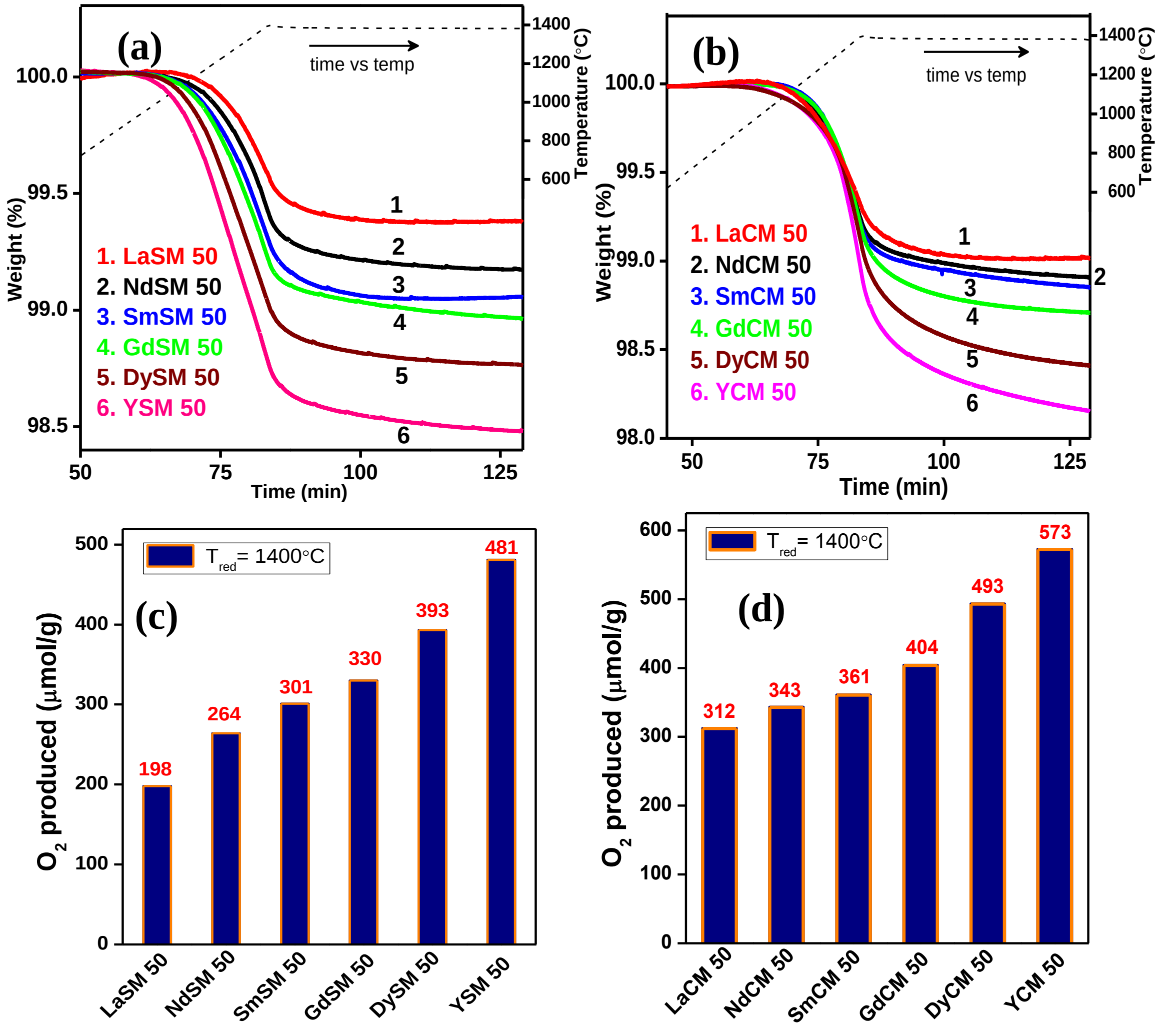

Figure 4. Thermogravimetric reduction profiles of (a) $Ln_{0.5}Sr_{0.5}MnO_3$ and (b) $Ln_{0.5}Ca_{0.5}MnO_3$ (Ln= Lanthanides). Reduction temperature is 1400°C. Histograms quantify the amount of O_2 produced by (c) $Ln_{0.5}Sr_{0.5}MnO_3$ and (d) $Ln_{0.5}Ca_{0.5}MnO_3$.

LnSM50 and LnCM50 are subjected to thermogravimetric redox reaction. The O_2 evolution profiles of LnSM50 and LnCM50 with different rare earth ions are shown in **Figures 4a** and b respectively. The weight loss due to reduction starts at a lower temperature and nearly reaches a plateau after 1400°C for LnSM50 compositions unlike some members of LnCM50 which continue to lose weight even after 45 mins of reaching the peak temperature. The observed weight loss increases with the decrease in size of the rare earth ion. In Figures 4c and d, we present the total amount of O_2 produced by the reduction of LnSM50 and LnCM50 at 1400°C respectively. The yttrium derivative shows the highest O_2 production, the O_2 released by YCM50 and YSM50 being 573 and 481 μmol/g respectively.

Table 3. Quantity of O_2 released (μmol/g, % X_{red}) and CO produced (μmol/g, % α) by LnSM50 and LnCM50 series. Reduction temperature (T_{red}) and CO_2 splitting temperature (T_{S,CO_2}) is 1400°C and 1100°C respectively.

Material	T_{red} (°C)	O_2 produced (μmol/g)	X_{red} (%)	T_{S,CO_2} (°C)	CO produced (μmol/g)	α (%)
LaSM 50	1400	198	34.2	1100	370	93.4
NdSM 50	1400	264	46.2	1100	441	83.5
SmSM 50	1400	301	53.4	1100	526	87.3
GdSM 50	1400	330	59.4	1100	487	73.8
DySM 50	1400	393	71.7	1100	554	70.5
YSM 50	1400	481	73.6	1100	571	59.4
LaCM 50	1400	312	48.0	1100	518	83.0
NdCM 50	1400	343	53.5	1100	538	78.4
SmCM 50	1400	361	57.2	1100	590	81.7
GdCM 50	1400	404	65.1	1100	637	78.8
DyCM 50	1400	493	80.5	1100	566	57.4
YCM 50	1400	575	77.0	1100	671	58.3

The quantity of O_2 produced (μmol/g) and the percentages of reduction (% X_{red}) are listed in **Table 3** for the reduction temperature of 1400°C (T_{red}). Notably, %X_{red} increases from 34% to 74% as we go from LaSM50 to YSM50 in the LnSM50 series whereas the value is even larger (77%) for YCM (Table 3).

The relation of the O_2 production to structural aspects of LnSM50 and LnCM50 is depicted in **Figure 5a and b**. Figure 5a shows that the O_2 production of LnSM50 increases with the decrease in the tolerance factor (τ) which in turn decreases with the decrease in the radius of the rare earth ion (ES10, see the experimental section, **Table 4**).

Decrease in τ indicates an increase in the tilting of the MnO_6 octahedra, accompanied by an increase in the lattice distortion,[79, 117] which would help in the removal of oxide ions. It should be noted that site disorder, σ^2, arising from size mismatch also increases with decrease in τ (Table 4).[88] Decrease in τ decreases the Mn-O-Mn bond angles significantly, which in turn reduces the spatial overlap of Mn e_g and O 2pσ orbitals.[86] This would favour O_2 evolution. Furthermore, Figure 5a illustrates how the decrease in τ favours oxygen removal resulting in highly nonstoichiometric perovskites as products after reduction. Thus, the final oxygen stoichiometry achieved for YSM50 and YCM 50 is 2.81 and 2.8 respectively after 45 mins of reduction at 1400°C. Figure 5b shows similar conclusions of O_2 evolution in case of LnCM50.

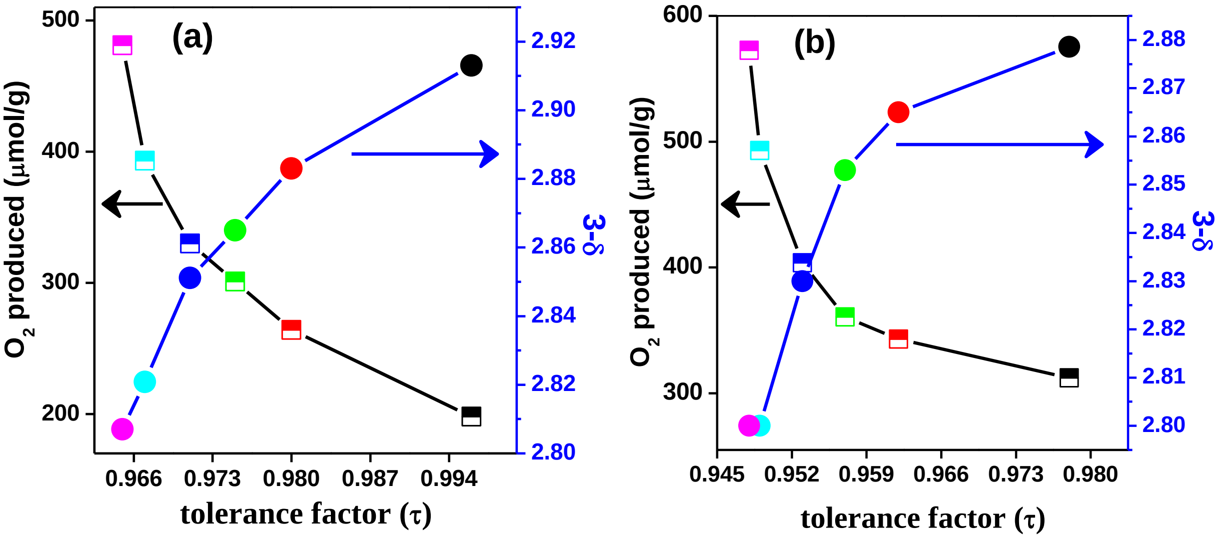

Figure 5. Variation of total amount of O_2 produced and the final oxygen content with the tolerance factor of the perovskites compositions of (a) $Ln_{0.5}Sr_{0.5}MnO_3$ and (b) $Ln_{0.5}Ca_{0.5}MnO_3$.

Table 4. Tolerance factor (τ) and size variance (σ^2) of LnSM50 and LnCM50 series.

Material	$<r_A>$ [a]	Tolerance factor (τ)	σ^2 ($\times 10^{-3}$) (Å^2)	O_2 produced (μmol/g)
LaSM 50	1.4	0.996	1.6	198
NdSM 50	1.355	0.980	7.0	264
SmSM 50	1.34	0.975	10	301
GdSM 50	1.33	0.971	12	330
DySM 50	1.319	0.967	14.6	393
YSM 50	1.314	0.965	15.6	481
LaCM 50	1.35	0.978	0.1	312
NdCM 50	1.30	0.962	1.2	343
SmCM 50	1.29	0.957	2.5	361
GdCM 50	1.28	0.953	3.7	404
DyCM 50	1.269	0.949	5.0	493
YCM 50	1.264	0.948	5.6	575

[a] $<r_A>$ is radii of A site cation in ABO_3 perovskite

Figure 6a shows the percentage of weight loss of LnSM50 as a function of temperature. It shows that as the size of the rare earth ion decreases, the O_2 evolution temperature gradually shifts towards lower temperatures. Thus, O_2 loss starts around 860°C in the case of YSM50. For LnCM50, the change in reduction temperature is not as significant, and YCM starts to get reduced around 970°C (Figure 6b).

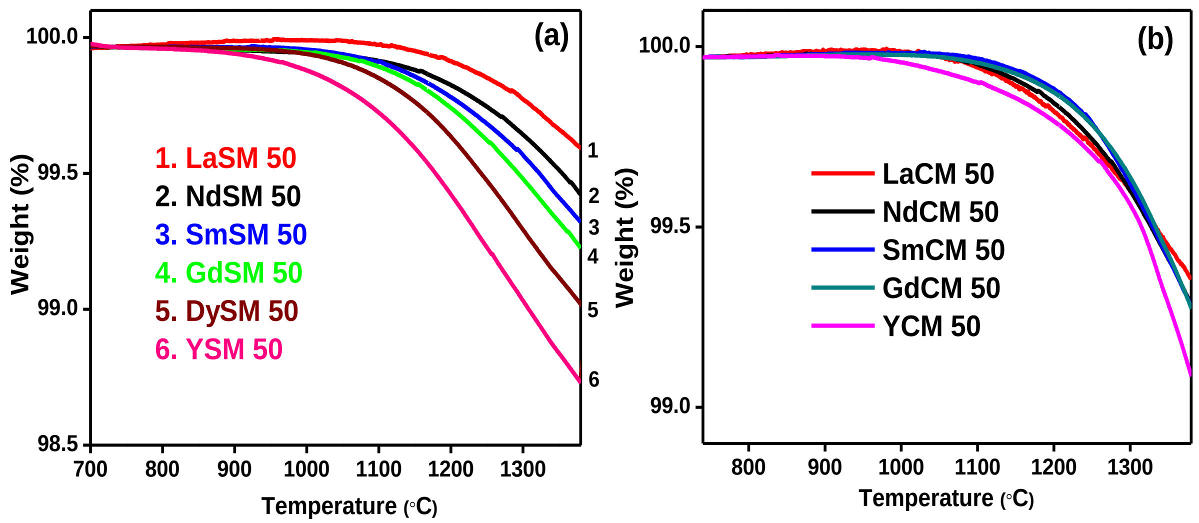

Figure 6. Representative mass loss profiles of (a) $Ln_{0.5}Sr_{0.5}MnO_3$ and (b) $Ln_{0.5}Ca_{0.5}MnO_3$ with respect to temperature during thermal reduction under Ar.

This can be explained based on the role of size variance factor (σ^2) and the tolerance factor (τ). The two variations are reconciled using a simple model as described in **Figure 7**. ATO_3, is an ideal cubic perovskite (τ=1, r_A^0 is the A cation radii) where each oxygen atom is co-ordinated by 1 linear T-O-T and 2 perpendicular A-O-A bridges (Figures 7a and b). Size disparity between a pair of A cations displaces the oxygen atom by σ Å (Figure 7c). On the other hand, two A cations having the same size ($r_A < r_A^0$) analogously displaces the oxygen atom by $r_A - r_A^0$ (Figure 7d).

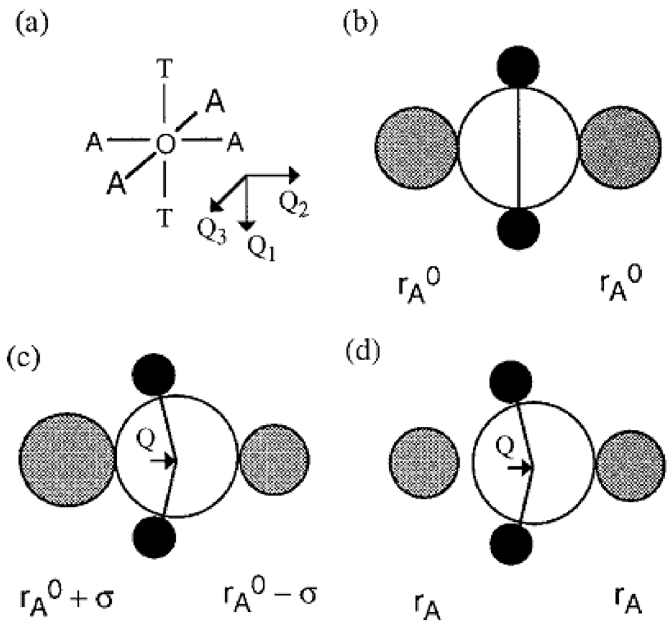

Figure 7. Hard sphere model for showing local oxygen position/displacement in ATO_3 perovskite varying the radii of A cation (b) to (c) to (d). Only one pair of A cation is shown for clarity. Reproduced by permission of American Chemical Society from Ref.[81].

Clearly, variation of σ^2 changes the mean Mn-O distances and Mn-O-Mn angles. High local disorder resulting from the mismatch between the radii of Ln and A cations in $Ln_{0.5}A_{0.5}MnO_3$ perovskites (ES11 and ES12, see the experimental section, Table 4) signifies the greater displacement of the oxygens from the mean position that can act as the driving force to remove oxygens easily.[88] Notably, σ^2 is higher for LnSM50 derivatives (Table 4) and highest for YSM50.

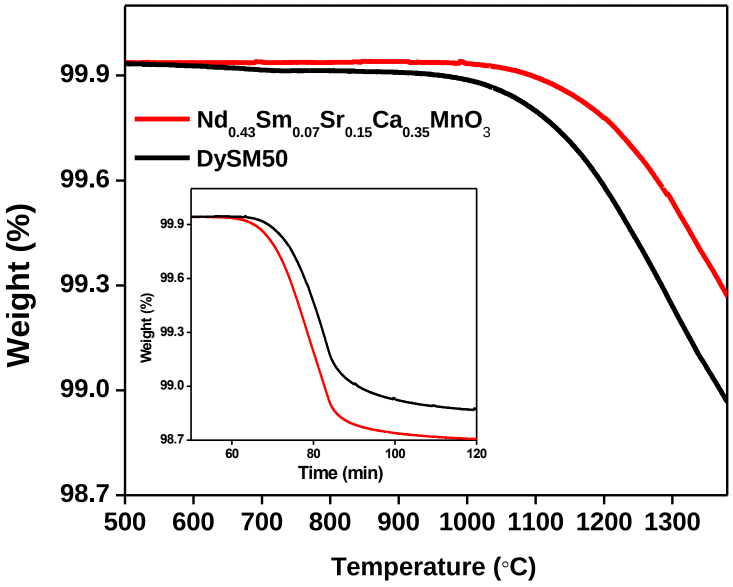

Figure 8. Mass loss profile of $Nd_{0.43}Sm_{0.07}Sr_{0.15}Ca_{0.35}$ MnO_3 **(τ=0.967, σ^2= 0.0038)** and DySM50 **(τ=0.967, σ^2= 0.014)** with respect to temperature. Inset shows the mass loss profile with time.

In order to investigate the impact of σ^2 alone, O_2 evolution was measured with $Nd_{0.43}Sm_{0.07}Sr_{0.15}Ca_{0.35}MnO_3$ and DySM50. These two perovskite having the same τ (τ=0.967) but with significantly different σ^2 such as 0.0038 and 0.014 for $Nd_{0.43}Sm_{0.07}Sr_{0.15}Ca_{0.35}MnO_3$ and DySM50 respectively. The one with higher σ^2 value starts reduction at a lower temperature than the one with a lower σ^2 value (**Figure 8**). It therefore, appears that the reduction characteristics of the manganites are clearly determined by both τ and σ^2.

Thermochemical CO_2 splitting activity of LnSM50 and LnCM50 has been investigated by injecting CO_2 at 1100°C (**Figure 9**). The total amount of CO produced is presented in Figure 9b for the LnSM50 series, showing the highest value for YSM50

(571μmol/g). CO production seems to be governed by the initial gain occurring within a few minutes followed by the slow gain due to diffusion. Similar kinetics is also observed for the LnCM50 derivatives (Figure 9c). The maximum amount of CO produced by YCM50 (671 μmol/g) is even higher than that with YSM50 (Figure 9d).

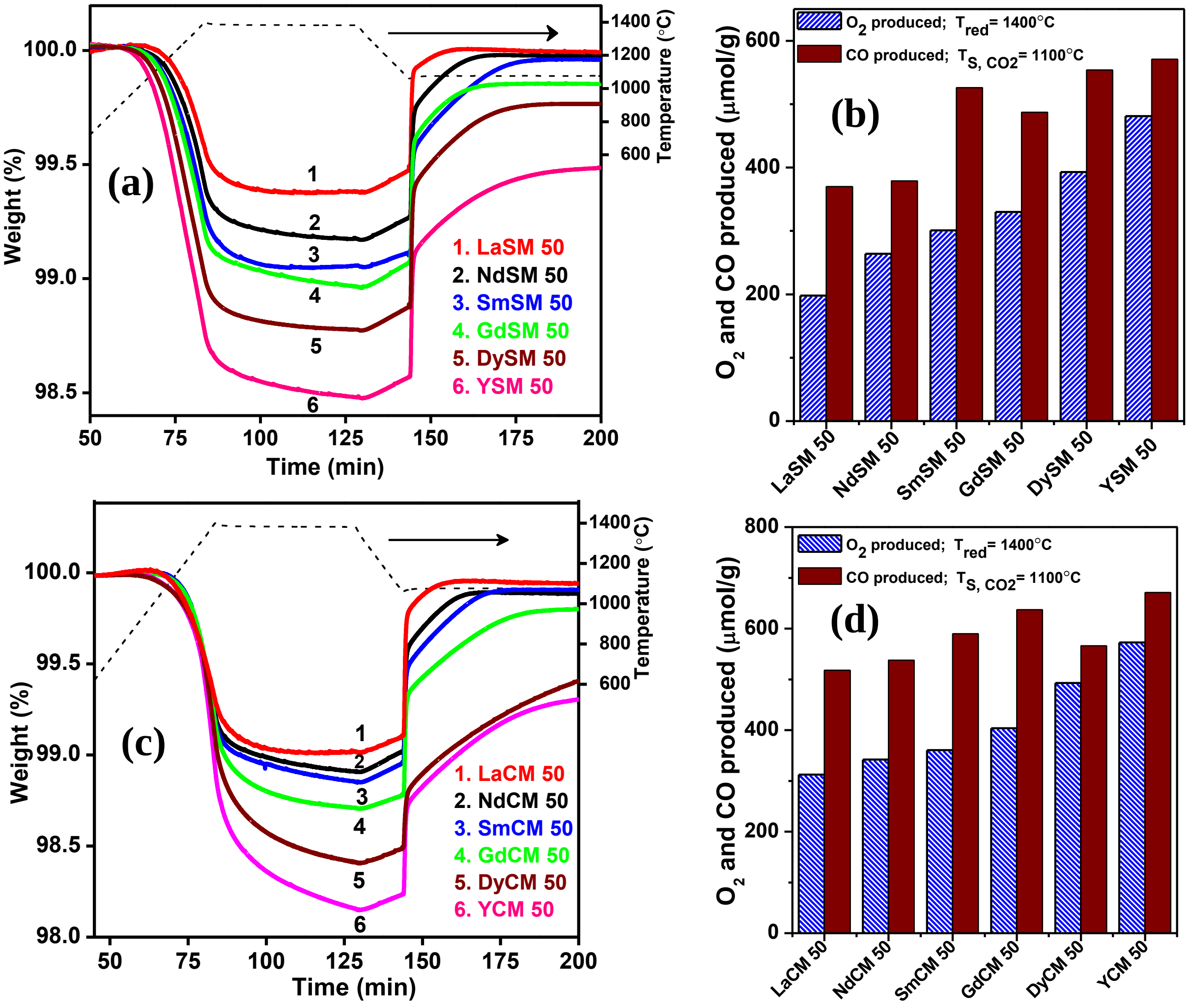

Figure 9. Representative TGA curves for the thermochemical splitting of CO_2 (a) by $Ln_{0.5}Sr_{0.5}MnO_3$ and (c) by $Ln_{0.5}Ca_{0.5}MnO_3$. Reduction and oxidation temperatures are 1400°C and 1100°C respectively. Figures (b) and (d) represent the total amount of O_2 (dashed bar) and CO (filled bar) produced by $Ln_{0.5}Sr_{0.5}MnO_3$ and $Ln_{0.5}Ca_{0.5}MnO_3$ respectively.

The oxidation yield (% α_{1100}) of LaSM50, NdSM50 and SmSM50 are 93%, 84% and 87% respectively which implies reversible mass gain (Table 3, ES5, see the experimental section). A decrease in oxidation yield is found from GdSM50 onwards and it becomes quiet significant for YSM50 (59%). As the kinetics of oxidation is reported to be faster at lower temperature, we have carried out CO_2 splitting at 900°C as well (**Figure 10**). GdSM50, DySM50 and YSM50 compositions show improvement in the oxidation yield at 900°C (α_{900}) in comparison with that one at 1100°C (α_{1100}). Strikingly, the highest improvement is observed for YSM50 which achieves an oxidation yield close to 80% at 900°C compared to 59% at 1100°C (**Table 5**). The reason for this may lie in the fact that the equilibrium driving force for the reverse reduction reaction is less significant at low temperatures.[67]

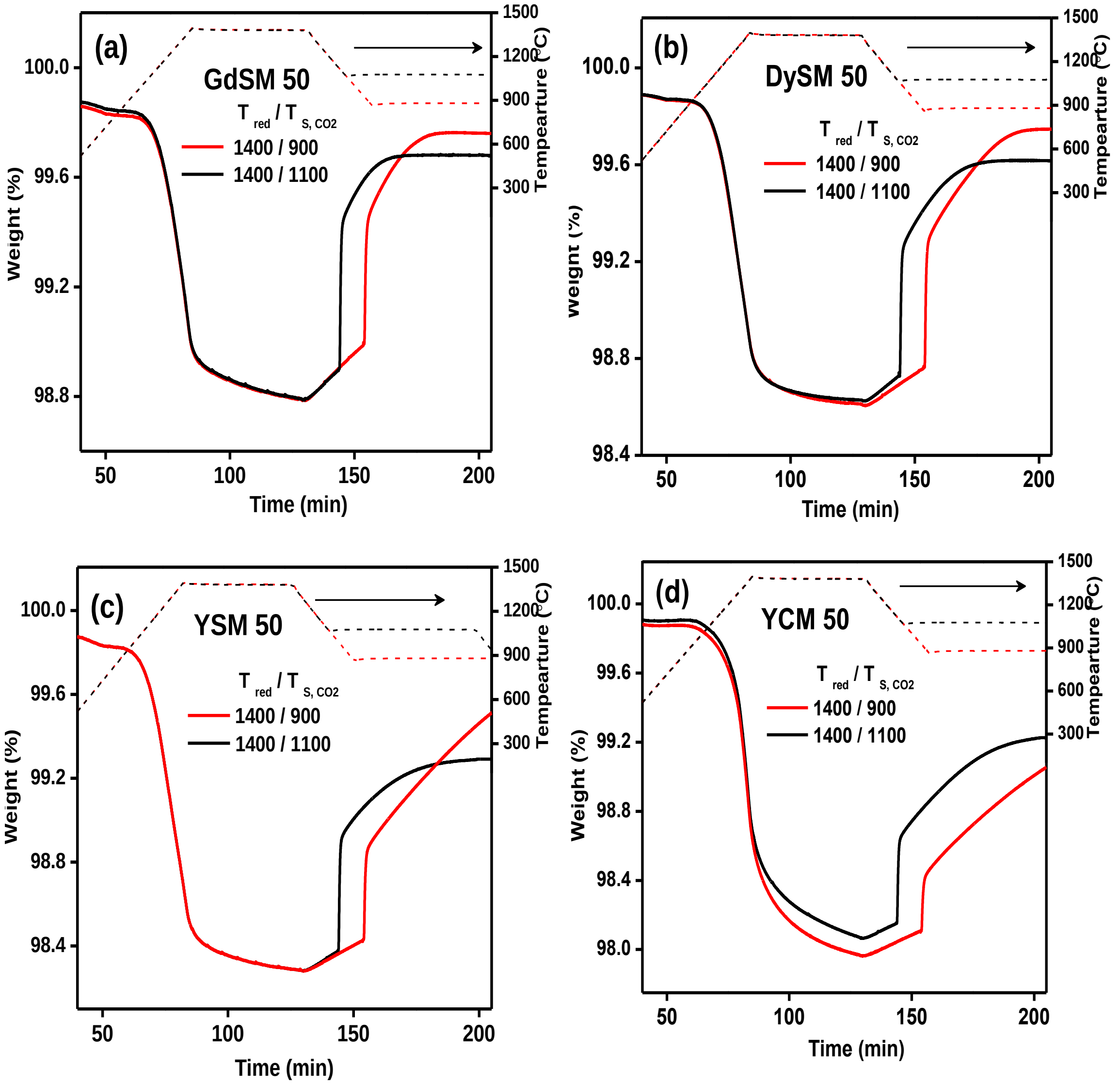

Figure 10. Representative TGA of thermochemical CO_2 splitting of (a) GdSM50 (b) DySM50 (c) YSM50 and (d) YCM50. Reduction temperature is 1400°C. CO_2 splitting (oxidation) is performed at 900°C and compared with 1100°C performances.

In the case of the LnCM50 series, the oxidation yield (α_{1100}) is in the range of 78- 85% except for DyCM50 and YCM50 which show a sharp decline to 58% (Table 2). Although oxidation thermodynamics is known to be favoured at lower temperatures,[55] no such improvement is apparent in the oxidation of YCM50 composition at 900°C (Figure S6d, Table 4). This may be due to the increase in diffusion lengths resulting from sintering or slower kinetics at lower temperature.[68]

Table 5. Oxidation yield at 900°C (α_{900}) is presented in comparison with 1100°C. (α_{1100}) for selective compositions.

Composition	T_{red} (°C)	O_2 produced (μmol/g)	X_{red} (%)	CO produced (μmol/g) 900°C	α_{900} (%)	CO produced (μmol/g) 1100°C	α_{1100} (%)
GdSM 50	1400	~327	~59	485	**74.6**	487	**73.8**
DySM 50	1400	~390	~71	613	**78.6**	554	**70.5**
YSM 50	1400	~481	~74	757	**78.7**	571	**59.4**
YCM 50	1400	~593	~78	647	**54.5**	671	**58.3**

As YSM50 starts to produce O_2 at a comparatively low reduction temperature and can also split CO_2 effectively even at 900°C, we explored CO_2 splitting activity at reduction temperatures (T_{red}) of 1200°C and 1300° followed by the oxidation at 900°C (**Figure 11**). YSM50 evolves 389 μmol/g of O_2 and 624 μmol/g of CO for the reduction /oxidation temperatures of 1300°C /900°C (Figure 11, **Table 6**). To the best of our knowledge, the performance of YSM50 with the reduction/oxidation temperatures of 1300°C/900°C is superior not only to ceria but to all other perovskite catalysts reported in the literature so far (Table 6). Furthermore, on reducing at 1200°C, YSM50 produces 258 μmol/g of O_2 followed by the production of 418 μmol/g of CO at 900°C (Figure 11). Notably, the O_2 production activity of YSM50 at 1200°C is comparable to that of LaSM50 reduced at 1400°C (Table 6) and the subsequent CO production activity of YSM50 at 900°C is also considerably superior.

Decrease in the reduction and oxidation temperatures along with the enhancement of fuel production activity is beneficial for energy applications.

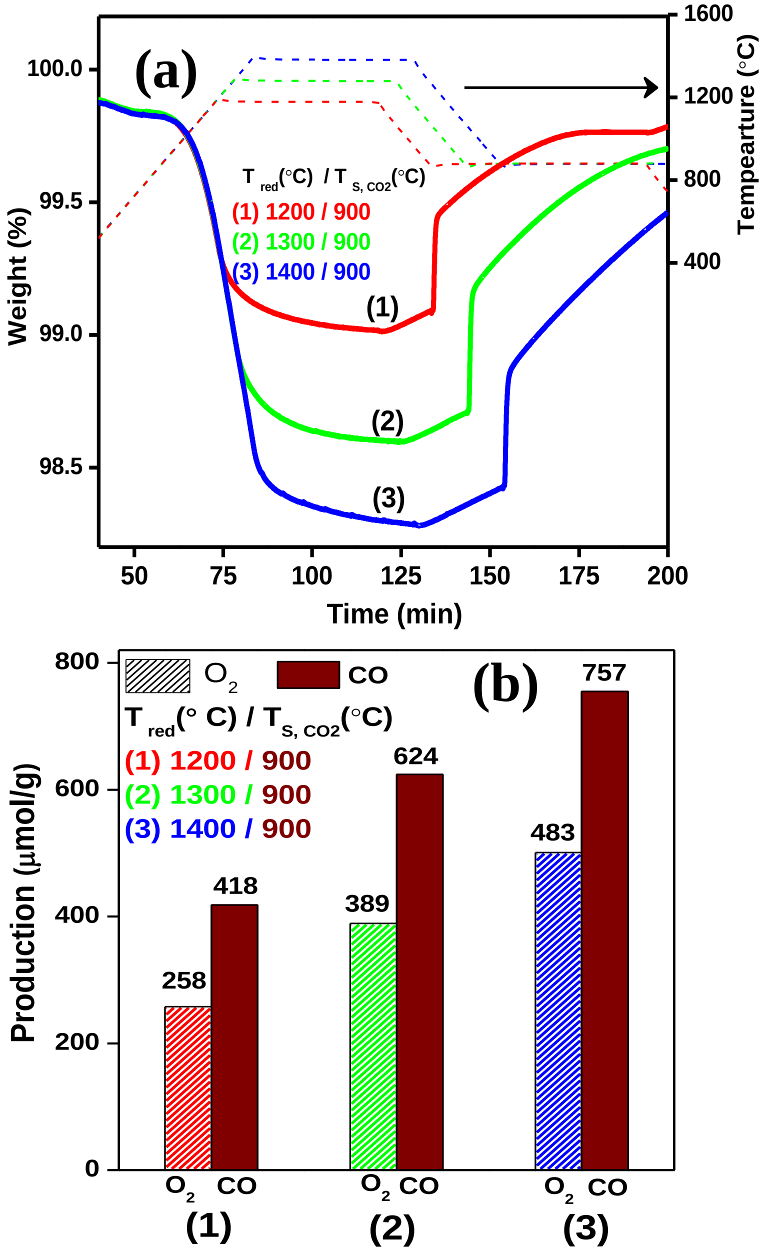

Figure 11. (a) Thermochemical CO_2 splitting profile and (b) the corresponding histogram for $Y_{0.5}Sr_{0.5}MnO_3$ (YSM50) derived from TG analysis. Reduction temperature is in the range of 1400°C to 1200°C. CO_2 splitting was performed at 900°C.

We have further tested the performance of YSM50 during three successive CO_2 splitting cycles for the reduction and oxidation temperature of 1200°C and 900°C respectively (**Figure 12**) and observed reversibility in both O_2 evolution and CO production.

Table 6. Comparison of thermochemical CO and/or H_2 evolution results of the present study with those reported for similar systems in the literature.

Material	**T_{red} (°C)**	**O_2 evolved (µmol/g)**	**T_{oxd} (°C)**	**CO (H_2)evolved (µmol/g)**	**References**
$Y_{0.5}Sr_{0.5}MnO_{3-\delta}$	**1400**	**483**	**900**	**757** [a]	Present Work
$Y_{0.5}Sr_{0.5}MnO_{3-\delta}$	**1300**	**389**	**900**	**624** [a]	Present Work
$Y_{0.5}Sr_{0.5}MnO_{3-\delta}$	**1200**	**258**	**900**	**418** [a]	Present Work
$Y_{0.5}Ca_{0.5}MnO_{3-\delta}$	**1400**	**575**	**1100**	**671** [a]	Present Work
$La_{0.5}Ca_{0.5}MnO_{3-\delta}$	1400	315	1100	525[a]	112
$La_{0.5}Sr_{0.5}MnO_{3-\delta}$	1400	201	1100	325 [a]	112
$La_{0.5}Sr_{0.5}MnO_{3-\delta}$	1400	298	1000	298 [b]	91
$La_{0.5}Sr_{0.5}MnO_{3-\delta}$	1400	236	900	224 [a]	86
$La_{0.6}Sr_{0.4}MnO_{3-\delta}$	1400	205[a]	800	397 [c]	23
$La_{0.6}Sr_{0.4}Al_{0.6}Mn_{0.4}O_{3-\delta}$	1350	120	1000	247 [a]	87
$LaSrCoO_4$	1300	268	800	161 [b]	91
$CeO_{2-\delta}$	1400	57	1200	98 [a]	97
$Ce_{0.75}Zr_{0.25}O_2$	1400	193	1200	148 [a,d]	97
$Ce_{0.75}Zr_{0.25}O_2$	1400	179.4	1050	323.9 [b,d]	94

[a] CO_2 splitting was investigated using TG analysis. [b] H_2O splitting was investigated using TG analysis. [c] H_2O splitting was investigated in alumina tube reactor using infrared furnace with 500°C/min heating rate. [d] Nanoparticle was used to perform the investigation.

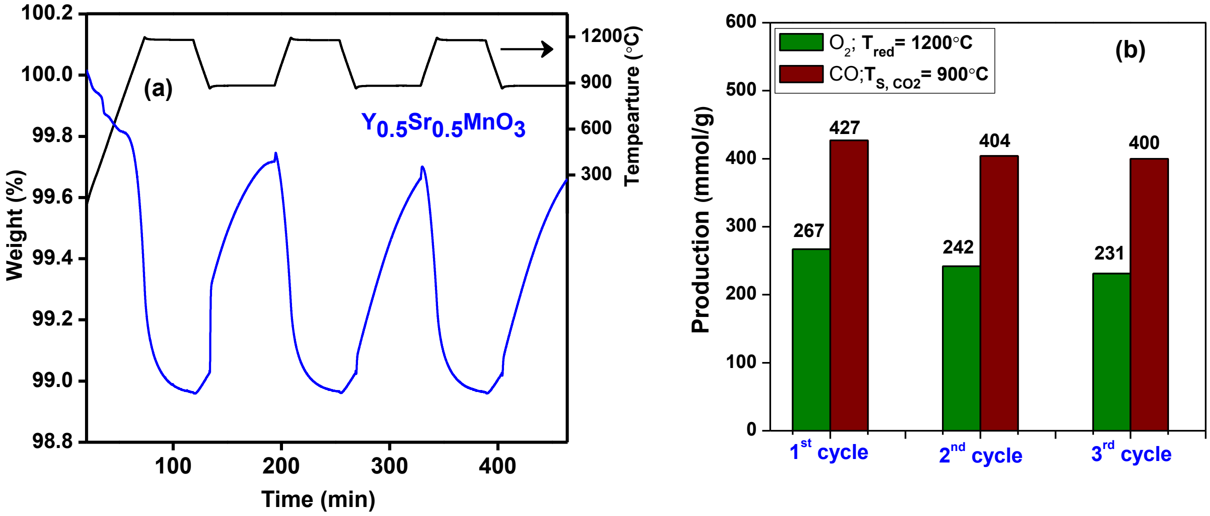

Figure 12. (a) TGA of $Y_{0.5}Sr_{0.5}MnO_3$ (YSM50) during three consecutive thermochemical CO_2 splitting cycles (reduction and oxidation temperature is 1200°C and 900°C respectively). (b) O_2 and CO production of YSM50 during three cycles.

No significant change in crystal structure and morphology is observed for YSM50 after multiple cycling (**Figure 13**), defines the stability of the material for practical applications.

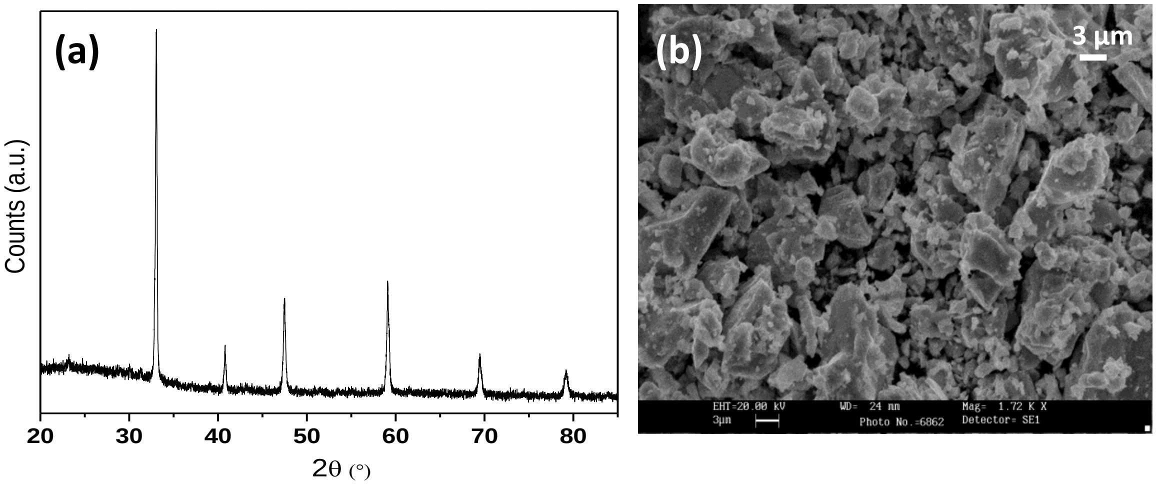

Figure 13. (a) PXRD pattern and (b) FESEM image of YSM50 after TGA cycling.

As YSM50 and YCM50 show superior CO production activity, we have investigated water splitting by these materials. The O_2 as well as H_2 evolution kinetics of YSM50 and YCM50 were measured using a gas chromatograph. The amount of O_2 produced by YSM50 and YCM50 are 481 and 593 μmol /g respectively, comparable to the values obtained from TGA measurements (**Figure 14**).

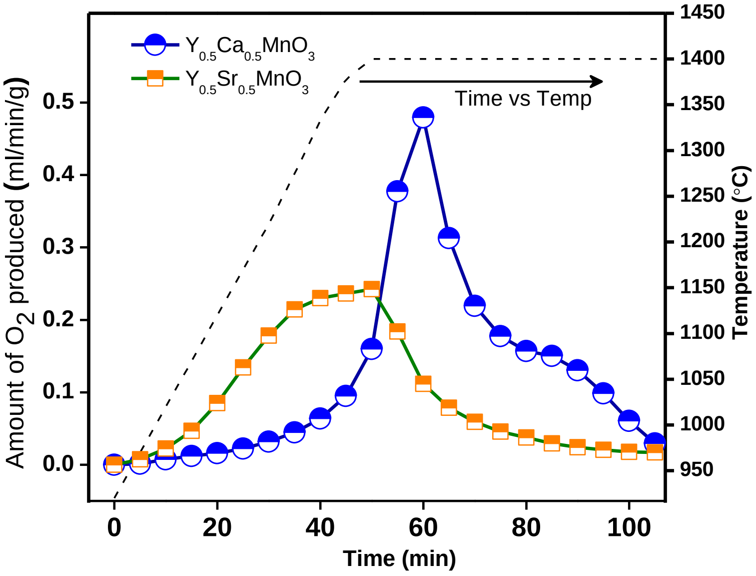

Figure 14. Oxygen evolution profiles of $Y_{0.5}A_{0.5}MnO_3$ (A= Sr, Ca) at the reduction temperature of 1400°C. YSM50 starts to evolve O_2 around 1000°C and reaches plateau around 1300°C whereas YCM starts to loss O_2 around 1275°C and reaches a peak after reaching 1400°C.

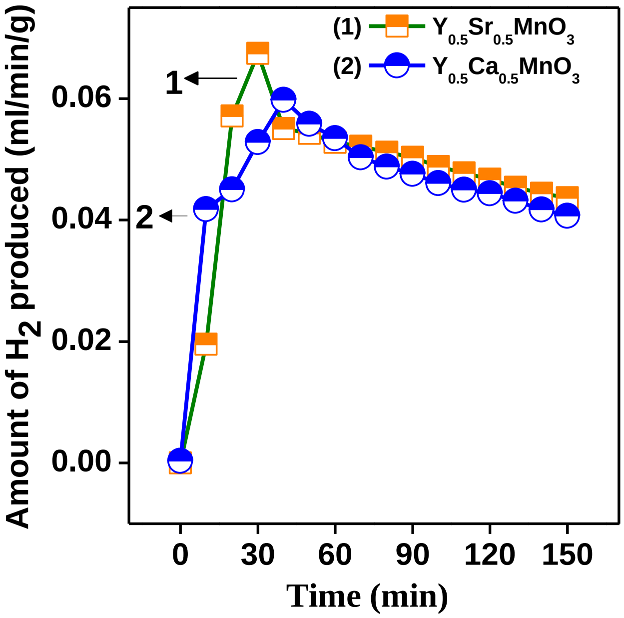

Figure 15. Hydrogen evolution profiles of $Y_{0.5}A_{0.5}MnO_3$ (A= Sr, Ca). H_2O splitting temperature is 1100°C.

The H_2O splitting activity was tested at 1100°C by introducing steam in a continuous N_2 flow. YSM50 and YCM50 show different kinetics of H_2 production by H_2O splitting from LaCM50 (**Figure 15**).[112] Thus, the production of H_2 starts immediately after the entry of H_2O in the gas stream, reaching a peak and then decreasing slowly resulting in a plateau after 40 minutes. The production of H_2 continues even after 140 minutes. The H_2 obtained for YSM50 and YCM50 in a span of 140 mins is 320 µmol/g and 310 µmol/g respectively (Figure 15). However, by extending the time to 250-300 minutes, one can obtain much higher H_2 yields.

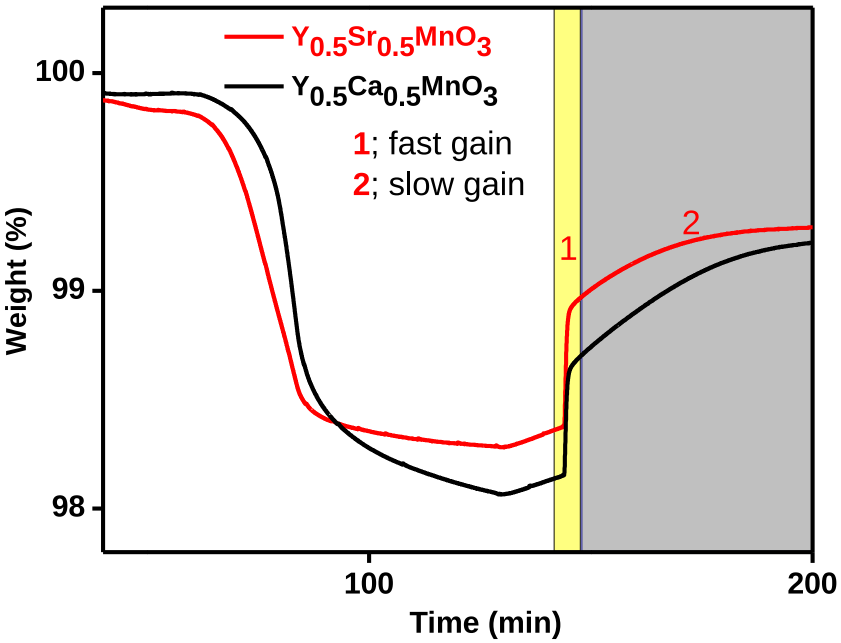

Figure 16. TGA curves of thermochemical CO_2 splitting of YSM50 and YCM50. The CO production (weight gain) region is highlighted to show two distinct kinetics. Step 1 (yellow colour) shows the fast gain of CO followed by step 2 (Grey colour) to highlight the slow process. CO_2 splitting temperature is 1100°C.

The kinetic behavior of H_2O splitting is similar to that of CO_2 splitting (**Figure 16, Table 7**). The yield of H_2 of YSM50 (YCM50) during the first 140 minutes of reaction arises from the fast kinetic regime (as in yellow region, step 1, Figure 16), followed by a slower regime (as in grey region, step 2, Figure 16) where diffusion plays a role.[68, 119]

Table 7. CO production in two distinct gain kinetics by YSM50 and YCM50.

	CO produced (µmol/g)		
Material	CO produced (µmol/g) **Fast kinetics (1)**	CO produced (µmol/g) **Slow kinetics (2)**	**Total CO produced** (µmol/g)
YSM 50	**326**	245	571
YCM 50	**293**	378	671

1.4.3

Effect of substitution of the Mn-site of $La_{0.5}Sr_{0.5}Mn_{1-x}A_xO_3$ by trivalent ions (A=Al, Ga, Sc) on the thermochemical generation of CO and H_2 from CO_2 and H_2O

1.4.3. Effect of substitution of Mn-site of $La_{0.5}Sr_{0.5}Mn_{1-x}A_xO_3$ by trivalent ions (A=Al, Ga, Sc) on the thermochemical generation of CO and H_2 from CO_2 and H_2O

Different proportions of Al^{3+}, Ga^{3+} and Sc^{3+} substitutions with Mn^{3+} of $La_{0.5}Sr_{0.5}MnO_3$ (LSM50) obtained $La_{0.5}Sr_{0.5}Mn_{1-x}A_xO_3$ (A=Al, Ga and Sc). We have prepared the Al^{3+}

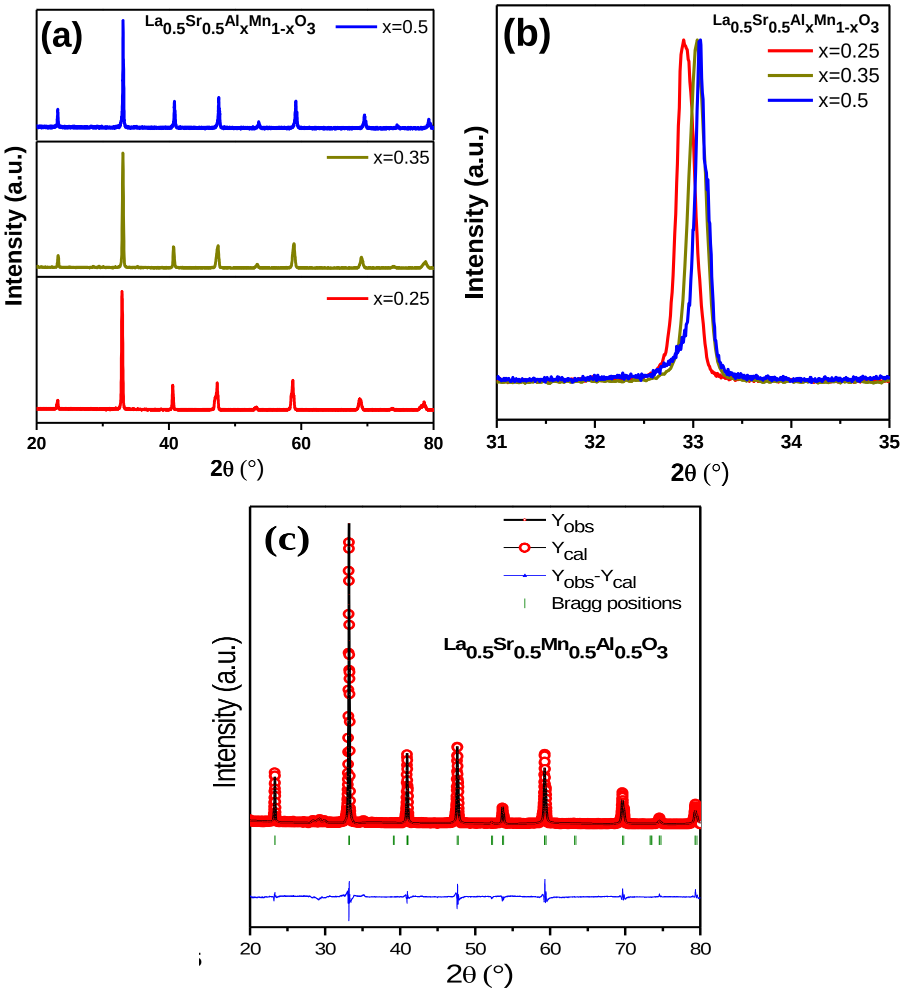

Figure 1. (a) PXRD patterns and (b) magnified view of the (110) reflections of $La_{0.5}Sr_{0.5}Mn_{1-x}Al_xO_3$ (x=0.25, 0.35, 0.5). (c) Lebail fitted PXRD patterns of $La_{0.5}Sr_{0.5}Mn_{0.5}Al_{0.5}O_3$ (lattice parameters are in Table 1).

All the $La_{0.5}Sr_{0.5}Mn_{1-x}A_xO_3$ (A= Ga and Sc) perovskite oxides crystallize in the R-3c space group, as observed by the PXRD patterns in **Figures 2-5** (**Table 1**). But in the case of Ga^{3+} the compositions were limited upto x=0.35 as the secondary phases precipitates for x>0.35 while for Sc^{3+}, Sc_2O_3 segregates[120] for x>0.1 respectively (Figures 3 and 5). The tolerance factor (τ) of the perovskite increases with x in the Al^{3+} and Ga^{3+} derivatives but decreases with x in the case of Sc^{3+} derivatives, as the size of Sc^{3+} is larger than Mn^{3+} (**Table 1**).

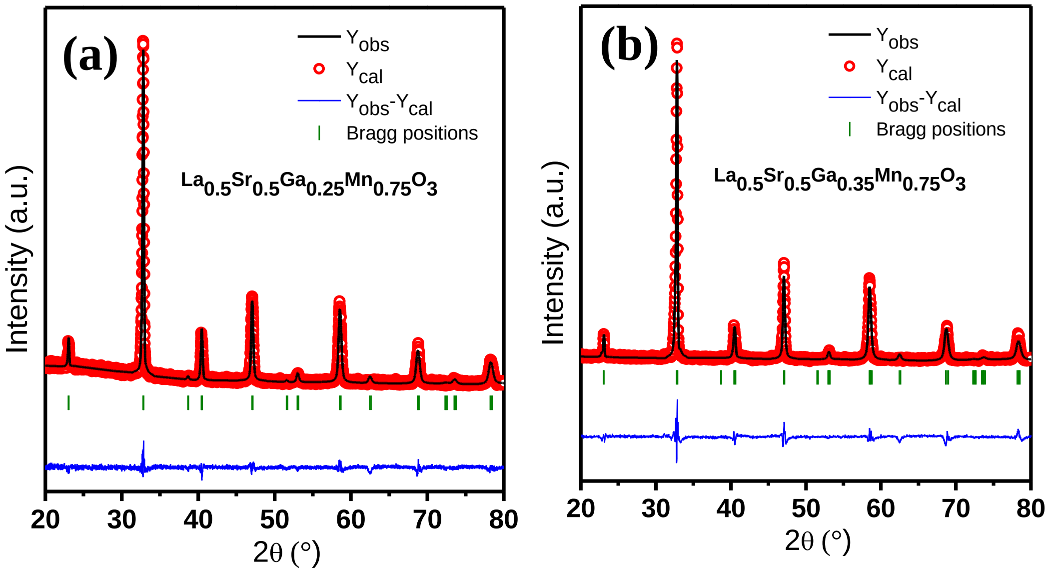

Figure 2. Lebail fitted PXRD patterns of (a) $La_{0.5}Sr_{0.5}Mn_{0.75}Ga_{0.25}O_3$ and (b) $La_{0.5}Sr_{0.5}Mn_{0.65}Ga_{0.35}O_3$ (lattice parameters are in Table 1).

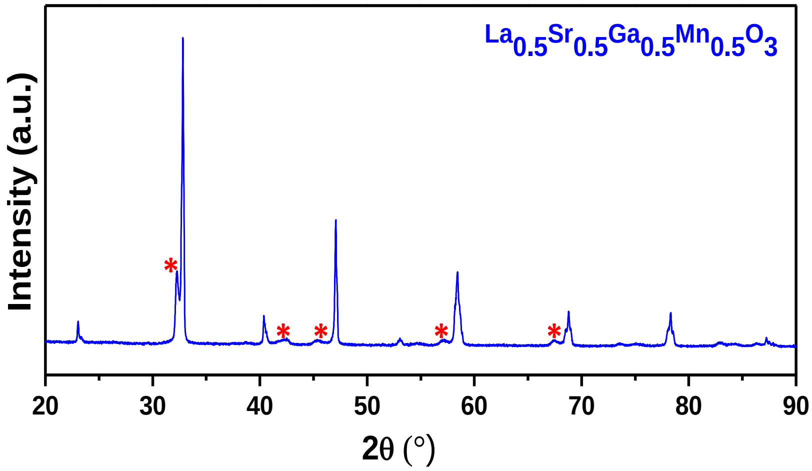

Figure 3. PXRD patterns of $La_{0.5}Sr_{0.5}Mn_{0.5}Ga_{0.5}O_3$. Extra diffraction peaks are marked by (*) shows the presence of secondary phases beside the formation of main perovskite structure.

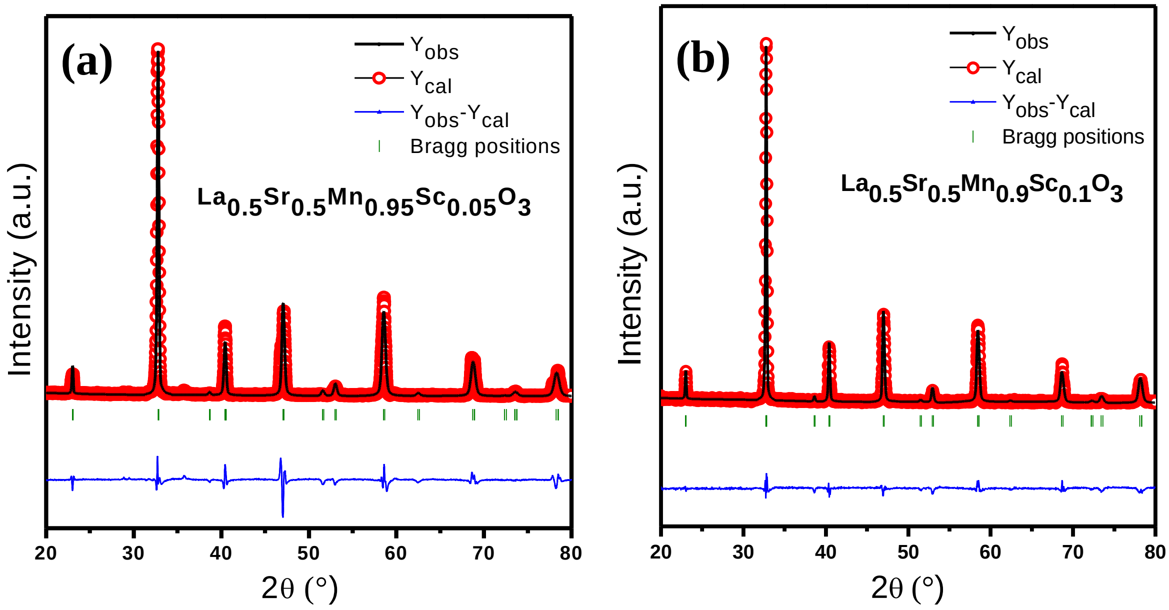

Figure 4. Lebail fitted PXRD patterns of (a) $La_{0.5}Sr_{0.5}Mn_{0.95}Sc_{0.05}O_3$ and (b) $La_{0.5}Sr_{0.5}Mn_{0.9}Sc_{0.1}O_3$ (lattice parameters are in Table 1).

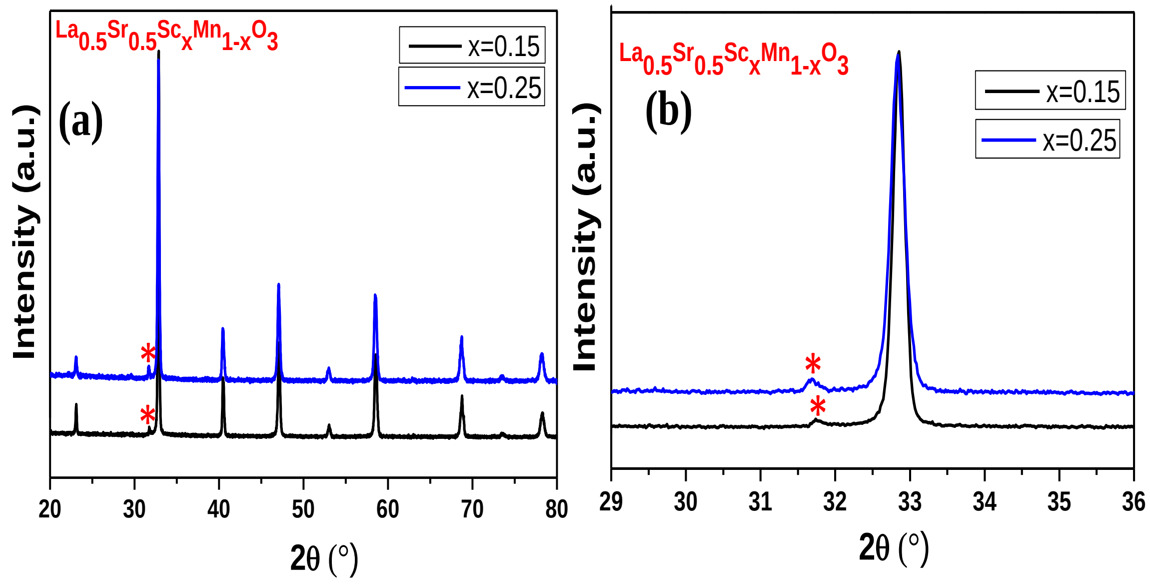

Figure 5. (a) Full range and (b) magnified PXRD patterns of $La_{0.5}Sr_{0.5}Mn_{1-x}Sc_xO_3$ (x=0.15, 0.25). Diffraction peaks marked by (*) confirms the presence of Sc_2O_3 (2θ~31.2˚) beside the formation of main perovskite structure.

Table 1. Summary of Space group (S.G.) and tolerance factor (τ) and lattice parameters of $La_{0.5}Sr_{0.5}Mn_{1-x}A_xO_3$ (A=Al, Ga and Sc). Shanon radii of the corresponding cations are mentioned in parenthesis are as follows; Mn^{3+} (0.645Å), Mn^{4+} (0.53Å), Al^{3+}(0.535Å), Ga^{3+}(0.62Å), Sc^{3+}(0.745Å), La^{3+}(1.36Å), Sr^{2+}(1.44Å), O^{2-}(1.4Å).

$La_{0.5}Sr_{0.5}Mn_{1-x}A_xO_3$	x	Tolerance factor (τ)	S. G.	a (Å)	b (Å)	c (Å)	Cell vol. ($Å^3$)
A=Al	**0.25**	1.01	R-3c	5.4409(7)	5.4409(7)	13.333(1)	**341.83**
	0.35	1.016	R-3c	5.3973(2)	5.3973(2)	13.2216(4)	**333.56**
	0.5	1.024	R-3c	5.3880(4)	5.3880(4)	13.2003(8)	**331.87**
A=Ga	**0.25**	0.999	R-3c	5.4592(3)	5.4592(3)	13.363(1)	**344.92**
	0.35	1.000	R-3c	5.4630(5)	5.4630(5)	13.330(2)	**344.54**
A=Sc	**0.05**	0.993	R-3c	5.4594(3)	5.4594(3)	13.3764(9)	**345.3**
	0.1	0.991	R-3c	5.4686(9)	5.4686(9)	13.393(2)	**346.9**

FESEM images and energy dispersive X-ray (EDX) mapping reveal that the as-synthesized oxides comprise of micron-sized particles and confirm the homogenous distribution of metal cations as shown in **Figures 6 and 7**. The BET surface area is of around 1-2 m^2/g. Reduction of the oxide and splitting of CO_2 accompanied by the formation of CO was studied by thermogravimetric analysis (TGA). Splitting of H_2O was studied by using a locally fabricated set-up incorporating a gas chromatograph-TCD (see reactivity test section).[118] The reduction and oxidation temperatures in CO_2 (or H_2O) splitting studies were 1400°C and 1100°C respectively.

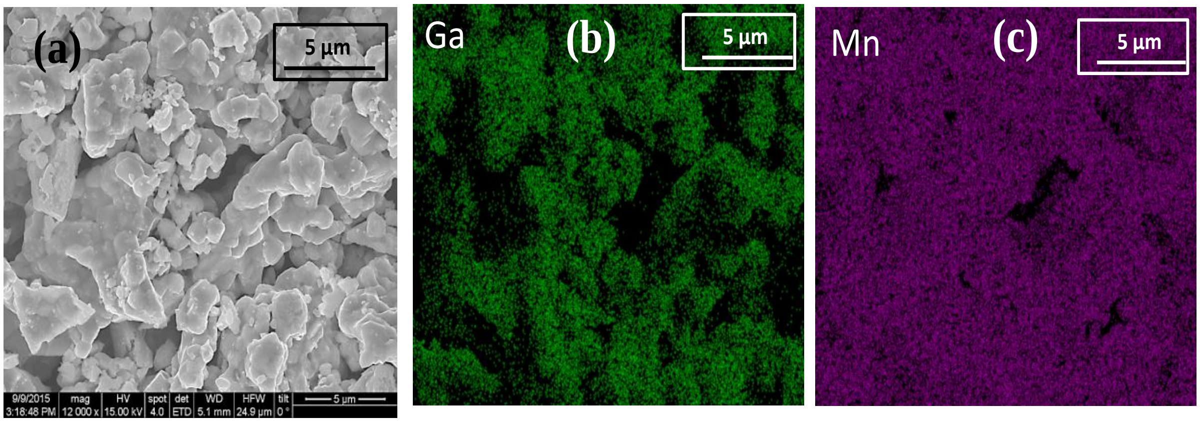

Figure 6. (a) FESEM image and (b, c) EDX mapping of synthesized $La_{0.5}Sr_{0.5}Mn_{0.75}Ga_{0.25}O_3$.

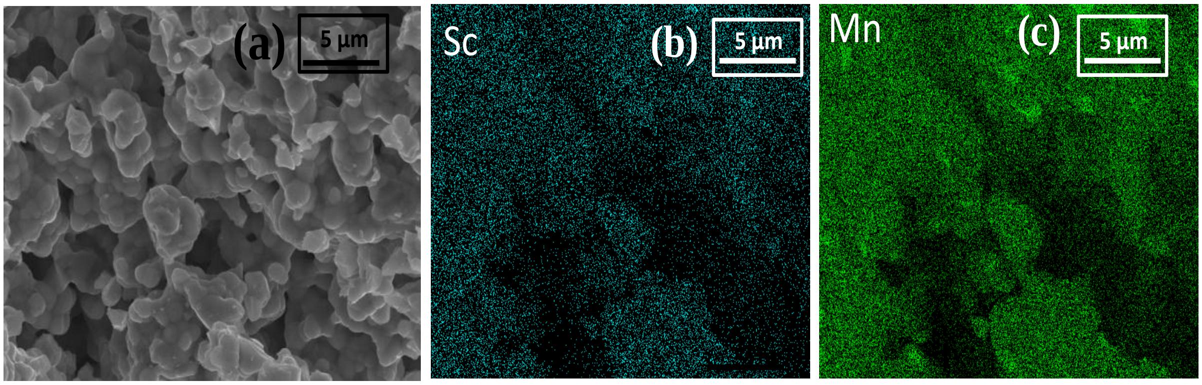

Figure 7. (a) FESEM image and (b, c) EDX mapping of as synthesized $La_{0.5}Sr_{0.5}Mn_{0.95}Sc_{0.05}O_3$

In **Figure 8**, we show representative TGA curves of $La_{0.5}Sr_{0.5}Mn_{1-x}Al_xO_3$ along with the histogram of thermochemical splitting of CO_2 for x=0.25-0.5. The amount of O_2 and CO produced increases with Al^{3+} content giving the highest values of O_2 and CO produced when x=0.5. Thus, the quantities of O_2 and CO produced by the x=0.5 composition are 322 and 388 μmol/g respectively. As shown in **Figure 9**, $La_{0.5}Sr_{0.5}Mn_{0.5}Al_{0.5}O_3$ was also subjected to multiple cycling in the temperature range of 1400-1100°C, and 370 μmol/g of CO on average was obtained during three successive cycles without significant deviation in activity.

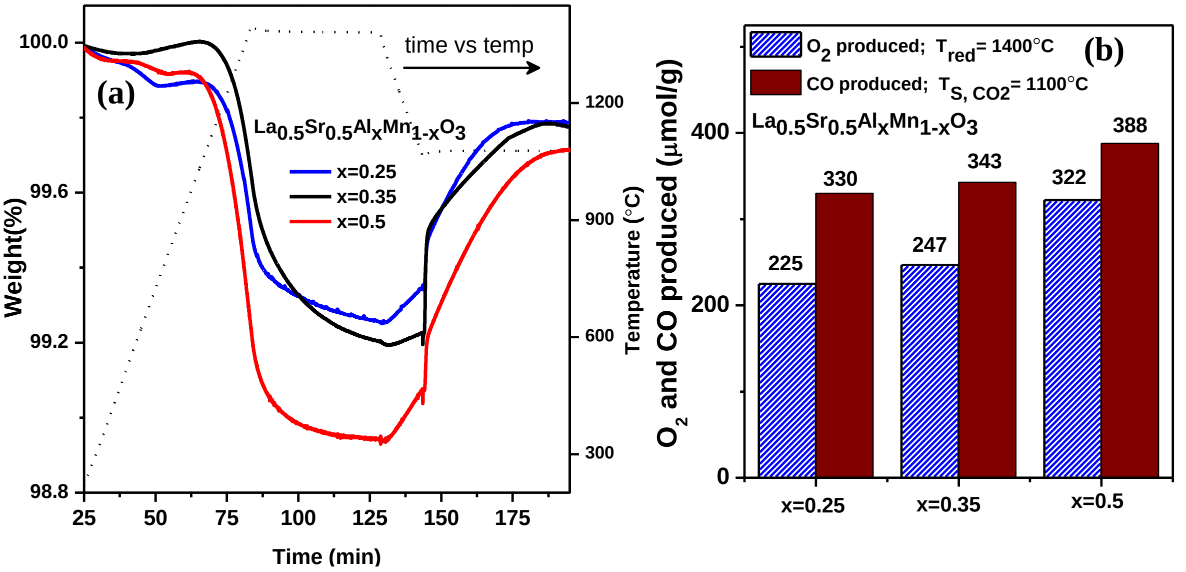

Figure 8. (a) Representative TGA and (b) corresponding histogram of thermochemical CO_2 splitting of $La_{0.5}Sr_{0.5}Mn_{1-x}Al_xO_3$ (x= 0.25, 0.35 and 0.5). Reduction and oxidation temperatures are 1400 °C and 1100°C respectively.

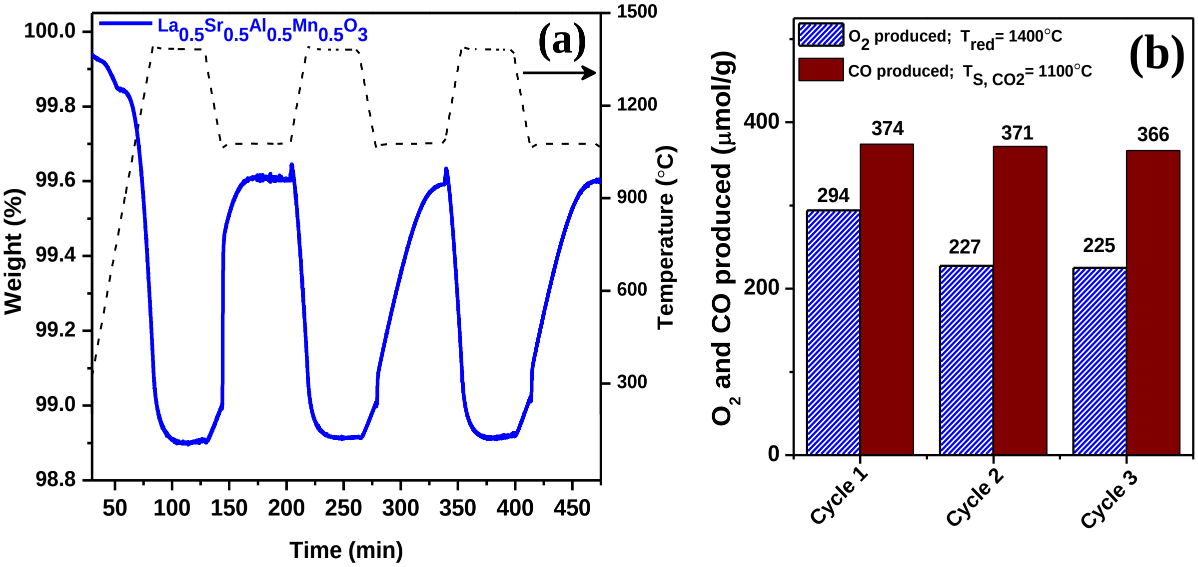

Figure 9. (a) TGA plot and (b) corresponding histogram of $La_{0.5}Sr_{0.5}Mn_{0.5}Al_{0.5}O_3$during three consecutive thermochemical CO_2 splitting cycles (reduction and oxidation temperature is 1400°C and 1100°C respectively)

The structures and compositions of the oxides remained the same after multiple cycling (**Figure 10**, **Table 2**).

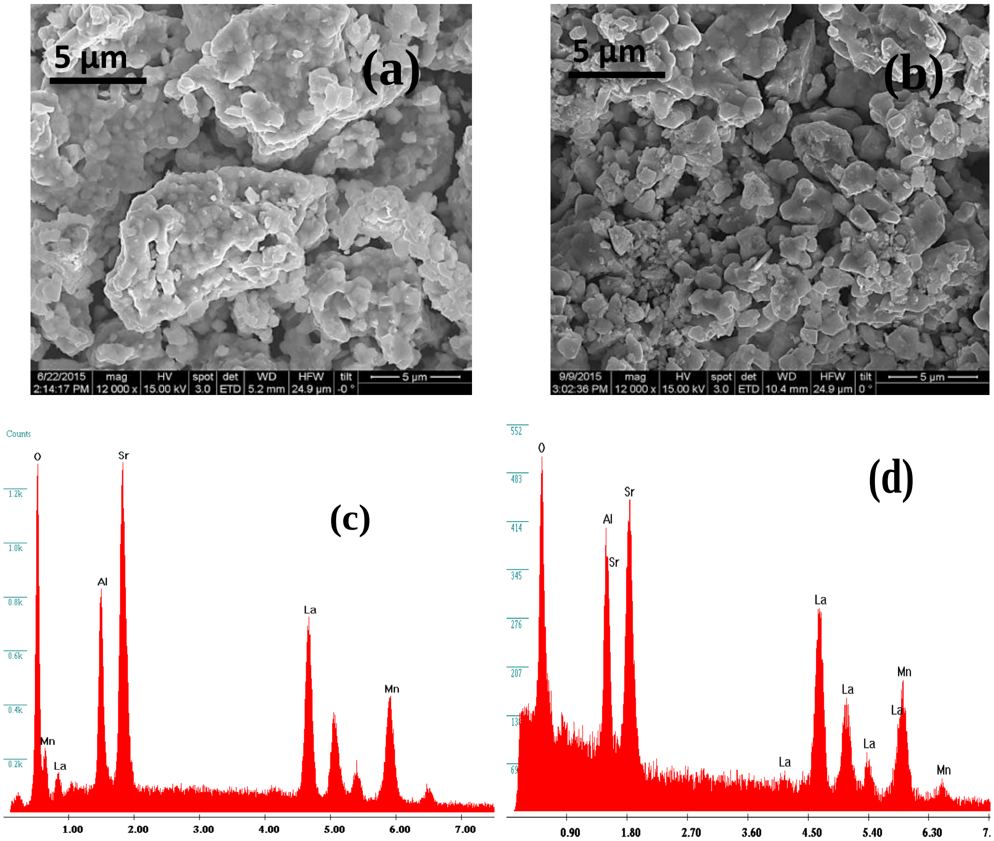

Figure 10. FESEM images of $La_{0.5}Sr_{0.5}Mn_{0.5}Al_{0.5}O_3$ (a) before and (b) after TG analysis. EDS (X and Y axis are Energy in KeV and counts respectively) of the same (c) before and (d) after TGA.

Table 2. Atomic % of La, Sr, Al and Mn present in $La_{0.5}Sr_{0.5}Mn_{0.5}Al_{0.5}O_3$before and after TG analysis as calculated from EDS analysis.

	La L	**Sr L**	**Al K**	**Mn K**	**O K**
$La_{0.5}Sr_{0.5}Mn_{0.5}Al_{0.5}O_3$	**Atomic %**	**Atomic %**	**Atomic %**	**Atomic %**	**Atomic %**
Before TGA	11.6	11.7	12.8	11.1	52.8
After TGA	11.2	10.9	11.6	11.3	54.9

$La_{0.5}Sr_{0.5}Mn_{1-x}Ga_xO_3$ behaves somewhat similar to the Al^{3+} substituted perovskites. The amount of O_2 evolved increases with x (**Figure 11**). For, x=0.35, O_2 evolved 323 µmol/g (δ=0.2; % X_{red}=57), higher than x=0.25 (δ=0.18; % X_{red}=54) (**Figure 12**).

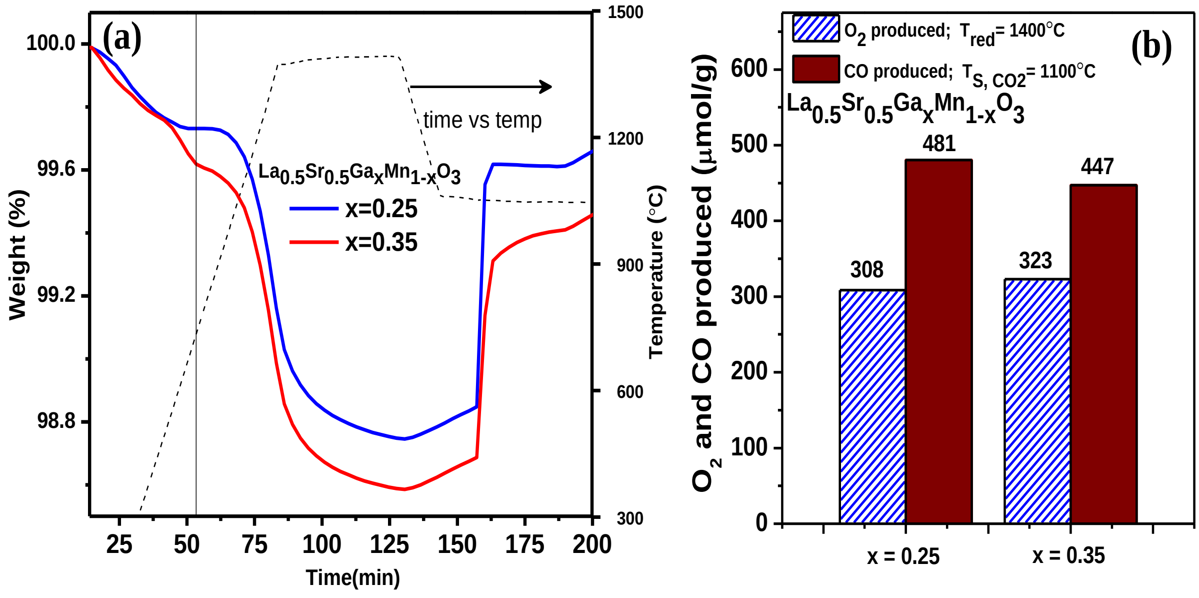

Figure 11. (a) Representative TGA and (b) corresponding histogram of thermochemical CO_2 splitting of $La_{0.5}Sr_{0.5}Mn_{1-x}Ga_xO_3$ (x= 0.25, 0.35). Reduction and oxidation temperatures are 1400 °C and 1100°C respectively.

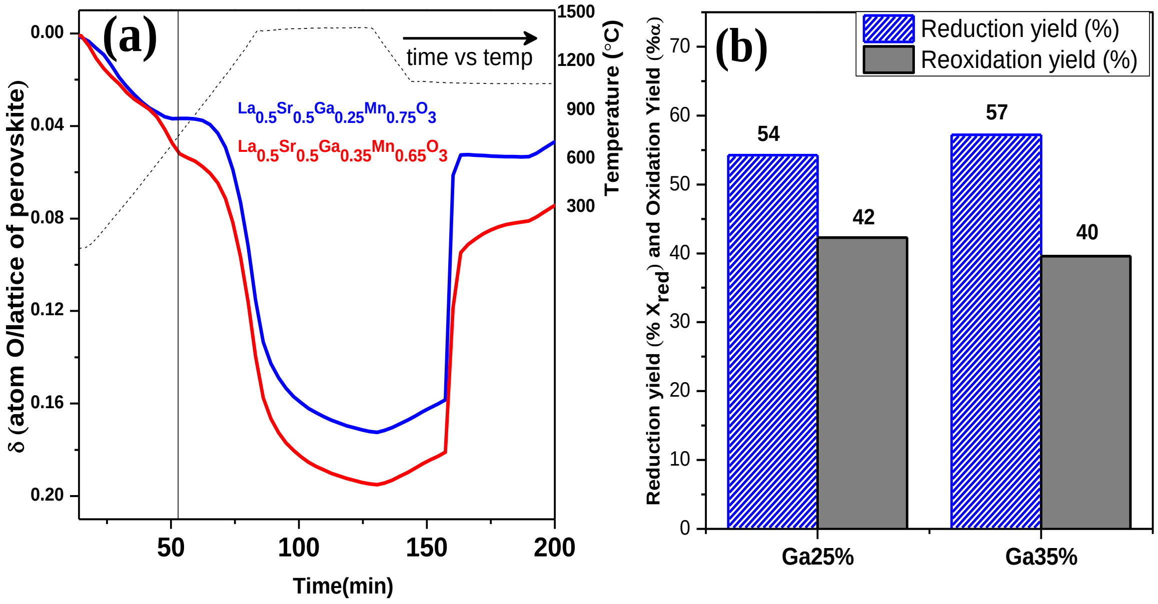

Figure 12. Evolution of oxygen nonstoichiometry of $La_{0.5}Sr_{0.5}Mn_{1-x}Ga_xO_3$ (x= 0.25, 0.35) during TGA. Histogram depicts reduction (% X_{red}) and reoxidation yield (%α) at temperature 1400°C and 1100°C respectively.

In earlier reports, besides Al^{3+}, doping of Ga^{3+} in the B site of La-Sr-Fe perovskite has been reported to decrease the Fe-O bond covalency and increase in oxygen nonstoichiometry.[121-

[125] The net decrease in Fe^{4+}/Fe ratio has been observed as a result of Ga^{3+} doping in La-Sr-Fe perovskite. In spite of the fact that, Ga^{3+} does not alter its oxidation state +3 during redox process, is reported to decrease the enthalpy and increase the entropy of oxygen vacancy formation in $La_{0.3}Sr_{0.7}FeO_3$ and also induce local lattice inhomogeneties.[122]

We have investigated the thermochemical splitting of CO_2 by $La_{0.5}Sr_{0.5}Mn_{1-x}Ga_xO_3$ (x=0.25, 0.35) by injecting CO_2 (Figure 11) at 1100°C. Ga^{3+} substituted perovskites yield a much higher quantity of CO (447 μmol/g) even for x=0.35. The quantity of CO obtained with x=0.25 is higher (480 μmol/g). The reoxidation yield (%α) of x=0.25 is 42%, higher than x=0.35 (40%) (Figure 12).

We could substitute Sc^{3+} in the B site of LSM only upto x=0.1 (Figure 5).[120] However, even with x=0.05, the yield of O_2 and subsequently CO are both high, the values being 417 μmol/g (δ=0.21; % X_{red}=72) and 545 μmol/g respectively (**Figures 13 and 14**). Increasing the Sc^{3+} content to x=0.1 does not improve O_2 production (426 μmol/g, δ=0.21; % X_{red}=73%) as well as CO production (491 μmol/g). The reoxidation yields are 65% and 58% respectively for x=0.05 and x=0.1 in the Sc^{3+} derivatives (Figure 14).

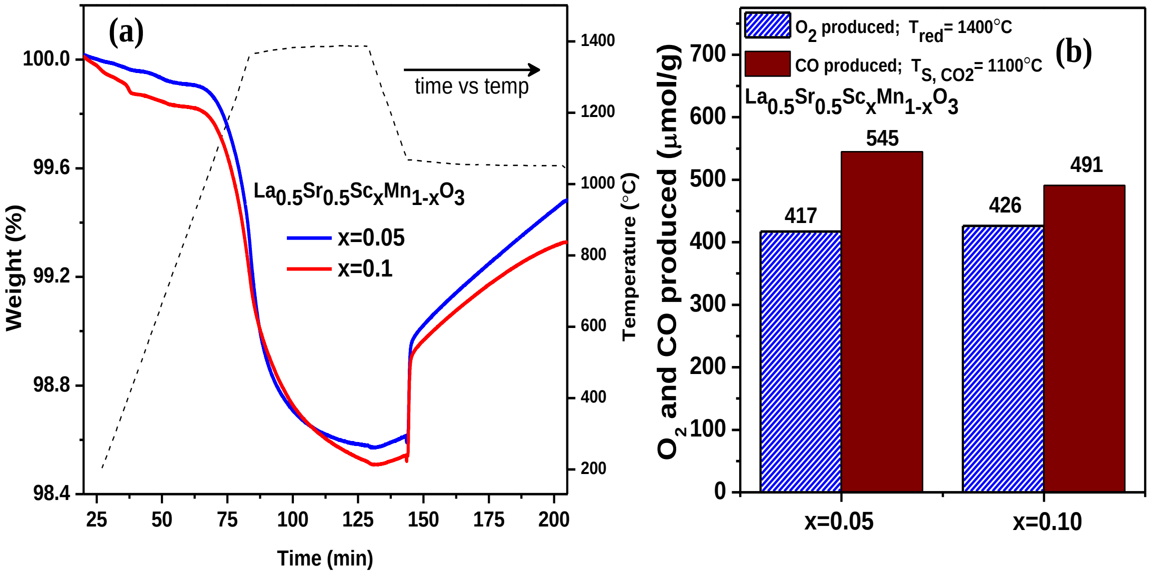

Figure 13. (a) Representative TGA and (b) corresponding histogram of thermochemical CO_2 splitting of (a) $La_{0.5}Sr_{0.5}Mn_{1-x}Sc_xO_3$ (x= 0.05, 0.1). Reduction and oxidation temperatures are 1400 °C and 1100°C respectively

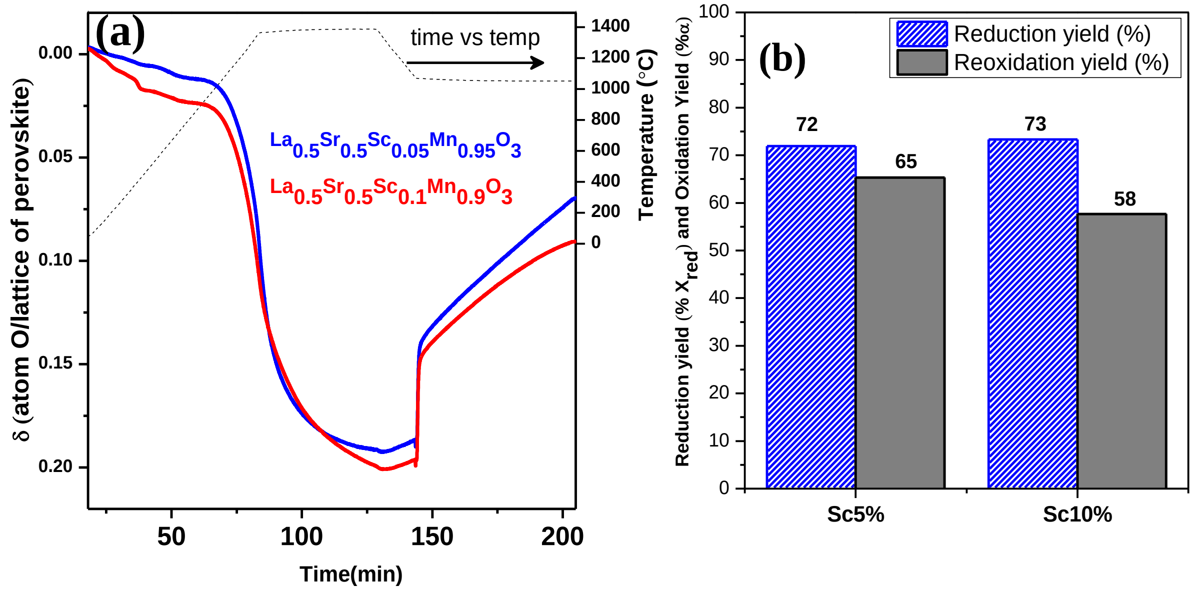

Figure 14. Evolution of oxygen nonstoichiometry of $La_{0.5}Sr_{0.5}Mn_{1-x}Sc_xO_3$(x= 0.05, 0.1) during TGA. Histogram depicts reduction (% X_{red}) and reoxidation yield (%α) of the same. Reduction and oxidation temperature is 1400°C and 1100°C respectively.

Optimum Sc^{3+} doping (5-10%) is reported to enhance the performance of $La_{0.8}Sr_{0.2}MnO_3$ (LSM20) as a SOFC cathode and in methane oxidation.[120, 126] Reduction in area specific polarization resistance and lowering of oxygen reduction overpotential is also observed for $La_{0.8}Sr_{0.2}MnO_3$(LSM20) by optimum Sc^{3+} doping.[91] This is because of the higher oxygen vacancy ratio and enhanced oxygen mobility related to the bigger size of Sc^{3+}.[120, 126-129] Alternatively, the remarkable increase of the O_2 production with substitution of as low as 5% of Sc^{3+} in LSM50 lattice can be related to its structural distortion connected with tolerance factor (τ) of perovskites (Table 1). Sequential replacement of smaller radii Mn^{3+} with larger radii Sc^{3+} gradually decreases the τ to 0.991 for $La_{0.5}Sr_{0.5}Sc_{0.1}Mn_{0.9}O_3$ in comparison to LSM50 (τ =0.990; Table 1). Earlier reports from our group indicates,[68] the decrease in τ results an increase in the tilting of the MnO_6 octahedra, accompanied by an increase in the lattice distortion, which helps in the removal of oxide ions. A decrease in τ decreases the Mn-O-Mn bond angles significantly, which in turn suppress the spatial overlap between Mn e_g and O 2p σ orbitals. This would definitely favor O_2 evolution.

Over doping of Sc^{3+} (>10%) in LSM20 acts as an anion vacancy trapping center through the association of Sc^{3+} with oxygen vacancy and is reported to deteriorate the oxygen conductivity in SOFC cathodes. This may be the reason why no further increment in O_2 evolution occurs beyond x=0.05. However, Sc^{3+} doping at B site of LSM_x has not been implemented for thermochemical fuel production yet.

Thermochemical CO_2 splitting cycle of $La_{0.5}Sr_{0.5}Sc_xMn_{1-x}O_3$ (x=0.05, 0.1) is shown in Figure 13. CO produced by $La_{0.5}Sr_{0.5}Sc_{0.05}Mn_{0.95}O_3$ and $La_{0.5}Sr_{0.5}Sc_{0.1}Mn_{0.9}O_3$ is 545 µmol/g and 491 µmol/g respectively, corresponding to the reoxidation yield (%α) of 65% and 58% respectively (Figure 14).

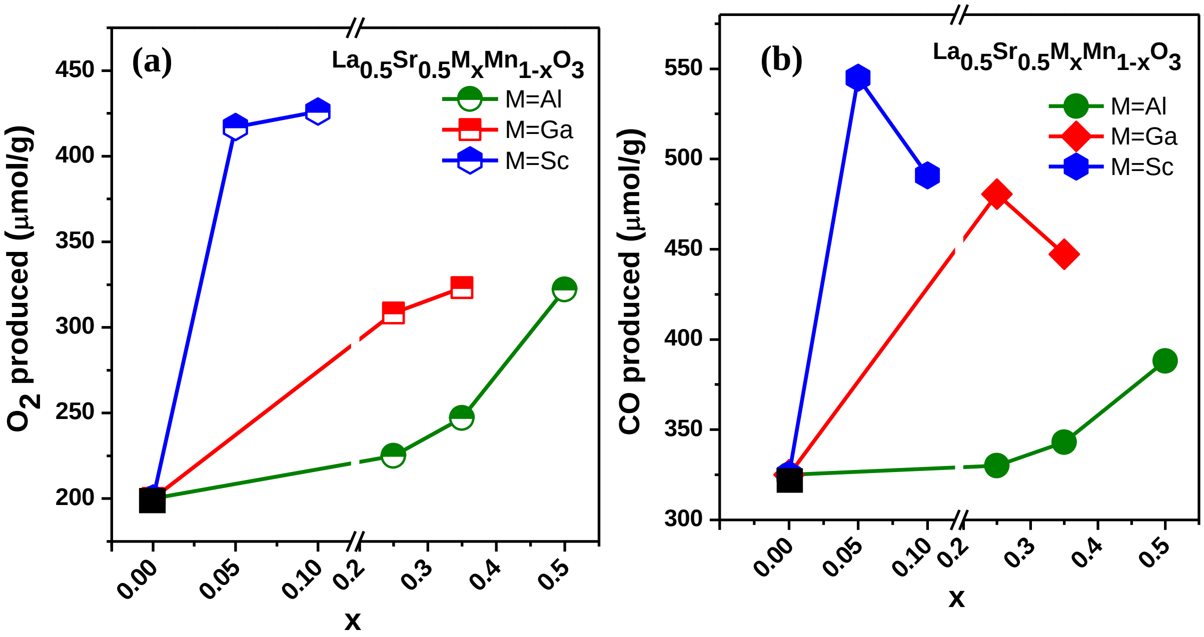

Figure 15. Comparative study of (a) O_2 (T_{red}=1400°C) and (b) CO (T_{oxd}=1100°C) evolution with amount of Mn site substituent of $La_{0.5}Sr_{0.5}Mn_{1-x}A_xO_3$ perovskites (A=Al, Ga, Sc; 100x=% of substituent).

In **Figure 15** we compare the relative performance of the Al^{3+}, Ga^{3+} and Sc^{3+} substituted LSMs. All these derivatives show better performance than the parent LSM. Clearly the effect of the valent ions varies as Sc>Ga>Al. For the same proportions of the trivalent ion (25%), yield of O_2 is 1.4 times higher in the Ga derivative compared to the Al derivative. Increase in O_2 yield is more remarkable in Sc derivative where the x=0.05 composition produces 1.9 times and 1.3 times O_2 compared to the x=0.25 and x=0.5 composite with Al (Figure 15a). CO yield of Ga derivative is of 1.5 times higher than Al derivative for similar proportions of x=0.25 (Figure 15b). The increase in CO yield due to 5% Sc substitution is 1.7 times and 1.4

times of x=0.25 and x=0.5 composite with Al respectively (Figure 15b). Notably, the CO production of x=0.25 Ga substitution and x=0.05 Sc substitution is of 1.5 times and 1.7 times of parent LSMs respectively

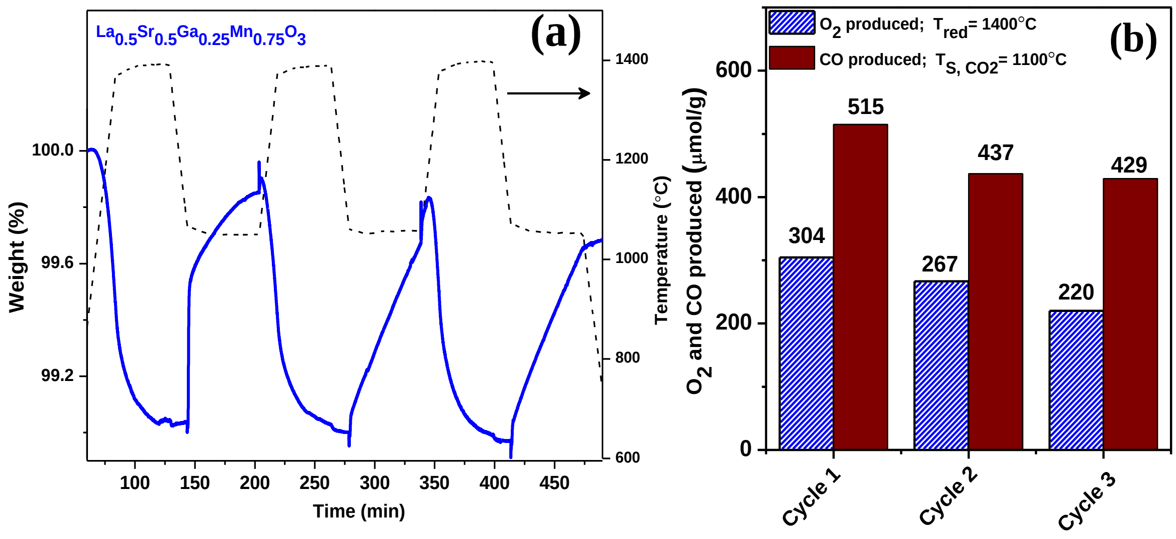

Figure 16. (a)TGA plot and (b) corresponding histogram for $La_{0.5}Sr_{0.5}Mn_{0.75}Ga_{0.25}O_3$ during three consecutive thermochemical CO_2 splitting cycles (reduction and oxidation temperature is 1400°C and 1100°C respectively).

In **Figures 16 and 17,** we have shown the fuel production by the Ga (25%) and Sc (5%) substituted LSMs over three cycles in the 1400˚C-1100˚C temperature range. The yields of O_2 and CO are affected marginally, the decrease after the third cycle less than 15-20%. The amount of CO produced by $La_{0.5}Sr_{0.5}Mn_{0.75}Ga_{0.25}O_3$ during the 1st, 2nd and 3rd cycles are 515, 437 and 429 µmol/g respectively while the CO produced by $La_{0.5}Sr_{0.5}Mn_{0.95}Sc_{0.05}O_3$ during the 1st, 2nd and 3rd cycles are 547, 496 and 476 µmol/g respectively. Decrease in fuel yield during multiple cycling is observed for most of the perovskites due to the sluggish kinetics or sintering.[87, 89, 91] Nonetheless, the CO produced in both Ga (25%) and Sc (5%) substituted perovskites even after the third cycle is higher than that found with parent LSM (316 µmol/g) or with x=0.5 substitution of Al (366 µmol/g).

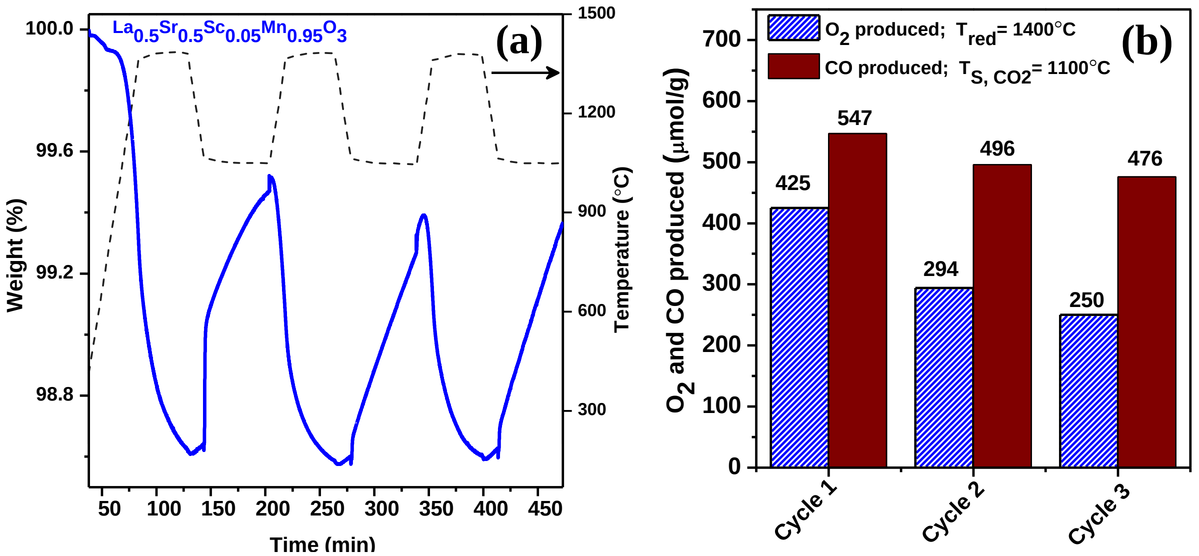

Figure 17. (a) TGA plot and (b) corresponding histogram for $La_{0.5}Sr_{0.5}Mn_{0.95}Sc_{0.05}O_3$ during three consecutive thermochemical CO_2 splitting cycles.

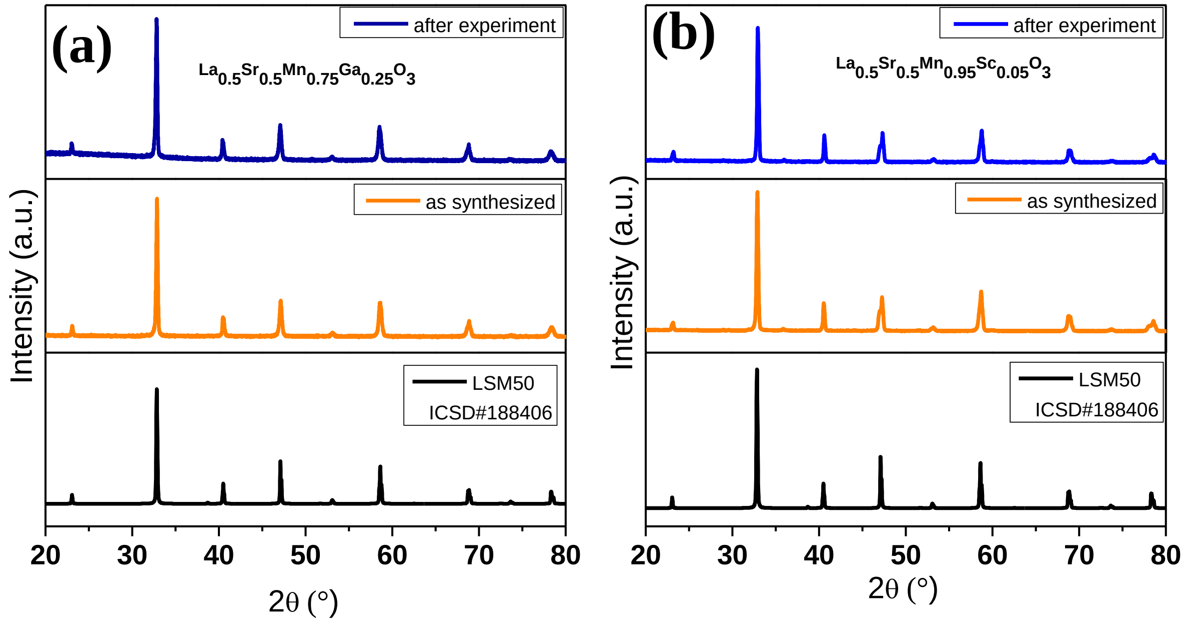

Figure 18. PXRD patterns of (a) $La_{0.5}Sr_{0.5}Mn_{0.75}Ga_{0.25}O_3$ and (b) $La_{0.5}Sr_{0.5}Mn_{0.95}Sc_{0.05}O_3$ before and after TGA.

The structures and compositions of perovskites remain unaltered after TGA cycling as observed in PXRD (**Figure 18**) and EDS analysis (**Figures 19 and 20**, **Tables 3 and 4**) Although sintering of the particles is observed during high temperature cycling for all the Ga and Sc substituted perovskites as revealed by the FESEM images of $La_{0.5}Sr_{0.5}Ga_{0.25}Mn_{0.75}O_3$ and $La_{0.5}Sr_{0.5}Sc_{0.05}Mn_{0.95}O_3$ (Figure 19), can be the reason of slower rate of CO production in long term cycling. In addition of extensive thermodynamic and kinetic analysis further tuning of pO_2, pCO_2, reaction temperatures, reactor system and composition and morphology of perovskite is needed to improve the kinetics of these kinds of materials.

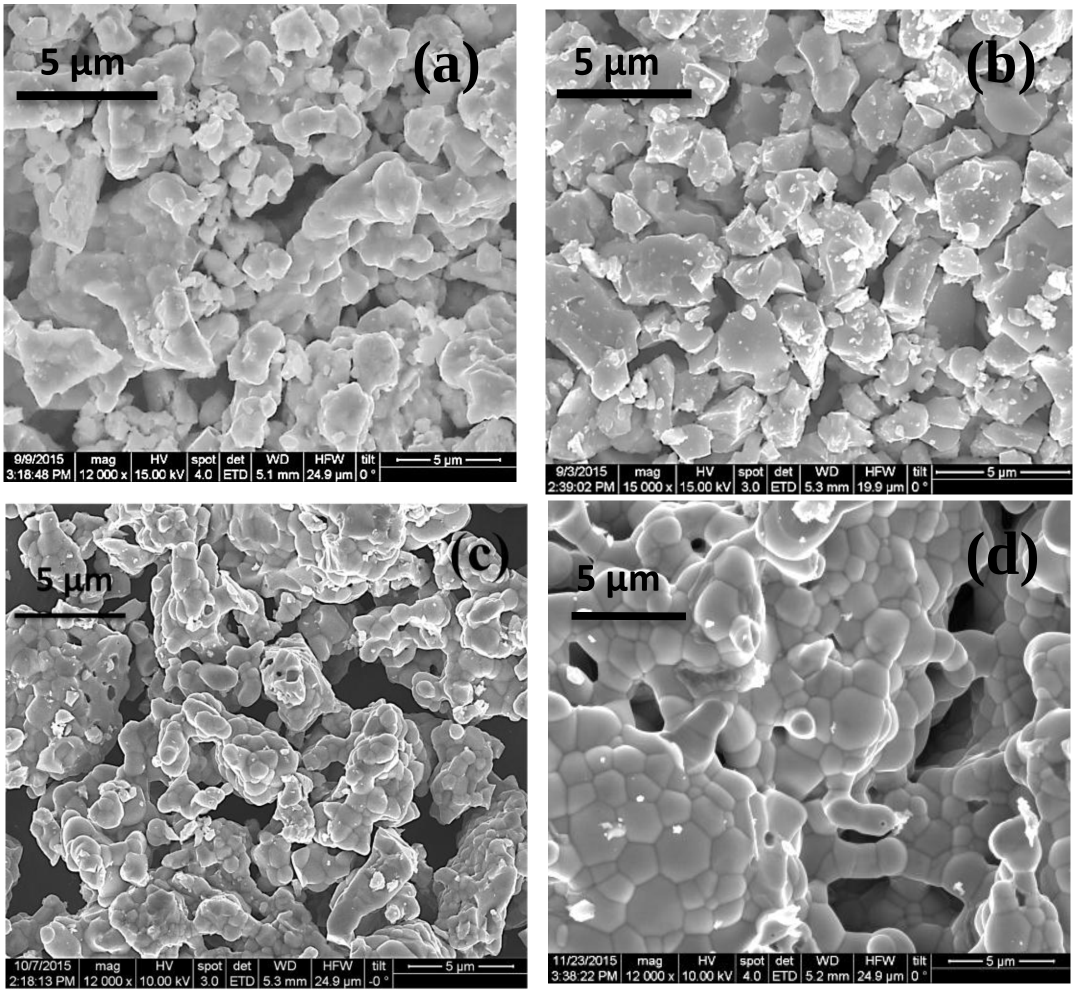

Figure 19. FESEM images of $La_{0.5}Sr_{0.5}Mn_{0.75}Ga_{0.25}O_3$ (a) before and (b) after TG analysis and of $La_{0.5}Sr_{0.5}Mn_{0.95}Sc_{0.05}O_3$ (c) before and (d) after TG analysis.

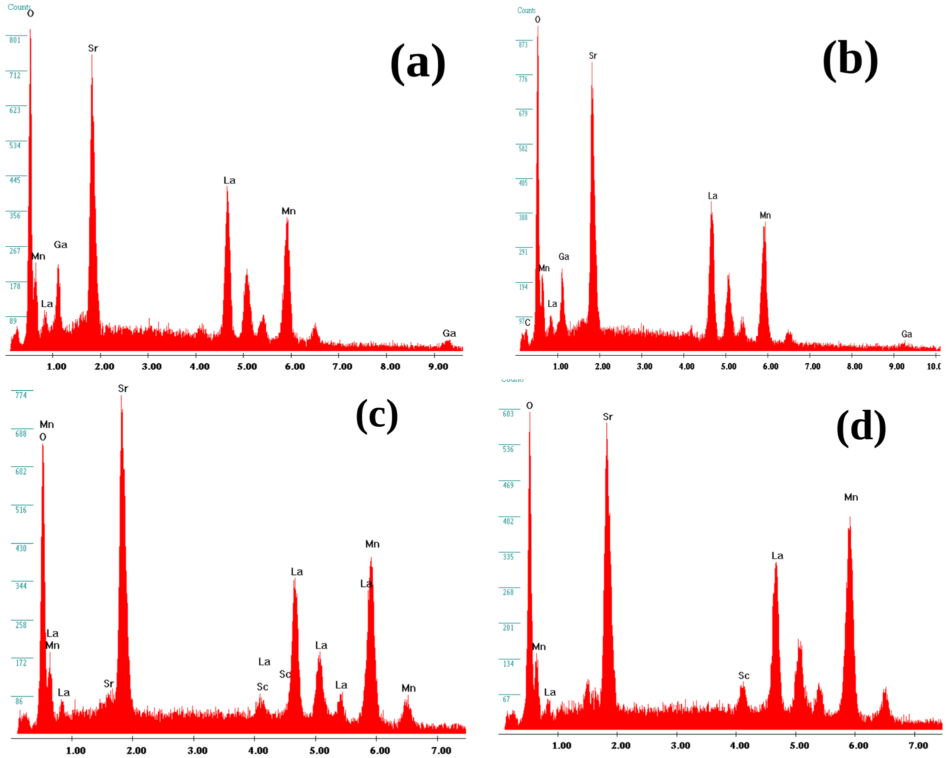

Figure 20. EDS (X and Y axis are Energy in KeV and counts respectively) of $La_{0.5}Sr_{0.5}Mn_{0.75}Ga_{0.25}O_3$ (a) before and (b) after TG analysis and of $La_{0.5}Sr_{0.5}Mn_{0.95}Sc_{0.05}O_3$ (c) before and (d) after TG analysis respectively.

Table 3. Atomic % of La, Sr, Ga and Mn present in $La_{0.5}Sr_{0.5}Mn_{0.75}Ga_{0.25}O_3$ before and after TG analysisas calculated from EDS analysis.

	La L	Sr L	Ga K	Mn K	O K
$La_{0.5}Sr_{0.5}Mn_{0.75}Ga_{0.25}O_3$	Atomic %	Atomic %	Atomic %	Atomic %	Atomic %
Before TGA	13.15	13.03	5.61	17.75	50.46
After TGA	13.27	12.48	5.95	18.11	50.18

Table 4. Atomic % of La, Sr, Sc and Mn present in $La_{0.5}Sr_{0.5}Mn_{0.95}Sc_{0.05}O_3$ before and after TG analysis as calculated from EDS analysis.

	La L	**Sr L**	**Sc K**	**Mn K**	**O K**
$La_{0.5}Sr_{0.5}Mn_{0.95}Sc_{0.05}O_3$	Atomic %	Atomic %	Atomic %	Atomic %	Atomic %
Before TGA	12.9	13.8	1.69	24.9	46.7
After TGA	12.13	14.1	1.77	26.9	45.2

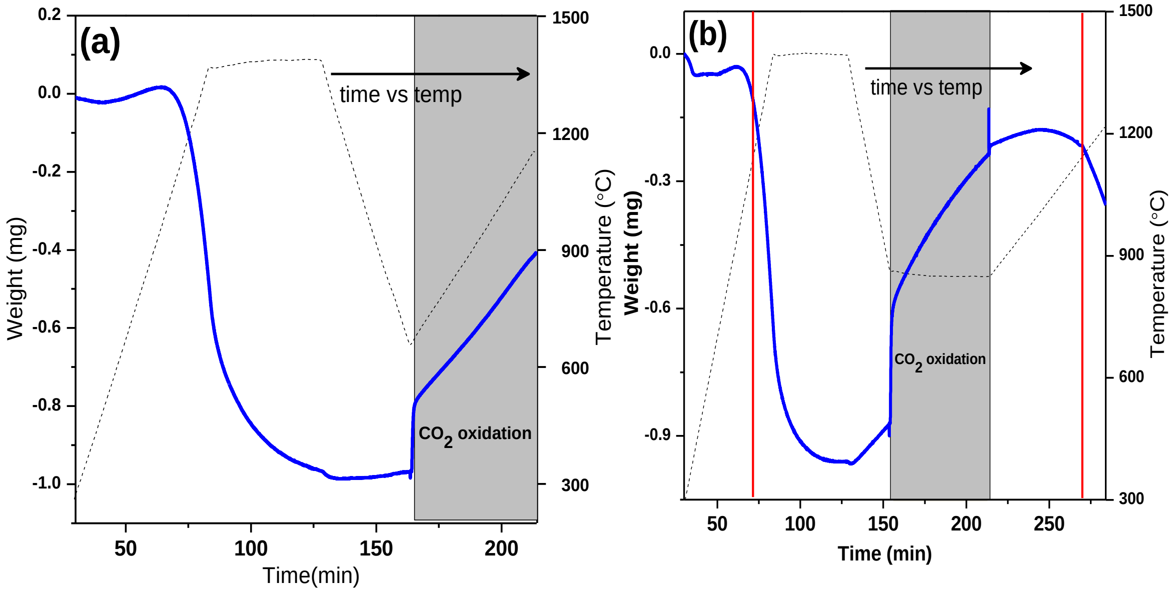

Figure 21. (a) TG reduction of $La_{0.5}Sr_{0.5}Mn_{0.75}Ga_{0.25}O_3$ (T_{red}=1400°C, Ar gas), followed by cooling at 700°C and subsequent temperature ramp from 700°C to 1200°C under CO_2 exposure (b) TG reduction of $La_{0.5}Sr_{0.5}Mn_{0.75}Ga_{0.25}O_3$ (T_{red}=1400°C, Ar gas), followed by CO_2 exposure at 850°C and further decomposition upto 1200°C under Ar (heating rate= 10°C/min). Red lines indicate the starting point of O_2 evolution during reduction under Ar. Experimental details are in reactivity test section.

The increase in the weight of the nonstoichiometric oxide on passing CO_2 could partly arise from carbonate formation instead of oxidation alone.[90] Substitution of Al in LSM lattice has shown to diminish the carbonate formation by Galvez et al.[90] However, the carbonates are decomposes well below 1000˚C, while the CO_2 decomposition temperature is 1100˚C in all our experiments. We also ensured no further gain in weight occurs at high temperature due to carbonate formation as well by performing separate TG experiments on Ga and Sc substituted perovskites (see carbonate formation test at 1.3.4). Figure 21a, we have shown the TGA plot obtained when $La_{0.5}Sr_{0.5}Ga_{0.25}Mn_{0.75}O_3$ was subjected to reduction at 1400°C (under Ar for 45 mins) followed by the cooling at 700°C and immediately ramp up to 1200°C under exposure of CO_2 (see experimental details at 3.4.3). $La_{0.5}Sr_{0.5}Mn_{0.75}Ga_{0.25}O_3$ shows no such weight loss corresponding to low temp decomposition (~940°C) of carbonate, while expose to CO_2 (**Figure 21a**). In Figure 21b we have shown the TGA plot obtained when the sample is subjected to reduction at 1400°C (under Ar for 45 mins) followed by the oxidation at 850°C under CO_2 (for 1 hr) and immediately ramp up to 1200°C (heating rate 10°C/min) in Ar. No extra weight gain is obtained during the oxidation under 850°C in compare to regular oxidation of 1100°C (Figure 21b), further reconfirms the weight gain is due to the CO_2 splitting.

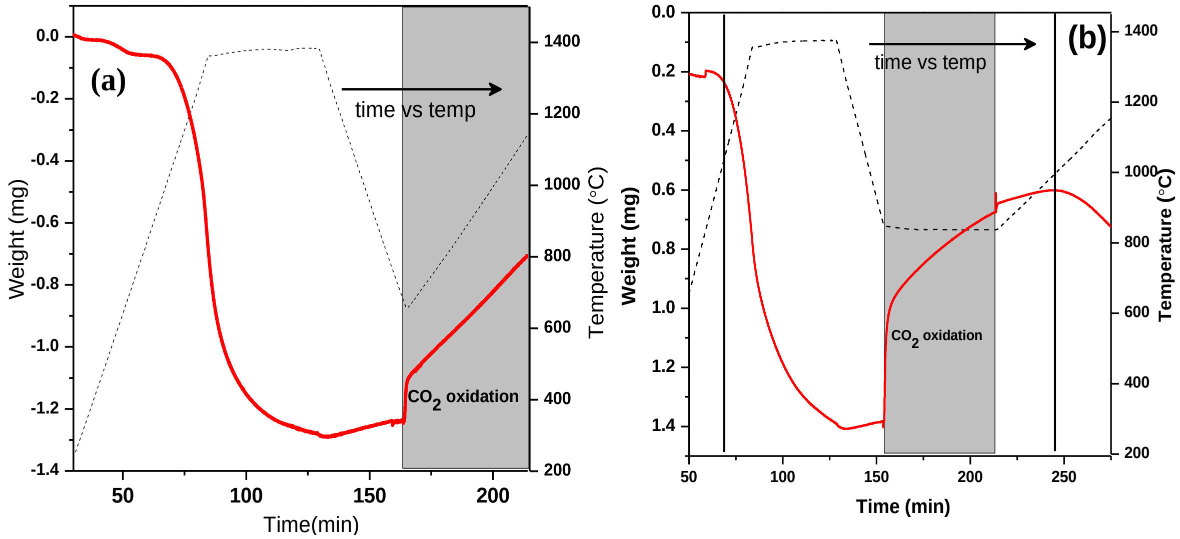

Figure 22. (a) TG reduction of $La_{0.5}Sr_{0.5}Mn_{0.95}Sc_{0.05}O_3$ (T_{red}=1400°C, Ar gas), followed by cooling and temperature ramp from 700°C to 1200°C under CO_2 exposure (b) TG reduction of $La_{0.5}Sr_{0.5}Mn_{0.95}Sc_{0.05}O_3$ (T_{red}=1400°C, Ar gas), followed by CO_2 exposure at 850°C and further decomposition upto 1200°C under Ar (heating rate= 10°C/min). Vertical lines indicate the starting point of O_2 evolution during reduction under Ar. Experimental details are in reactivity test section.

Similar conclusion has been obtained with $La_{0.5}Sr_{0.5}Mn_{0.95}Sc_{0.05}O_3$ (**Figure 22**). The slow rate of oxidation can be due to kinetic barriers, as the oxidation is performed at a significantly lower temperature (700°C/850°C). The onset of mass loss remains the same during reduction under Ar as shown by the vertical lines in Figures 21b and 22b. Interestingly, few earlier reports suggested that Sc^{3+} doping on LSMs suppress the SrO segregation, which actually promotes carbonate formation by CO_2 adsorption.[126, 127] It further strengthens our observation and highlighted the advantages of $Sc^{3+}$and Ga^{3+} doping.

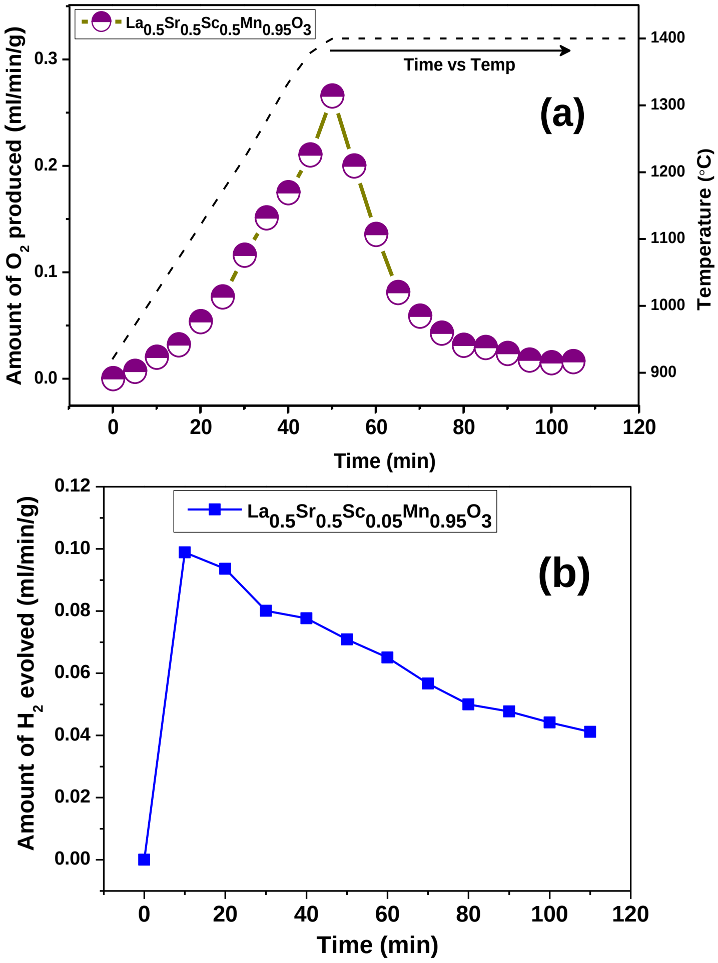

Figure 23. (a) O_2 and (b) H_2 evolution profile of $La_{0.5}Sr_{0.5}Mn_{0.95}Sc_{0.05}O_3$. Reduction and H_2O splitting temperatures are 1400 °C and 1100°C respectively.

$La_{0.5}Sr_{0.5}Mn_{0.95}Sc_{0.05}O_3$ gave superior performance with high CO productivity even during multiple cycling; we have employed it for water splitting. Production of O_2 and H_2 was detected by gas chromatograph, shown in **Figure 23**. The O_2 production starts at 900°C and completes within 40 min after reaching 1400°C. The total amount of O_2 produced is 390 µmol/g, close to the yield during TG measurements. H_2 is detected immediately after the entrance of H_2O in the gas stream (T_{oxd}=1100˚C), and the quantities reaches a maximum and decreases thereafter (Figure 23b). The amount of H_2 produced in a span of 100 mins is approximately 250 µmol/g. H_2 evolution has not been completed even after 100 mins.

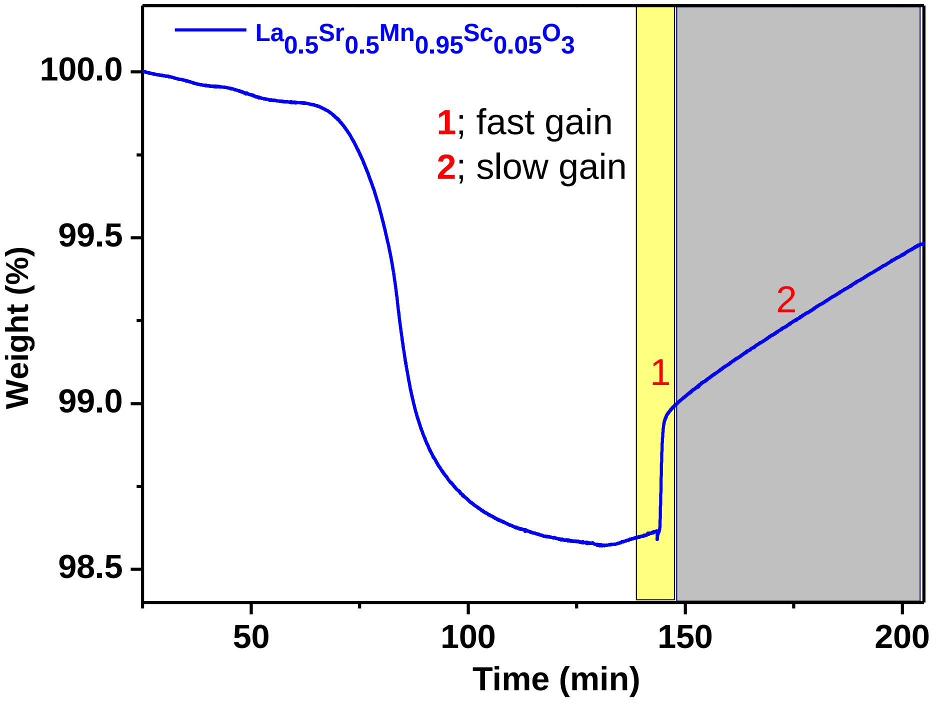

Figure 24. TGA curves of thermochemical CO_2 splitting of $La_{0.5}Sr_{0.5}Mn_{0.95}Sc_{0.05}O_3$. The weight gain (CO production) region is highlighted to show two different kinetics. Step 1 (yellow colour) shows the rapid gain of CO. Step 2 (grey colour) highlights the slow kinetics. CO_2 splitting temperature is 1100°C.

Table 5. CO production in two different kinetics by $La_{0.5}Sr_{0.5}Mn_{0.95}Sc_{0.05}O_3$

	CO produced (µmol/g)		
Material	CO produced (µmol/g) **Fast kinetics(1)**	CO produced (µmol/g) **Slow kinetics (2)**	**Total CO produced** (µmol/g)
$La_{0.5}Sr_{0.5}Mn_{0.95}Sc_{0.05}O_3$	**243**	300	543

The kinetic behavior of H_2O splitting of $La_{0.5}Sr_{0.5}Mn_{0.95}Sc_{0.05}O_3$ is comparable to that of CO_2 splitting (**Figure 24** and **Table 5**). H_2 is produced in the initial 100mins of the reaction in the fast kinetic regime (yellow region, step 1, Figure 24), followed by a slower kinetic regime (grey region, step 2, Figure 24).

1.4.4

The isothermal thermochemical splitting of CO_2 using manganite perovskites

1.4.4. The isothermal thermochemical splitting of CO_2 using manganite perovskites

CeO_2 crystallizes in cubic fluorite structure (S.G. Fm-3m) with the crystal size of ~ 101 nm as reveal by the powder X-ray diffraction pattern (**Figure 1 and Table 1**). FESEM image confirms the porus structure (porosity~60%). The BET surface area of CeO_2 is 10 m^2g^{-1}.

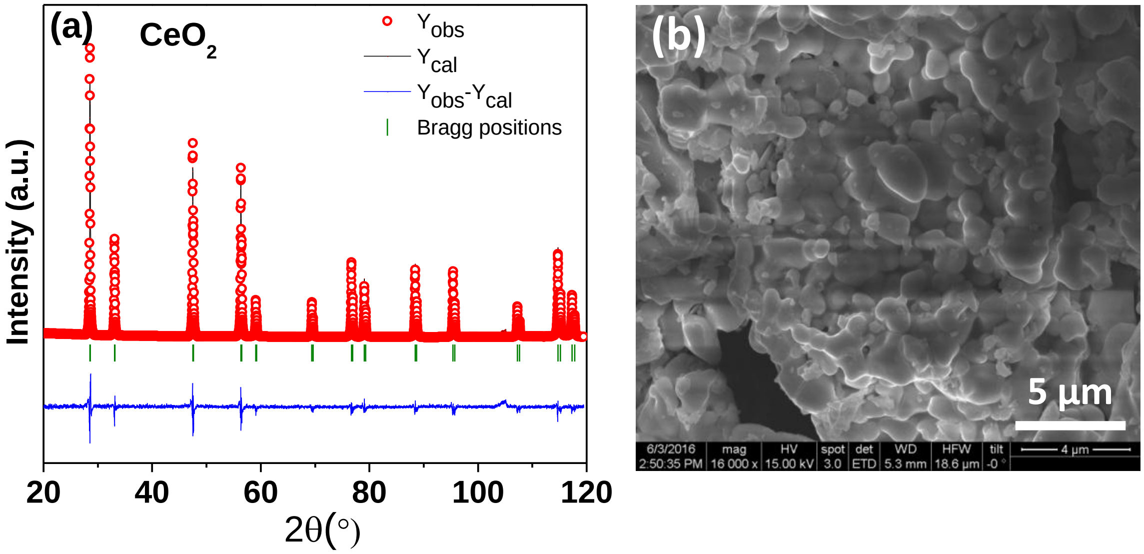

Figure 1. (a) Lebail fitted PXRD patterns and (b) FESEM image of as synthesized CeO_2.

$La_{1-x}Sr_xMnO_3$ with x=0.3, 0.4, 0.5 and $Y_{0.5}Sr_{0.5}MnO_3$, designated LSM30, LSM40, LSM50 and YSM50 respectively were characterized by X-ray diffraction (**Figure 2** and Table 1). Increasing the Sr^{2+} substitution with La^{3+} ions, increases the Mn^{4+} (r=0.645 Å) content over Mn^{3+} (r=0.53Å), shifts the diffraction peaks at higher 2θ value (**Figure 3**), consistent with the decrease in cell volume as calculated from Rietveld refinement (Table 1). Lattice parameters decreases further for YSM50 ($r_{Y^{3+}}$=1.08 Å; $r_{La^{3+}}$=1.36Å), shifts the Bragg peak at higher 2θ than LSM50 (Figure 3b). The crystal size of the oxides was ~ 83 nm for LSM 30 and LSM40 and ~50 nm for LSM50 as calculated by employing Scherrer formula to the [110] peak of perovskites (Table 1).

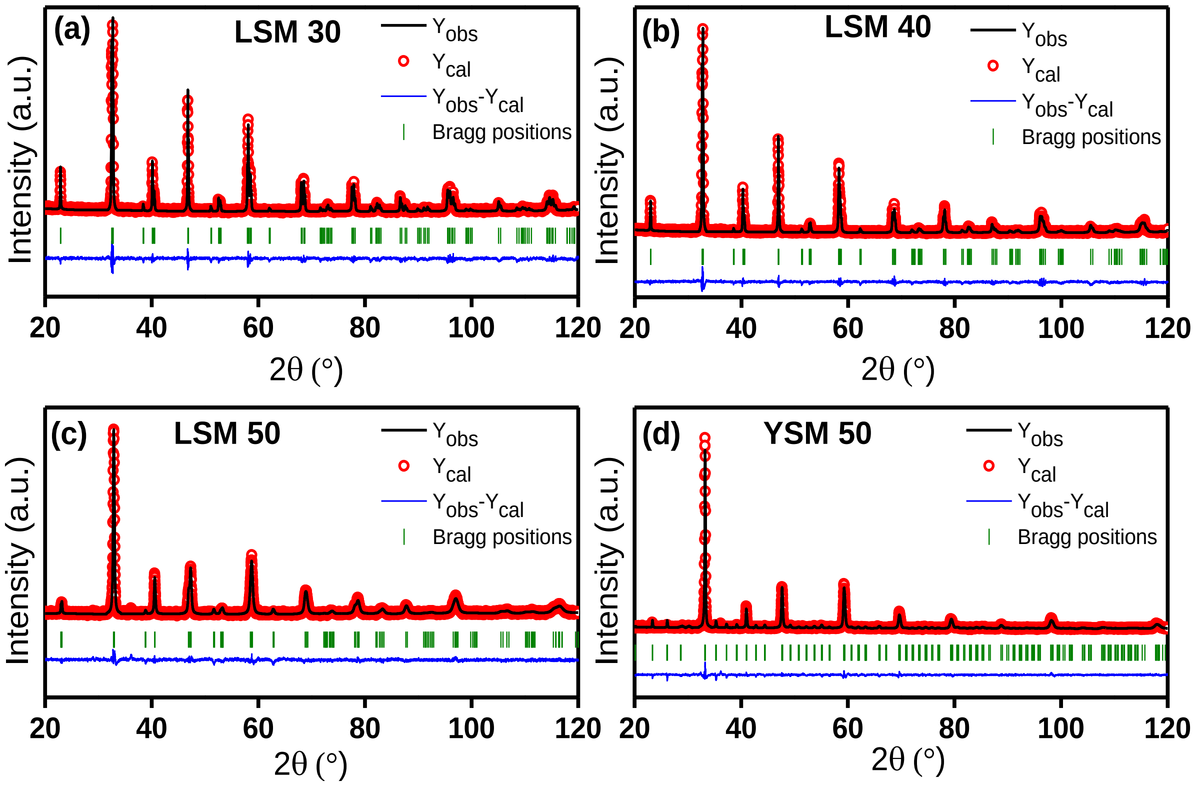

Figure 2. Lebail fitted PXRD patterns of (a) LSM30 (b) LSM40 (c) LSM50 and (d) YSM50. LSM 30 and LSM 40 crystallize in the rhombohedral structure (Space group R-3c) whereas LSM50 adopts tetragonal symmetry (S.G. I4/mcm). YSM50 crystallizes in orthorhombic symmetry (S.G. Pnma).

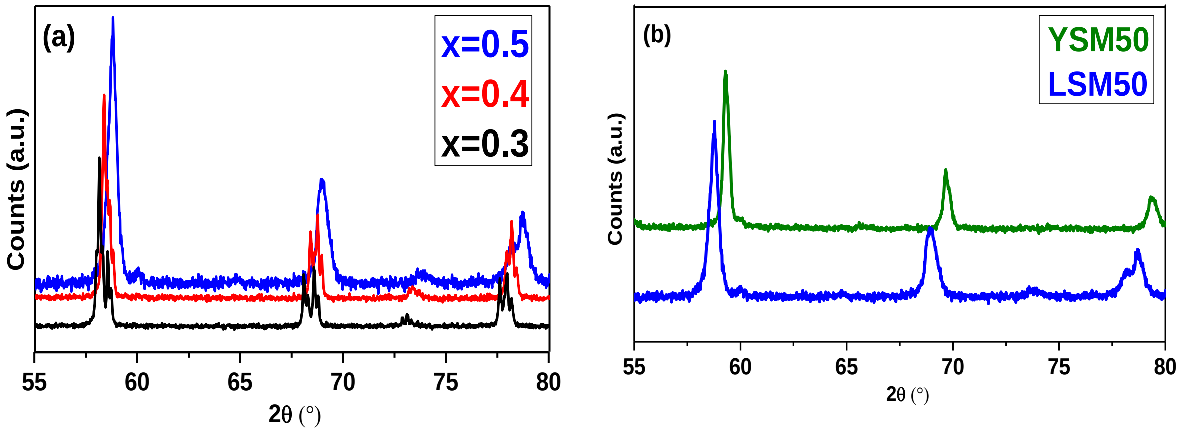

Figure 3. Magnified 2θ range of 55°-80° to show (a) the systematic change in PXRD due to increasing x in $La_{1-x}Sr_xMnO_3$ (x=0.3, 0.4 and 0.5) and (b) the shifts in Bragg peak of YSM50 than LSM50.

Table 1. Summary of Space group (S.G.), crystalline sizes (calculated using Debye-Scherrer equation based on PXRD peak at 2θ~ 33°) and lattice parameters (obtained from Lebail fitting of LSM30, LSM40, LSM50 and YSM50.

Materials	Crystal size (nm)	S. G.	a (Å)	b (Å)	c (Å)	Cell vol. ($Å^3$)
LSM 30	81	R-3c	5.6086(1)	5.6086(1)	13.3622(4)	350.93
LSM 40	87	R-3c	5.4858(2)	5.4858(2)	13.3514(7)	347.98
LSM 50	52	I4/mcm	5.4344(4)	5.4344(4)	7.7416(6)	228.64
YSM 50	62	Pnma	5.4001(4)	5.392(2)	7.6256(4)	222.37

FESEM images of the manganite perovskites are presented in **Figure 4**. Large pores of around 5 to 10 µm formed due to the association of smaller grains ensure the gas transport inside the monolith whereas small pores of less than micron increases the reactive sites. Porosity is nearly constant for all the compositions (~60%). BET surface areas of LSM30, LSM40, LSM50 and YSM50 are 15, 23, 25 and 13 m^2g^{-1} respectively. EDAX confirms the composition of the perovskites as summarizes in **Figure 5** and **Table 2**.

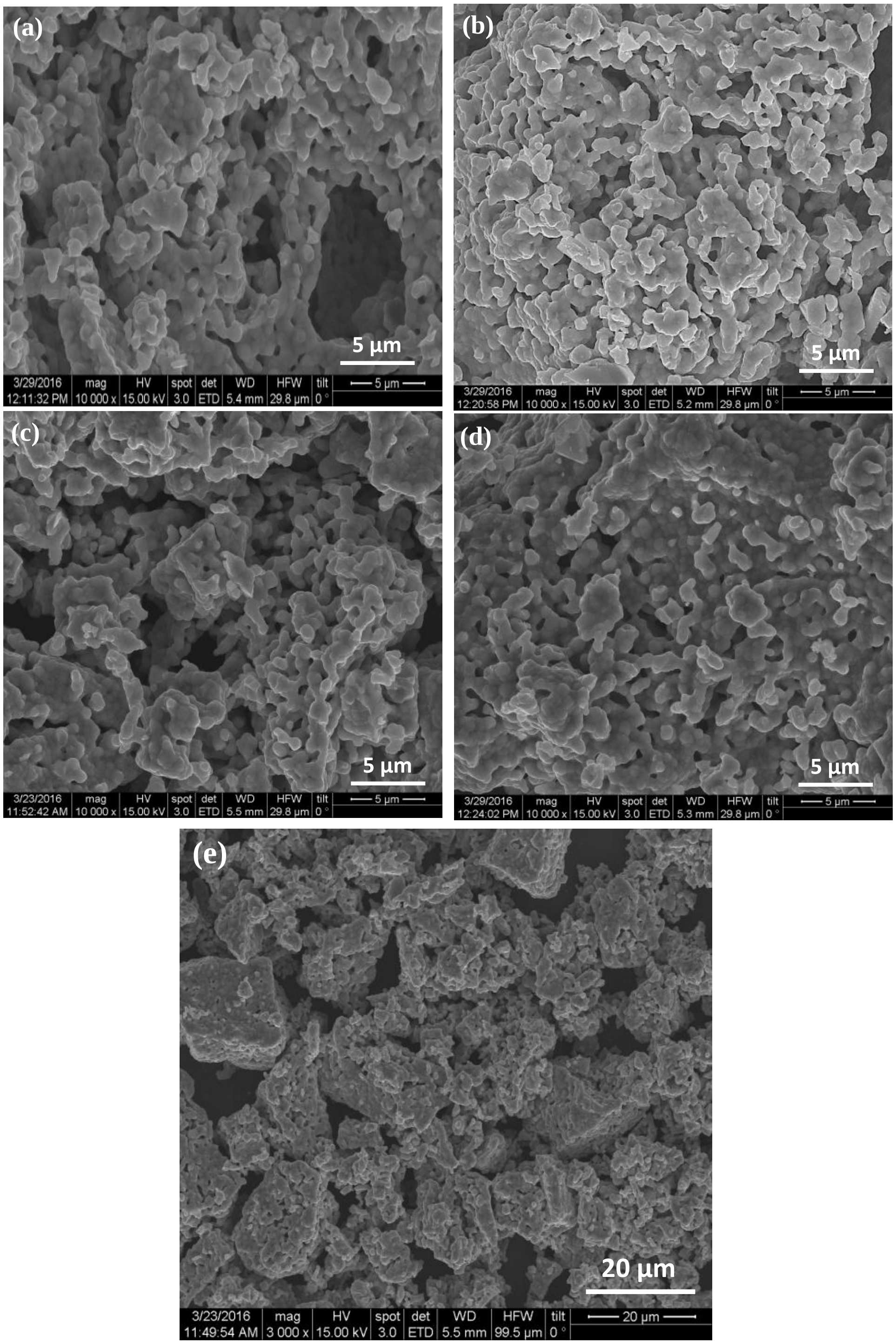

Figure 4. FESEM images of the porous structural features of (a) LSM30, (b) LSM40, (c) LSM50 and (d) YSM50 before high temperature thermogravimetric cycles. (e) Overall porus structure morphology in lower magnification for LSM50.

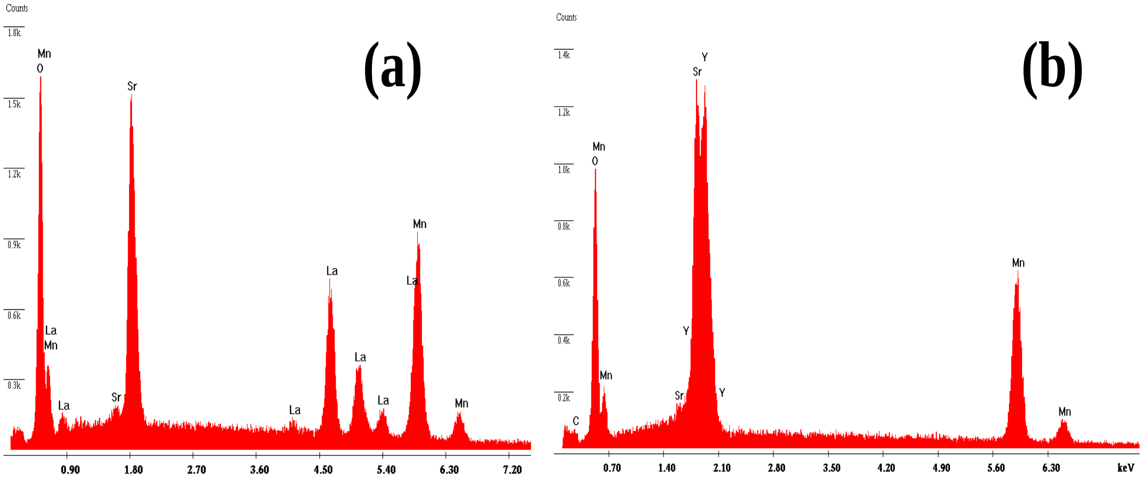

Figure 5. EDAX (X and Y axis are Energy in KeV and counts respectively) of as synthesized (a) LSM50 and (b) YSM50.

Table 2. Atomic % of La, Y, Sr, Mn and O present in $La_{1-x}Sr_xMnO_3$ {(a) x=0.3, (b) x=0.4, (c) x=0.5} and $Y_{0.5}Sr_{0.5}MnO_3$ as calculated from EDAX analysis.

	La L	**Y L**	**Sr L**	**Mn K**	**O K**
Material	**Atomic %**	**Atomic %**	**Atomic %**	**Atomic %**	**Atomic %**
LSM30	16.5	---------	8.3	21.59	53.54
LSM40	13.5	---------	11.5	24.63	50.33
LSM50	12	---------	13	25.01	49.99
YSM50	---------	12.4	11.2	22.84	53.44

Figures 6a and b show the thermodynamically calculated oxygen nonstoichiometry isotherms of LSM30, LSM40 and LSM50 at 1673K and 1773K respectively. For the purpose of calculations, low-temperature (873K-1273K) oxygen nonstoichiometry data of Mizusaki [130] and Tagawa et. al [131] (**Figure 7**) were extended to higher temperature (**Figures 8 and 9**).

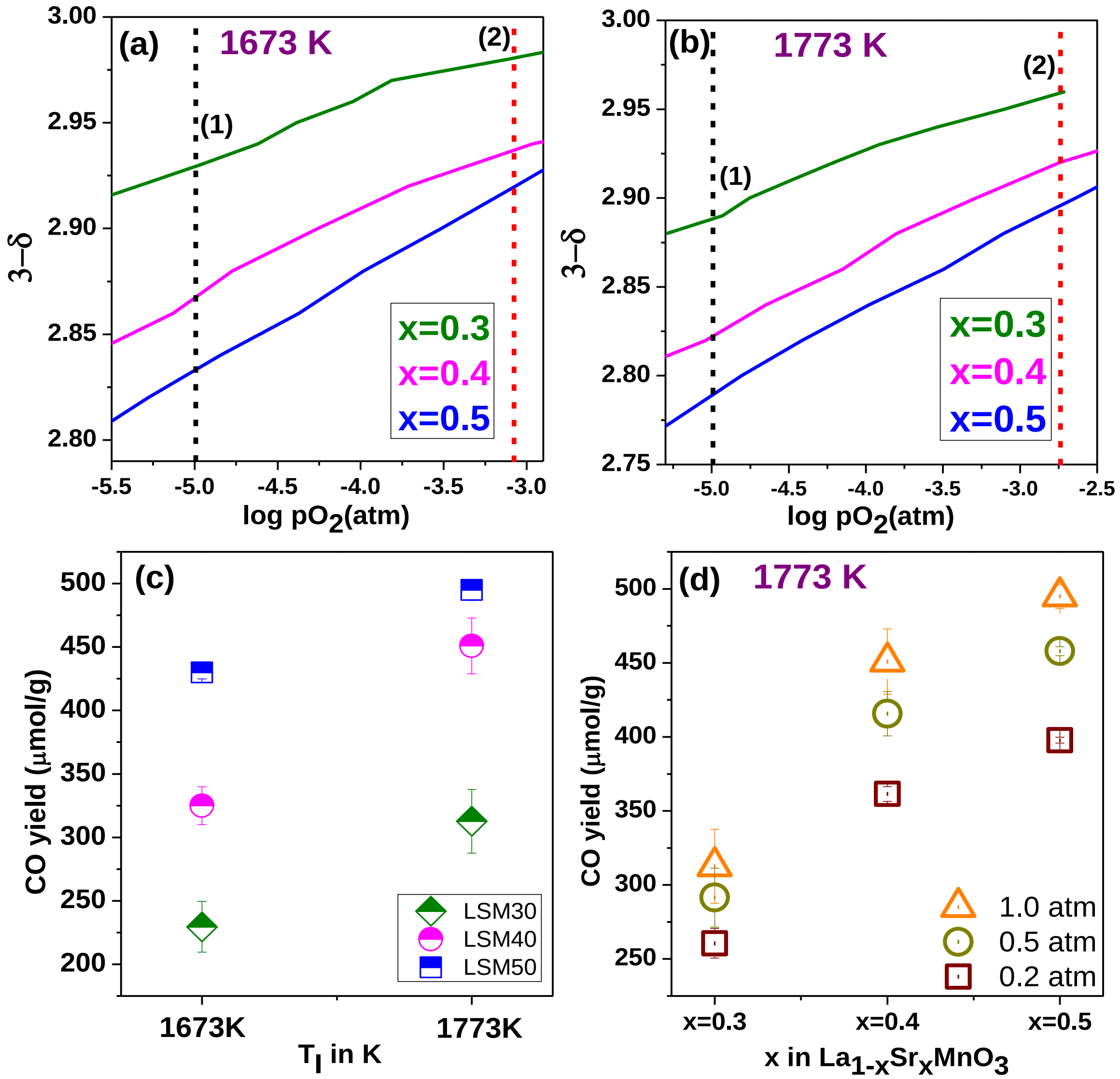

Figure 6. Thermodynamically predicted oxygen nonstoichiometry of LSM30, LSM40 and LSM50 under isothermal CO_2 splitting temperatures of (a) 1673 K and (b) 1773 K. These values are derived by extrapolating the experimental datas of Mizusaki et al.[130] and Tagawa et al.[131]as described in the text in detail. Black and red vertical lines indicate the expected value oxygen nonstoichiometry upon reduction under 10 ppm of O_2 and oxidation under $p_{CO_2}$of 1 atm respectively. (c) Estimated CO productivity at equilibrium and (d) Effect of variations of p_{CO_2}on the CO productivity of LSM compositions at particular isotherm (1773 K).

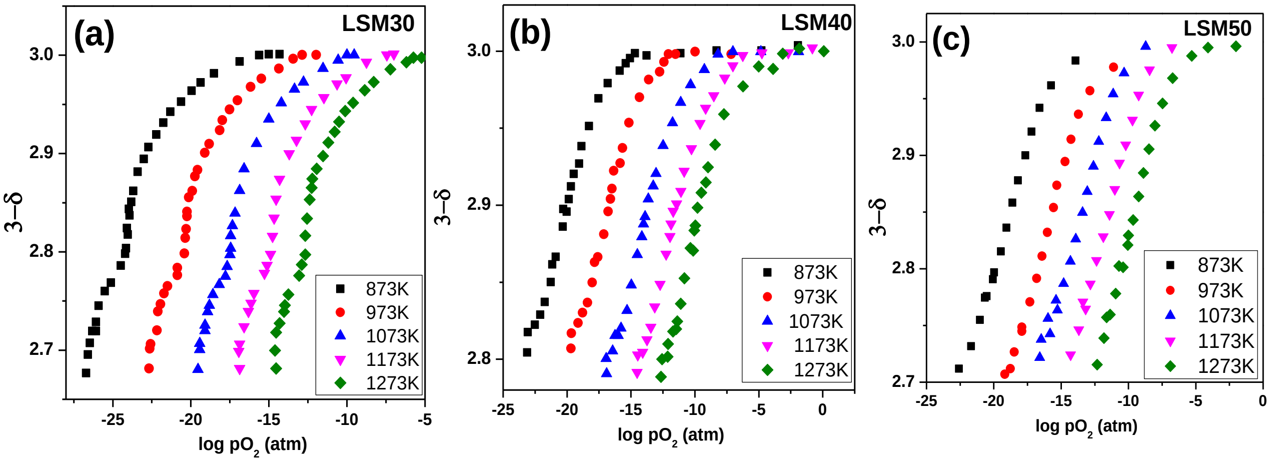

Figure 7. Oxygen nonstoichiometry as a function of temperature (873K-1273K) for different $La_{1-x}Sr_xMnO_3$ (x=0.3, x=0.4 and x=0.5) compositions as experimentally measured by Tagawa et. al and Mizusaki et.al (adapted from refs. 130 and 131). These values are extrapolated to obtain the oxygen nonstoichiometry at high temperatures (1673K and 1773K) as mentioned in detail in the main text.

For ABO_3 type perovskites, the reduction reaction can be explained as,

$$\frac{1}{\alpha}\mathrm{ABO}_{3-\delta-\alpha} + \frac{1}{2}\mathrm{O}_2(\mathrm{g}) \leftrightarrow \frac{1}{\alpha}\mathrm{ABO}_{3-\delta} ----(1)$$

The Gibbs free energy for this redox reaction is given by,

$$\Delta G_r^0 = -RT\ln K_r = \Delta H_r^0(\delta) - T\Delta S_r^0(\delta) ----(2)$$

Hence, K_r is the equilibrium constant, R the universal gas constant and H^0 and S^0 are the standard enthalpy and entropy of redox reactions. Taking activities of solids as unity and O_2 as an ideal gas, in the limit of $\alpha \rightarrow 0,$ eqn. (1) gives,

$$K_r = (pO_2^{\emptyset})^{\frac{1}{2}} ----(5),$$

where $pO_2^{\emptyset}$ is the oxygen partial pressure with respect to standard state.

Combining eqns. (1) to (3) gives,

$$\frac{1}{2}\ln pO_2^{\emptyset}(\delta) = -\frac{\Delta H_r^0(\delta)}{RT} + \frac{\Delta S_r^0(\delta)}{T} --- (3)$$

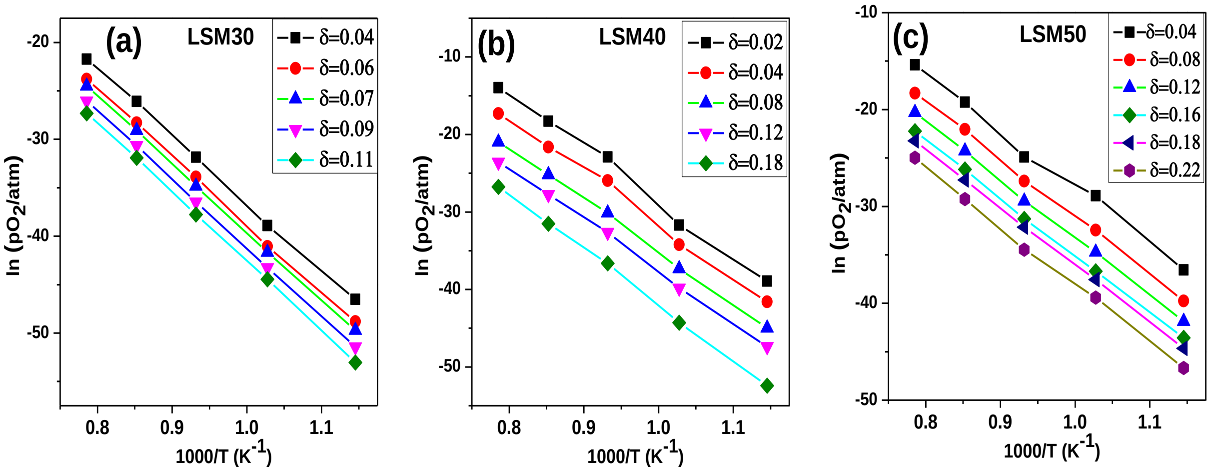

Figure 8. Arrhenius type plots of oxygen partial pressure as a function of temperature for selected δ values for different $La_{1-x}Sr_xMnO_3$ (x=0.3, x=0.4 and x=0.5) compositions derived from the isotherm of Figure 7. The slope and intercept of each straight line defines the molar enthalpy and molar entropy at that particular δ.

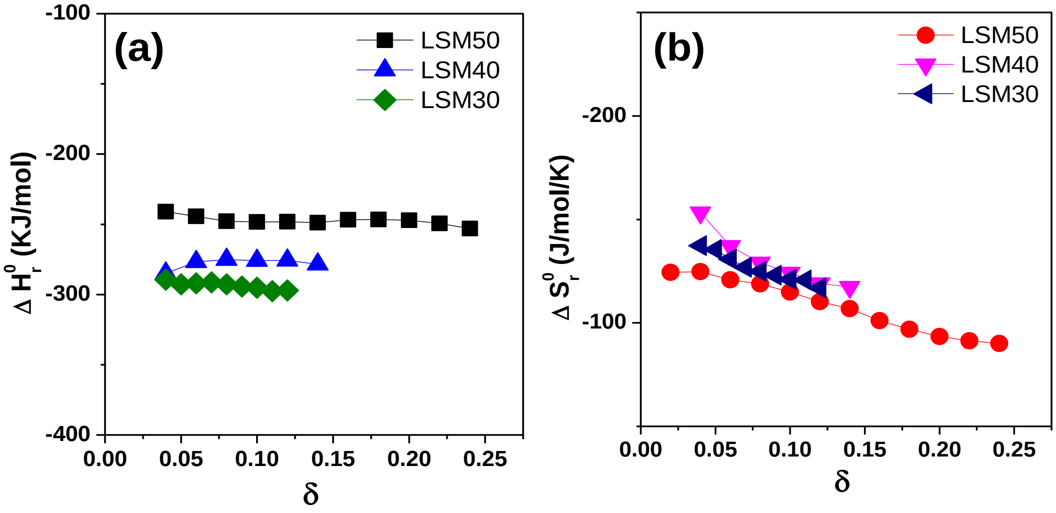

Figure 9. Variations of thermodynamic functions, namely (a) partial molar enthalpy and (a) partial molar entropy of $La_{1-x}Sr_xMnO_3$ (x=0.3, x=0.4 and x=0.5) as a function of oxygen nonstoichiometry δ.

The Arrhenius plots of ln $pO_2^{\emptyset}$ as a function T^{-1} for a set of δ are obtained considering ΔH_r^0 and ΔS_r^0 to be independent of temperature (**Figure 8**). From the linear plots we obtain the standard enthalpy change (ΔH_r^0) and entropy change (ΔS_r^0) at different δ values (**Figure 9**). These ΔH_r^0 and ΔS_r^0 values can be used to extrapolate the datas at higher temperatures through numerical treatment of eqn. 4. A significant decrease in reduction enthalpy (ΔH_r^0)

occurs with increasing Sr content (Figure 9), suggesting the ease in reducibility with higher Sr content.

In **Figure 10**, we have presented our results in comparison with those of Takacs et. al and [25] Yang et. al[23]. Our results are similar to those of Yang et al. for both LSM40 and LSM50 as the mode of calculations are same in both the studies. The defect model used by Takacs et al is different.

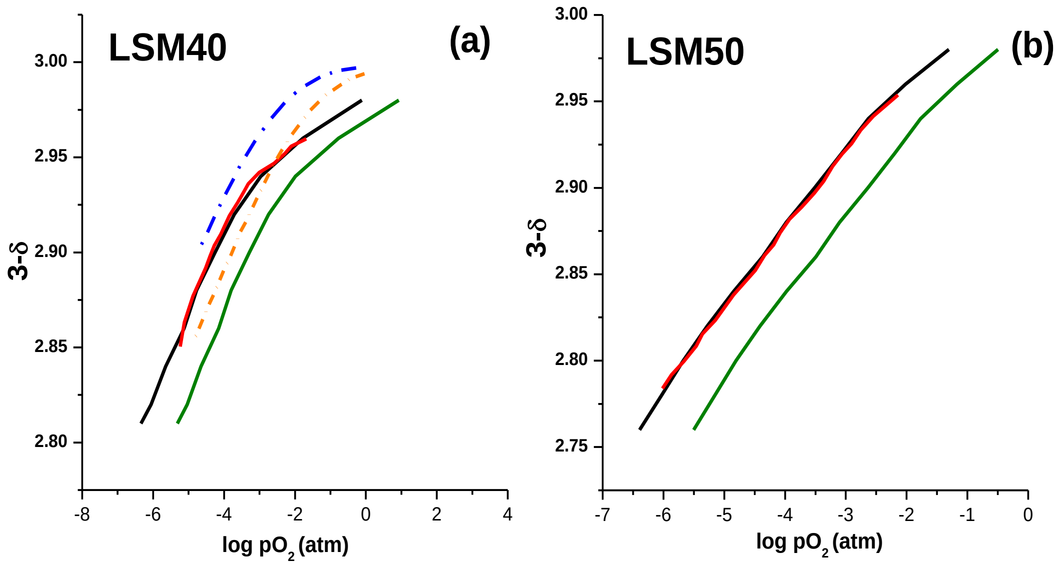

Figure 10. Theoretically obtained oxygen nonstoichiometry of present work as a function of oxygen partial pressure at 1673K (green curve) and 1773K (black curve) is presented in comparison with the data points from refs. 23 and 25. The red curve corresponds to data from ref 23 (1673K). The orange (1673K) and blue curve (1773K) corresponds to data from ref 25.

In Figures 6a and b, black (position 1) and red (position 2) vertical lines mark p_{O_2}values during the reduction for the sweep gas of 10 ppm O_2 and oxidation under 1 atm of $p_{CO_2}$of (obtained from Ellingham diagram). The difference between the nonstoichiometry corresponding to these two points gives the Δδ along with O_2 (CO) yields. The estimated CO yields with LSM30, LSM40 and LSM50 are 229.5, 325 and 428.6 μmol/g respectively at 1673K. The yield increases at 1773K to 495.1 μmol/g of CO in the case of LSM50 (Figure 6c). Varying the p_{CO_2}affects the CO(O_2) production (Figure 6d and **Figure 11**), the effect being more pronounced at low p_{CO_2}. The increase in $p_{O_2}$is greater for a change in $p_{CO_2}$from 0.2 atm to 0.5 atm than from 0.5 atm to 1 atm (Figure 6d).[72]

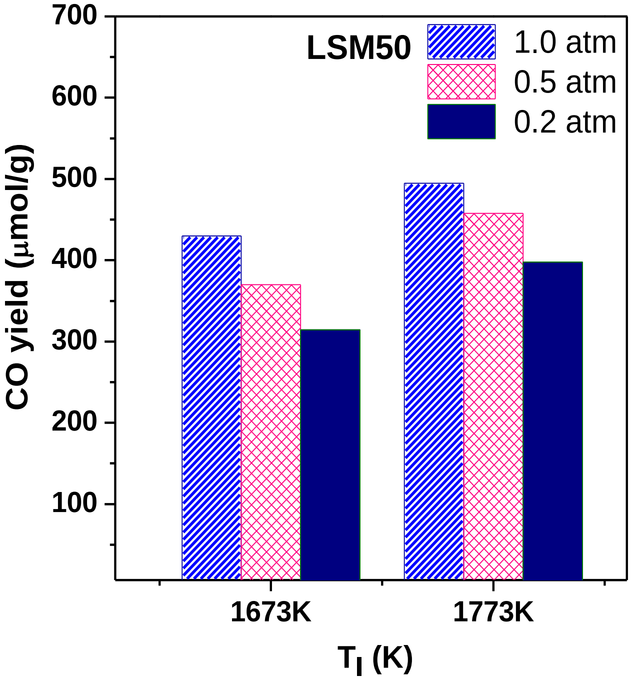

Figure 11. Variations in equilibrium CO productivity of LSM50 with several p_{CO_2} values as shown for two different isothermal CO_2 splitting temperatures (1673K and 1773K).

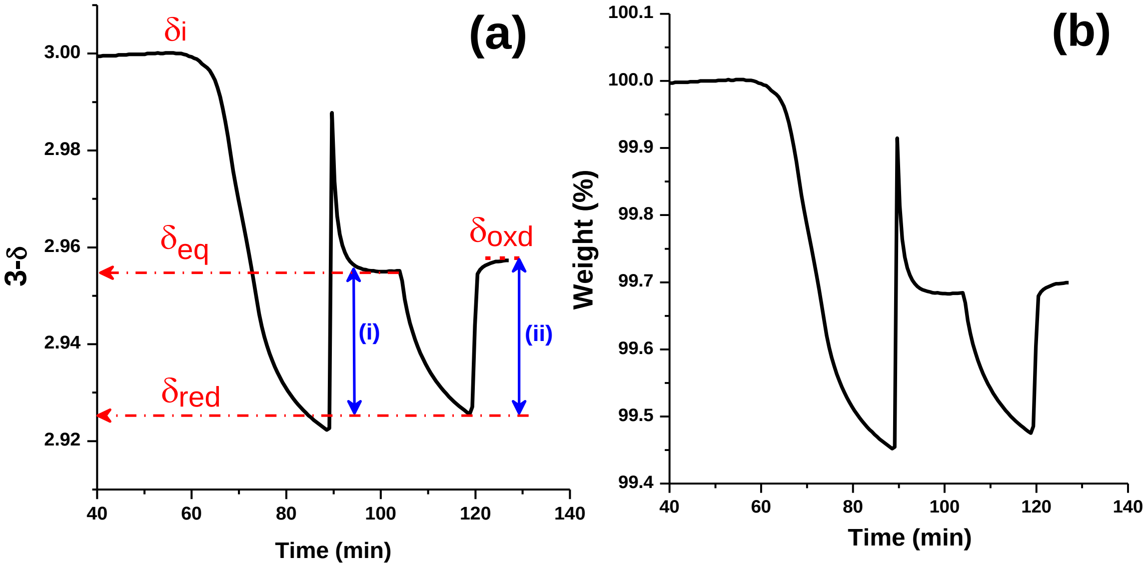

Figure 12. (a) Representative TG plots (oxygen nonstoichiometry as a function of time) to mark the oxygen nonstoichiometry during initial equilibration (δ_{eq}), after reduction (δ_{red}) and after oxidation (δ_{oxd}) where (i) difference between δ_{red} and δ_{eq} is the reduction yield and (ii) difference between δ_{red} and δ_{oxd} is the oxidation yield. (b) Actual TG plot (% weight vs time) obtained from the instrument is given for reference.

The LSM perovskites were subjected to three consecutive redox cycles for thermochemical CO_2 splitting at a constant temperature of 1773K or 1673K (T_I). In the first cycle, the samples were initialized to equilibrium nonstoichiometry (δ_{eq}) in the presence of CO_2 (**Figure 12a**). The sample (oxygen nonstoichiometry, δ_i) is heated to T_I under the sweep gas flow which is accompanied by weight loss due to reduction. Again at T_I , the gas is switched to CO_2 and sustained for 15 min accompanied by initial weight gain and later reaching thermodynamic equilibrium (equilibrium nonstoichiometry, δ_{eq}). δ_{eq} changes with composition and T_I (**Table 3**). During the 2nd cycle, the gas is changed cyclically to sweep gas (weight loss, δ_{red}) and to CO_2 (reversible weight gain for CO_2 splitting, δ_{oxd}). The O_2 and CO yields (mole/mole of oxides) are the differences of δ_{red} with δ_{eq} and δ_{oxd} respectively (Figures 12).

Table 3. Summarize the values of oxygen nonstoichiometry at initial equilibration (δ_{eq}), after reduction (δ_{red}) and reduction yield ($\Delta\delta$) as a function of temperature and composition of perovskites.

Materials	**T_I = 1673K**			**T_I = 1773K**		
	δ_{eq}	δ_{red}	$\Delta\delta$	δ_{eq}	δ_{red}	$\Delta\delta$
LSM 30	**0.033**	0.05	0.017	**0.045**	0.075	0.03
LSM 40	**0.067**	0.088	0.021	**0.081**	0.117	0.036
LSM 50	**0.179**	0.21	0.031	**0.188**	0.24	0.052

ITCS studies of porous CeO_2 have been reported in the literature, where the sample is placed in packed bed and evolved gases detected by a mass spectrometer.[98, 103] We subjected CeO_2 to thermogravimetric analysis (TGA) during ITCS and measured the quantity of CO generated on interaction with CO_2 (**Figure 13**). The δ_{eq} value for CeO_2 is 0.018 at 1773K, similar to that report of Venstrom et al.[103] The CO evolved by CeO_2 is 48.7 μmol/g and 66.5 μmol/g at T_I of 1673K and 1773K respectively (Figure 13).

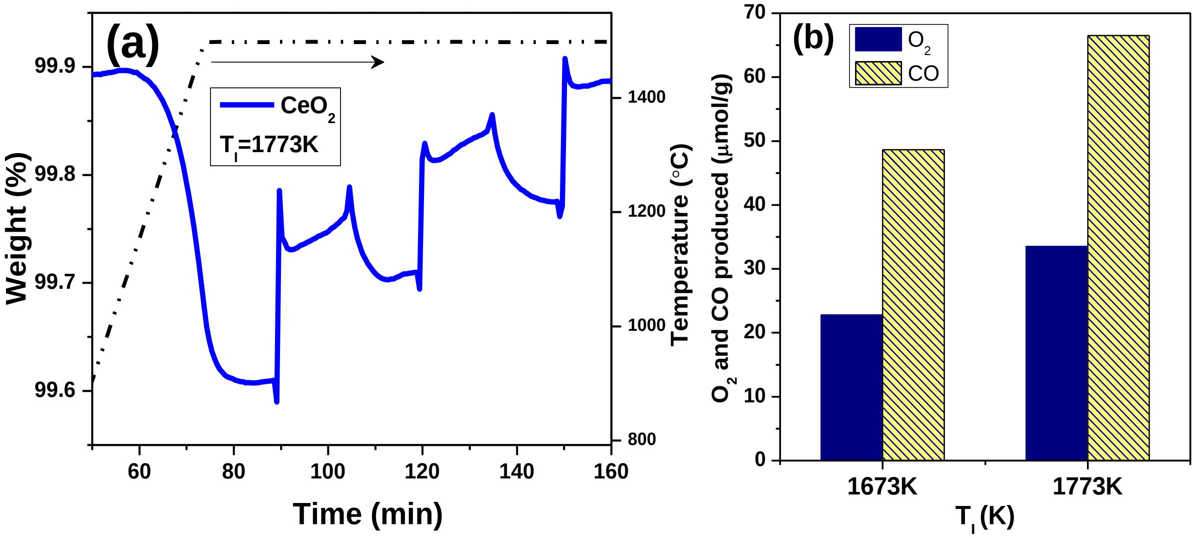

Figure 13. (a) Representative TGA and (b) corresponding histogram of ITCS of CeO$_2$ at 1773 K. t_{red} and t_{oxd} are 15 min and 10 min respectively. p_{O_2}=10^{-5} atm during reduction and p_{CO_2}= 1 atm during oxidation with flow rates of gases being 1000 ml/min/g.

Representative TGA curves of LSM30, LSM40 and LSM50 at 1673 K and 1773K (**Figures 14a and c**) are presented along with the histograms which quantify the O$_2$ and CO yields (Figures 14b and d). Increasing Sr^{2+} or the redox active Mn^{4+}/ Mn^{3+} ratio increases the O$_2$ production as well as the CO yield as the oxidation occurs reversibly. The CO yield with LSM30, LSM40 and LSM50 are 75.9, 98.2 and 134.8 µmol/g respectively at 1673 K. CO (O$_2$) production increases further at 1773K, with the highest production by LSM50 (230 µmol/g of CO yield).

A slow exponential decay is observed towards the new mass while reaching equilibrium during first oxidation. Although the slope obtained from the linear fit of mass variation near equilibrium (last 4 mins during equilibrium) is of order LSM50>LSM40>LSM30, but the values are very close to zero indicates stable weight changes when the equilibrium were deemed to be reached. In addition the δ_{eq} varies as LSM50>LSM40>LSM30 (Table 3), indicating that with increasing Sr^{2+} content greater amount of CO$_2$ is required to stabilize the equilibrium (oxidation) during ITCS. The δ_{eq} values of LSMs are higher than CeO$_2$, but more importantly CO production is considerably higher than CeO$_2$ by ITCS. Thus with LSM50, the CO yield is ~3.5 times and ~2.8 times higher than CeO$_2$ at 1773K and 1673K respectively.

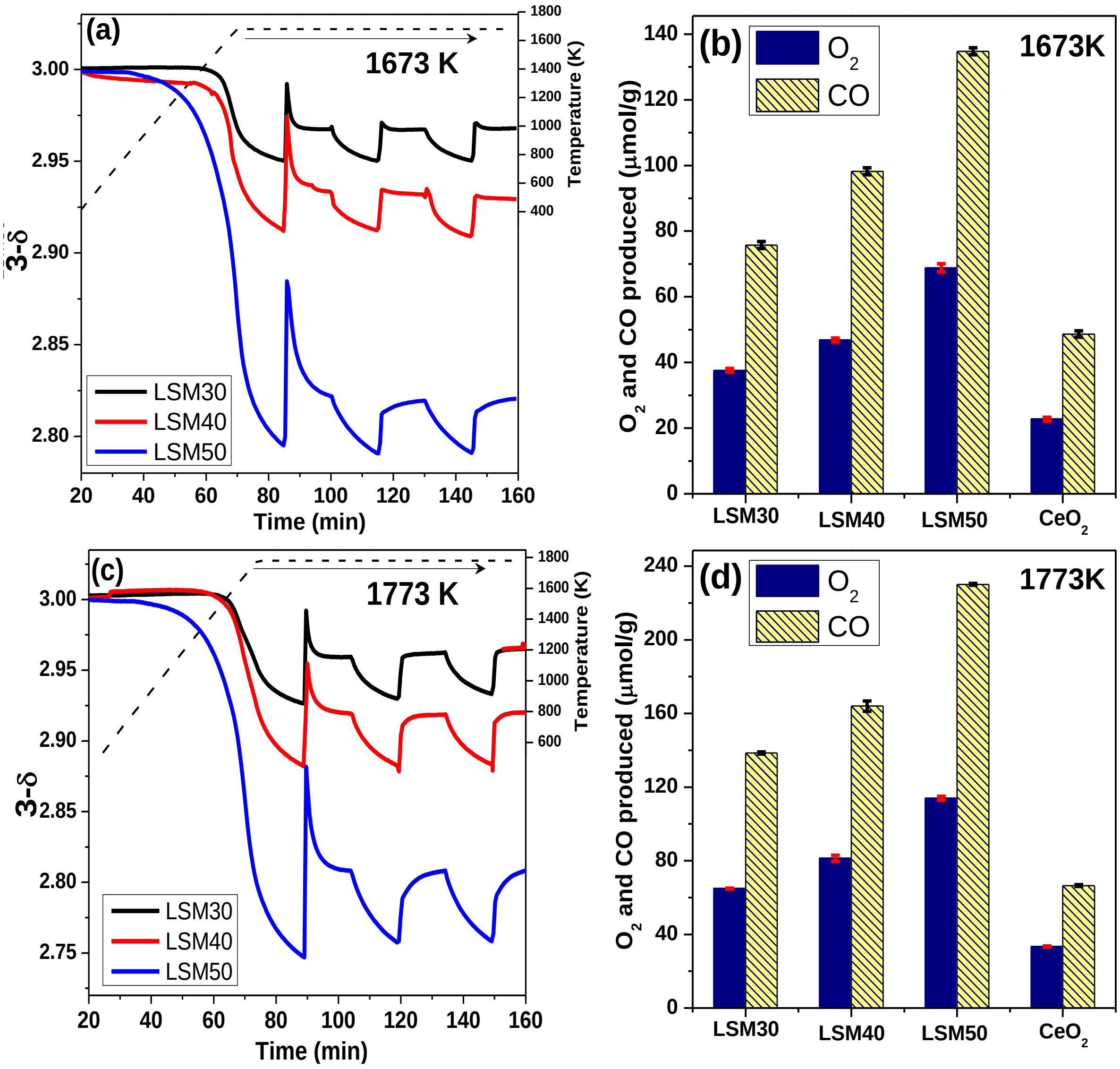

Figure 14. Representative TGA of isothermal thermochemical CO_2 splitting of $La_{1-x}Sr_xMnO_3$ (x=0.3, 0.4 and 0.5) at (a) 1673K and (c) 1773K respectively. The compound is heated to T_I initially under 10 ppm O_2 and then subsequent oxidation (p_{CO_2}= 1 atm) and reduction take place cyclically under gas flow rates of 1000 ml/min/g. t_{red} and t_{oxd} half cycle times are 15 min. Corresponding histograms to show the O_2 and CO production for (b) 1673K and (d) 1773K measurements. Error bars indicate max/min values of multiple runs.

Entering CO_2 during first oxidation shows sudden gain in weight which immediately decreases with reaching equilibrium. As the oxidation is kinetically more favored at high temperatures, the entrance of CO_2 results in a sudden weight gain, but the oxygen activity of CO_2 is not sufficient to maintain the equilibrium at that initial stoichiometry and the reduction continues until equilibrium is established. In separate experiments (**Figure 15**) we have heated LSM40 at 1673 K under CO_2 flow (pCO_2=1 atm). LSM40 establishes equilibrium in the presence of CO_2 (Figure 15) and the δ_{eq} (~0.07) is found similar as observed in Figure 14a (~0.067). Further replacement of CO_2 flow with sweep gas and followed by CO_2 continues the regular isothermal process.

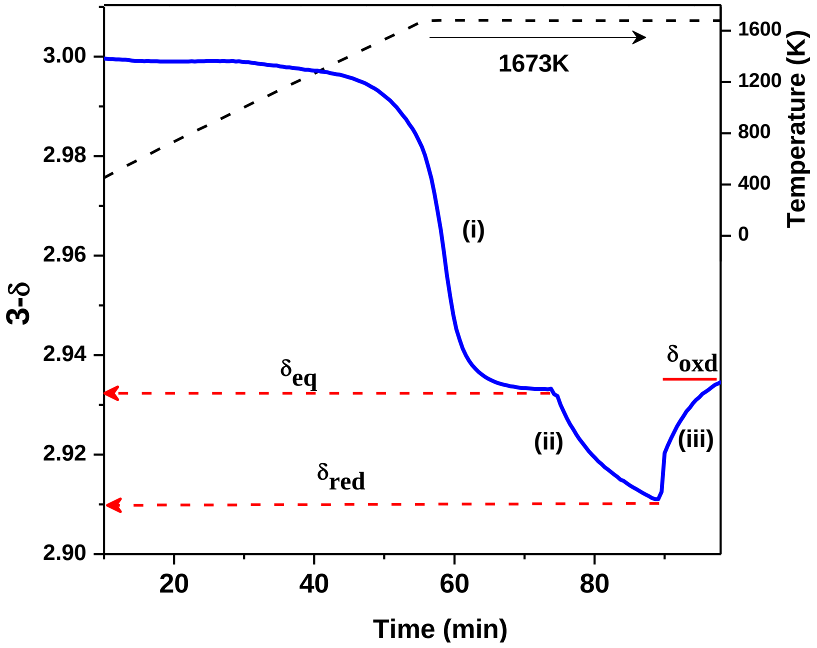

Figure 15. Representative TG plot (oxygen nonstoichiometry as a function of time) of LSM40 to mark the oxygen nonstoichiometry during initial equilibration (δ_{eq}), after reduction (δ_{red}) and after oxidation (δ_{oxd}), (i) LSM40 is first heated at 1673K under CO_2 and maintains for 15 mins to reach δ_{eq} (ii) CO_2(g) is replaced with sweep gas, reduces for 15 mins and reaches δ_{red} (iii) oxidation under CO_2 is carried out isothermally.

The product gases of oxidation were collected in a metal collector attached to pressure a gauge and analyzed by a gas chromatograph equipped with a TCD detector (GC-TCD). The CO peak was detected at 0.9 min while CO_2 appears after that (**Figure 16**). Gas chromatograph results indicate an increasing amount of CO with the increasing Sr substitution in LSM materials. The amount of CO detected by GC-TCD is in close agreement (variation of 10%-15%) with the values measured by TGA.

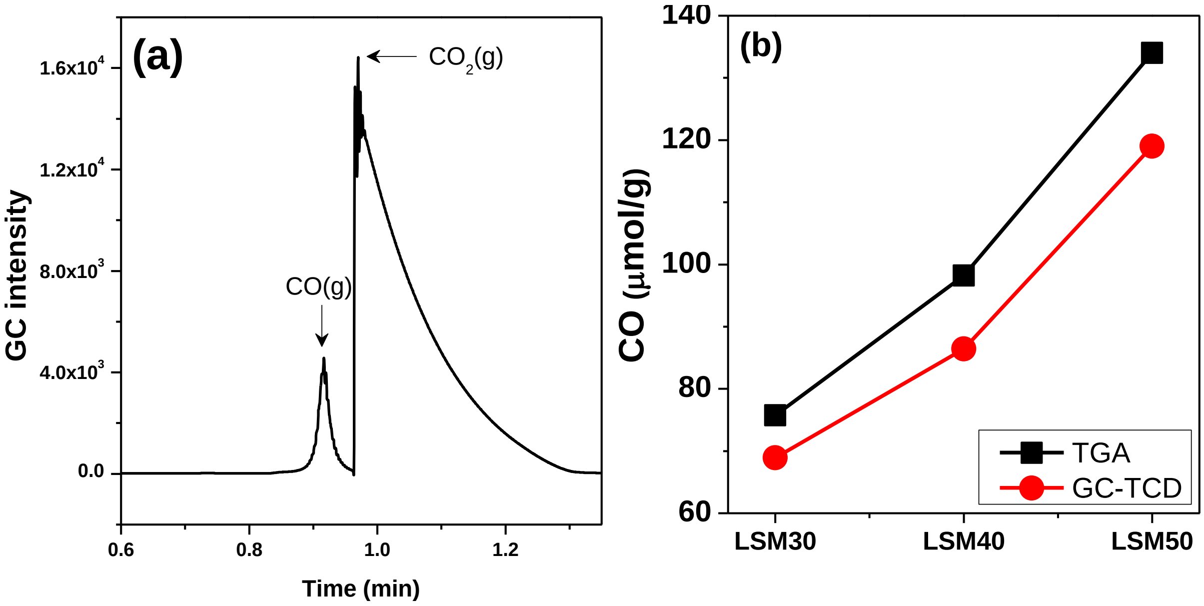

Figure 16. (a) CO and CO$_2$ signal in GC-TCD and (b) thermo gravimetrically estimated CO in comparison with TCD detected CO of LSM40 at 1673K.

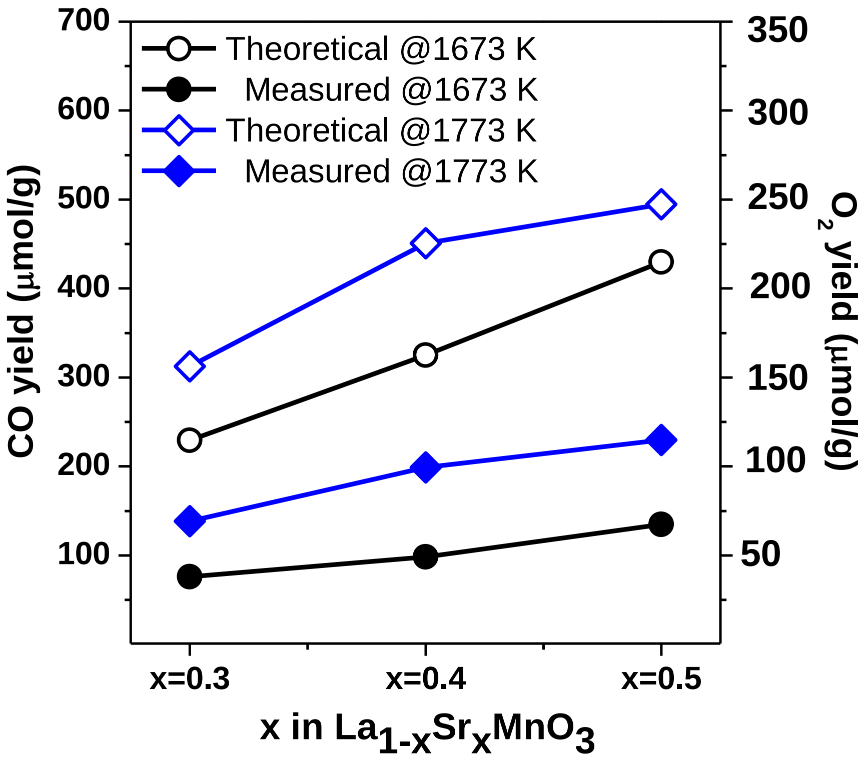

Figure 17. Thermo gravimetrically measured and theoretically estimated O$_2$ and CO yield of La$_{1-x}$Sr$_x$MnO$_3$ (x=0.3, 0.4 and 0.5). Theoretical calculations estimated the maximum yield possible under reduction at p_{O_2}=10^{-5} atm and oxidation under infinite supply of CO$_2$ at p_{CO_2}= 1

atm (no time bounds). Experiments are undertaken in 15 min and 10 min of t$_{red}$ (p_{O_2}=10^{-5} atm) and t$_{oxd}$ (p_{CO_2}= 1 atm) respectively with the flow rates being 1000 ml/min/g of each gases.

The CO yield increases monotonically with Sr^{2+} content of LSM and the yields are higher at 1773K than 1673K, agreeing with the trends predicted by calculations (**Figure 17**). The experimentally obtained yields of CO are around ~32% and ~45% of the theoretically predicted yields at 1673K and 1773K respectively (**Table 4**). The theoretical estimated values represent the maximum possible yield under thermodynamically preferred conditions, where in the content of oxidative CO_2 is assumed as infinite. During experiments the gas flow rates and the total cycle period were limited. Incomplete reduction can be one of the possible reasons for this discrepancy which is limited by slow gas phase mass transport and surface reaction kinetics.[98, 103] Microstructural evolution (as observed in FESEM images) with cycling also limits the reaction rates. Slower oxidation kinetics (which increases δ_{eq}) can also cause lower CO yields.

Table 4. Experimentally obtained CO yield of perovskites are presented along with theoretically estimated values. Values are in µmol/g.

Materials	**1673K**			**1773K**		
	theoretical	experiment	% obtained	theoretical	experiment	% obtained
LSM 30	229.5	75.9	33	312.5	138.4	44
LSM 40	325.9	98.2	30	450.9	200.9	44.5
LSM 50	430	134.8	31	495.1	229.9	46.4

In view of the difference between the experimental and theoretical CO productivity, the effect of reduction time and gas flow rates were investigated over in the case of LSM50 at 1773K (for details see the additional experiments section). By increasing the reduction time (t_{red}) from 15 min to 25 min enhances O_2 production from 111.6 µmol/g to 140.6 µmol/g (**Figure 18**).

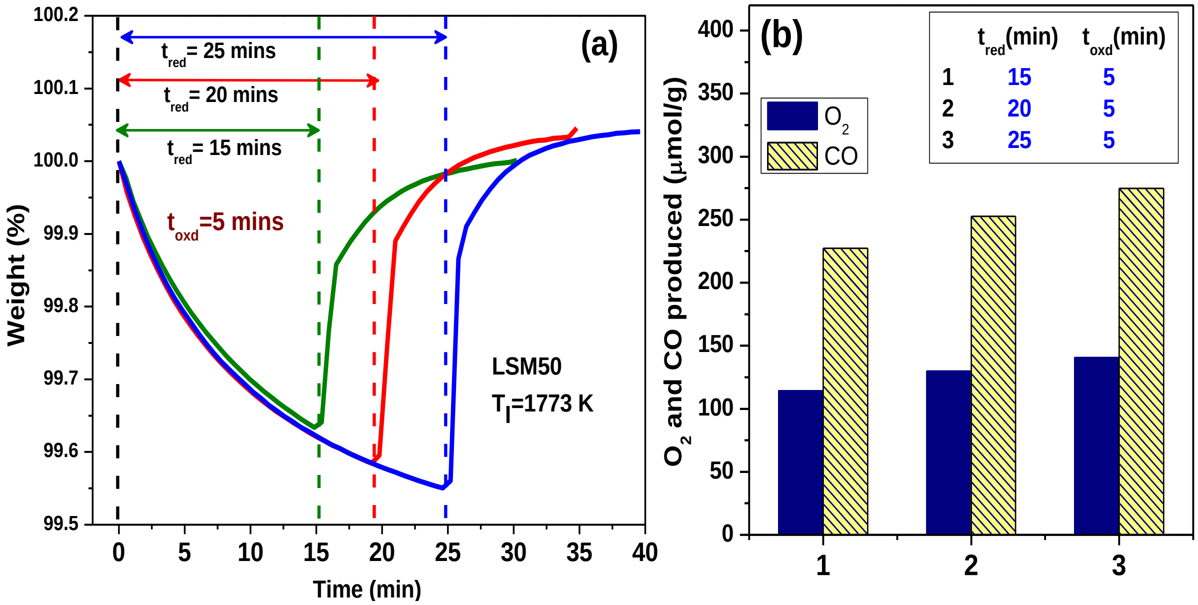

Figure 18. (a) O_2 production (CO yield) varies as a function of reduction time (t_{red}) for LSM50 during ITCS at 1773K. t_{red} was ascended from 15 min to 25 min keeping the t_{oxd} constant at 5 min. Flow rates of sweep gas (p_{O_2}=10^{-5} atm) and CO_2 (p_{CO_2}= 1 atm) are being 1000 ml/min/g. (b) Corresponding histogram quantifies the total O_2 and CO yield as observed during TG measurement.

Table 5. Conversion % of CO (experimentally) as a function of reduction time (t_{red}).

t_{red} (min)	Experimental CO yield (µmol/g)	Predicted CO yield (µmol/g)	% Conversion
15	227	494.6	**46**
20	252.7	494.6	**51**
15	274.8	494.6	**56**

Notably LSM50 reoxidizes completely during 5 min of CO_2 exposure (t_{oxd} = 5 min) even for the t_{red} of 25 min, yields upto 274.5 µmol/g of CO. Notably, 56% of theoretically predicted CO is achieved experimentally for t_{red} of 25 min (**Table 5**). Further increase in CO

(O_2) yield could be achieved by increasing t_{red} as evidenced by linear dependence of CO yield over t_{red} (**Figure 19**). Increasing t_{red} also increases the total cycle period ($t_{total} = t_{red} + t_{oxd}$), altering the time averaged rate of CO production. Increasing the total cycle period from 20 min (t_{red}=15 min) to 30 min (t_{red}=25 min) increases the CO yield from 227.7 µmol/g to 274.5 µmol/g but estimated to reduce the time averaged rate of CO production from 683 µmol/g/hr to 549 µmol/g/hr (Figure 19, blue curve).

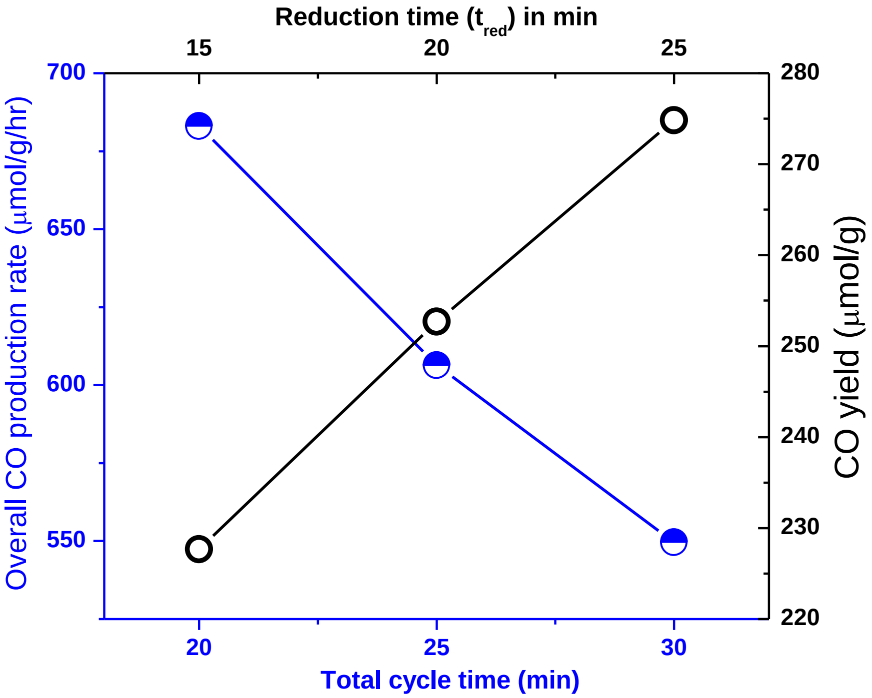

Figure 19. Estimated rate of overall CO production with total cycle time (blue curve) and CO yield as a function of t_{red} (black curve) for LSM 50. The total cycle time is the addition of t_{red} and t_{oxd}. t_{oxd} is 5 min for all the measurements. T_I is 1773K. Flow rates of sweep gas and CO_2 are being 1000ml/min/g.

The influence of sweep gas (10^{-5} atm O_2) flow rate over the average rate of O_2 production of LSM50 is shown in **Figure 20** (see the experimental section for details). Although the total reduction time (t_{red}) was 15 mins, more than 75% of expected O_2 evolved within the initial 10 mins. As shown in Figure 20b, the average rate of O_2 production (time averaged over 9.9 mins) increases monotonically with increasing sweep gas flow rate upto 1000 ml/min/g and remains nearly constant with further increase in flow rate. Hence the maximum rate of O_2 production is 8.5 µmol/min/g achieved at 1000 ml/min/g of sweep gas flow rate. The total O_2 yield (t_{red} is 15 mins) is also increases with increasing sweep gas flow rate and a maximum yield of ~105 µmol/g is achieved with 1000ml/min/g of sweep gas flow rate (inset of Figure 20). LSM50 was oxidized reversibly (t_{oxd} ~ 5 mins) and maintaining the CO: O_2 yield of 2:1 during each cycle (inset of Figure 20b). A constant CO yield of ~215 µmol/g is reached with sweep gas flow rate of 1000 ml/min/g.

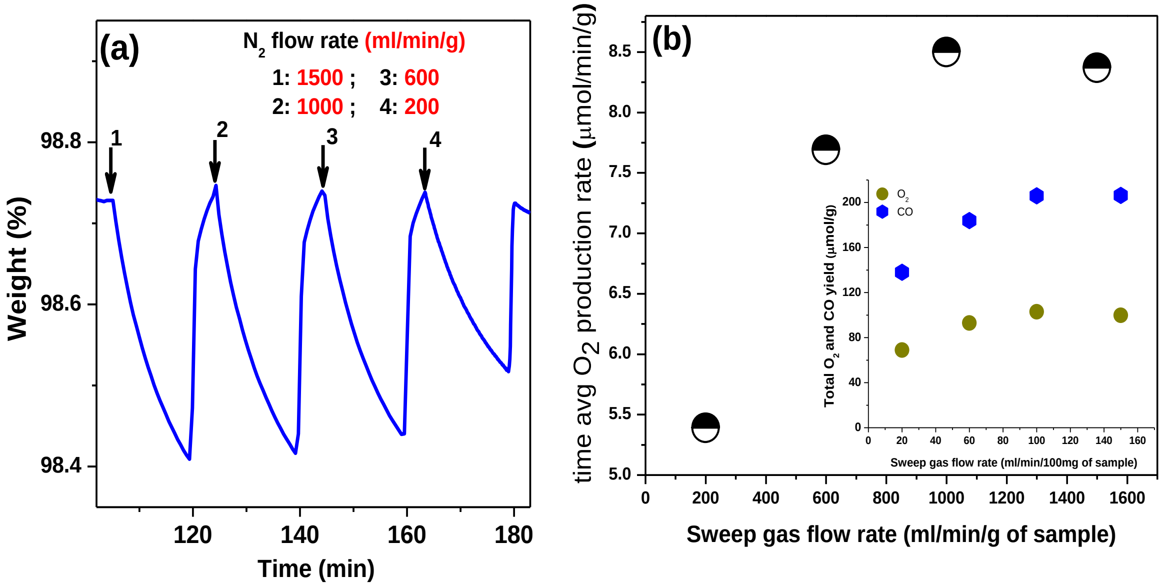

Figure 20. (a) Representative TGA (weight % vs time) and (b) average rate of O_2 production (µmol/min/g) of LSM50 over 9.9 min (T_l is 1773K) as a function of sweep gas ($p_{O_2}=10^{-5}$ atm) flow rates of 1500 to 200 ml/min/g. In Fig. a, the points marked by arrow numbered 1-4 specifies the entry timings of sweep gas at various flow rates. Inset quantifies the total O_2 and CO yield as a function of variable sweep gas flow rates. t_{red} (15 min) is greater than t_{oxd} (5 min) during this experiment with constant CO_2 (p_{CO_2}= 1 atm) flow rates of 800 ml/min/g during oxidation.

The influence of CO_2 flow rates on the rate of CO production is shown in **Figure 21** (see the experimental section for details). The impact of CO_2 flow rate on the global CO production rate as well as on the production rate averaged over initial 3 mins of oxidation can be seen in Figures 21b and c respectively. The CO production rate increases with increasing CO_2 flow rate upto 500 ml/min/g with a plateau occurring beyond this volume. Maximum CO production rate of 46 µmol/min/g (Figures 21c) is obtained. CO yield too increases with the CO_2 flow rates upto 600 ml/min/g with a maximum yield of ~185 µmol/g. The CO: O_2 ratio of 2:1 is maintained in each cycle (Figure 21d). As inferred from Figures 20 and 21, the maximum rate of O_2 production and CO production are achieved with 1000 ml/min/g of sweep gas flow and 600 ml/min/g of CO_2 flow respectively (T_I is 1773K). Below these flow rates gas phase mass transport limits the production. The total yield of CO varies with the flow rates, reaching the limit with 1000 ml/min/g sweep gas flow and 600 ml/min/g CO_2 flow.

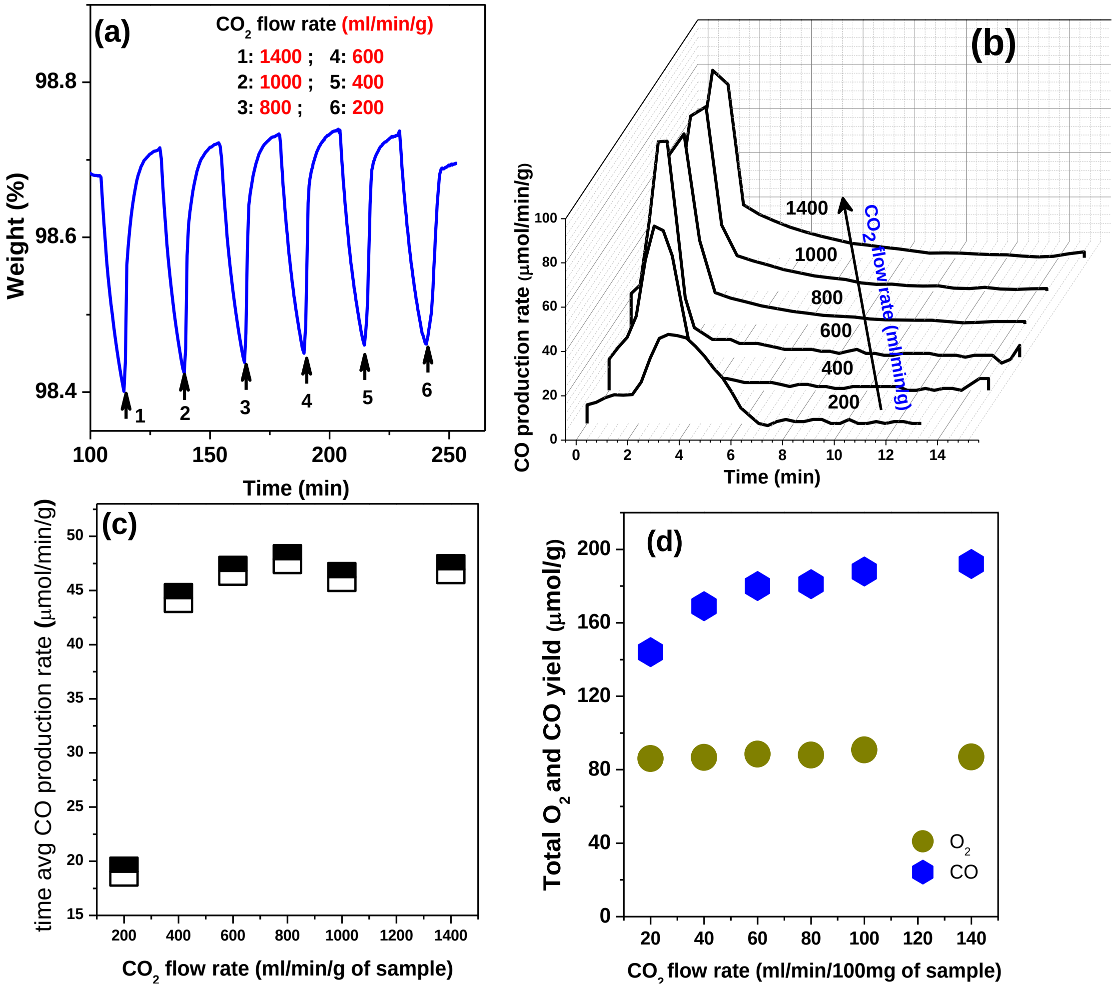

Figure 21. (a) Representative TGA (weight % vs time) (b) global rate of CO production (µmol/min/g) (c) average rate (initial 3 min of oxidation) of CO production (µmol/min/g) and (d) corresponding total O_2 and CO yield (µmol/g) of LSM50 (T_I is 1773K) as a function of CO_2 (p_{CO_2}= 1 atm) flow rates of 1400 to 200 ml/min/g. In Fig. a, the points marked by arrow numbered 1-6 specifies the entry timings of oxidant at various flow rates. t_{oxd} (15 min) is greater than t_{red} (10 min) during this experiment with constant flow of sweep gas (p_{O_2}=10^{-5} atm) of 1000 ml/min/g during reduction.

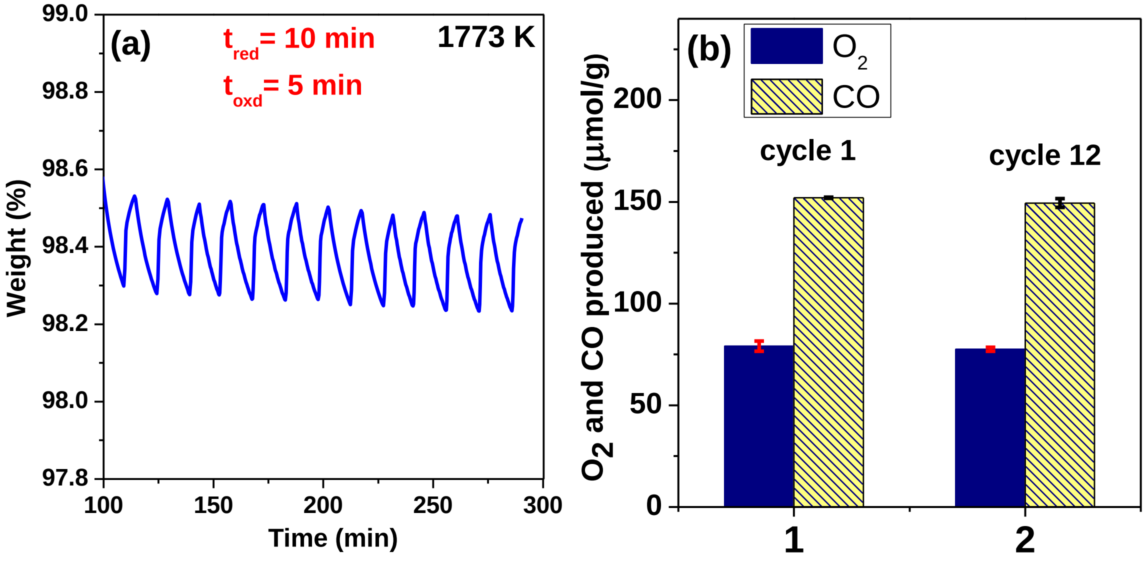

Figure 22. Representative TGA of LSM50 shows the O_2 and CO production rate during 13 consecutive ITCS cycles at 1773K. (b) Histogram represents the O_2 and CO yield of LSM50 during 1st and at the end of 13th thermogravimetric cycles. Error bars indicate max/min values of multiple runs.

Multiple cycling of LSM50 was carried out at 1773K, under the restriction of t_{red} (p_{O_2}=10^{-5} atm, flow rate 1000 ml/min/g) and t_{oxd} (p_{CO_2}=1 atm, flow rate 400 ml/min/g) of 10 min and 5 min per cycle respectively (**Figure 22**). The yield of CO was nearly the same even after 13th cycle (149.5 µmol/g) as found during 1st cycle (151.8 µmol/g). An average production of 150.4 µmol/g of CO (per cycle) was obtained, which leads to a time-averaged CO production rate of 601.8 µmol/g/hr. This is significantly higher than that found with CeO_2 (200.9 µmol/g/hr).

Our previous investigation of $Ln_{0.5}A_{0.5}MnO_3$ (Ln= La, Nd, Sm, Gd, Dy and Y; A=Sr, Ca) family of perovskites has shown $Y_{0.5}Sr_{0.5}MnO_3$ to be the best performing material for the two-step process. $Y_{0.5}Sr_{0.5}MnO_3$ not only enhances the O_2 and CO production but it also lowers the reduction/oxidation temperature significantly. The performance of $Y_{0.5}Sr_{0.5}MnO_3$ is much superior to all the other manganite perovskites due to its low tolerance factor and high size disorder. In the present study, we have investigated $Y_{0.5}Sr_{0.5}MnO_3$ for isothermal CO_2 splitting.

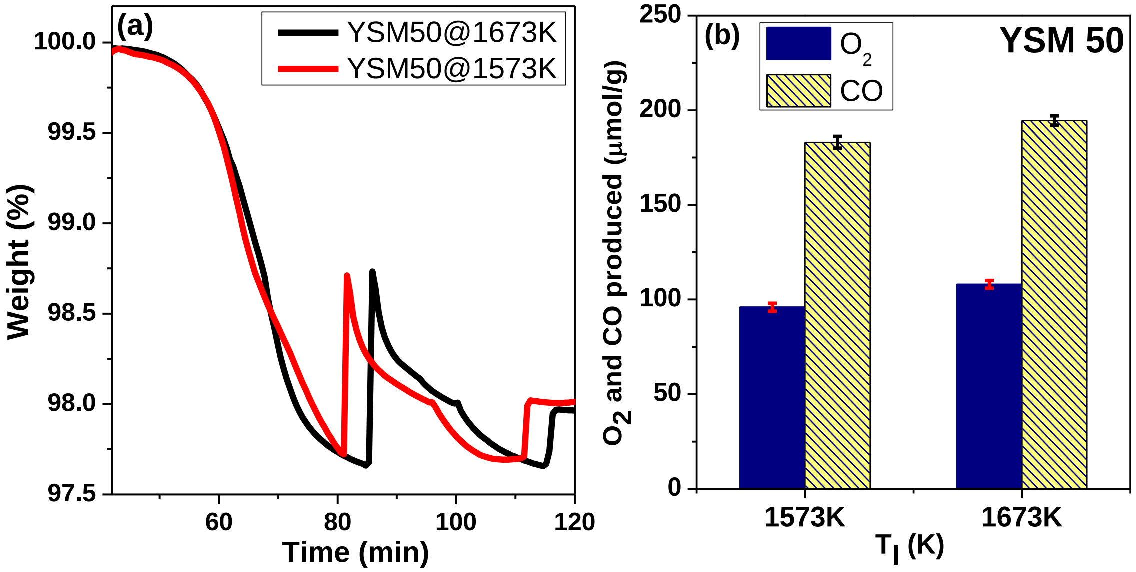

Figure 23. (a) Representative TGA and (b) corresponding histogram of ITCS of YSM50 (T_I= 1573K and 1673K). Reduction (p_{O_2}=10^{-5} atm) and oxidation (p_{CO_2}= 1 atm) half cycle times are 15 min with flow rates of gases are 1000 ml/min/g of oxides. Error bars indicate max/min values of multiple runs.

$Y_{0.5}Sr_{0.5}MnO_3$ (YSM50) undergoes reduction at a much lower temperature (~1200K) in comparison with LSM50 (~1320K) during TSCS. We have, therefore, carried out a ITCS study with YSM50. YSM50 shows remarkably good CO (O_2) production of 183 µmol/g (96 µmol/g) and 196.4 µmol/g (108 µmol/g) at 1573K and 1673K respectively (**Figure 23**). In comparison with LSM50, the CO yield of YSM50 is ~1.25 times higher at 1673K and ~1.8 times higher even at 1573K (**Figure 24**). The average CO production rate of YSM50 was 61.2 µmol/min/g, significantly higher than LSM50 (34 µmol/min/g) at 1673K. It is noteworthy that the CO yield of YSM50 is about 3.8 times higher than CeO_2 at 1673K. As YSM50 has a higher reducibility (δ_{eqm}) or lower enthalpy of reduction than LSM50 under similar T_I, it encounters the need of more oxidant supply for reversible CO production. But, considering the system with heat recovery facilities from fluid might make YSM50 perovskite more applicable, in view of their higher fuel productivity, lower irradiance loss of solar reactor ($\eta_{abs} = f(T, C)$)[83, 96] and lower thermal stress related to significantly lower reaction temperature.

Decreasing the rare earth ion sizes decreases the tolerance factor (τ) of manganites.[79] Decrease in τ indicates an increase in the lattice distortion, accompanied by increase in the tilting of the MnO_6 octahedra which would favor O_2 evolution.[79] Increase in τ decreases the Mn-O-Mn bond angles, which in turn reduces the spatial overlap of Mn e_g and O 2pσ orbitals,[79] which would ease oxide ions removal. $Y_{0.5}Sr_{0.5}MnO_3$ with the smallest tolerance factor (τ= 0.965) and therefore shows the highest O_2 yield and CO production. $Y_{0.5}Sr_{0.5}MnO_3$ shows activity at a lower isotherm as expected from the large size variance factor (σ^2) and the small tolerance factor (τ). The size variance factor, σ^2, arises from radii mismatch of Ln and A cations in $Ln_{0.5}A_{0.5}MnO_3$ perovskites.[81] It indicates greater displacement of the oxygens from the mean position which helps their easy removal.[81] The σ^2 value of $Y_{0.5}Sr_{0.5}MnO_3$ (15.6×10^{-3}) is higher than that of $La_{0.5}Sr_{0.5}MnO_3$ (1.6×10^{-3}).

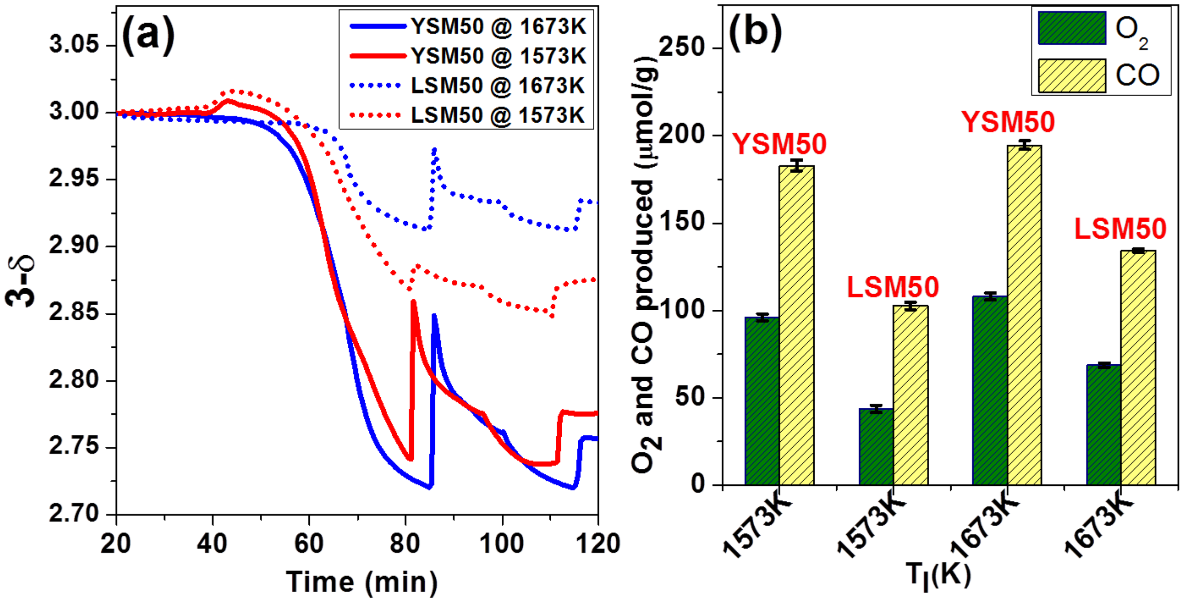

Figure 24. (a) TG plots of ITCS of YSM50 (solid line) in comparison with LSM50 (dotted line). Blue and red lines belong to measurements at T_I of 1673K and 1573K respectively. Reaction conditions are same as in figure 23. (b) Histograms quantifies the CO production of YSM50 with respect to LSM50 (1573K and 1673K).[15] Error bars indicate max/min values of multiple runs.

After high temperature cycling, the structures of the perovskites were investigated by PXRD. LSM30, LSM40 and LSM50 remain chemically stable after isothermal cycles and no secondary phase was detected (**Figure 25a**). Sintering of the porus structure leads to the formation of larger crystallites (≥ 20 µm) besides smaller grains (~1-2 µm) as shown for LSM50 in Figure 25b. YSM50 shows structural stability for isothermal cycling at1673K (blue curve in **Figure 26**) and no impurity phase occurs. Hexagonal $YMnO_3$ is formed as impurity phase due on heating at temperatures above 1673K as indicated by asterisk in the Figure 25.

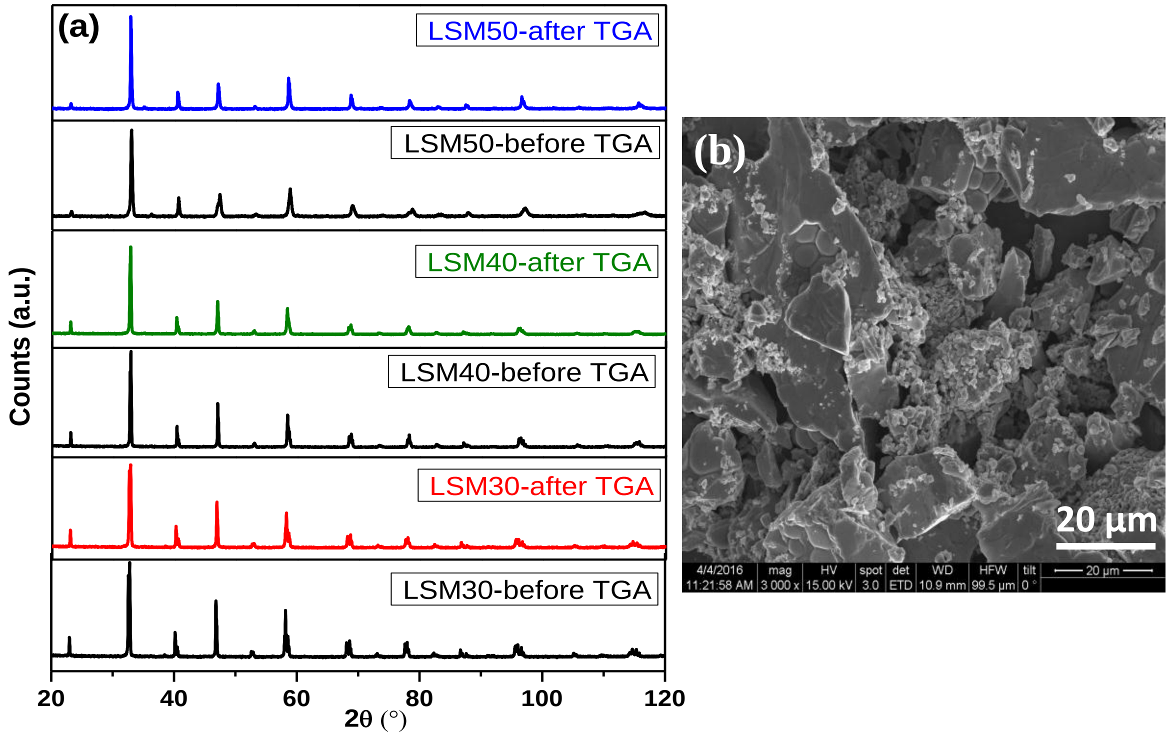

Figure 25. (a) PXRD patterns of $La_{1-x}Sr_xMnO_3$ (x=0.3, x=0.4 and x=0.5) after high temperature thermogravimetric analysis in comparison with as synthesized perovskites. (b) FESEM image of LSM50 after multiple cycles of thermogravimetric CO production.

The weight gain of the nonstoichiometric oxide on passing CO_2 can arise from carbonate formation instead of CO_2 splitting alone.[90] The CO_2 splitting temperature is generally higher than 1573K in all the present experiments. Decomposition of Sr and La carbonates is reported around 1213K and 1073K respectively, which are well below 1273K.[90, 132] Carbonate formation is therefore most unlikely in the present study. Galvez et. al[90] has observed segregation of CaO or $CaCO_3$ related phases during low temperature oxidation of $La_{0.6}Ca_{0.4}MnO_3$ perovskites by high magnification FESEM images. We have recorded FESEM images (magnification 30000x- 200000x) over multiple places throughout the samples (**Figure 27**). Other than sintering of the microstructural perovskites we have not observed any distinct phase separation related to SrO or $SrCO_3$ segregation. The PXRD patterns of the perovskites before and after thermogravimetric measurements do not show the presence of carbonate peaks (Figure 25). Besides, the CO measured by GC-TCD is in good agreement with the CO expected from TGA measurements, ruling out the possibility of carbonate formation.

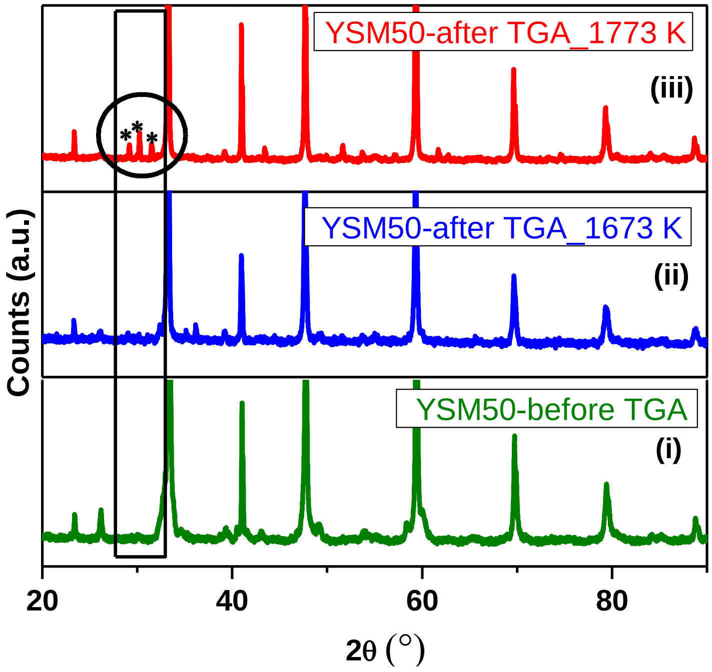

Figure 26. PXRD patterns of YSM50 (i) as synthesized and after isothermal TG measurement at (ii) 1673K and (iii) 1773K. The black circular area highlighted the difference in diffraction pattern due to the formation of $YMnO_3$ phase after fuel production at 1773K.The impurity peaks are marked with (∗).

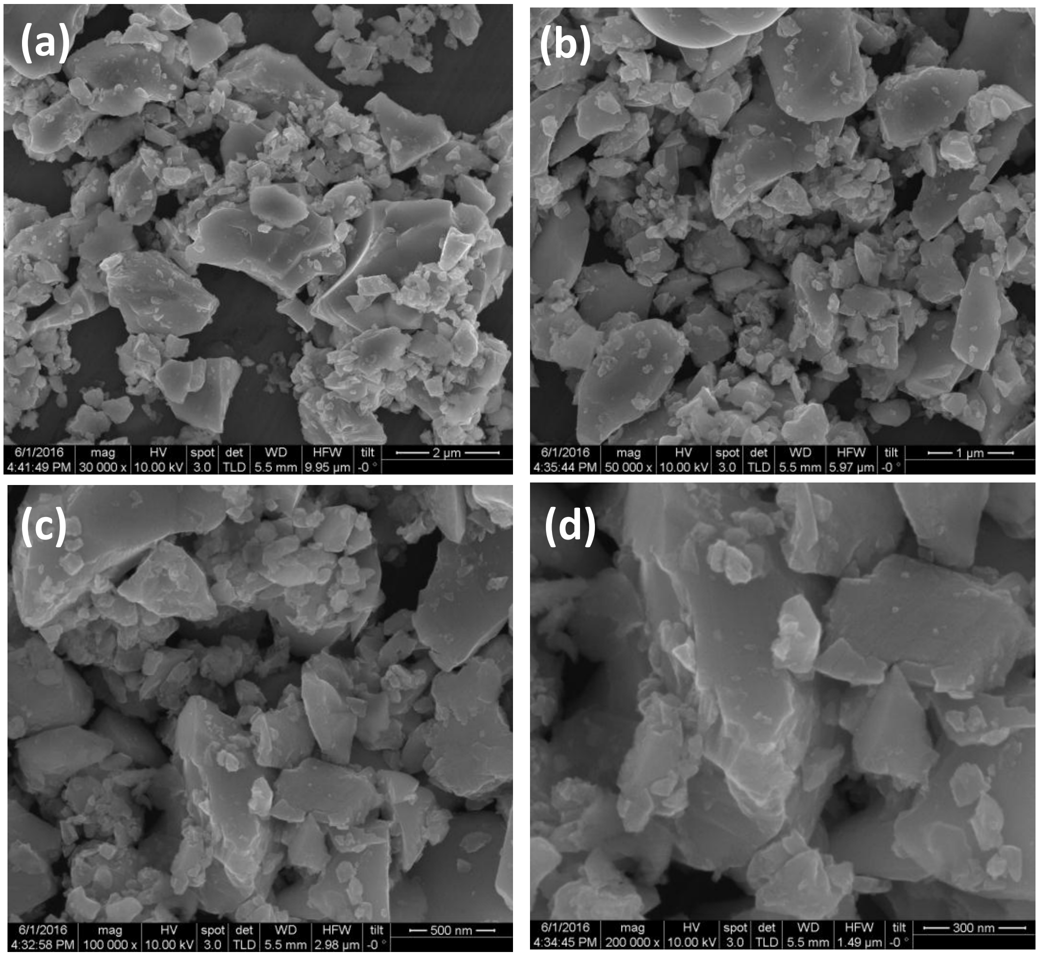

Figure 27. FESEM images of LSM40 after high temperature thermogravimetric cycles. Magnifications are (a) 30000 x, (b) 50000 x, (c) 100000x and (d) 200000x.

1.5. Conclusions

In conclusion, $La_{1-x}Ca_xMnO_3$ manganites are excellent materials for the thermochemical splitting of both H_2O and CO_2. The performance of $La_{1-x}Ca_xMnO_3$ is superior to that of the state of art material, CeO_2, as well as of the corresponding $La_{1-x}Sr_xMnO_3$ compositions (section 1.4.1). The amount of O_2 and CO evolved by $La_{0.5}Ca_{0.5}MnO_3$ is 1.6 times and 5 times more than the $La_{0.5}Sr_{0.5}MnO_3$ and ceria respectively. Our investigation also infers the superior performance of orthorhombic perovskite over rhombohedral one in thermochemical fuel production. In conclusion, it would be profitable to attempt high temperature fuel production using LCM perovskites.

As shown in section 1.4.2., $Ln_{0.5}Sr_{0.5}MnO_3$ and $Ln_{0.5}Ca_{0.5}MnO_3$ (Ln=rare earth ions) families of perovskite oxides both show excellent performance in the thermochemical reduction of CO_2 and H_2O. Enhancement of oxygen production and hence CO production is observed as the size of the rare earth ion decreases, resulting in the highest activity for yttrium derivatives. Furthermore, a significant decrease in the reduction and oxidation temperatures is achieved with the manganites of small rare earth ions. Thus, the temperature of oxidation can be brought down to as low as 900°C with $Y_{0.5}Sr_{0.5}MnO_3$, producing the highest amount of O_2 and CO at 1300°C and 900°C respectively, superior to all the perovskite oxides reported so far. The remarkable fuel production activity with reduction/oxidation carried out at 1200°C/900°C using $Y_{0.5}Sr_{0.5}MnO_3$ is indeed noteworthy. These results could be of direct benefit for syngas production and other applications.

Ga and Sc substituted LSM based perovskites have been exploited for the first time for thermochemical CO_2 and H_2O splitting and these oxides show superior performance in comparison with Al substituted LSMs or the parent LSM as presented in section 1.4.3. It is noteworthy that the oxidation state of Ga and Sc remain +3 throughout and the effect of the trivalent cations varies in the order, Sc>Ga>Al. For the same proportion of the trivalent ion (25%), the yields of O_2 and CO are 1.4 and 1.5 times higher in the Ga derivative compared to the Al derivative. The performance obtained with substitution of 5% Sc^{3+} ($La_{0.5}Sr_{0.5}Mn_{0.95}Sc_{0.05}O_3$) is remarkable with O_2 and CO yields of almost 2 and 1.7 times more than the parent LSM. Carbonate formation has not observed to contribute in weight gain during oxidation. Furthermore, 250 µmol/g of H_2 is produced with $La_{0.5}Sr_{0.5}Mn_{0.95}Sc_{0.05}O_3$ at 1100˚C.

Incorporation of Ga^{3+} and Sc^{3+} in the LSM50 perovskite is beneficial in the two-step fuel production process and can be employed for high temperature syngas production and other applications.

Our study shows (section 1.4.4) how manganite perovskites perform well in the isothermal thermochemical CO_2 splitting process. What is especially noteworthy is that the CO production with LSM50 is around 2.8 times and 3.5 times higher than with CeO_2 at 1673 and 1773K respectively. Increasing the reduction time increases CO production further, reaching about 56% of thermodynamically estimated CO_2 conversion. What is more interesting is that one can lower the redox temperature to 1573K by using $Y_{0.5}Sr_{0.5}MnO_3$ (YSM50). Even at 1573K, YSM50 produces ~1.8 times more CO than LSM50. The CO yield of YSM50 at 1673K is 3.8 times higher than CeO_2. These results are significant for possible use in practical solution considering that solar thermal splitting of CO_2 has been demonstrated with CeO_2.

1.6. References

1 A. Kudo and Y. Miseki, *Chem. Soc. Rev.*, 2009, **38**, 253-278.

2 G. P. Smestad and A. Steinfeld, *Ind. Eng. Chem. Res.*, 2012, **51**, 11828-11840.

3 C. N. R. Rao, S. R. Lingampalli, S. Dey and A. Roy, *Phil. Trans. R. Soc. A*, 2016, **374**, 20150088.

4 S. Ihara, *Int. J. Hydrogen Energy*, 1980, **5**, 527-534.

5 T. Nakamura, *Solar Energy*, 1977, **19**, 467-475.

6 S. Abanades, P. Charvin, G. Flamant and P. Neveu, *Energy*, 2006, **31**, 2805-2822.

7 A. B. Munoz-Garcia, A. M. Ritzmann, M. Pavone, J. A. Keith and E. A. Carter, *Acc. Chem. Res.*, 2014, **47**, 3340-3348.

8 R. Perret, *Solar Thermochemical hydrogen production research (STCH)*, Sandia National Laboratories, 2011.

9 S. Sato, S. Shimizu, H. Nakajima, K. Onuki, Y. Ikezoe and T. Suwa, *Int. J. Hydrogen Energy*, 1984, **9**, 191-196.

10 G. E. Beghi, *Int. J. Hydrogen Energy*, 1986, **11**, 761-771.

11 J. H. Norman, K. J. Mysels, R. Sharp and D. Williamson, *Int. J. Hydrogen Energy*, 1982, **7**, 545-556.

12 L. E. Brecher, S. Spewock and C. J. Warde, *Int. J. Hydrogen Energy*, 1977, **2**, 7-15.

13 T. Kodama and N. Gokon, *Chem. Rev.*, 2007, **107**, 4048-4077.

14 M. Roeb, M. Neises, N. Monnerie, F. Call, H. Simon, C. Sattler, M. Schmucker and R. Pitz-Paal, *Materials*, 2012, **5**, 2015.

15 S. Yalccin, *Int. J. Hydrogen Energy*, 1989, **14**, 551-561.

16 J. R. Scheffe and A. Steinfeld, *Materials Today*, 2014, **17**, 341-348.

17 J. E. Miller, A. Ambrosini, E. N. Coker, M. D. Allendorf and A. H. McDaniel, *Energy Procedia*, 2014, **49**, 2019-2026.

18 C. L. Muhich, B. D. Ehrhart, I. Al-Shankiti, B. J. Ward, C. B. Musgrave and A. W. Weimer, *WIREs Energy Environ*, 2015, DOI: 10.1002/wene.1174.

19 W. C. Chueh and S. M. Haile, *Phil. Trans. R. Soc. A*, 2010, **368**, 3269-3294.

20 T. Nakamura, *Sol. Energy*, 1977, **19**, 467-475.

21 B. Meredig and C. Wolverton, *Phys. Rev. B*, 2009, **80**, 245119.

22 B. Xu, Y. Bhawe and M. E. Davis, *Proc. Natl. Acad. Sci. U. S. A.*, 2012, **109**, 9260-9264.

23 C. K. Yang, Y. Yamazaki, A. Aydin and S. M. Haile, *J. Mater. Chem. A*, 2014, **2**, 13612-13623.

24 T. Cooper, J. R. Scheffe, M. E. Galvez, R. Jacot, G. Patzke and A. Steinfeld, *Energy Technology*, 2015, **3**, 1130-1142.

25 M. Takacs, M. Hoes, M. Caduff, T. Cooper, J. R. Scheffe and A. Steinfeld, *Acta Materialia*, 2016, **103**, 700-710.

26 A. Steinfeld, *Int. J. Hydrogen Energy*, 2002, **27**, 611-619.

27 S. Abanades, *Int. J. Hydrogen Energy*, 2012, **37**, 8223-8231.

28 I. Alxneit, *Solar Energy*, 2008, **82**, 959-964.

29 A. Steinfeld, S. Sanders and R. Palumbo, *Solar Energy*, 1999, **65**, 43-53.

30 I. Bransky and A. Z. Hed, *J. Am. Ceram. Soc.*, 1968, **51**, 231-231.

31 L. Darken and R. W. Gurry, *J. Am. Chem. Soc.*, 1945, **67**, 1398-1412.

32 O. N. Salmon, *J. Phys. Chem.*, 1961, **65**, 550-556.

33 E. N. Coker, A. Ambrosini, M. A. Rodriguez and J. E. Miller, *J. Mater. Chem. A*, 2011, **21**, 10767-10776.

34 T. Kodama, Y. Nakamuro and T. Mizuno, *J. Solar Energy Eng.*, 2006, **128**, 3-7.

35 N. Gokon, H. Murayama, J. Umeda, T. Hatamachi and T. Kodama, *Int. J. Hydrogen Energy*, 2009, **34**, 1208-1217.

36 J. R. Scheffe, M. D. Allendorf, E. N. Coker, B. W. Jacobs, A. H. McDaniel and A. W. Weimer, *Chem. Mater.*, 2011, **23**, 2030-2038.

37 K. Ehrensberger, A. Frei, P. Kuhn, H. R. Oswald and P. Hug, *Solid State Ionics*, 1995, **78**, 151-160.

38 H. Kaneko, T. Kodama, N. Gokon, Y. Tamaura, K. Lovegrove and A. Luzzi, *Solar Energy*, 2004, **76**, 317-322.

39 T. Kodama, Y. Kondoh, R. Yamamoto, H. Andou and N. Satou, *Solar Energy*, 2005, **78**, 623-631.

40 M. D. Allendorf, R. B. Diver, N. P. Siegel and J. E. Miller, *Energy & Fuels*, 2008, **22**, 4115-4124.

41 R. Subramanian and R. Dieckmann, *J. Phys. Chem. Solids*, 1994, **55**, 59-67.

42 T. Kodama, N. Gokon and R. Yamamoto, *Solar Energy*, 2008, **82**, 73-79.

43 N. Gokon, H. Murayama, A. Nagasaki and T. Kodama, *Solar Energy*, 2009, **83**, 527-537.

44 J. H. Raeder, J. L. Holm and O. T. Sorensen, *Solid State Ionics*, 1984, **12**, 155-159.

45 J. R. Scheffe, A. H. McDaniel, M. D. Allendorf and A. W. Weimer, *Energy Environ Sci.*, 2013, **6**, 963-973.

46 E. N. Coker, J. A. Ohlhausen, A. Ambrosini and J. E. Miller, *J. Mater. Chem.*, 2012, **22**, 6726-6732.

47 J. R. Scheffe, J. Li and A. W. Weimer, *Int. J. Hydrogen Energy*, 2010, **35**, 3333-3340.

48 D. Arifin, V. J. Aston, X. Liang, A. H. McDaniel and A. W. Weimer, *Energy Environ. Sci.*, 2012, **5**, 9438-9443.

49 M. Lundberg, *Int. J. Hydrogen Energy*, 1993, **18**, 369-376.

50 M. Sturzenegger, J. Ganz, P. NueschM and T. Schelling, *J. Phys. IV France*, 1999, **09**, Pr3-331-Pr333-335.

51 H. Kaneko, Y. Hosokawa, N. Gokon, N. Kojima, N. Hasegawa, M. Kitamura and Y. Tamaura, *J. Phys. Chem. Solids*, 2001, **62**, 1341-1347.

52 Y. Tamaura, A. Steinfeld, P. Kuhn and K. Ehrensberger, *Energy*, 1995, **20**, 325-330.

53 K. Otsuka, M. Hatano and A. Morikawa, *Inorganica Chimica Acta*, 1985, **109**, 193-197.

54 S. Abanades and G. Flamant, *Solar Energy*, 2006, **80**, 1611-1623.

55 W. C. Chueh and S. M. Haile, *ChemSusChem*, 2009, **2**, 735-739.

56 S. Abanades, A. Legal, A. Cordier, G. Peraudeau, G. Flamant and A. Julbe, *J. Mater. Sci.*, 2010, **45**, 4163-4173.

57 R. J. Panlener, R. N. Blumenthal and J. E. Garnier, *J. Phys. Chem. Solids*, 1975, **36**, 1213-1222.

58 O. T. Sorensen, *J. Solid State Chem.*, 1976, **18**, 217-233.

59 M. Mogensen, N. M. Sammes and G. A. Tompsett, *Solid State Ionics*, 2000, **129**, 63-94.

60 M. A. Panhans and R. N. Blumenthal, *Solid State Ionics*, 1993, **60**, 279-298.

61 G. J. VanHandel and R. N. Blumenthal, *J. Electrochem. Soc.*, 1974, **121**, 1198-1202.

62 R. Dieckmann and H. Schmalzried, *Ber. Bunsen. Phys. Chem.*, 1977, **81**, 344-347.

63 M. Kang, X. Wu, J. Zhang, N. Zhao, W. Wei and Y. Sun, *RSC Adv*, 2014, **4**, 5583-5590.

64 Q.-L. Meng, C.-i. Lee, T. Ishihara, H. Kaneko and Y. Tamaura, *Int. J. Hydrogen Energy*, 2011, **36**, 13435-13441.

65 Q.-L. Meng, C.-i. Lee, S. Shigeta, H. Kaneko and Y. Tamaura, *J. Solid State Chem.*, 2012, **194**, 343-351.

66 Q.-L. Meng and Y. Tamaura, *J. Phys. Chem. Solids*, 2014, **75**, 328-333.

67 J. R. Scheffe and A. Steinfeld, *Energy & Fuels*, 2012, **26**, 1928-1936.

68 J. R. Scheffe, R. Jacot, G. R. Patzke and A. Steinfeld, *J. Phys. Chem. C*, 2013, **117**, 24104-24114.

69 P. Singh and M. S. Hegde, *Chem. Mater.*, 2010, **22**, 762-768.

70 A. Le Gal and S. Abanades, *J. Phys. Chem. C*, 2012, **116**, 13516-13523.

71 A. Le Gal and S. Abanades, *Int. J. Hydrogen Energy*, 2011, **36**, 4739-4748.

72 Y. Hao, C.-K. Yang and S. M. Haile, *Chem. Mater.*, 2014, **26**, 6073-6082.

73 P. R. Shah, T. Kim, G. Zhou, P. Fornasiero and R. J. Gorte, *Chem. Mater.*, 2006, **18**, 5363-5369.

74 M. Kuhn, S. R. Bishop, J. L. M. Rupp and H. L. Tuller, *Acta Mater.*, 2013, **61**, 4277-4288.

75 M. Takacs, J. R. Scheffe and A. Steinfeld, *Phys. Chem. Chem. Phys.*, 2015, **17**, 7813-7822.

76 C. N. R. Rao, *J. Phys. Chem. B*, 2000, **104**, 5877-5889.

77 G. Niu, X. Guo and L. Wang, *J. Mater. Chem. A*, 2015, **3**, 8970-8980.

78 Z. Song, S. C. Watthage, A. B. Phillips and M. J. Heben, *J. Photon. Energy*, 2016, **6**, 022001-022001.

79 P. M. Woodward, T. Vogt, D. E. Cox, A. Arulraj, C. N. R. Rao, P. Karen and A. K. Cheetham, *Chem. Mater.*, 1998, **10**, 3652-3665.

80 P. M. Woodward, *Acta Crystallographica Section B: Structural Science*, 1997, **53**, 44-66.

81 J. P. Attfield, *Chem. Mater.*, 1998, **10**, 3239-3248.

82 A. Evdou, V. Zaspalis and L. Nalbandian, *Int. J. Hydrogen Energy*, 2008, **33**, 5554-5562.

83 J. R. Scheffe, D. Weibel and A. Steinfeld, *Energy Fuels*, 2013, **27**, 4250-4257.

84 L. Nalbandian, A. Evdou and V. Zaspalis, *Int. J. Hydrogen Energy* 2009, **34**, 7162-7172.

85 L. Nalbandian, A. Evdou and V. Zaspalis, *Int. J. Hydrogen Energy*, 2011, **36**, 6657-6670.

86 A. Demont and S. Abanades, *RSC Adv.*, 2014, **4**, 54885-54891.

87 A. H. McDaniel, E. C. Miller, D. Arifin, A. Ambrosini, E. N. Coker, R. O'Hayre, W. C. Chueh and J. Tong, *Energy Environ Sci.* , 2013, **6**, 2424-2428.

88 A. M. Deml, V. Stevanovic, A. M. Holder, M. Sanders, R. O'Hayre and C. B. Musgrave, *Chem. Mater.*, 2014, **26**, 6595-6602.

89 A. Demont and S. Abanades, *J. Mater. Chem. A*, 2015, **3**, 3536-3546.

90 M. E. Galvez, R. Jacot, J. Scheffe, T. Cooper, G. Patzke and A. Steinfeld, *Phys. Chem. Chem. Phys.*, 2015, **17**, 6629-6634.

91 A. Demont, S. Abanades and E. Beche, *J. Phys. Chem. C*, 2014, **118**, 12682-12692.

92 A. H. Bork, M. Kubicek, M. Struzik and J. L. M. Rupp, *J. Mater. Chem. A*, 2015, **3**, 15546-15557.

93 Q. Jiang, J. Tong, G. Zhou, Z. Jiang, Z. Li and C. Li, *Solar Energy*, 2014, **103**, 425-437.

94 W. C. Chueh, C. Falter, M. Abbott, D. Scipio, P. Furler, S. M. Haile and A. Steinfeld, *Science*, 2010, **330**, 1797-1801.

95 B. Bulfin, A. J. Lowe, K. A. Keogh, B. E. Murphy, O. Lubben, S. A. Krasnikov and I. V. Shvets, *J. Phys. Chem. C*, 2013, **117**, 24129-24137.

96 R. Bader, L. J. Venstrom, J. H. Davidson and W. Lipinski, *Energy Fuels*, 2013, **27**, 5533-5544.

97 A. Le Gal, S. Abanades, N. Bion, T. Le Mercier and V. Harle, *Energy Fuels*, 2013, **27**, 6068-6078.

98 Y. Hao, C. K. Yang and S. M. Haile, *Phys. Chem. Chem. Phys.*, 2013, **15**, 17084-17092.

99 C. L. Muhich, B. W. Evanko, K. C. Weston, P. Lichty, X. Liang, J. Martinek, C. B. Musgrave and A. W. Weimer, *Science*, 2013, **341**, 540-542.

100 R. B. Diver, J. E. Miller, N. P. Siegel and T. A. Moss, ASME 2010 4th International Conference on Energy Sustainability, **2010**.

101 I. Ermanoski, J. E. Miller and M. D. Allendorf, *Phys. Chem. Chem. Phys.*, 2014, **16**, 8418-8427.

102 R. Michalsky, V. Botu, C. M. Hargus, A. A. Peterson and A. C. Steinfeld, *Adv. Energy Mater.*, 2015, **5**, 1401082(1401081-1401010).

103 L. J. Venstrom, R. M. De Smith, Y. Hao, S. M. Haile and J. H. Davidson, *Energy Fuels*, 2014, **28**, 2732-2742.

104 P. Furler, J. R. Scheffe and A. Steinfeld, *Energy Environ. Sci.*, 2011, **5**, 6098-6103.

105 P. T. Krenzke and J. H. Davidson, *Energy & Fuels*, 2014, **28**, 4088-4095.

106 P. Furler, J. Scheffe, M. Gorbar, L. Moes, U. Vogt and A. Steinfeld, *Energy & Fuels*, 2012, **26**, 7051-7059.

107 P. Furler, J. Scheffe, D. Marxer, M. Gorbar, A. Bonk, U. Vogt and A. Steinfeld, *Phys. Chem. Chem. Phys.*, 2014, **16**, 10503-10511.

108 S. G. Rudisill, L. J. Venstrom, N. D. Petkovich, T. Quan, N. Hein, D. B. Boman, J. H. Davidson and A. Stein, *J. Phys. Chem. C*, 2013, **117**, 1692-1700.

109 C. D. Malonzo, R. M. De Smith, S. G. Rudisill, N. D. Petkovich, J. H. Davidson and A. Stein, *J. Phys. Chem. C*, 2014, **118**, 26172-26181.

110 C. Agrafiotis, M. Roeb, A. G. Konstandopoulos, L. Nalbandian, V. T. Zaspalis, C. Sattler, P. Stobbe and A. M. Steele, *Sol. Energy*, 2005, **79**, 409-421.

111 T. Kodama, T. Hasegawa, A. Nagasaki and N. Gokon, *J. Solar Energy Eng.*, 2009, **131**, 021008.

112 H. Kaneko, A. Fuse, T. Miura, H. Ishihara and Y. Tamaura, 13th International Symposium on Concentrating Solar Power and Chemical Energy Technologies, Seville, Spain, 2006.

113 J. E. Miller, L. R. Evans, J. N. Stuecker, M. D. Allendorf, N. P. Siegel and R. B. Diver, In Proceedings of ISEC2006 ASME 2006 International Solar Energy Conference, Denver, CO, USA, 8–13 July,, 2006.

114 R. D. Shannon, *Acta Crystallogr.*, 1976, 32751.

115 http://abulafia.mt.ic.ac.uk/shannon/ptable.php.

116 A. Arulraj, R. Mahesh, G. N. Subbanna, R. Mahendiran, A. K. Raychaudhuri and C. N. R. Rao, *J. Solid State Chem.*, 1996, **127**, 87-91.

117 A. Arulraj, P N. Santhosh,R. S. Gopalan, A. Guha, A. K. Raychaudhuri, N. Kumar, C. N. R. Rao, *J. Phys. Condens. Matter* 1998, **10**, 8497–8504.

118 S. Dey, B. S. Naidu, A. Govindaraj, C. N. R. Rao,*Phys. Chem. Chem. Phys.* 2015, **17**, 122–125.

119 A. H. McDaniel, A. Ambrosini, E. N. Coker, J. E. Miller, W. C. Chueh, R. O'Hayre, J. Tong, *Energy Procedia* 2014, **49**, 2009–2018.

120 X. Yue, A. Yan, M. Zhang, L. Liu, Y. Dong and M. Cheng, *J. Power Sources*, 2008, **185**, 691–697.

121. V. V. Kharton, M. V. Patrakeev, J. C. Waerenborgh, V. A. Sobyanin, S. A. Veniaminov, A. A. Yaremchenko, P. Gaczynski, V. D. Belyaev, G. L. Semin and J. R. Frade, *Solid State Sci.*, 2005, **7**, 1344–1352.

122 M. V. Patrakeev, E. B. Mitberg, A. A. Lakhtin, I. A. Leonidov, V. L. Kozhevnikov, V. V. Kharton, M. Avdeev and F. M. B. Marques, *J. Solid State Chem.*, 2002, **167**, 203–213.

123 E. N. Naumovich, M. V. Patrakeev, V. V. Kharton, M. S. Islam, A. A. Yaremchenko, J. R. Frade and F. M. B. Marques, *Solid State Ionics*, 2006, **177**, 457–470.

124 V. V. Kharton, E. V. Tsipis, A. A. Yaremchenko, I. P. Marozau, A. P. Viskup, J. R. Frade and E. N. Naumovich, *Mater. Sci. Eng., B*, 2006, **134**, 80–88.

125 M. V. Patrakeev, V. V. Kharton, Y. A. Bakhteeva, A. L. Shaula, I. A. Leonidov, V. L. Kozhevnikov, E. N. Naumovich, A. A. Yaremchenko and F. M. B. Marques, *Solid State Sci.*, 2006, **8**, 476–487.

126 C. Zhang, Y. Zheng, Y. Lin, R. Ran, Z. Shao and D. Farrusseng, *J. Power Sources*, 2009, **191**, 225–232.

127 H. Gu, Y. Zheng, R. Ran, Z. Shao, W. Jin, N. Xu and J. Ahn, *J. Power Sources*, 2008, **183**, 471–478.

128 D. Lybye, F. W. Poulsen and M. Mogensen, *Solid State Ionics*, 2000, **128**, 91–103.

129 H. Ullmann and N. Trofimenko, *Solid State Ionics*, 1999, **119**, 1–8.

130 J. Mizusaki, N. Mori, H. Takai, Y. Yonemura, H. Minamiue, H. Tagawa, M. Dokiya, H. Inaba, K. Naraya and T. Sasamoto, *Solid State Ionics*, 2000, **129**, 163-177.

131 H. Tagawa, N. Mori, H. Takai, Y. Yonemura, H. Minamiue, H. Inaba, J. Mizusaki and T. Hashimoto, Proceedings of the Fifth International Symposium on Solid Oxide Fuel Cells (SOFC-V), 1997.

132 R. Sarbajna, A. S. Devi, K. Purandhar and M. V. Suryanarayana, *Int. J. ChemTech Res.*, 2013, **5**, 2810-2820.

Part 2

Significant reduction in the operating temperature of the multi-step Mn(II)/Mn(III) oxide-based thermochemical water splitting cycle brought about by the use of nanoparticles

Part 2

Significant reduction in the operating temperature of the multi-step Mn(II)/Mn(III) oxide-based thermochemical water splitting cycle brought about by the use of nanoparticles*

Summary

Among the many efforts to devise low temperature thermochemical cycles to generate H_2 by water splitting, the Mn(II)/Mn(III) oxide based cycle operating at 850°C is a significant one and involves no toxic and corrosive materials. The essential process in this cycle is the shuttling of Na^+ ions in and out of Mn oxides. In an effort to bring down the temperature of this cycle, we have found use of nanoparticles of Mn_3O_4 is particularly effective. Thus the temperature of the solid state reaction between nanoparticles of Na_2CO_3 and Mn_3O_4 occurs at a temperature 200°C lower than with bulk samples. One of the challenges of this particular cycle lies on its slow H_2 evolution. It has been possible to operate this cycle and generate H_2 at much faster rates at 750°C and even at 700°C by this means. Furthermore, in a step in the cycle involving hydrolysis of $NaMnO_2$ can also be performed at lower temperature (50°C) instead of what reported in literature (80°C-100°C).

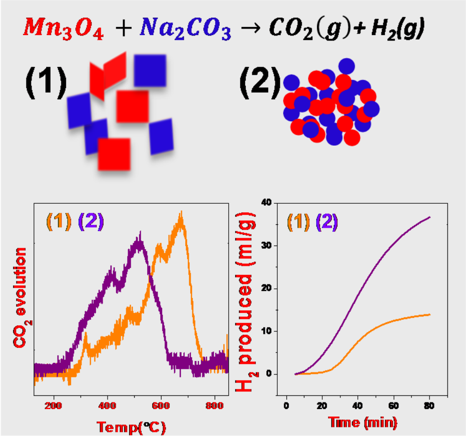

---

*A paper based on this part of the thesis has been accepted in ***J. Mater. Chem. A(2016).***

2.1. Introduction

Multi step processes of thermochemical H_2O splitting which utilizes more than two-step can be operated below 1273K as formulated and discussed extensively in introduction in Part 1.[1, 2] It has attracted considerable attention starting from1970s[3] as it allow the use of broader spectrum of heat sources available from nuclear power plants [4, 5] as well as solar receiver.[6, 7] The use of solar reactor is beneficial as the low temperature restricts the irradiance loss. A great deal of research has been conducted in the past decades amongst which the performance of few cycles are really notable such as S-I cycle,[8-10] S-Br cycle, Fe-Cl cycle, Hg-Br cycle and hybrid Cu-Cl cycle.[3, 11, 12] Inspite of producing steady amount of H_2 all of these cycles are suffering with engineering challenges and environmental issues associated with the separation of acid mixtures, decomposition of acids, heavy metal processing, production of halide mixture, production of toxic or corrosive intermediates and many more.[13] Even the most studied S-I cycle involves at least one of the following hazardous chemicals in each step such as SO_3, I_2, HI, H_2SO_4.[8] Besides, involving more number of reaction steps always associated with additional problem of product losses and efficiency deterioration.[1]

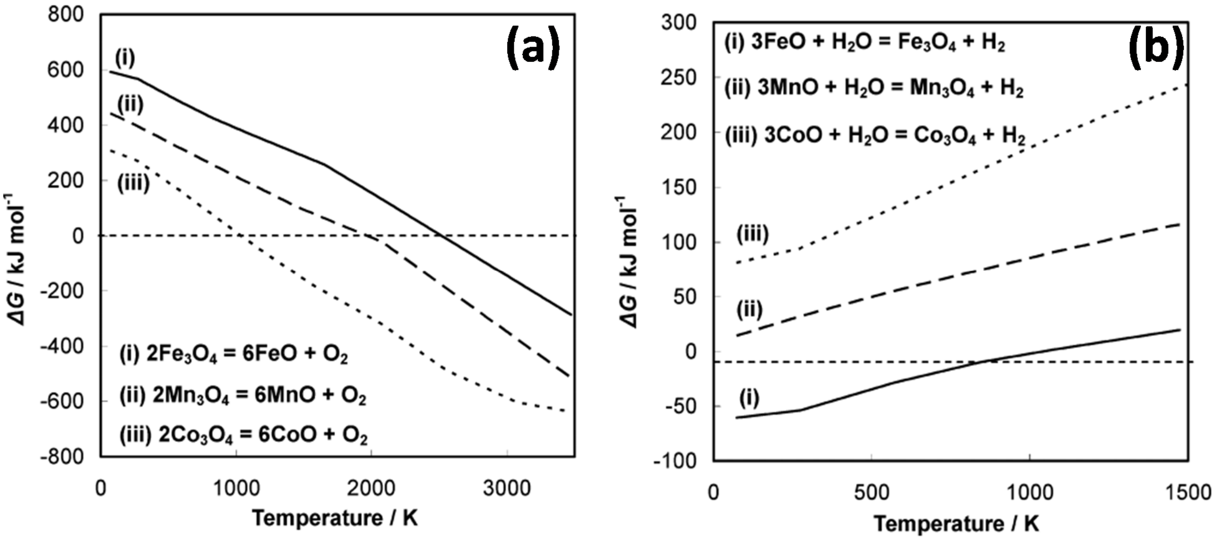

Figure 1. Variation ΔG^0 for (a) thermal decomposition and (b) water decomposition with temperature at 1 bar for various M_3O_4/MO (M= Mn, Fe and Co) systems. Reproduced by permission of American Chemical Society from Ref.[14].

In this regard transition metal oxides based multi-step cycle is one of the novel choices considering its abundances and an embargo on corrosive intermediates. Initially the use of M_3O_4/MO (M= Mn, Fe and Co) based two-step cycles were considered (**Figure 1**). [14, 15] The reducibility is in the order of Fe_3O_4> Mn_3O_4> Co_3O_4 whereas the H_2 production on reaction with H_2O shows opposite trend. Solid solutions of $M_xFe_{3-x}O_4$ were found to be optimized for better activity and lots of research has been reported.[16, 17] However, Mn_3O_4 was found to reduce to MnO at extremely high temperature, whereas the H_2 production yield was only 0.002% which surmises that Mn_3O_4/MnO two-step redox process cannot be used for two-step splitting of H_2O.[18, 19]

A manganese oxide based multistep cycle has been proposed which consists of four steps as depicted in **Figure 2**.[20, 21] In this redox process, in step 1 Mn_2O_3 reduces to MnO with the evolution of O_2. NaOH oxidizes the Mn(II) to Mn (III) as $NaMnO_2(s)$ with the evolution of H_2 at 900K. Extraction Na^+ happens trough hydrolysis followed by evaporation of H_2O to convert back NaOH(l) to NaOH(s) for recycling. The best efficiency for this cycle was calculated to be 74% considering 100% heat recovery by Sturzenegger and Nuesch.[20] However, even under the worst scenario of without any heat recovery exergy efficiency has been calculated to be in between 16-22%.[20]

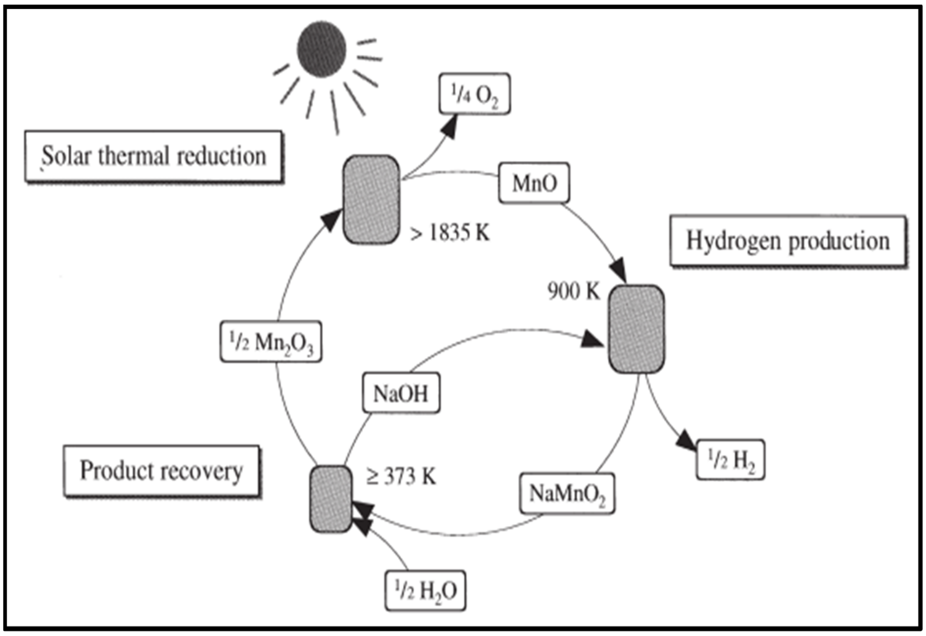

Figure 2. Schematic representation of cycle. Reproduced by permission of Elsevier from Ref.[20].

There are few serious issues associated with this cycle which hinders its practical implementation. The reaction temperature of second step is in between 900-1100K but the volatility of NaOH at > 800°C creates the problem of material recovery and reactor corrosion.[21] Moreover Mn_2O_3 needs to be separated out from NaOH-H_2O solution in order to recycle and this causes uttermost difficulty. Besides the higher temperature of Mn_2O_3 to MnO conversion is an issue of concern.[13, 20, 22, 23]

Instead of NaOH, the production of H_2 using Na_2CO_3 with spinel $MnFe_2O_4$ was pioneered by Tamura et. al.[24, 25] The reaction consists of following steps:

$$2MnFe_2O_4 + 3Na_2CO_3 + H_2O(g) \rightarrow 6Na(Mn_{1/3}Fe_{2/3})O_2(s) + 3CO_2(g) + H_2(g) \quad --- \quad (1)$$

$$6Na(Mn_{1/3}Fe_{2/3})O_2(s) + 3CO_2(g) \rightarrow 3Na_2CO_3(s) + 2MnFe_2O_4 + 0.5O_2(g) --- \quad (2)$$

Although the cycle gets closed below 1273 K, the stoichiometric quantity of O_2 was not found to evolve due to the incomplete extraction of Na^+ even in presence of CO_2(g). Further modification of step 2 is proposed by Kaneko et. al[26-28] with the introduction of Fe_2O_3 as a sacrificial agent as illustrated in steps 3 and 4. The use of Fe_2O_3 doesn't close the cycle. In addition Fe_2O_3 needs to be separated out from the $MnFe_2O_4/Na_2CO_3/Fe_2O_3$ mixture before $MnFe_2O_4+Na_2CO_3$ can be reused for next cycle. This solid-solid separation is the most practically non-feasible step. A wide range of work has been conducted on Mn_2O_3-$NaMnO_2$ and $MnFe_2O_4/Na_2CO_3$ based systems by changing the reaction conditions, composition, particle sizes and many more.[29-37]

$$6Na(Mn_{1/3}Fe_{2/3})O_2(s) + 3Fe_2O_3(s) \rightarrow 2MnFe_2O_4 + 6NaFeO_2(s) + 0.5O_2(g) --- \quad (3)$$

$$2NaFeO_2(s) + CO_2 \rightarrow Na_2CO_3 + Fe_2O_3 --- \quad (4)$$

The improvisation of the Mn(II)/Mn(III) oxide based multi-step cycle has recently been done by Xu et. al[1] who has solved the Na^+ extraction issue with the achievement of complete recycling at < 1000°C of operating temperature. The cycle consist of four steps as described below,

$$2Mn_3O_4 + 3Na_2CO_3 \rightarrow 4NaMnO_2(s) + 2MnO + Na_2CO_3 + 2CO_2(g) \quad -------- (\text{step } 1)$$

$$2MnO + Na_2CO_3 + H_2O(g) \rightarrow 2NaMnO_2(s) + CO_2(g) + H_2(g) \quad ---------- (\text{step } 2)$$

$$\begin{aligned}&6NaMnO_2(s) + ayH_2O(l) + (3+b)CO_2(g)\\ &\quad \rightarrow 3Na_2CO_3(aq) + aH_xMnO_2.yH_2O(s) + bMnCO_3 + cMn_3O_4 ----- (\text{step } 3)\end{aligned}$$

$aH_xMnO_2.yH_2O(s) + bMnCO_3 \rightarrow (2-c)Mn_3O_4(s) + ayH_2O(g) + bCO_2(g) + 0.5O_2(g)$ – (step 4)

where a+b+3c=6 and (4-x)a+2b+8c=18

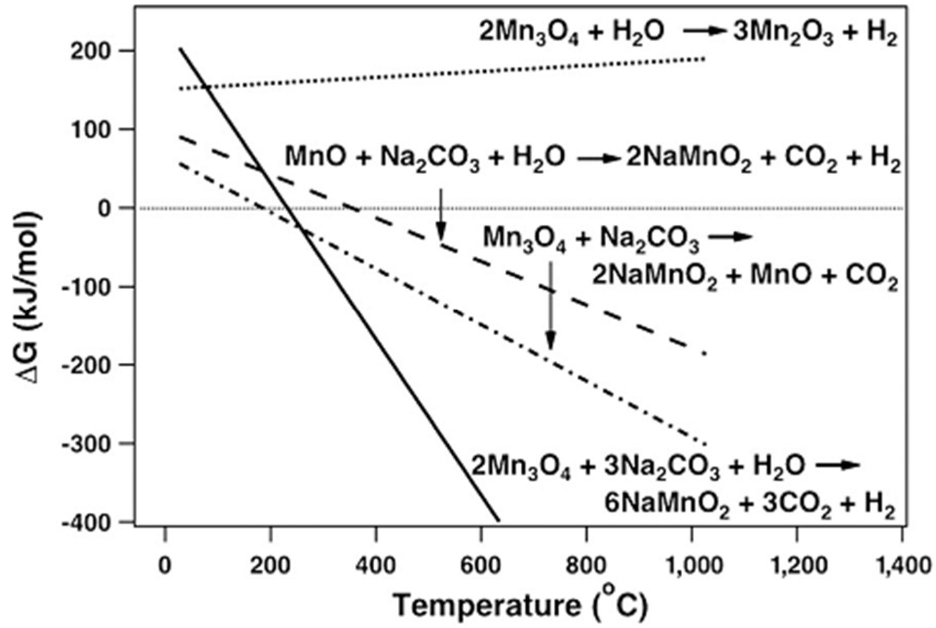

Figure 3. Thermodynamic estimation of Gibbs free energy of oxidation of Mn_3O_4 with H_2O in presence and absence of Na_2CO_3. Reproduced by permission of American chemical society from Ref.[1].

In step 1, solid state reaction between Mn_3O_4 and Na_2CO_3 at 850°C evolves CO_2 (g) along with the formation of MnO(s) and α-$NaMnO_2$(s). In step 2, the introduction of H_2O (g) at 850°C oxidizes the MnO to α-$NaMnO_2$ with the production of H_2(g). As shown in **Figure 3**, the oxidation of Mn_3O_4 to Mn_2O_3 is always thermodynamically unfavorable but the presence of Na_2CO_3 enables the conversion of Mn(II) to Mn(III) become favorable after 400°C.[14] In step 3, extraction of Na^+ from layered $NaMnO_2$(s) is performed in H_2O(l) with bubbling CO_2(g) at 80°C, giving rise to protonic birnessite as the main product. H_2O molecules intercalate in between the MnO_6 sheets, increases the interlayer distances which inturn enhances the mobility of Na^+ ions and results in an easy exchange with protons. Presence of CO_2 drives the equillibrioum towards protonic birnessite production as the hydrolysis in acidic condition is shown to be more feasible.[38] In step 4, reduction of birnessite to Mn_3O_4(s) completes the H_2O

splitting cycle at 850°C with the release of stoichiometric amount of $O_2(g)$. The essential process in this cycle is the shuttling of Na^+ ions in and out of Mn oxides. Xu et. al[39] has recently explored the combinations of three metal oxides (Fe_3O_4, Mn_3O_4 and Co_3O_4) with three alkali carbonates (Li_2CO_3, Na_2CO_3 and K_2CO_3) for thermochemical H_2O splitting. The H_2 evolution rate and onset temperature is of order $Fe_3O_4 > Mn_3O_4 > Co_3O_4$ and $Li_2CO_3 > Na_2CO_3 > K_2CO_3$. Inspite of having higher reactivity the extraction of Li^+ ions during step 3 was found to be impossible which discards the applicability of Li_2CO_3. Notably the Fe_3O_4 has lower H_2 evolution temperature than Mn_3O_4 but at the same time its oxidation tempearture is ~1150°C, is significantly higher than the latter. In addition the most reactive oxide and carbonate has found to be more active in CO_2 reduction although CO evolution can be controlled by monitoring the operating tempearture ($\mathbf{\Delta G_{H_2O\rightarrow H_2}} < \mathbf{\Delta G_{CO_2\rightarrow CO}\ at < 1100K}$) and increasing the supply of H_2O. The combination of the Mn_3O_4 with Na_2CO_3 has found to be the best match for successful H_2O splitting as it succefully close the cycle below <1000°C with stoichiometric production of H_2 and O_2.

2.2. Scope of the present investigations

The cyclability of low temperature, multistep based thermochemical cycles involving Mn_3O_4-Na_2CO_3 at 850°C is a good choice for H_2 production as it is devoid of use or production of any toxic materials. One of the main challenges of this particular cycle lie on its slow H_2 evolution and effort to improve this method has not been explored in literature so far. It took more than 3 hrs for Davis and co-workers[1, 39] for complete H_2 evolution at 850°C. In an effort to bring down the temperature of this cycle, we have used the nanoparticles of Mn_3O_4 and Na_2CO_3 and found the use of nanoparticles of Mn_3O_4 is to be particularly effective. Notably, Davis and co-workers didn't observe any H_2 evolution < 850°C. In view of the attractive features of this cycle, we considered it is purposeful to bring down the operating temperature further by using nanomaterial reactants. Thus the temperature of the solid state reaction between nanoparticles of Na_2CO_3 and Mn_3O_4 occurs at a temperature 200°C lower than with bulk samples. It has been possible to operate this cycle and generate H_2 at much faster rates at 750°C and even at 700°C by this means. Furthermore, various hydrolysis conditions has been investigated in detail in order to modify the step 3 and reduce its energy and material consumption. Our findings include the fact that hydrolysis of $NaMnO_2$ can also be performed at 50°C instead of 100°C even within 1 hr.

2.3. Experimental Section

2.3.1. Synthesis: Mn_3O_4 (97%, sigma) and Na_2CO_3 (99.5%, MERCK) were used as starting materials for ball milling. Around 1.5 gms of sample (Mn_3O_4/ Na_2CO_3) was ball milled in Fritsch Pulverisette 5 (container volume 50 cm^3; ball/powder mass ratio=10:1) under rotation of 400 rpm for various time durations (15 mins to 1.5 hr) and the changes are monitored by PXRD patterns at regular intervals. Unlike Na_2CO_3 exceeding the milling time more than 1.5 hrs starts to oxidize Mn_3O_4 slowly and Mn_2O_3 began to appear. Bulk particles of Mn_3O_4 (Mn-HT) were synthesized by heating the commercial MnO at 1100°C for 12 hrs under ambient conditions. MnO nanoparticles were obtained by ball-milling the commercial MnO (99%, sigma) under rotation of 300 rpm for various time durations (15 mins to 1.5 hr). Exceeding the milling time more than 1.5 hrs start to oxidize it further as monitored by PXRD.

2.3.2. Characterizations: Phase identification was performed by PXRD analysis with a Bruker D8 Advance diffractometer using Cu Kα radiation. FESEM imaging and Energy Dispersive X-Ray analysis (EDAX) was carried out by FEI Nova Nanosem 600. Transmission electron microscope (TEM) images were recorded with FEI Technai T20 instrument at an accelerating voltage of 200 kV. BET measurements were performed in Quanta-chrome Autosorb instrument at 77K from N_2 absorption. Thermogravimetric analysis (TGA) was done using Perkin-Elmer Pyris1instrument.

2.3.3. Reactivity tests: Mn_3O_4 and Na_2CO_3 were mixed mechanically and placed in a Pt pan to hang inside the TG furnace. Mixture was heated upto 850°C (heating rate 20°C/min) under Ar (99.5%) and maintained for 1hr to investigate step 1. We have investigated the splitting of water by employing the experimental set up described in our earlier report.[40, 41] Manganese oxide (Mn_3O_4 or MnO) and Na_2CO_3 were mixed mechanically for 20 mins and packed to an alumina reaction tube supported in between thin layers of Al_2O_3. The reaction tube was placed inside the furnace and heated to reaction temperature (ramp rate 20°C/min) under continuous flow of N_2 (99.9999%, 50 cc/min). Water vapor was introduced in the reaction chamber by sweeping the N_2 through a water bubbler. The connection in between the furnace and water bubbler was insulated with heating tape to avoid water condensation. Evolved H_2 was detected and measured with a gas chromatograph (PerkinElmer Clarus ARNEL 580) equipped with a TCD detector while total amount of H_2 was calculated by the water displacement method. After H_2 evolution, Sodium was extracted by bubbling CO_2 (10 ml/min) through the aqueous dispersion of α-$NaMnO_2$ (0.5-2 wt%) at different temperature for different periods. For O_2 desorption the hydrolyzed sample was heated upto 850°C (heating rate 5°C/min) under Ar.

2.4. Results and discussion

We have employed the multi-step low-temperature thermochemical cycle involving the use of Mn_3O_4 and Na_2CO_3 described by Davis and coworkers,[1] to generate H_2. We present a version of the thermochemical cycle in **Figure 4**, involving the four steps as described in Eqs. step 1 to step 4.

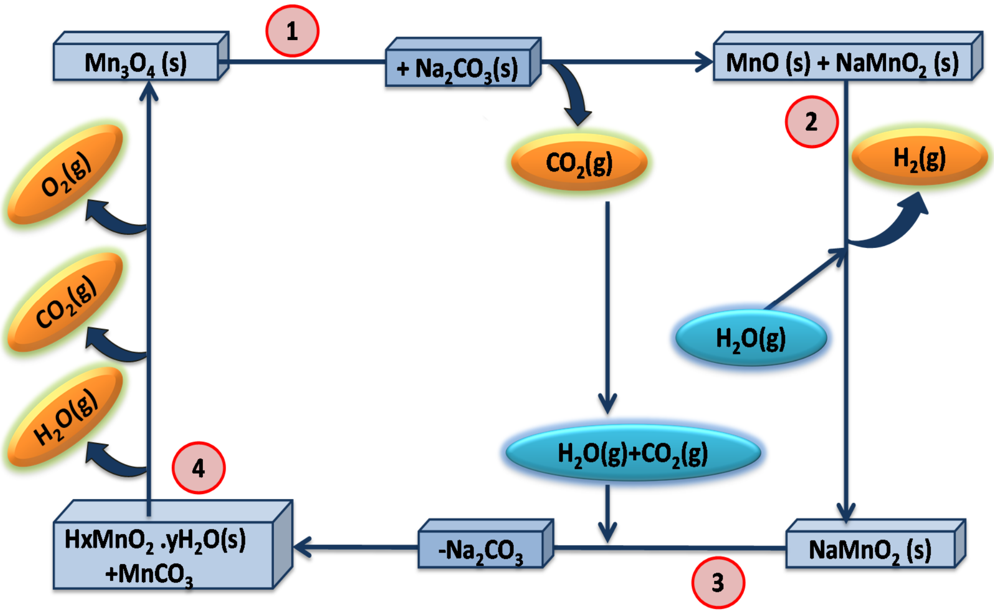

Figure 4. Schematic representation of Mn(II)/Mn(III) based low-temperature thermochemical cycle.

In the context of the present study steps 1 and 2 involving the solid state reaction between Mn_3O_4 or MnO and Na_2CO_3 is most crucial, since the reaction would be strongly affected by the size of the particles. We have ball milled Mn_3O_4 for different periods to obtain much smaller particles than the bulk commercial sample. As indicated in **Figure 5**, all the Mn_3O_4 samples show exclusively the PXRD reflection of hausmannite having tetragonal symmetry (S.G $I4_1$/amd, JCPDS 024-0734). Increasing the ball milling time results in the broadening of PXRD peaks associated with the gradual decrease in crystallite sizes of Mn_3O_4 and Na_2CO_3 (**Figures 5-6** and **Table 1**). Gradual increase in ball milling duration decreases the particle sizes enormously as indicated by FESEM (**Figure 7**) and TEM images (**Figure 8**) associated with the increment of BET surface area (Table 1). Thus, after ball milling the bulk samples (Mn-C) of ~1-2μm size for 30 and 60 minutes, we could obtain particles in the size ranges of 100-500 nm and 100-200 nm respectively (Figure 7 and Table 1). Ball milling for a further period had only a small effect on the size. Ball milling commercial Na_2CO_3 (Na-C) of ~ 5 μm size for 30 and 60 minutes brought down the size to the 250nm-2μm and 250nm-1μm ranges respectively (Table 1, **Figure 9**).

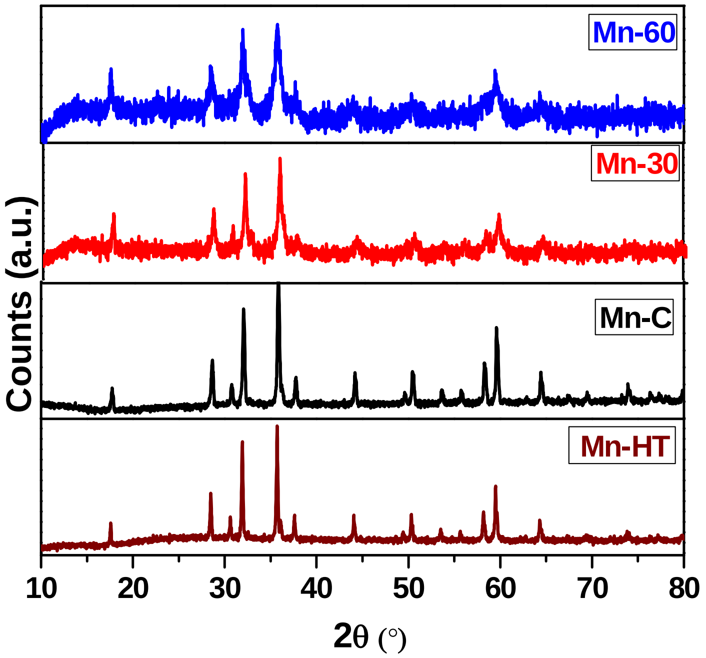

Figure 5. PXRD pattern of bulk and nanoparticles of Mn_3O_4

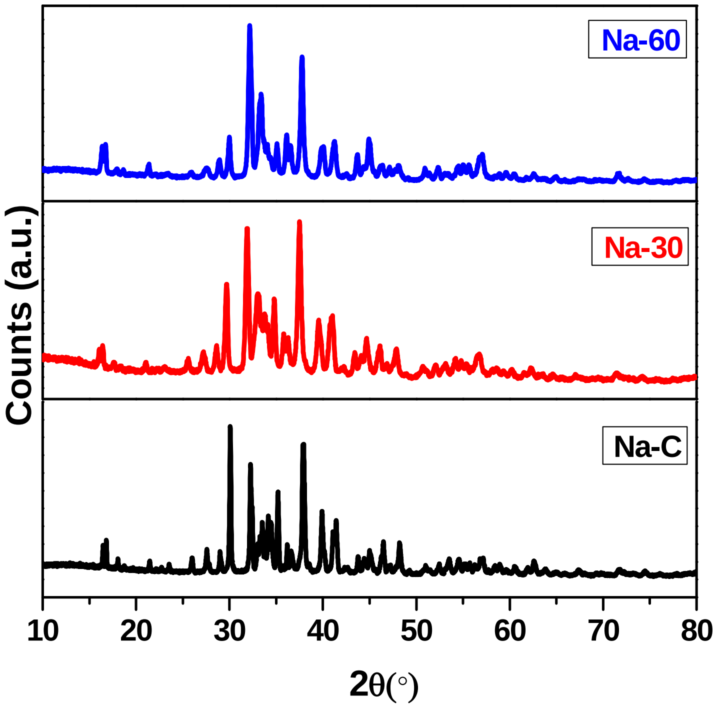

Figure 6. PXRD pattern of bulk and nanoparticles of Na_2CO_3.

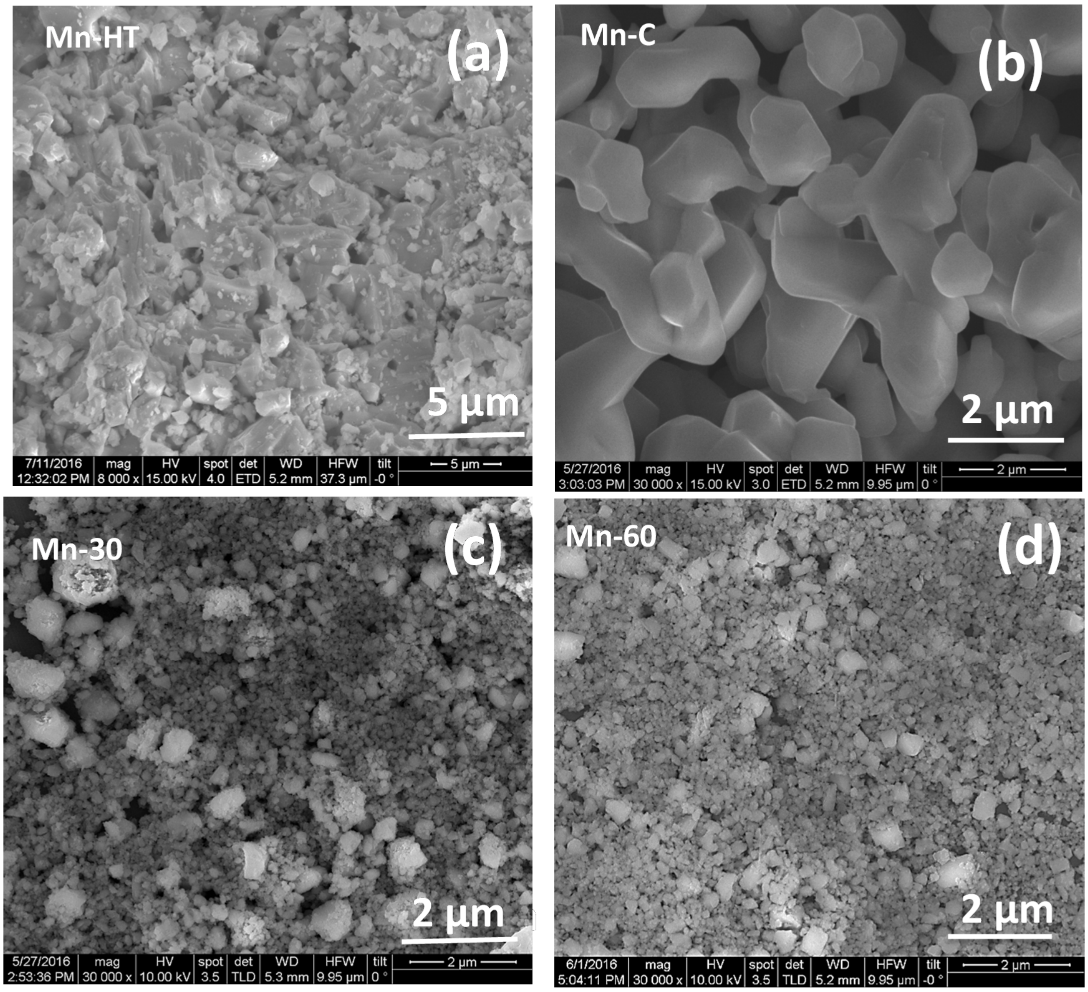

Figure 7. FESEM images of (a) high temperature annealed Mn_3O_4 (Mn-HT), (b) commercial Mn_3O_4 (Mn-C), (c) 30 mins ball milled Mn_3O_4 (Mn-30), (d) 60 mins ball milled Mn_3O_4 (Mn-60).

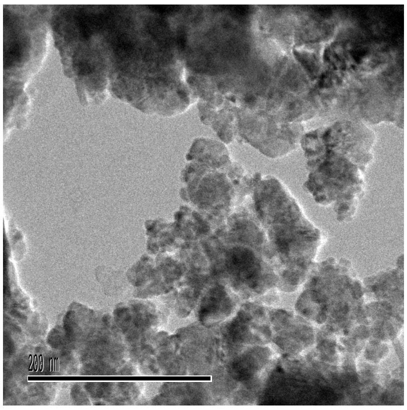

Figure 8. Transmission electron microscope (TEM) image of 60 mins ball milled Mn_3O_4 (scale bar is of 200 nm).

Table 1. Physiochemical properties of Mn_3O_4 and Na_2CO_3 samples.

Materials	**Abbreviations**	**Crystallite size** [b]	**Particle size** [c]	**BET surface area (m^2/g)**	**% of CO_2 evolved within 600°C** [d]	**H_2 yield (%)** [e] **@850°C @80min**
Mn_3O_4-commercial	**Mn-C** [a]	43	1-2 µm	~1	54.1	35
Mn_3O_4-high temp annealed	**Mn-HT**[a]	75	>3 µm	<0.5	22.4	<15
Mn_3O_4-ball mill 30 min	**Mn-30** [a]	27	100-500 nm	13	74.4	---------
Mn_3O_4-ball mill 60 min	**Mn-60** [a]	15	100-250 nm	15	81	---------
Na_2CO_3-commercial	**Na-C**	48	~5 µm	~1	---------	---------
Na_2CO_3-ball mill 30 min	**Na-30**	34	250nm-2 µm	5	---------	---------
Na_2CO_3-ball mill 60 min	**Na-60**	30	250nm-1 µm	6	---------	---------
Mn_3O_4& Na_2CO_3-ball mill 30 min	**MnNa-30**	---------	---------	---------	96.4	69
Mn_3O_4& Na_2CO_3-ball mill 60 min	**MnNa-60**	---------	---------	---------	97.54	75

[a] Samples are grinded with commercial Na_2CO_3.

[b] Calculated using Debye-Scherrer equation.

[c] Obtained from FESEM analysis.

[d] $\%\text{ of }CO_2\text{ evolved} = \frac{\text{experimentally measured} \times 100}{\text{theoretically calculated}}$.

[e] Measured over the H_2 collected at 850°C for 80 mins.

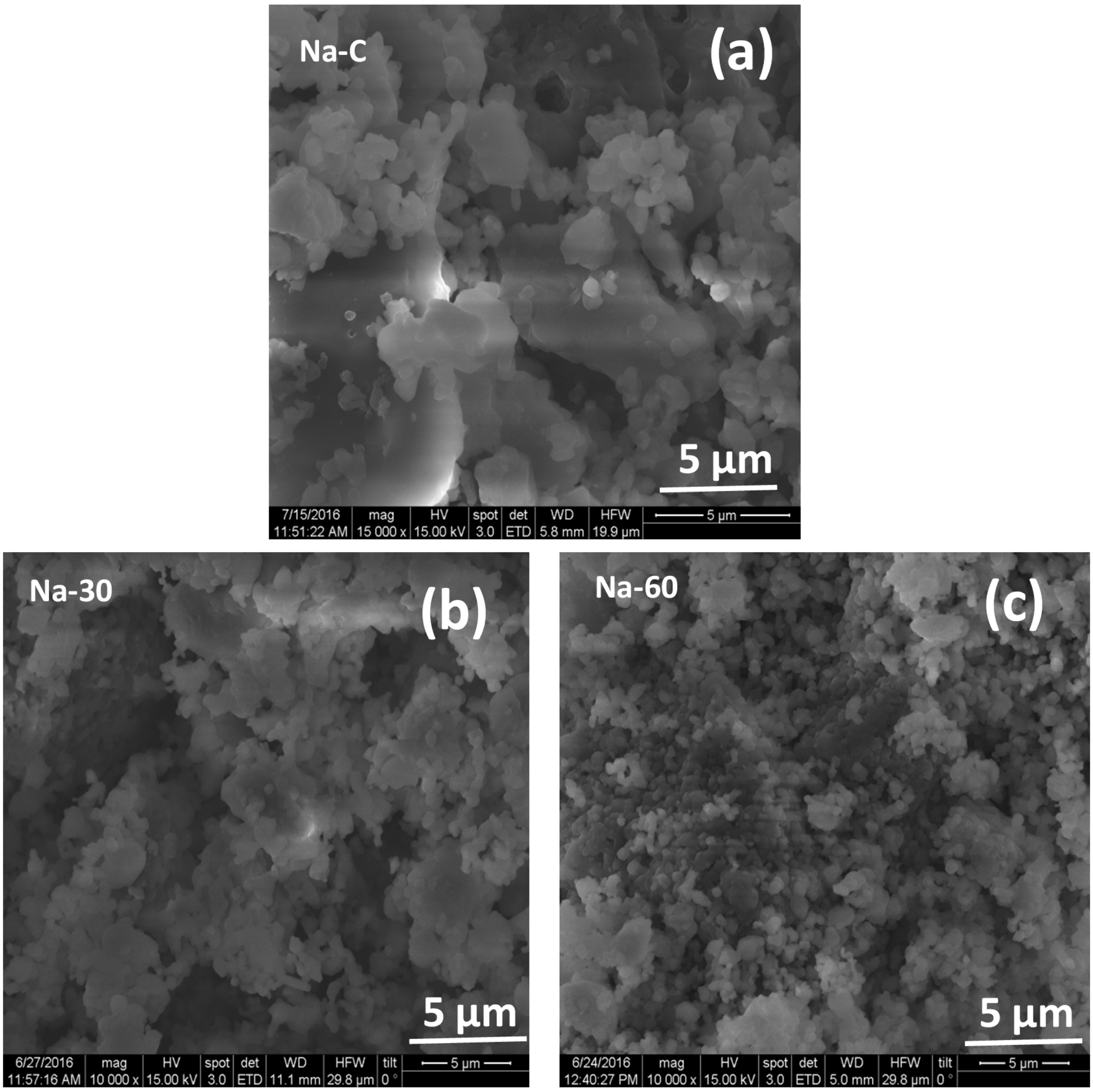

Figure 9. FESEM images of (a) commercial Na_2CO_3 (Na-C),(b) 30 mins ball milled Na_2CO_3 (Na-30) and (c) 60 mins ball milled Na_2CO_3 (Na-60).

In **Figure 10**, we present thermogravimetric (TGA) curves of intimate mixtures of Mn_3O_4 and Na_2CO_3 (in 2:3 ratio) showing weight loss during step 1, involving the loss of 2 moles of CO_2 (g). When smaller particles of Mn_3O_4 (Mn-30/Mn-60) are used along with bulk Na_2CO_3 (Figure 10), the decomposition reaction occurs at a considerably lower temperature compared to the commercial Mn_3O_4. Thus, Mn-60 in Figure 8a shows the major weight loss around 600°C, which is nearly 100°C lower than with the commercial sample (Mn-C). The decrease in temperature is even larger (≥200°C) compared to that with Mn_3O_4 sintered at 1100°C (Mn-HT).

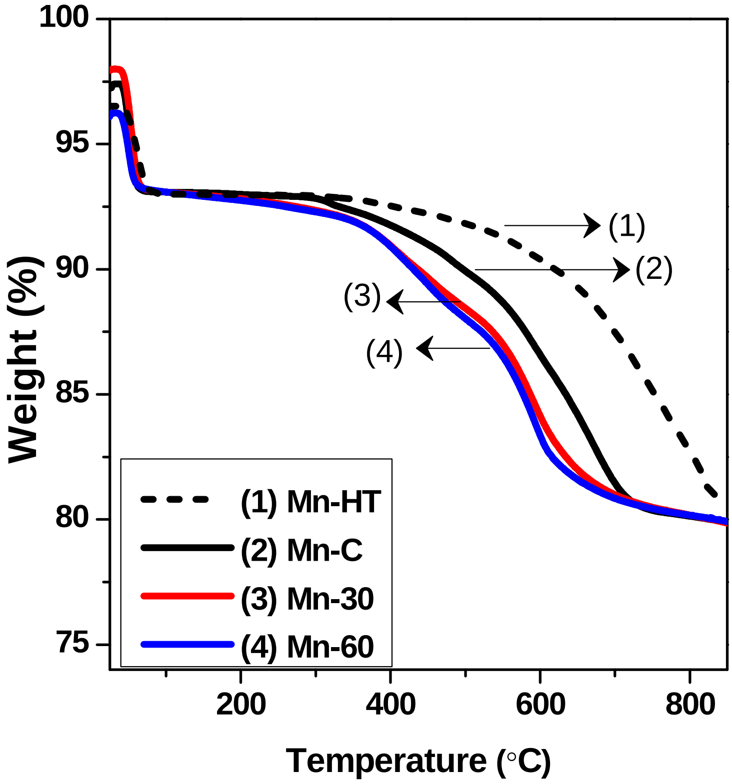

Figure 10. Thermogravimetric weight loss vs reaction temperature due to CO_2 evolution (step 1) for mixture of ball-milled Mn_3O_4 with bulk Na_2CO_3 (designated as Mn). 30 and 60 represent the ball milling time in minute. In both the plots the black curve and the dashed curve represent the reaction of bulk Na_2CO_3 with commercial(C) and sintered (HT) Mn_3O_4 respectively.

When nanoparticles of both Mn_3O_4 and Na_2CO_3 were used (**Figure 11**), the weight loss occurs more sharply well below 600°C, releasing ~100% of CO_2. The use of nanoparticles of Na_2CO_3 alone has negligible effect (**Figure 12**) but the mixture with Mn_3O_4 nanoparticles, we observe good activity in step 1. Interestingly while Mn-30 evolves only 60% (7 weight % in TGA) of expected CO_2 at 600°C, use of MnNa-30 releases almost 100% at that temperature (Figure 11). We thus surmise that it is more important to have nanoparticles of Mn_3O_4 to enhance the reactivity in step 1 although the best results are obtained with the use of both nanoparticles together.

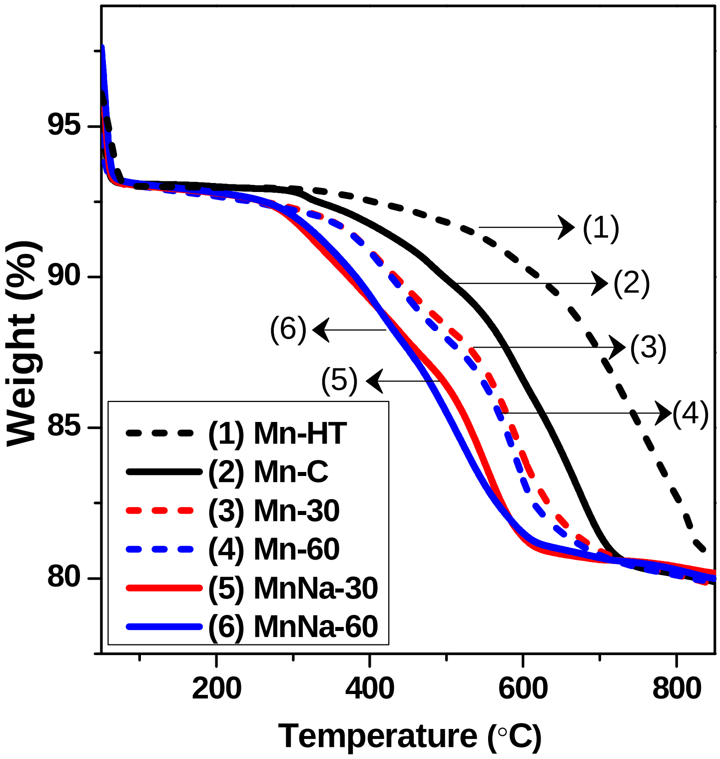

Figure 11. Thermogravimetric weight loss vs reaction temperature due to CO_2 evolution (step 1) for mixture of ball-milled Mn_3O_4 with bulk Na_2CO_3 (designated as Mn) and ball-milled Na_2CO_3 (designated as MnNa). 30 and 60 represent the ball milling time in minute. In both the plots the black curve and the dashed curve represent the reaction of bulk Na_2CO_3 with commercial(C) and sintered (HT) Mn_3O_4 respectively.

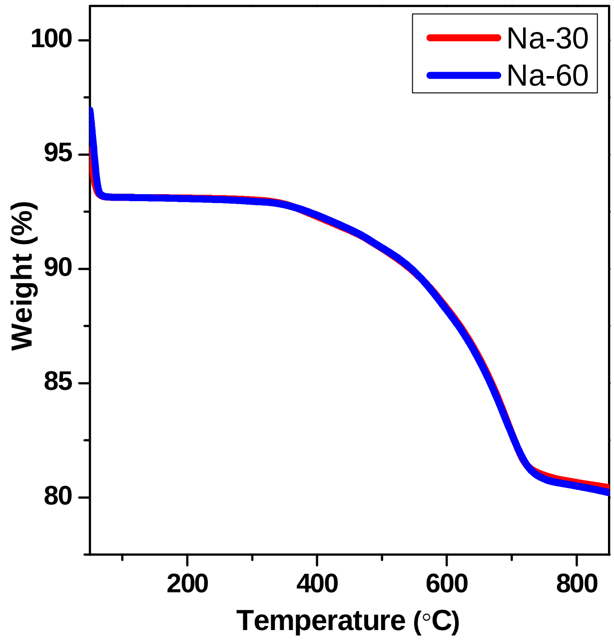

Figure 12. Thermogravimetric weight loss vs reaction temperature due to CO_2 evolution (step 1) for Mn_3O_4 (Mn-C) mixed with ball-milled Na_2CO_3. 30 and 60 represent the ball milling time in minutes.

As shown in **Figure 13**, the mixing of commercial Na_2CO_3 (Na-C) with Mn-C shows a phase separation while the mixing of Mn_3O_4 nanoparticles (Mn-60) found to be more homogenous with Na_2CO_3 nanoparticles (Na-60), results in enhancement of reactive interfaces. More inhomogeneous mixing of Na-C has been observed with Mn-HT. EDAX shows the uniform distribution Mn and Na throughout the nanoparticle samples even for the spot size of 500 nm (**Figure 14**). The nanoparticle systems promotes the reactants to be placed in closer proximity as well as shorter diffusion length makes the kinetics typically faster and results in the rapid CO_2 evolution of all MnNa systems within 600°C.[22, 42]

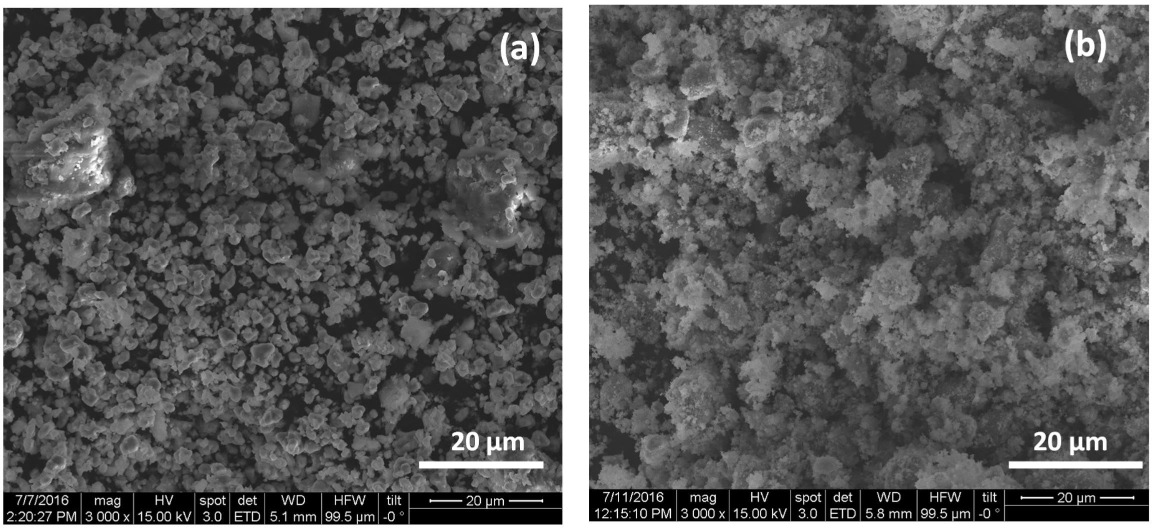

Figure 13. FESEM images of mixture of (a) commercial Mn_3O_4 with commercial Na_2CO_3 and (b) nanoparticles of both Mn_3O_4 and Na_2CO_3 (60 mins ball milled, MnNa-60). The mixture of commercial Na-C with Mn-C shows a phase separation while the nanoparticles result in more homogenous mixture due to their smaller particle sizes.

The performance of 90 minutes ball milled sample has found to detoriate can be due to the decrease in crystallinity and due to the presence of amorphous Mn_2O_3 (As 120 mins milled Mn_3O_4 shows clear reflections in PXRD of Mn_2O_3). By recording X-ray diffraction patterns, we have ensured after the weight loss due to evolution of CO_2, MnO and α-$NaMnO_2$ and α-$Na_{0.7}MnO_{2.14}$ are formed with complete disappearance of Mn_3O_4 and Na_2CO_3 (**Figure 15**).[43]

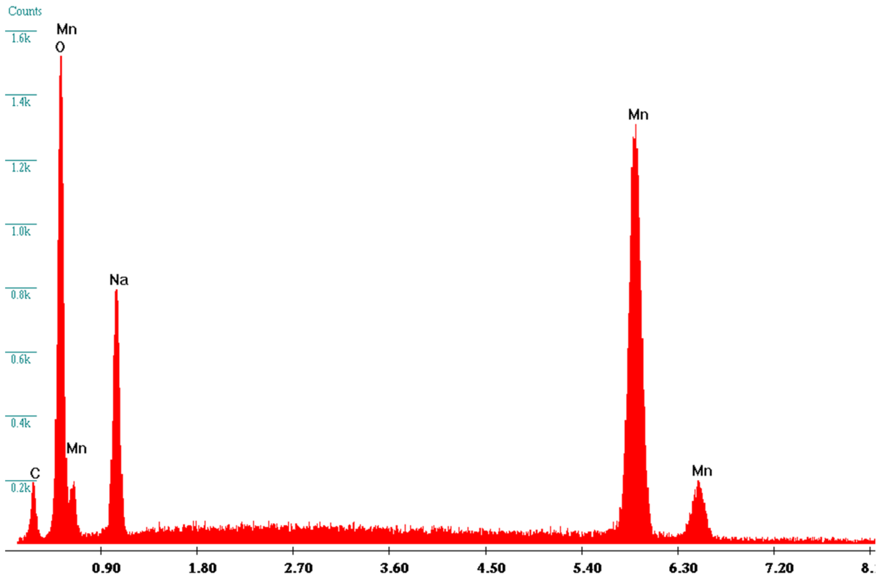

Figure 14. EDAX shows the uniform distribution Mn and Na throughout the nanoparticle samples of MnNa-60 (recorded at spot size of 500 nm). X and Y axis are Energy in KeV and counts respectively.

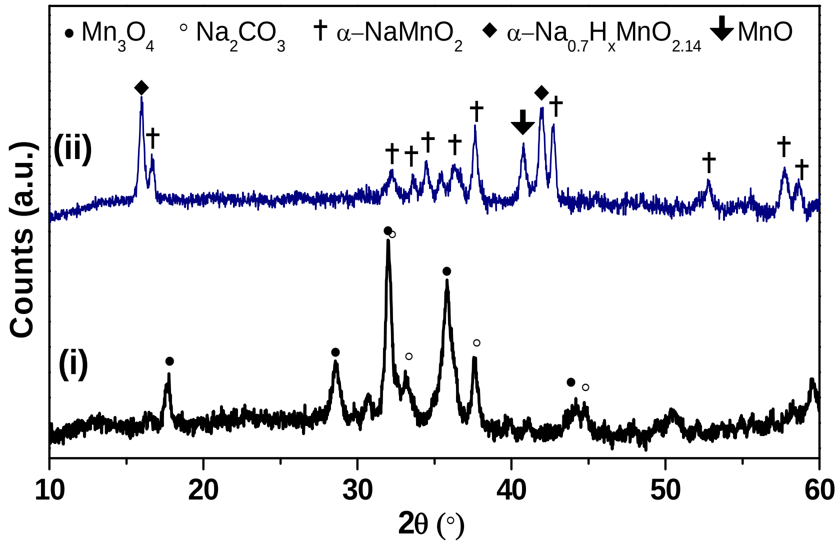

Figure 15. Powder X-ray diffraction (PXRD) patterns of MnNa-60 before (i) and after (ii) step 1. Peaks shows the presence of (i) nanoparticles of Mn_3O_4+Na_2CO_3 and (ii) MnO, α-$NaMnO_2$ and α-$Na_{0.7}MnO_{2.14}$. α-$Na_{0.7}MnO_{2.14}$ forms due to exposure of atmospheric moisture.

The water vapor flow rate passed through a mixture of commercial Mn_3O_4 and Na_2CO_3 (steps 1 and 2 together) was found to play an important role to vary the rate and amount of H_2 production as shown in **Figure 16.** The vapor flow rate was varied by boiling water at different temperatures. Introducing of the vapor corresponding to H_2O (l) at low flow rate (0.12 ml/min) shows H_2 production after 30 mins with a slow increase to reach the plateau while the higher flow rate (1.3 ml/min) shows the H_2 production as soon as H_2O enters. With increasing the H_2O flow rate the H_2 peak reaches its maximum at earliest (Figure 16b) along with an increase in the rate of H_2 production. The highest H_2 production rate was observed for 1.3 ml/min of H_2O flow rate which is 2 and 3 times higher than 0.5 ml/min and 0.2 ml/min of H_2O flow rates respectively. Besides, the total amount of H_2 produced for 1.3 ml/min of H_2O flow rate is 1.4 and 2.6 times higher than 0.5 ml/min and 0.2 ml/min of H_2O flow rates respectively (considering first 60 mins reaction). A large amount of water shifts the equilibrium toward the oxidation of Mn_3O_4 with rapid release of H_2(g). It is true that heating excess of H_2O cost high energy input but on the other side rapid H_2 release will save the energy in terms of heating the samples for longer time and decrease the deactivation of sample due to sintering. All further experiments are carried out at 1.3 ml/min of H_2O(l) flow rate.

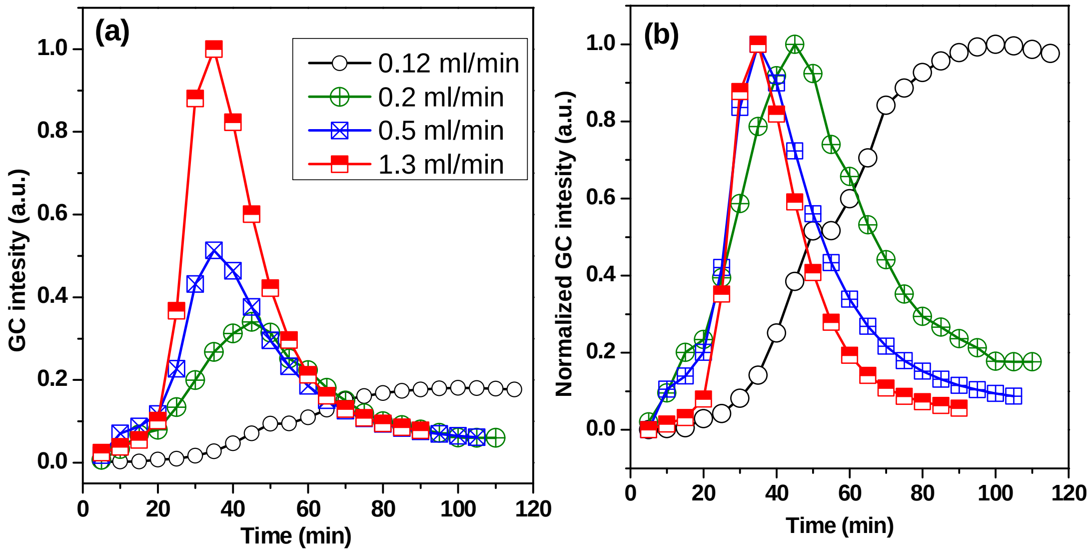

Figure 16. (a) Relative GC intensity to show the effect of H_2O flow rate on the production of H_2 during the oxidation of Mn_3O_4 to α-$NaMnO_2$ at 850°C (Steps 1 and 2 together). Both Mn_3O_4 and Na_2CO_3 are commercial bulk sample. (b) GC intensity normalized with respect to peak position.

We have examined H_2 evolution by step 2 by passing H_2O vapour over the bulk as well as the nanoparticle samples of Mn_3O_4 + Na_2CO_3 mixtures at 850°C (**Figure 17**). We see that the H_2 evolution activity is significantly enhanced by the use of nanoparticles. In the case of bulk samples, H_2 production is observed 15 min after the H_2O vapour enters showing a maximum value at around 35 mins. In contrast, the ball milled samples show a high rate of H_2 production soon after the entry of H_2O, at an elevated speed even after reaching the maximum, resulting in faster completion of the reaction. The maximum rate of H_2 evolution achieved using MnNa-60 is 0.8 ml/min/g, is notably 1.5 times higher than that achieved with Mn-C. With MnNa-60 we obtain the 75% of the expected H_2 within 80 min which is much higher (>2 times) than that evolved by Mn-C (35%) during the same period, although there is an extended tail of H_2 evolution in all the samples (Table 1, Figure 17). H_2 evolution rate with the sintered Mn_3O_4 samples (Mn-HT) is very much lower and completes after 6 hrs.

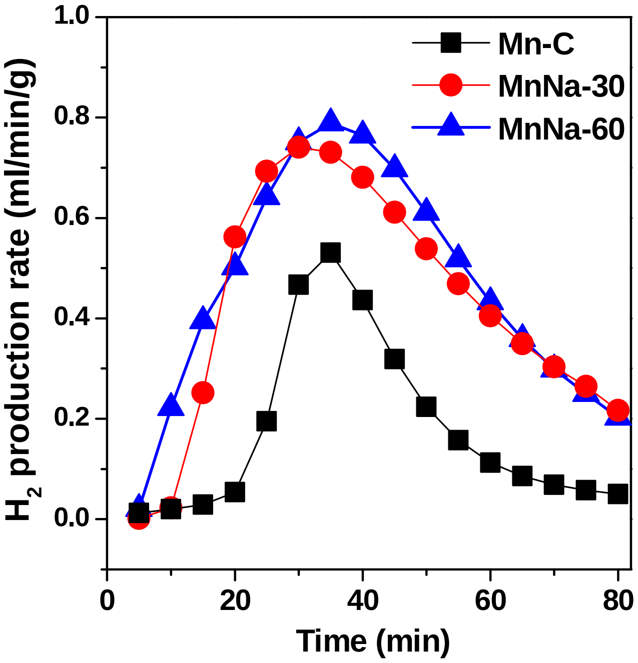

Figure 17. H_2 evolution plots of reaction of Mn_3O_4 with Na_2CO_3 (steps 1 and 2) at 850 °C. Both ball-milled Mn_3O_4 and Na_2CO_3 designated as MnNa. 30/60 represents the ball milling time in minutes.

Clearly, the high rate of H_2 evolution by nanoparticles is due to the higher surface area.[22, 23] (Table 1). The performance degraded with the use of 90 min ball milled samples

(MnNa-90) can be due to the decrease in crystallinity which hints that the effect of surface area saturates after some threshold value and crystalline size start to contribute more on the reaction rate. PXRD confirms the presence of α-$NaMnO_2$ along with the hydrated product α-$Na_{0.7}MnO_{2.14}$ after H_2 evolution with complete disappearance of MnO (**Figure 18**).[43, 44] The effect of surface area on the H_2 evolution rate was also checked independently by carrying out step 2 with a mixture of MnO with Na_2CO_3. The MnO nanoparticles are prepared by ball milling and reacted with H_2O in presence of Na_2CO_3 (step 2). Here again the MnO nanoparticles were found to evolve H_2 much faster rate (**Figure 19**) than the bulk samples.

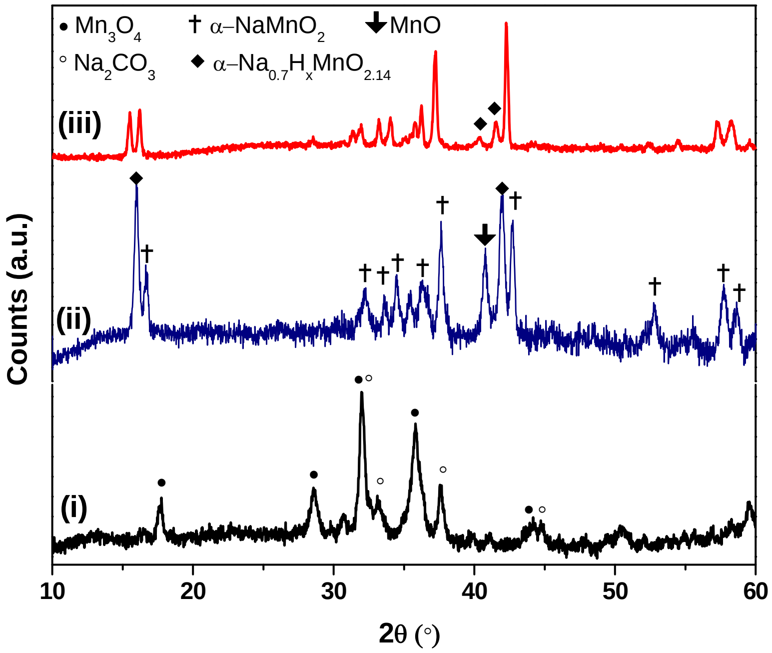

Figure 18. PXRD patterns to identify the solid forms after H_2 evolution of MnNa-60 at 850°C (steps 1 and 2 together). (iii) After H_2 evolution α-$NaMnO_2$ and α-$Na_{0.7}MnO_{2.14}$ formed with the disappearance of MnO peaks. For comparison PXRD patterns of solids (i) before and (ii) after step 1 is given.

Davis and co-workers[1] did not observe any H_2 production below 850°C with the use of a mixture of bulk Mn_3O_4 and Na_2CO_3. With the use of mixture of nanoparticles, we found H_2 evolution even at 750 °C, although the rate of evolution is slower in comparison to that at 850 °C (**Figure 20**). The H_2 yield by MnNa60 at 750 °C is ~ 40% (over 80 mins)

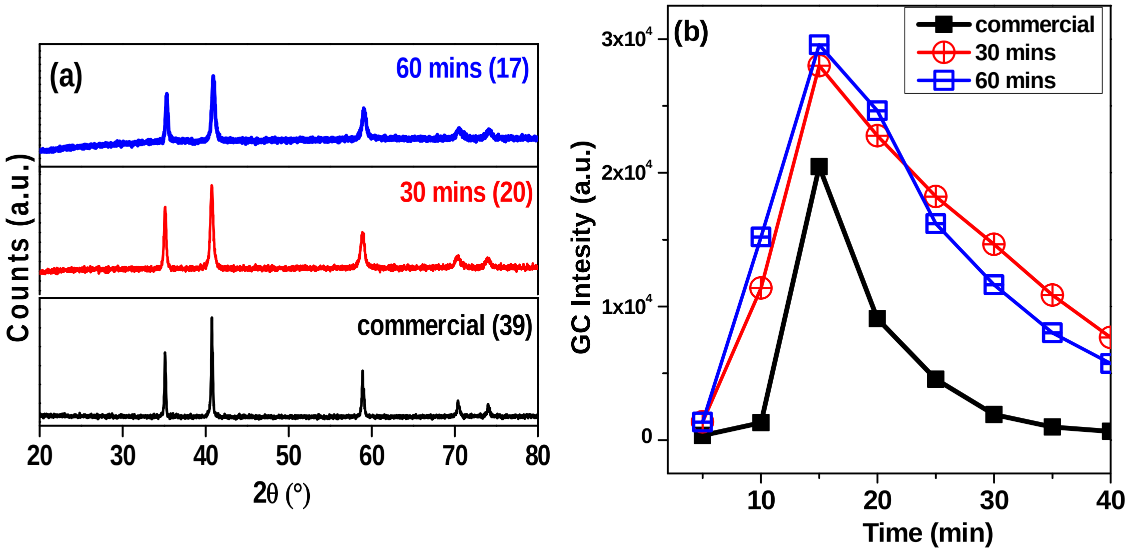

Figure 19. (a) PXRD reflections of bulk and nanoparticles (ball milled for 30 and 60 mins) of MnO. The crystal sizes are given in the parenthesis after each legend. (b) The H_2 evolution profile of reaction of MnO with Na_2CO_3 in presence of H_2O (step 2) at 850°C.

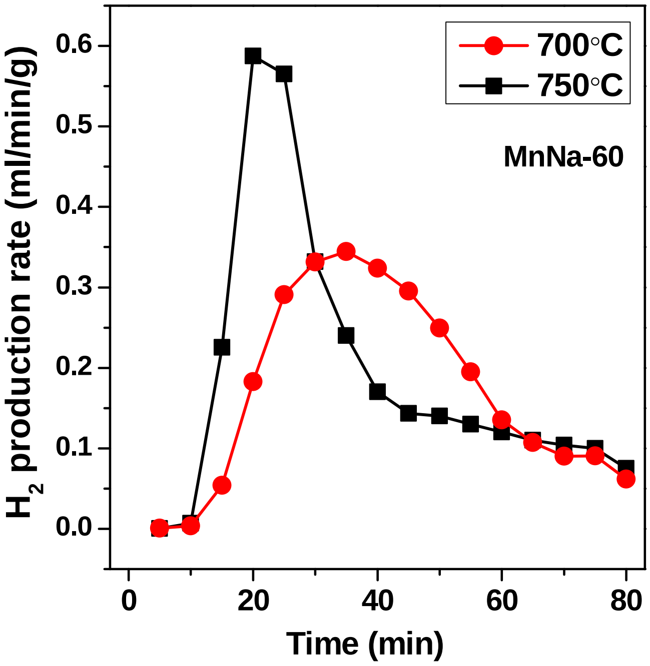

Figure 20. H_2 evolution plots of reaction of Mn_3O_4 with Na_2CO_3 (steps 1 and 2) at 750 °C as well as 700 °C. 60 minutes ball milled sample has been used in this reaction (MnNa60).

with an extended tail to show further continuation of H_2 evolution over a period of time. Interestingly we found reasonable H_2 evolution even at 700°C by use of nanoparticles (Figure 20). High temperature annealed samples of Mn_3O_4 did not show any H_2 evolution at 750° or 700°C.

In step 2, the in-situ formed MnO actually reacts with H_2O in the presence of Na_2CO_3 to produce H_2. The use of nanoparticles brings down the formation temperature of MnO to 600°C and promotes reaction with H_2O at lower temperatures.

Table 2. Summary of CO_2 assisted hydrolysis step (step 3).

Serial no.	**Weight % of sample** [a, b]	**Time (hr)**	**Temperature (°C)**	**PXRD** [c]	**~% Na recovery** [d]
1 (Ref. conditions)	0.5	3	100	☑	97.5
2	0.5	3	**50**	☑	97
3	0.5	3	**25**	☒	-----
4	0.5	**1**	50	☑	97
5	0.5	**0.25**	50	☒	-----
6	**2**	1	50	☑	96.6

[a] CO_2 buubling rate was 10 ml/min, [b] Red mark is to specify the changes in condition during each step than reference conditions, [c] '☑' indicates the detection of PXRD patterns after hydrolysis. '☒' indicates the formation of amorphous phase after hydrolysis, [d] calculated from Na/Mn ratio obtained using EDAX and ICP analysis.

As α-$NaMnO_2$ cannot reduced thermally below 1000°C,[21] hydrolysis through intercalating water in between the adjacent sheets is suggested as the feasible route for extracting Na^+ with the formation of birnessite, complete extraction of Na^+ becoming possible under acidic conditions, due to the formation of H^+-birnessite. Davis and co-workers[1] achieved this conversion in the acidic environment created with continuous bubbling of CO_2 in an aqueous suspension of α-$NaMnO_2$ at 80°C for 3 hr. We have optimized the CO_2 assisted hydrolysis conditions in order to reduce the temperature and time further. The main results are summarized in **Table 2**. The PXRD reflection confirms the formation of protonic birnessite as its characteristic diffraction peak appears at 12.7° with the disappearance of α-$NaMnO_2$ peak at 16.7° due to the expansion of interlayer spacing having quantified the content of extracted Na in birnessite with EDAX and ICP analysis (**Figure 21**).

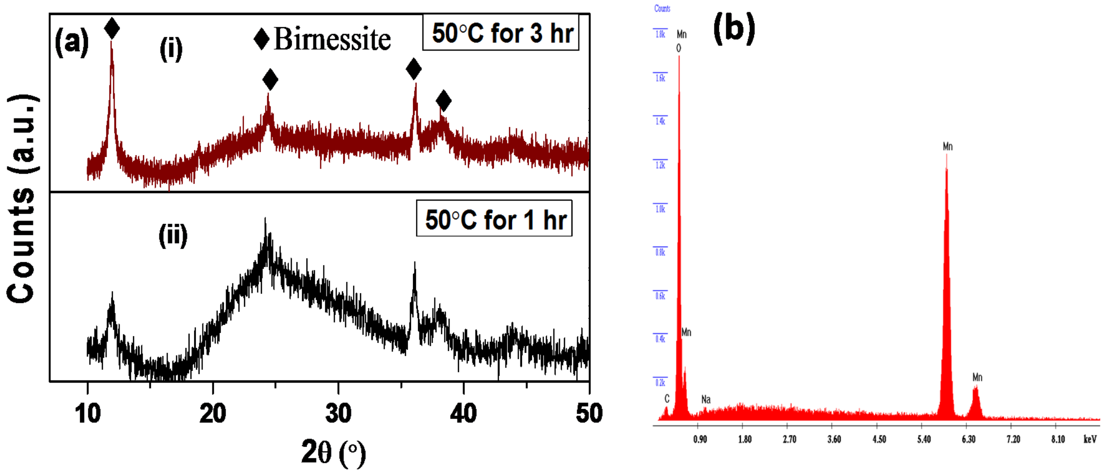

Figure 21. (a) PXRD patterns after CO_2 assisted hydrolysis of α-$NaMnO_2$ at 50°C for 3 hr (i) and 1 hr (ii) confirms the formation of protonic birnessite phase. (b) EDAX image of the product obtained after CO_2 assisted hydrolysis at 50°C for 1 hr. X and Y axis are Energy in KeV and counts respectively.

Initially α-$NaMnO_2$ (0.5 wt%) was hydrolysed at three different temperature (25°, 50° and 100°C) for 3 hrs (bubbling rate of CO_2 was 10 ml/min). Efficiency of hydrolysis at 50°C was found to be similar with 100°C. For hydrolysis at 25°C the characteristics peaks corresponding α-$NaMnO_2$ disappears but the peaks of H-birnessite is not clearly distinguishable from background noise implying the formation of amorphous phase. In the next step the hydrolysis time was varied gradually from 3hr to 1 hr and then to 0.5 hr at 50°C. CO_2 assisted hydrolysis can extract Na^+ even within 1 hr. Instead of varying the water content we have increased the sample weight% (w/v) upto 2. As MnNa-60 gives the best activity, after H_2 evolution it is subjected to hydrolysis and shows extraction of ~96% Na within 1 hr at 50°C.

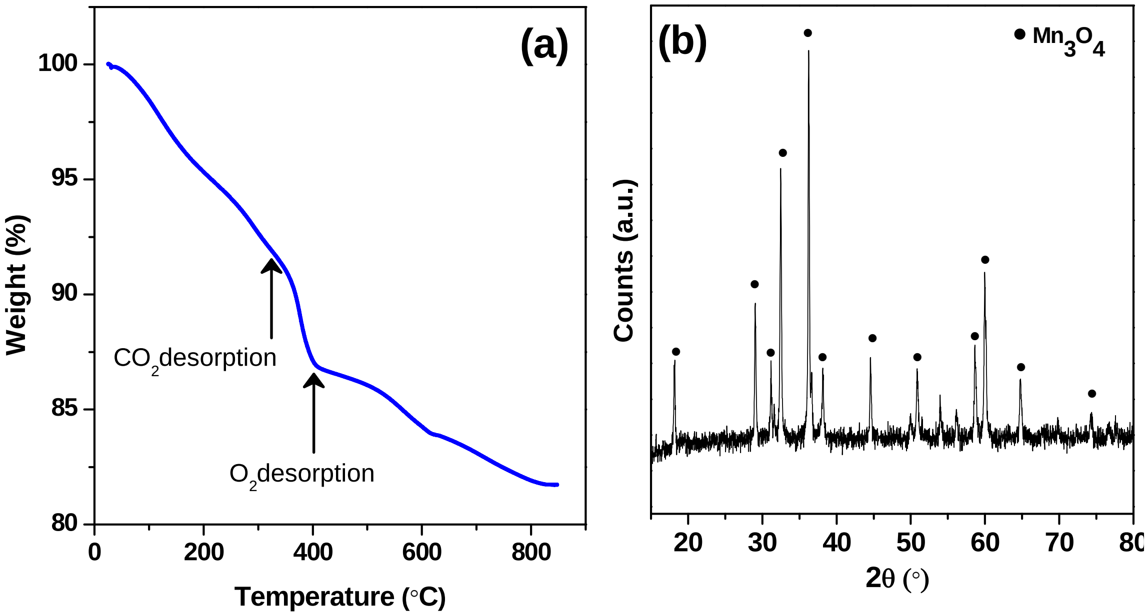

Figure 22. (a) Thermogravimetric plots to show the thermal reduction of Na^+ extracted $NaMnO_2$ (step 4) and (b) PXRD of thermally reduced (~820°C, under Ar) Na^+ extracted α-$NaMnO_2$ confirms the formation of Mn_3O_4 in pure phase (Step 4).

The hydrolysed products are subjected to thermal reduction upto 850°C under Ar to recover back Mn_3O_4. We observe the weight loss in three stages. The initial weight loss below 300°C is mainly due to the dehydration of birnessite and decomposition of surface formed bicarbonates.[23] The sharp weight loss in between 300-400°C is due to the release of CO_2 from the decomposition of $MnCO_3$. We observe a continuous weight loss after 400°C, extending with a long tail upto ~800°C, resulting in the formation of Mn_3O_4 due to desorption of O_2. The O_2 release is mainly due to Mn_2O_3 to Mn_3O_4 type conversion.[1, 23, 39] Complete reduction to Mn_3O_4 is possible at ~810°C, although within ~750°C the release of >88% of the expected O_2 is observed (**Figure 22a**). The amount of O_2 was also confirmed by gas chromatography and the formation of the pure Mn_3O_4 was detected (Figure 22b) by PXRD.

2.5. Conclusions

In conclusion the uses of nanoparticles are found to be useful to bring down the operation temperature with enhancing the H_2 evolution kinetics for Mn_3O_4-Na_2CO_3 based thermochemical cycle. The particle sizes of Mn_3O_4 matters the most although the best results are obtained using the nanoparticles of Mn_3O_4 and Na_2CO_3 together. The high surface areas along with the improving solid-solid contacts are the reason behind the extraordinary properties showed by nanoparticles. The temperature of solid state reaction between Mn_3O_4 and Na_2CO_3 decreases down by ~200°C accompanied by an early release of CO_2 with the use of nanoparticles of Mn_3O_4 and Na_2CO_3. Two-fold increase in H_2 evolution kinetics was observed. Our findings include the observation of H_2 release even at 750°C in presence of nanoparticles which is reported not to happen for bulk mixtures. Further recycling of the material has been done with CO_2 assisted hydrolysis followed by thermal reduction. Investigation of various hydrolysis conditions led us to conclude that even at 50°C within 1 hr successful Na^+-extraction is possible. The present study demonstrates how the thermochemical cycle involving Mn(II)/Mn(III) oxides can be operated at a lower temperature than 850°C as reported. The decrease in the temperature can be at least 100°C. The cycle can be repeated by ball milling the Mn_3O_4 obtained as the product at the end of the cycle.

2.6. References

1 B. Xu, Y. Bhawe and M. E. Davis, *Proc. Natl. Acad. Sci. USA,*, 2012, **109**, 9260-9264.

2 B. Meredig and C. Wolverton, *Phys. Rev. B*, 2009, **80**, 245119.

3 G. E. Beghi, *Int. J. Hydrogen Energy*, 1986, **11**, 761-771.

4 J. E. Funk, *Int. J. Hydrogen Energy*, 1976, **1**, 33-43.

5 J. E. Funk and R. M. Reinstrom, *Ind. Eng. Chem. Process Des. Dev.* , 1966, **5**, 336-342.

6 W. C. Chueh, C. Falter, M. Abbott, D. Scipio, P. Furler, S. M. Haile and A. Steinfeld, *Science*, 2010, **330**, 1797-1801.

7 A. Steinfeld and A. W. Weimer, *Opt. express*, 2010, **18**, A100-A111.

8 K. Onuki, S. Shimizu, H. Nakajima, S. Fujita, Y. Ikezoe, S. Sato and S. Machi, in *Hydrogen energy progress 5678*, 1990.

9 S. Goldstein, J.-M. Borgard and X. Vitart, *Int. J. Hydrogen Energy*, 2005, **30**, 619-626.

10 S. Kasahara, S. Kubo, R. Hino, K. Onuki, M. Nomura and S.I. Nakao, *Int. J. Hydrogen Energy*, 2007, **32**, 489-496.

11 L. C. Brown, G. E. Besenbruch, K. R. Schultz, A. C. Marshall, S. K. Showalter, P. S. Pickard and J. F. Funk, Proc. Int Congress on Advanced Nuclear Power Plants, 2002.

12 M. F. Orhan, I. Dincer and M. A. Rosen, *Chem. Eng. J.*, 2009, **155**, 132-137.

13 M. Sturzenegger, J. Ganz, P. Nuesch and T. Schelling, *J. Phys IV France*, 1999, **9**, Pr3-331-Pr333-335.

14 T. Kodama and N. Gokon, *Chem. Rev.*, 2007, **107**, 4048-4077.

15 M. Roeb, N. Gathmann, M. Neises, C. Sattler and R. Pitz-Paal, *Int. J. Energy Res.*, 2009, **33**, 893-902.

16 M. D. Allendorf, R. B. Diver, J. E. Miller and N. P. Siegel, ASME International Solar Energy Conference, 2006.

17 T. Kodama, *Prog. Energy Combust. Sci.*, 2003, **29**, 567-597.

18 E. Alonso, C. Hutter, M. Romero, A. Steinfeld and J. Gonzalez-Aguilar, *Energy & Fuels*, 2013, **27**, 4884-4890.

19 M. Lundberg, *Int. J. Hydrogen Energy*, 1993, **18**, 369-376.

20 M. Sturzenegger and P. Nuesch, *Energy*, 1999, **24**, 959-970.

21 P. B. Kreider, H. H. Funke, K. Cuche, M. Schmidt, A. Steinfeld and A. W. Weimer, *Int. J. Hydrogen Energy*, 2011, **36**, 7028-7037.

22 A. Bayon, A. Victor, D. P. Serrano and J. M. Coronado, *Int. J. Hydrogen Energy*, 2013, **38**, 13143-13152.

23 A. Bayon, A. Victor, J. M. Coronado and D. P. Serrano, *Int. J. Hydrogen Energy*, 2016, **41**, 113-122.

24 Y. Tamaura, A. Steinfeld, P. Kuhn and K. Ehrensberger, *Energy*, 1995, **20**, 325-330.

25 Y. Tamaura, M. Kojima, T. Sano, Y. Ueda, N. Hasegawa and M. Tsuji, *Int. J.Hydrogen Energy*, 1998, **23**, 1185-1191.

26 H. Kaneko, Y. Hosokawa, N. Gokon, N. Kojima, N. Hasegawa, M. Kitamura and Y. Tamaura, *J. Phys. Chem. Solids*, 2001, **62**, 1341-1347.

27 H. Kaneko, Y. Ochiai, K. Shimizu, Y. Hosokawa, N. Gokon and Y. Tamaura, *Solar Energy*, 2002, **72**, 377-383.

28 Y. Tamaura, Y. Ueda, J. Matsunami, N. Hasegawa, M. Nezuka, T. Sano and M. Tsuji, *Solar Energy*, 1999, **65**, 55-57.

29 C. Alvani, M. Bellusci, A. La Barbera, F. Padella, L. Seralessandri and F. Varsano, *J. Sol. Energy Eng.* , 2010, **132**, 031001.

30 C. Alvani, G. Ennas, A. La Barbera, G. Marongiu, F. Padella and F. Varsano, *Int. J. Hydrogen Energy*, 2005, **30**, 1407-1411.

31 C. Alvani, A. La Barbera, G. Ennas, F. Padella and F. Varsano, *Int. J. Hydrogen Energy*, 2006, **31**, 2217-2222.

32 L. Seralessandri, F. Varsano, A. La Barbera and F. Padella, *Scripta Mater.*, 2006, **55**, 875-877.

33 L. Seralessandri, M. Bellusci, C. Alvani, A. La Barbera, F. Padella and F. Varsano, *J. Solid State Chem.*, 2008, **181**, 1992-1997.

34 L. Seralessandri, M. Bellusci, F. Padella, A. Santini and F. Varsano, *Int. J. Hydrogen Energy*, 2009, **34**, 4546-4550.

35 F. Varsano, M. A. Murmura, B. Brunetti, F. Padella, A. La Barbera, C. Alvani and M. C. Annesini, *Int. J. Hydrogen Energy*, 2014, **39**, 20920-20929.

36 F. Varsano, F. Padella, A. La Barbera and C. Alvani, *Solid State Ionics*, 2011, **187**, 19-26.

37 F. Varsano, F. Padella, C. Alvani, M. Bellusci and A. La Barbera, *Int. J. Hydrogen Energy*, 2012, **37**, 11595-11601.

38 Y. Omomo, T. Sasaki and M. Watanabe, *Solid State Ionics*, 2002, **151**, 243-250.

39 B. Xu, Y. Bhawe and M. E. Davis, *Chem. Mater.*, 2013, **25**, 1564-1571.

40 S. Dey, B. S. Naidu, A. Govindaraj and C. N. R. Rao, *Phys. Chem. Chem. Phys.*, 2015, **17**, 122-125.

41 S. Dey, B. S. Naidu and C. N. R. Rao, *Chem. Eur. J.*, 2015, **21**, 7077-7081.

42 Z. Chen, Q. Jiang, J. Tong, M. Yang, Z. Jiang and C. Li, *Solar Energy*, 2016, **129**, 236-243.

43 P. Le Goff, N. Baffier, S. Bach, J. P. Pereira-Ramos and R. Messina, *Solid State Ionics*, 1993, **61**, 309-315.

44 X. Ma, H. Chen and G. Ceder, *J. Electrochem. Soc.*, 2011, **158**, A1307-A1312.

Part 3

Investigations of carbon quantum dots

Part 3

Investigations of carbon quantum dots[*]

Summary

Doping of a hetero atom such as nitrogen in carbon nanomaterials provides a means to tailor their electronic properties and chemical reactivities. In this article, we present simple methods to synthesize carbon quantum dots with high nitrogen doping content (18-22 %), involving the reaction of glucose in the presence of urea under hydrothermal conditions or by microwave irradiation. The N-doped carbon quantum dots (N-CQDs) show high aqueous solubility and tunable photoluminescence. Interaction of N-CQDs with exfoliated graphene or dimethylaniline quenches the photoluminescence. Interaction of N-doped as well as undoped C-dots with electron-donating tetrathiafulvalene and electron-withdrawing tetracyanoethylene has been examined. The intense blue photoluminescence of carbon quantum quantum dots (CQDs) has been exploited to produce white light by mixing the CQDs with yellow light emitting ZnO nanoparticles or graphene oxide. The N-doped CQDs exhibit superior photocatalytic activity compare to pristine carbon quantum dots.

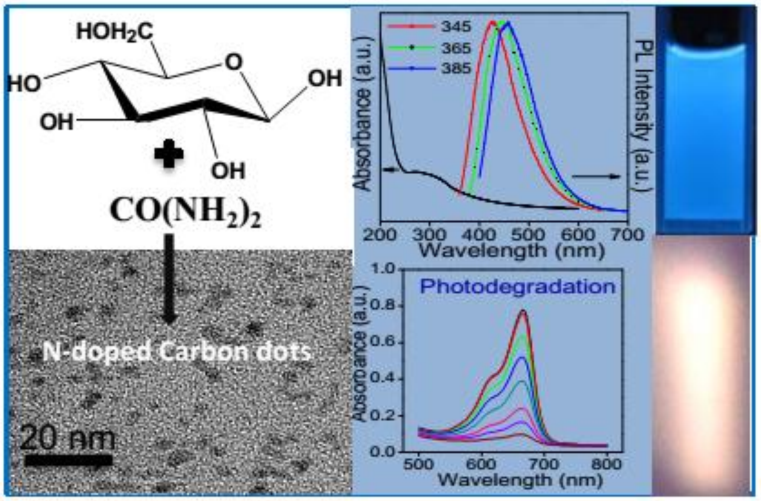

Substitution of heteroatoms in graphene is known to tailor its band gap. Another approach to alter the band gap of graphene is to create zero-dimensional graphene quantum dots (GQDs). Here we present the synthesis and photoluminescence properties of B-doped graphene quantum dots (B-GQDs) for the first time, having prepared the B -GQDs by chemical scissoring of B-doped graphene generated by arc-discharge in gas phase. We compare the photoluminescence properties of B-GQDs with nitrogen-doped GQDs and pristine GQDs. Besides, excitation wavelength independent PL emission, excellent upconversion of PL emission is observed in GQDs as well as B- and N- doped GQDs.

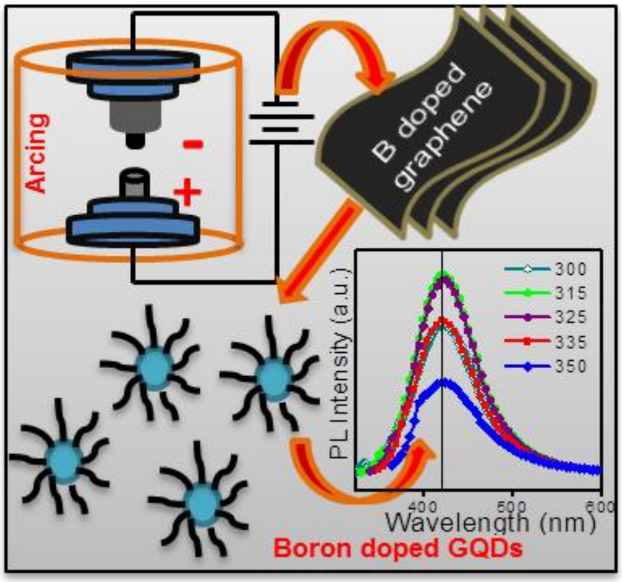

∗Papers based on this part of the thesis have been published in ***J. Mater. Res. (2014) and Chem. Phys. Lett. (2014).***

3.1. Introduction

Among the novel nano carbons of recent origin, carbon dots (CDs) constitute an important class of zero-dimensional nanostructures with a diameter of $\geq$ 10-30 nm. Such small CDs have recently attracted wide attention. They are easy to functionalize, highly soluble, biocompatible, highly resistant to photo bleaching, inexpensive and abundant. They exhibit strong fluorescence as discovered serendipitously by Xu et. al[1] while purifying arc discharge generated carbon nanotubes. Ponomerenko et. al discoverd graphene quantum dots (GQD) in 2008.[2] Within the last few years this material has become an area of considerable research. A few informative reviews are also available addressing those.[3, 4]

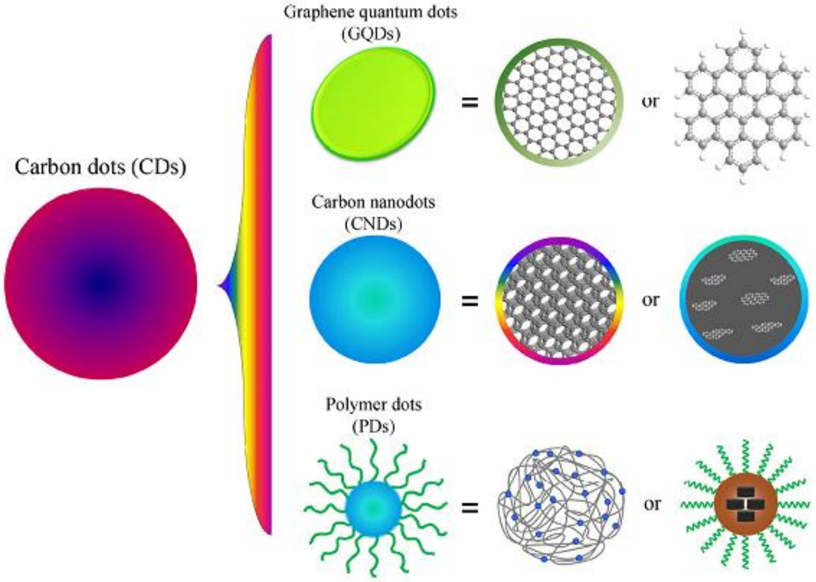

Figure 1. The various types of carbon dots available in literature. The distinction is based on their structure, composition and shape. Reproduced by permission of Springer from Ref.[4].

CDs can be classified into three categories-GQDs, CNDs and PDs (**Figure 1**). GQDs possess one to few layers of graphene with functional groups on the edges. CNDs are divided based on the presence and absence of crystal lattice as carbon particles and carbon quantum dots. PDs one made of a carbon core with polymer functionality or cross-linked monomer.

3.1.1. Synthesis of carbon dots

"Top-down" approach is oxidative-cutting of graphitic sources in presence of strong acid and "Bottom-up" approaches utilizing pyrolysis, carbonization and assembling of organic molecules are the major routes taken up for synthesizing CDs. In **Figure 2** we have listed the important routes adopted for CDs synthesis.

i) Cutting mechanism

Disordered graphene sheets formed after the reduction of graphene oxide (GO), undergoes oxidization induced cutting with conc. H_2SO_4 and HNO_3 to produce smaller CD particles having oxygen containing functional groups. Cracking of GO results due to ordered oxidation and followed by subsequent unzipping **(Figure 3)**. Unzipping is initiated by the formation of epoxy group on the GO surface.[5] Epoxy group attachment convert the planar sp^2 hybridized C into strained sp^3 hybridization which induces the breaking of underneath C-C bond (Figure 3a).[5] It has been proposed that once two epoxy group attaches to opposite site of a hexagon, then there is a strong tendency of co-operative alignment of other epoxy groups along a straight line (Figure 3b),[5, 6] the already formed epoxy chains favor the formation of epoxy pair structure which results in the formation of carbonyl structure (Figure 3b).[6]

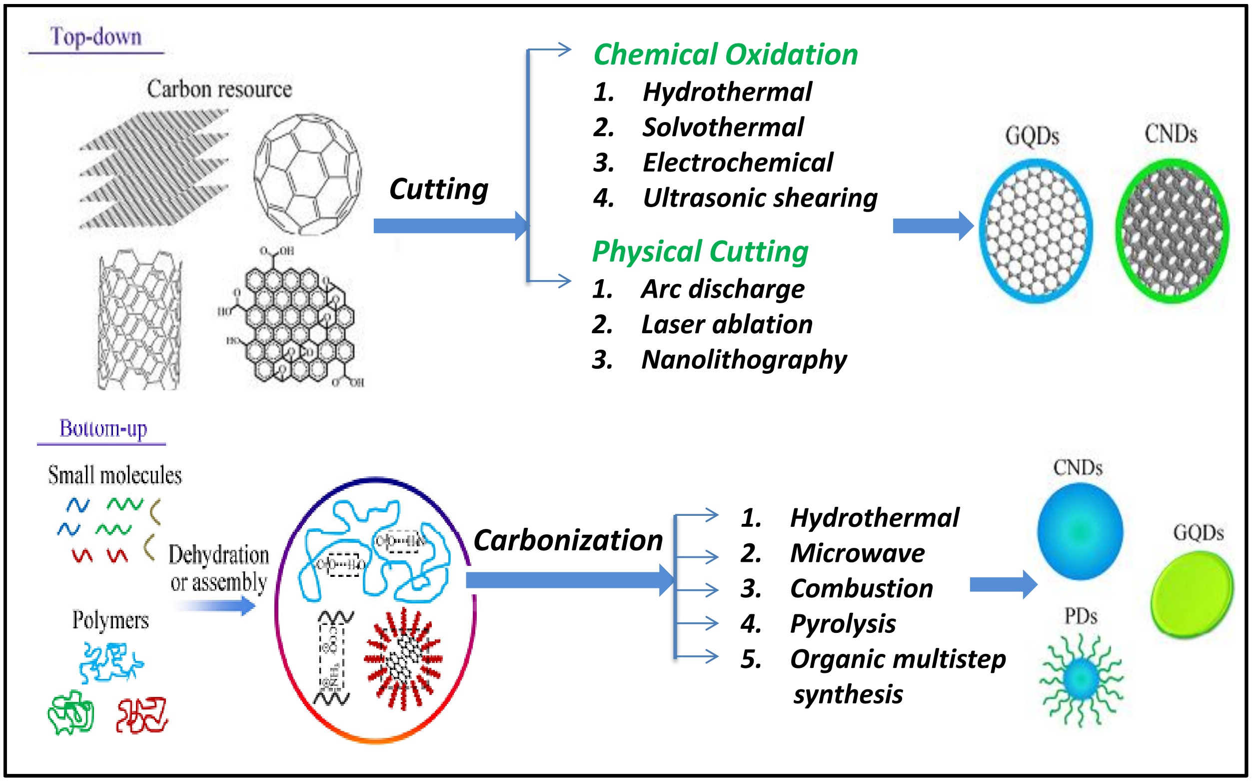

Figure 2. Summary of the synthesis approahes of various carbon dots. Adopted by permission of Springer from Ref.[4].

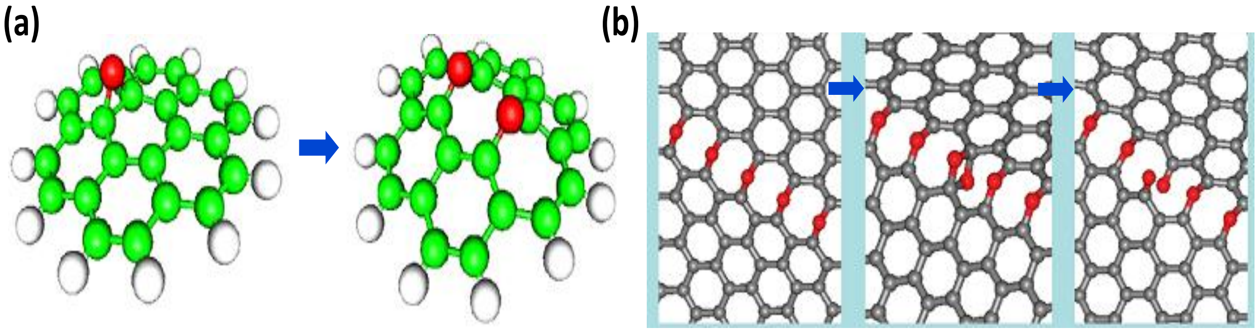

Figure 3. (a) An epoxy group attachment on graphene sheet breaks the underneat C-C bond. The distance of C-C bond increase from ~1.58 Å to ~2.3 Å. Reproduced by permission of Americal Physical Society from Ref.[5] (b) Stepwise oxidation of a graphene sheet with the formation of epoxy chain to epoxy pair to carbonyl group. Reproduced by permission of American Chemical Society from Ref.[6].

ii) Carbonization

Pyrolysis followed by carbonization of organic molecules is one of the easy and simple bottom-up approach to produce highly luminescent CDs. Carbon sources such as citric acid, glucose undergo pyrolysis at around 200°C within 2 hrs with the elimination of water molecules followed by partial carbonization to obtain CDs self-passivized with –OH, -COOH, -C=O groups (**Figure 4**).[7]

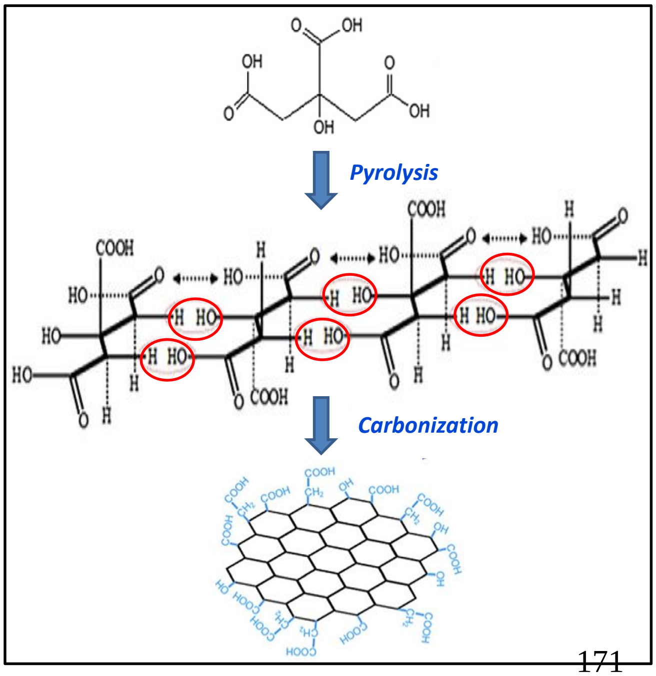

Figure 4. Schematic representation of carbon dot formation mechanism by dehydration followed by carbonization of citric acid. Adapted by permission of Elsevier from Ref.[7].

Hydrolysis and Microwave-assisted techniques have been widely applied for pyrolysis due to its rapid and uniform heating. Heating for longer time results in graphene oxide due to extended carbonization.

3.1.2. Optical properties

CDs show optical absorption in the 230–320 nm region, with an extended tail into the visible range. Peak at ~230 nm and shoulder ~300 nm are ascribed due to the π–π* transition of C–C aromatic bonds and the n–π* transition of C=O bonds respectively. The PL properties of CDs are the most important issue for novel applications purposes. Excitation wavelength-dependent PL emission is common for CDs. Although the exact PL mechanism of CDs/GQDs is not entirely understood, few recent efforts have confirmed the origin of the PL successfully. Size of conjugated π domains (quantum confinement effects), edge effects and surface states are cited as the major reasons behind PL.

Very recent studies have observed the edge effect to be more probable reason behind PL of GQDs. Cutting graphene sheets along different crystallographic directions can result in armchair and/or zigzag edges. Reports shown that zigzag sites are carbene-like having triplet ground state being the most common while the armchair sites are carbyne-like, with a singlet ground state being the most available.[8] Pan et al.[9] have suggested that the blue PL shown hydrothermally cut GQDs attributed to free zigzag sites. They have conducted the pH dependent investigation where under acidic conditions the pH quenches due to the complex formation between the free zigzag sites and H^+. Under basic pH conditions, the PL is restored reversibly. Lin et al.[10] prepared GQDs starting with CNTs or graphite flakes and traced clear zigzag edges by TEM and AFM investigation. The two types of GQDs of different sizes have showed similar emission behavior, which strengthen their observation further.

Different functional groups of CDs have various energy levels which may create multiple emissive traps. In CDs the surface groups are in hybridization with carbon core. The wide range of PL, ranged from blue to red is reported to be induced by different surface functionalities. A higher degree of surface oxidation with –COOH and epoxy groups are reported to emit green wavelength and induces nonradiative recombination whereas –OH functionalities have shown to suppress the non-radiative process. Multiple reports have shown that the emission of CDs have been changed from green to blue by surface reduction.[3,4] So proper surface engineering can transfer GQDs defect-state emission into intrinsic-state emission.

However, for GQDs with a perfect graphene core and lesser surface groups, the band gap due to conjugated π-domains is the intrinsic PL center. Various DFT calculations have shown that with increasing numbers of conjugated benzene rings the band gap decreases in GQDs. [3,4] Peng et al.[11] have prepared GQDs of three different size ranges by varying the reaction temperatures and found PL emission ranging from blue and green to yellow with increasing sizes. Therefore, by varying the size, shape, edge-states the electronic transitions of GQDs, can be modified to produce strong visible PL emissions in a controlled manner.

Up conversion photoluminescence (UCPL) is an attractive optical features showed by CQDs. CQDs could emit strongly in the visible region under excitation by higher wavelength photons. Two different UCPL mechanisms were proposed in literature. Two-photon or multi photo excitation in the near-infrared range (800 nm) is reported to give UCPL of CQDs.[12] Another meachanism suggest UCPL emission could be an anti-Stokes transition as depicted in **Figure 5**. Low-energy photons excite π state electrons to high-energy state LUMO (Lowest unoccupied molecular orbital) and then these electrons fall back to a low-energy σ state, gives high energy UCPL (Figure 5a). Whereas in case of normal PL, the electrons get excited from σ to LUMO and fall back from LUMO to π state (Figure 5b).[13]

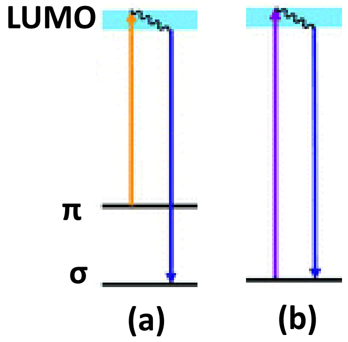

Figure 5. (a) Up conversion and (b) normal photoluminescence mechanism of carbon dots. Adapted by permission of Elsevier from Ref.[13].

3.1.3. N- and B- substitution

Doping of nanocarbons with heteroatoms such as boron and nitrogen allows one to alter their electronic, chemical and surface properties which rouse academic interest and yield results having practical value. For example, N-doped carbon nanotubes show highly effective electro catalytic activities for the ORR. Doping B/N in graphene makes it a semimetal or a semiconductor, with possible applications in the field effect transistors, semiconducting devices,[14] supercapacitors, electrocatalysis and sensing.[3, 4]

Motivated by the exotic properties of B/N doped graphene, carbon nanotubes and graphene nanoribbon, doping of heteroatoms in CDs have been carried out in order to tailor their structural and luminescence properties.[9, 15-27] The first successful synthesis of N-GQDs was reported by Li et.al[19] in 2012 relying on the fact that N atom possess similar atomic size as of C atoms. There are a few repots in the synthesis of N-CQDs synthesized such as hydrothermal method,[20, 27] ultrasonication,[21] and microwave treatment[22] by using an apparent carbon source in the presence of a nitrogen precursor such as ammonia or amines. Pyrolysis of nitrogen containing carbon precursors has also been used to obtain N-CQDs.[23] Nitrogen-doped graphene quantum dots have been synthesized by solution chemistry as well as by electrochemical means.[19] In the course of last four years N-doping is the most widely used method to obtain the exceptional properties of CDs.

There are still very few reports in the successful doping of B in CDs. Boric acid (H_3BO_3) is the most commonly used source of B.[28-31] Other sources are Borax[32], BBr_3[33] and B_2O_3[34]. Pyrolytic decomposition of precursors,[30] electrochemical method[32], combustion flame method,[29] microwave route[35] and oxidative cutting of B doped graphene[34] are the synthetic methods adopted for doping B in CDs. Blue shift in $n\rightarrow\pi*$ transition is observed due to B-doping.[30] Blue shift in the PL band position due to B doping is also reported and attributed to its electron withdrawing ability.[33] Although it is not consistent in all the cases and the exact reason behind PL band is unknown. Most of the reports indicate excitation wavelength independent emissive nature of B-CDs which can be due to the presence of single emissive sites. Barman et. al[30] has found B doping decreases the PL intensity and hence the QY as it promotes non radiative quenching of emission. On the contrary, reports showing the significant enhancement of luminescence intensity and QYs due to B doping are present in the literature too.[28, 29, 33] Importantly, quenching of BCDs fluorescence emission due to the charge and/or electron transfer has been utilized for Al^{3+}, Hg^{2+}, glucose, H_2O_2, picric acid, TNP (2, 4, 6-trinitro phenol) and carcinogenic dye sensing.[28, 30, 31, 33, 36-39] Other than doping in the carbon motif, boronic acid functionalization of CDs establishes as one of the viable routes for selective sensing of glucose in the mixture of saccharides using the property of luminescence enhancements. In alkaline pH the boronic acid functionalized negatively charged CDs form self-aggregate using glucose as a connector which further restricts the rotational movements and block the non-radiative emission.[34] BCDs also known to enhance the non-linear optical activity[35] while B-N co doped GQD enhances the ORR activity.

3.1.4. Other dopants

In order to alter the optical properties of CQDs various dopants other than B/N were substituted on carbon site which includes single components like P, S, Se, F and Cl as well as co-doping of type N-S, N-B, N-P. Besides optical properties, doping flourishes the performances CQDs in many diverse fields among which the activities in bio-imaging, sensing, electrocatlysis, photo catalysis, and photovoltaic are applauding. Few recent reviews have discussed these issues in detail.[3, 4]

3.1.5. Applications

As compared with metal composed QDs, GQDs are made of non-toxic element, carbon, which makes them useful particularly in biological applications. Beside bioimaging they have been widely used for sensing, catalytic, photovoltaics and many other applications. Optimum doping of CQDs with nitrogen has found to enhance luminescence quantum yield which is inturn useful in bioimaging and light emitting technologies. N-CQDs show improved catalytic applications such as in ORR, degradation of organic dyes and water splitting. Composities CQDs with various other oxides such as TiO_2, SiO_2, ZnO, Fe_2O_3, Ag_3PO_4, Cu_2O were synthesized and found to show execllent photocatalytic activities such as degradation of dye molecules.[40, 41] CQD works mainly in two ways either as a light absorber or as conducting matrix. Recently the activity of TiO_2/CQD and SiO_2/CQD composites are explained based on the upconversion luminescence properties of C-dots.[41, 42] The photocatalytic reaction process is explained as shown in **Figure 6a**. Upon illumination the CDs absorb visible light, and emit shorter wavelength light via UCPL, which in turn excites TiO_2 or SiO_2 and forms electron/hole pairs. The electron/hole pairs then react with oxidants/reducers to produce active radicals, which degrades the organic dyes.

Composite of CQDs with TiO_2,[43, 44] g-C_3N_4[45] produces H_2 by photocatalytic H_2O splitting. In recent report, Yeh et. al[46] has exploited N-GQDs of band gap of approximately 2.2 eV for overall water-splitting under visible-light irradiation. They have shown both p- and n-type conductivities in GQDs in which sp^2 clusters proposed to act as the interfacial junction. The active sites for H_2 and O_2 production are the p- and n-domains of N-GQDs, respectively (Figure 6b).

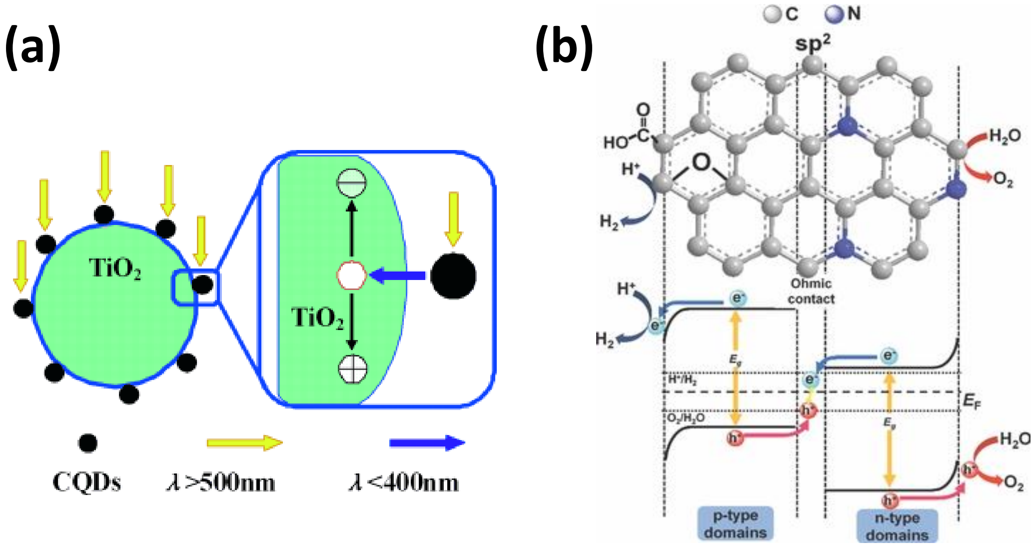

Figure 6. Proposed mechanism of (a) photo catalytic dye degradation for TiO_2/CQDs and (b) photocatalytic H_2O splitting of N-GQDs under visible light. Reproduced by permission of Royal Society of Chemistry from Ref.[41] and Wiley-VCH from Ref.[46].

3.2. Scope of the present investigations

The N/C atomic ratio in the CQD's reported so far is in the range of 2-18 %, most of them with a low content of less than 10%. In search of a simple, new method of preparing N-CQDs, we have carried out the decomposition of glucose in the presence of urea under hydrothermal conditions as well as by microwave (MW) irradiation. Here, the decomposition of urea gives ammonia which acts as the nitrogen source, a reaction that has been used to synthesize various nitrides, as well as N-doped graphene.[10, 47-50] We have characterized the N-CQDs so prepared and studied some of their properties. These N-CQDs, possessing high nitrogen doping content with N/C ratios of 18-22%, and exhibit good aqueous stability and tunable photoluminescence. The N-CQDs show the characteristic blue emission in the 400-500 nm region. We have examined the interaction of both N-doped and undoped CQDs with graphene, tetrathiafulvalene and tetracyanoethylene. N-CQDs exhibit show superior visible light induced catalytic activity for the photodegradation of methylene blue compared to undoped CQDs. It is noteworthy that mixtures of N-CQDs with ZnO and graphene oxide in proper proportions emit white light.

Extensive research has been carried out on the doping of electrons and holes in graphene by N and B substitution of C to suitably change the electronic and chemical properties.[51-53] Such doping of GQDs has been reported only for nitrogen. Considering the importance of doping the GQDs with holes, we have carried out synthesis of B-GQDs (4-6 nm) for the first time and studied their luminescence properties. For this purpose, we first prepared few layer B-doped graphene by gas phase arc-discharge of graphite in the presence of diborane gas or boron powder[51, 52], followed by chemical scissoring. In order to properly compare the properties of so prepare B-doped GQDs with N-doped GQDs, we have prepared the latter as well as pure un-doped GQDs by the arc-discharge method, followed by chemical scissoring. Excitation wavelength independent strong blue PL emission have been observed in all the GQDs and B/N-GQDs samples, which may be due to the narrow size distribution as well as highly crystallinity of GQDs obtained under present synthetic conditions. Mention must be made that up conversion of PL emission is observed in all the cases.

3.3. Experimental Section

3.3.1. Synthesis

i) Nitrogen doped Carbon Quantum Dots

Hydrothermal route (Method 1): Glucose (0.1 g) and urea (1g) were dissolved in 5 ml distilled water. The solution was kept in teflon lined autoclave of 23 ml capacity and heated in 150°C for 1 hr.

Microwave synthesis (Method 2): We have placed the glucose-urea solution (1: 10 mass ratio) in a domestic microwave oven (600 W) and heated for 7 mins. The yellow colour solution obtained in both the methods was dialyzed (10,000 Da dialysis membrane) for 3 days and dried under freeze drying. We have synthesized CQD by the literature reported method.[54] CQD were prepared by microwave heating glucose with few drops of dilute NaCl solution in 5 ml distilled water. Rest of the procedures was same as for the synthesis of N-CQDs.

ii) Synthesis of Boron and Nitrogen doped Graphene Quantum Dots

Boron and nitrogen doped graphene: Boron doped graphene was synthesized by arc discharge of graphite in the atmosphere of H_2+He+B_2H_6 mixture or by using boron powder stuffed graphite electrode.[51, 52] B_2H_6 vapor was generated by the drop wise addition of BF_3-diethyletherate to sodium borohydride in tetraglyme solvent. The B_2H_6 vapor was carried to the arc chamber by flowing hydrogen (200 torr) and He (500 torr). In another method, boron powder stuffed graphite electrode has been used as anode in arcing in H_2+He mixture. Nitrogen doped graphene was prepared by the arc discharge of graphite electrode in presence of mixed H_2+He+NH_3 gas. Pure graphene sheets with 2-3 layers were prepared by the arc discharge (discharge current was 100-150 A, maximum open circuit voltage was 60 V) of graphite electrodes in hydrogen (200 torr) and He (500 torr) atmosphere as reported previously by our group.[51, 52]

Boron and nitrogen doped GQD: We prepared B or N doped GQDs by chemical scissoring of corresponding B/N doped graphenes.[9] For this purpose B/N doped graphene oxide (GO) sheets were prepared from B/N-doped graphene (~5 mg) by modified Hummers method.[8] As-synthesized B/N doped GO sheets were further thermally deoxidized by heating in 300°C for 3 h in nitrogen atmosphere. B/N-doped reduced graphene sheets (RGO) were then cut by prolonged (~24 hrs) ultra-sonication in the presence of concentrated H_2SO_4+ HNO_3 mixture (1:3 volume). The mixture was diluted with water and product recovered by centrifugation. The purified sample was dispersed in 40 ml of deionized water and pH tuned to 8 with the addition of NaOH. This suspension was then transferred to a teflon lined autoclave (50 ml) and heated at 200°C for 10 h. After cooling to room temperature, the suspension was cleaned by dialysis and used for characterization.

3.3.2. Characterizations

UV-Vis absorption spectra were recorded using a Perkin Elmer lambda 650(UV/VIS/NIR spectrometer) and PL measurement were carried out by Horiba Jobin Yvon Spectrometer (iHR 320). X-ray photoelectron spectroscopy (XPS) was recorded with Mg-K_α (1253.6 eV) X-ray source to analyze the composition of samples. Transmission electron microscope (TEM) images were recorded with FEI Technai T20 instrument at an an accelerating voltage of 200 kV. Atomic force microscopy (AFM) measurement was carried out on Bruker Innova Microscope instrument in tapping mode using antimony *n*-doped Si tip of 10 nm resolution. FT-IR characterization was carried out on Bruker IFS 66v/S instrument.

3.3.3. Interaction with electron donor and acceptor molecules

We have added different concentration of TCNE (conc. in range of 10^{-4} M to 10^{-2} M), TTF (conc in range of 10^{-4} M to 10^{-2} M), N, N dimethyl aniline (0.1 to 1M) with same amount of N-CQDs and pristine CQD individually in ethanol solution (final volume 3 ml). We have freeze dried the CQD solution to get dry CQD sample and redispersed it again in ethanol to make a solution of the concentration of 0.2mg/ 1ml. Finally, 1 ml of this solution of CQD/N-CQD was diluted to 3 ml in the presence of the required concentration of donor/acceptor molecules in ethanol (molar extinction coefficient of CQD is ~2×10^5 M^{-1} cm^{-1}). In case of graphene 1 mg/ml concentration of exfoliated graphene solution in ethanol has been obtained by mild sonication. Then it was added to CQD and N-CQDs solution to achieve the concentration in range of 0.005 M to 0.05 M. We have sonicated the final solution for 15 mins and recorded the luminescence spectrum.

3.3.4. *White light emission*

ZnO nanoparticles with an average size of 5 nm were prepared by the procedure described in literature.[55] Aqueous dispersion of ZnO (conc. 1mg/ml) was made by 1 hr sonication. Different amount of aqueous N-CQDs solution (0.1 ml to 1.2 ml) was mixed with 3 ml dispersion of ZnO, sonicated for 15 mins and PL emission was recorded at excitation wavelength 325 nm. Aqueous GO solution was made by constant sonication of 1 hr. N-CQDs was admixed (0.05 ml, 0.1 ml) with 3ml GO solution, sonicated for 15 mins and PL emission was recorded at excitation wavelength 350 nm.

3.3.5. *Photodegradation*

Photodegradation of methylene blue (MB) was monitored using absorption measurement. In a typical measurement 5 ml of N-CQDs was mixed with 10 ppm of aqueous MB solution (5 ml), transferred to a quartz vessel and stirred under dark for 30 mins. Under vigorous stirring, reaction vessel was exposed to 300 W Xenon lamp (equipped with $\lambda< 400$ nm cutoff filter) which was placed 12 cm away from the reaction vessel. Reaction was monitored by recording the changes in absorption of MB (at absorption maxima 664 nm) at each 5 mins interval. The same experiments were carried out with as prepared CQDs for comparison.

3.3.6. *Photocatalytic H_2O splitting*

Aqeous solution of N-CQDs was mixed with chloroplatinic acid solution containing different weight percentages of Pt (1, 5 and 10 wt %) and was stirred for 1 hour at room temperature. The chloroplatinic acid was in situ reduced to Pt with the addition of $NaBH_4$ to obtain the N-CQDs/Pt composite. Photocatalytic H_2 evolution experiments were performed in a air-tight quartz vessel. For dye sensitized water splitting, 10 mg of catalyst was dispersed in 50 ml of aqueous solution in presence of 0.014 mM Eosin Y (EY, sensitizer) and 15% v/v triethnaolamine (sacrificial donor) by ultrasonication. The vessel was purged thoroughly with N_2 before irradiation. Samples were irradiated under 100 W halogen lamp (Newport). The amount of H_2 evolved was calculated using gas chromatography (Perkin Elmer, Clarus 580 GC) equipped with TCD detector by manually injecting 1 ml of generated gases from the headspace of the quartz vessel during constant interval.

3.3.7. Activity calculation

i) <u>fluorescence quantum yield</u>:

Quninine sulfate in 0.1 (M) H_2SO_4 was chosen as a standard (Φ =0.57). The quantum yield were measured in water using following equation,

$$\Phi_x = \Phi_{st} \frac{I_x \eta_x^2 A_{st}}{I_{st} \eta_{st}^2 A_x} \text{-------------------------------------(ES1)}$$

The subscript “x” refers to sample and “st” to standard (known quantum yield).Where, Φ is the quantum yield, I the integrated emission intensity, η the refractive index of solvent and A the optical density.

ii) <u>Stern-Volmer constant</u>

Stern-Volmer equation,

$$\frac{F_0}{F} = 1 + k_q \tau_0 [Q] \text{------------------------------- (ES2)}$$

Here F_0 and F is the emission intensity without and with quencher respectively; τ_0 is the lifetime of emissive excited state and [Q] is the conc. of quencher.

iii) <u>Rate of dye degradation:</u>

We have calculated the percentage degradation of methylene blue as a function of irradiation time using the following equation,

$$\% \text{ degradation} = \frac{A_0 - A_t}{A_t} \times 100 \text{---------------} \quad \text{(ES3)}$$

where, A_0 is the absorbance at time t = 0 min and A_t is the absorbance at given time interval t.

3.4. Results and discussion

3.4.1

N-doped carbon dots-synthesis, characterization, properties and applications

3.4.1. N-doped carbon dots-synthesis, characterization, properties and applications

Urea is known to release NH_3 upon heating and this reaction helps to incorporate nitrogen in the carbon matrix of graphene.[47, 56] In the present study, hydrothermal conditions with high autogeneous pressure and temperature or microwave (MW) irradiation with localized superheating enables the rapid dehydration of glucose in the presence of NH_3 released by the decomposition of urea, to form N-CQDs with high nitrogen content.[57] Generally, C-N bond formation occurs in the nucleation step, followed by further carbonization and growth to generate N-CQDs.[21, 58] Moreover, ammonia acts as both the N-dopant as well as a surface passivator without the addition of any external capping agent. Interestingly, in the absence of urea, carbonization of glucose does not occur under the same reaction conditions, which is also confirmed by controlled photoluminescence and TEM studies. Previously, CQDs are formed at 150°C by the decomposition of carbohydrate after much longer reaction times.[59] The rapid formation of N-CQDs in the present synthesis may be due to the presence of ammonium and hydroxyl ion from aqueous ammonia, which are known to catalyze the carbonization of carbohydrates.[54, 60]

XPS measurements were carried out to establish the elemental composition of N-CQDs (**Figure 1**). The survey scan spectrum indicates a pronounced N 1s peak at ~399.5 eV, a predominant C 1s peak at ~284 eV and a O 1s peak at 532 eV (Figure 1), which indeed confirms the successful formation of N-CQDs by the both hydrothermal reaction and MW irradiation. The N/C atomic ratio was calculated to be ~18 % for hydrothermally produced N-CQDs, whereas for MW synthesis it is ~22 %, which is higher than that of previously reported N-CQDs.[21, 27] The high resolution N 1s spectrum of N-CQDs synthesized by hydrothermal method reveals the presence of both pyrrolic (399.6 eV) and N-H like (400.3 eV) N atoms (Figure 1b), whereas the N-CQDs formed under MW irradiation shows only pyrrolic N at 399.4 eV (Figure 1c). In addition, the high resolution C 1s spectrum of N-CQDs further confirms the presence of C-C (284.5 eV), C-O (288.3 eV) and most importantly C-N (285.8 eV) bonds (Figure 1).

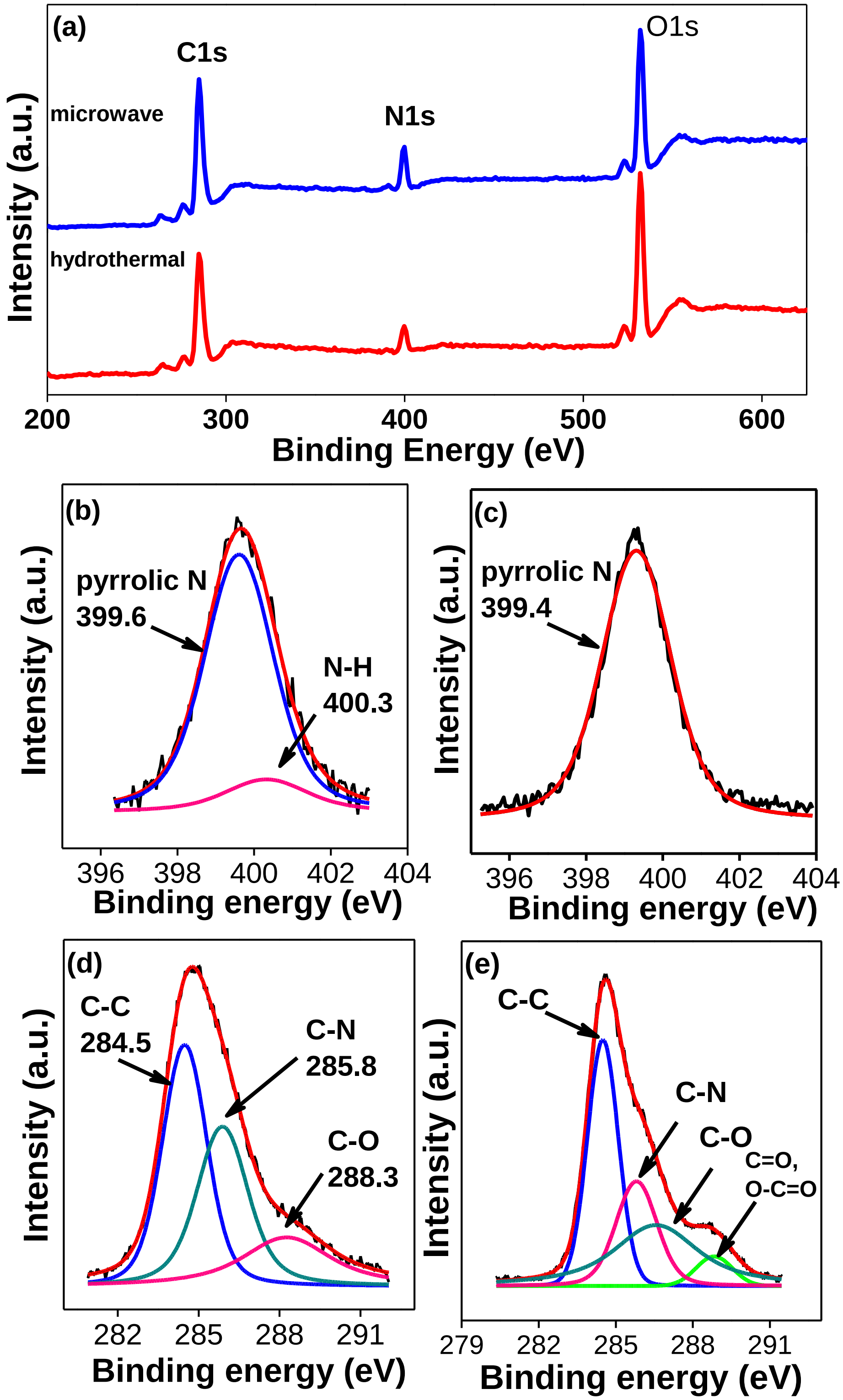

Figure 1. (a) X-ray photoelectron spectra of N-CQDs. High resolution N1s and C1s signals of N-CQDs prepared by hydrothermal (b, d) and microwave (b, e) methods.

Fourier transform infrared (FTIR) spectra demonstrates the presence stretching vibration of N-H (from 3500 to 3150 cm^{-1}), C=C (1604 cm^{-1}), and aromatic C-N heterocycles (from 1500 to 1150cm^{-1}) (**Figure 2**).[21] The predominant presence of C compared to N was further confirmed by elemental analysis which shows the N content to be comparable with XPS results (**Table 1**).

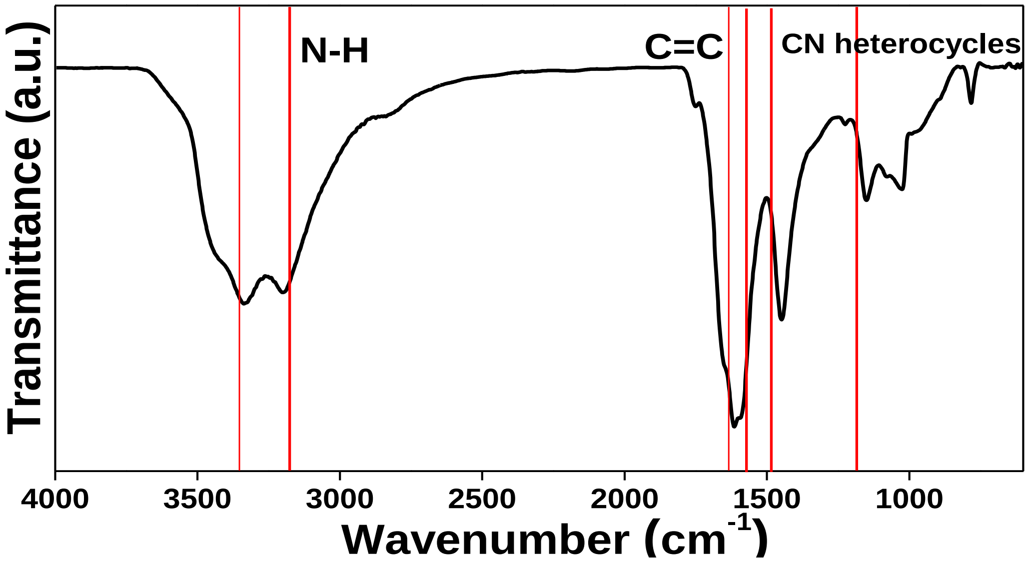

Figure 2. FTIR spectra of N-CQDs.

Table 1. The C, H, N content of the samples synthesize at different reaction conditions

Materials	%C	%N	%H	%O (calculated)
N-CQD (hydrothermal)	49.89	20.3	6.53	23.29
N-CQD (microwave)	53.49	23.3	6.54	16.67

We have characterized the N-CQDs by transmission electron microscopy (TEM) and atomic force microscopy (AFM) (**Figure 3**). Figure 3a and its inset show the TEM images of

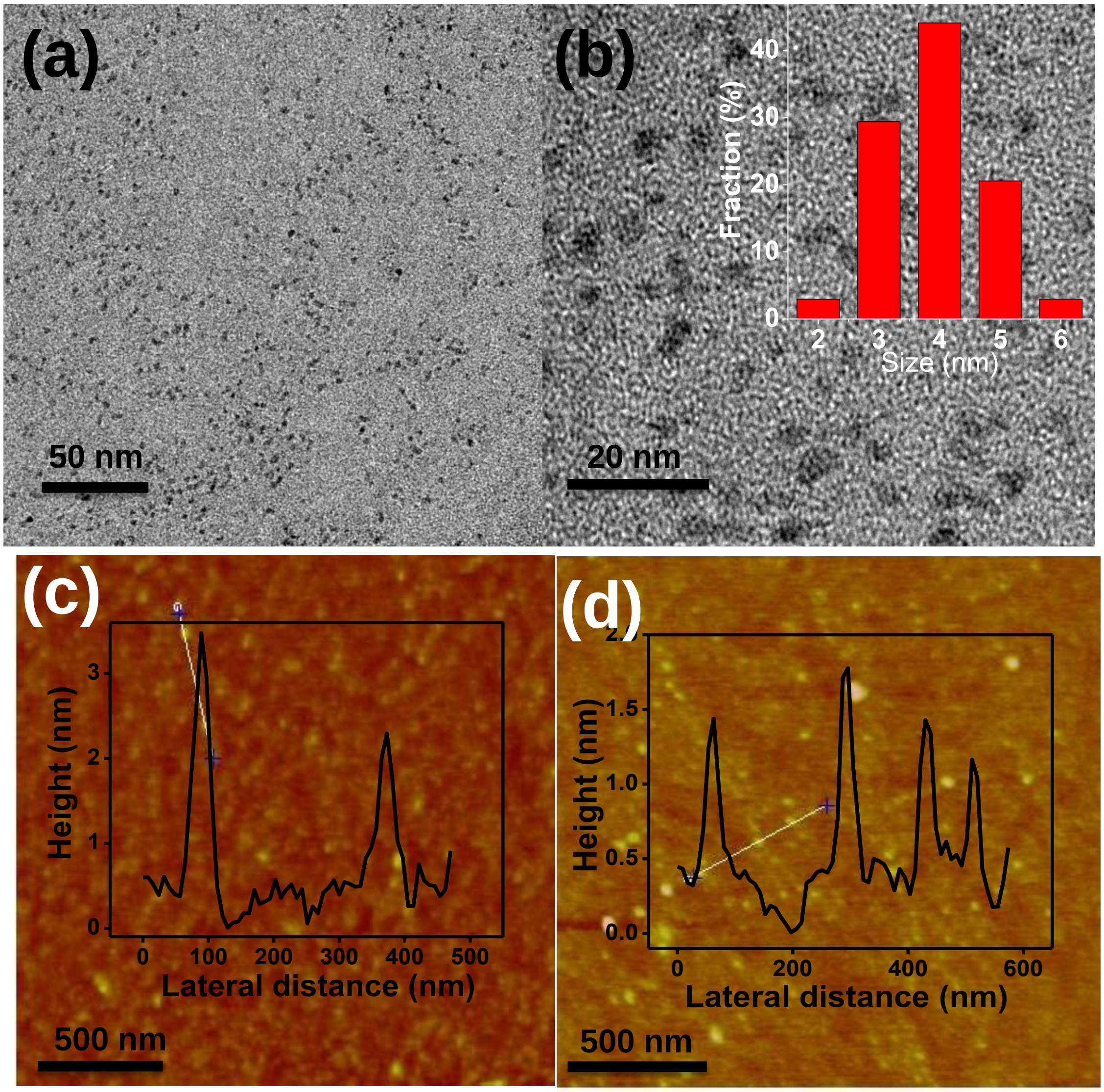

Figure 3. (a, b) TEM images of N-CQDs prepared by hydrothermal method with size distribution. AFM images of N-CQDs prepared by (c) hydrothermal and (d) microwave methods. Insets of (c, d) show height profiles of N-CQDs.

N-CQDs synthesized by hydrothermal reaction and MW irradiation, respectively. In Figure 3b, high magnification TEM images shows a relatively narrow size distribution (3 to 5 nm) of hydrothermally prepared N-CQDs with an average diameter of ~4 nm. N-CQDs synthesized by MW irradiation have the average diameter of ~4.5 nm. Figures 3c and d show typical AFM images of N-CQDs synthesized by hydrothermal and MW irradiation, respectively. The topographic height distributions are in the range of 2-3 nm and 1-2 nm for N-CQDs synthesized by hydrothermal and MW treatment, respectively. The respective average heights are ~2.5 nm and ~1.5 nm, which suggest that most of them are consist of 1-5 graphene layers.

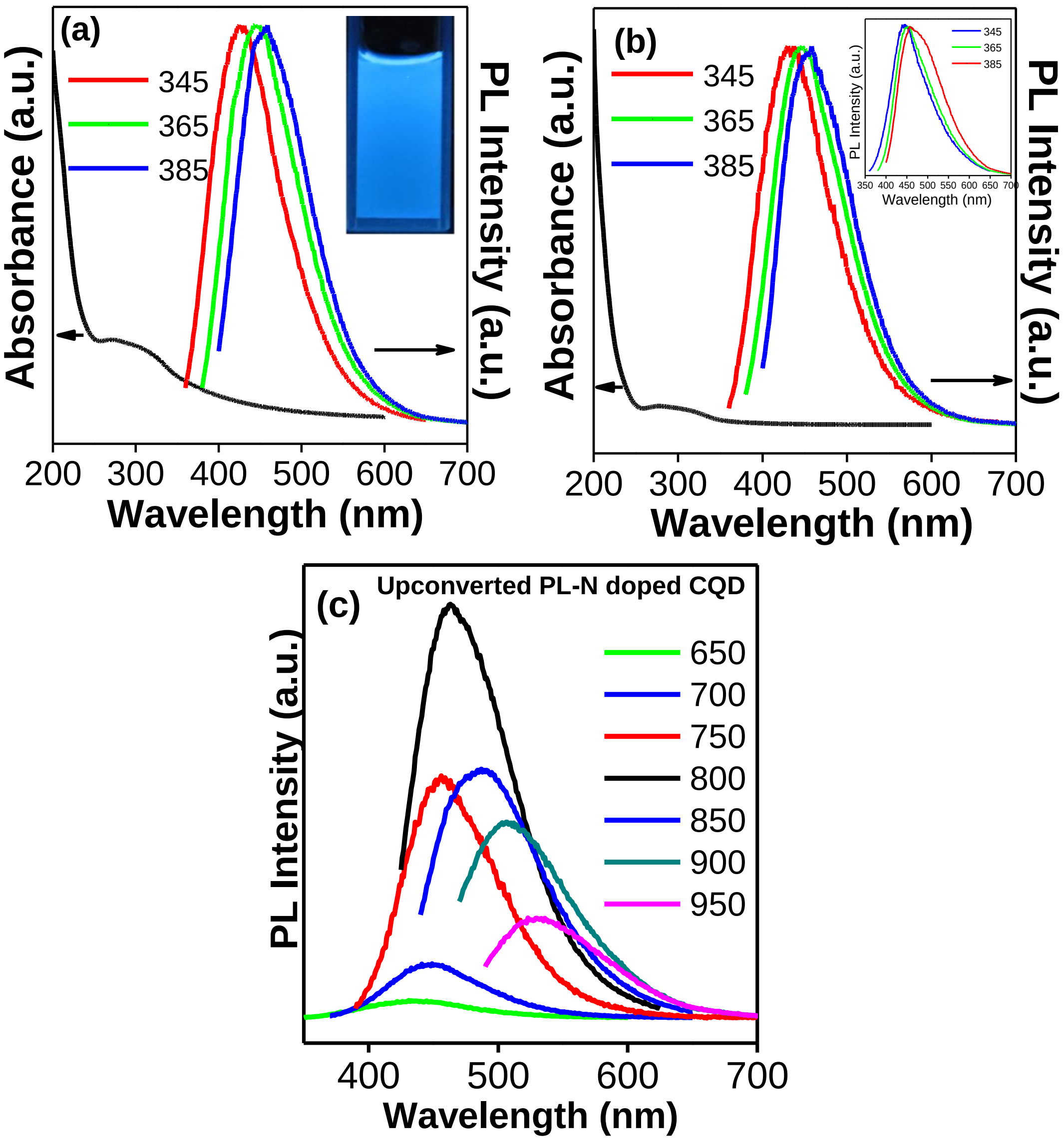

Figure 4. UV-Vis and PL spectra (recorded at different excitation wavelengths) of N-CQDs prepared by (a) hydrothermal and (b) microwave methods. Inset in (a) shows a photograph of N-CQDs illuminated under UV light, (b) PL spectra of undoped CQDs. (c) Up converted PL spectra of N-CQDs (prepared by hydrothermal method) at different excitation wavelengths.

We have recorded absorption and photoluminescence (PL) spectra of the N-doped CQDs prepared by us (**Figure 4**). Typical UV-Vis spectra of the N-CQDs synthesized by the two methods show a broad absorption band in 250-350 nm region with a tail extending to the visible region, characteristic of a polycyclic aromatic π system (Figures 4a and b).[61] PL spectra show an excitation wavelength dependent intense PL emission (Figures 4a and b). The PL emission band shifts from 428 nm to 456 nm (Figure 4a) and 432 nm to 457 nm (Figure 4b) for N-CQDs synthesized by hydrothermal and MW methods respectively, on changing the excitation wavelengths in the 345 to 365 nm range. Bright blue light is emitted when N-CQDs are irradiated under UV light (Photograph in Figure 4a). N-CQDs also show strong-excitation dependent PL emission (Figure 4c). The exact origin of the intense PL emission and the mechanism behind its excitation wavelength dependent emission is not understood properly,[41, 62] although the luminescence is suggested to arise from a π-π* transition, due to emissive traps or free zig-zag sites and/or edge states. [41, 62, 63] We observe a slight blue-shift in the PL band position of N-CQDs compared to that of undoped CQDs.[18] Similar blue-shifts in the PL emission band of N-CQDs has been reported by Li et al,[18] and Zhang et al.[27]

We have also measured the quantum yield of N-CQDs. Coumarin 102 in ethanol was chosen as a standard (Φ =0.74). The quantum yield of NCQDs were measured in water using following equation,

$$\Phi_x = \Phi_{st} \frac{\mathrm{I}_x \eta_x^2 \mathrm{A}_{st}}{\mathrm{I}_{st} \eta_{st}^2 \mathrm{A}_x} -----------(1)$$

Where, Φ is the quantum yield, I is the integrated emission intensity, η is the refractive index of solvent and A is the optical density. The subscript “x” refers to the sample and “st” to the standard with known quantum yield.

The quantum yields of N-CQDs prepared by hydrothermal and MW methods are 0.7% and 1% respectively (**Table 2**). Absence of any external surface passivating agent in the as-prepared N-CQDs may be the reason of the low quantum yield, though it is comparable with the values reported in the literature.[11, 64, 65] N-CQDs prepared by the hydrothermal reaction and MW irradiation show PL decay (measured at 385 nm excitation) with average lifetimes of 2.6 and 2.5 ns respectively.

Table 2. Quantum yield calculation of N-CQDs prepared at different reaction conditions.

Materials	Integrated emission intensity (I)	Absorbance at 385 nm (A)	Refractive index of solvent (η)	Quantum Yield (Φ)
COUMARIN 102	1.2×10^9	0.02	1.36	74%
N-CQDs (hydrothermal)	2.9×10^9	0.51	1.33	0.7%
N-CQDs (microwave)	1.3×10^9	0.17	1.33	1.0%

Graphene is reported in the literature to be a good PL quencher for fluorescent dyes, conjugated polymers and semiconductor dots.[66-69] The origin of quenching is considered as resonance energy transfer, electron transfer or dipole-dipole coupling in between graphene and the fluorescent species.[66-69] Recently, fluorescence resonance energy transfer from amine functionalized carbon quantum dots to reduced graphene oxide has been studied to sense metal ions.[70] We have observed quenching of PL emission of both N-CQDs and pristine CQDs by graphene (**Figure 5**). Small size CQDs can easily adsorb on the basal plane of graphene through noncovalent π-π interaction. There can be photo-induced energy transfer from N- doped or un-doped CQDs to graphene through the mutual overlap of their π cloud. Besides, the defect sites, emissive traps, dangling bonds, functional moieties presents in the CQD and graphene surface are may be expected to play role as PL quencher of CQDs. Linear Stern-Volmer plot has been observed in case of pristine CQDs upon interaction with graphene unlike the case of N-CQDs which shows positive deviation from the linearity (Figure 5b). The linear Stern-Volmer plot in the case of CQDs indicates dynamic quenching, while the nonlinear curve observed in the case of N-CQDs suggests that the quenching process follows both static and dynamic energy transfer.[71]

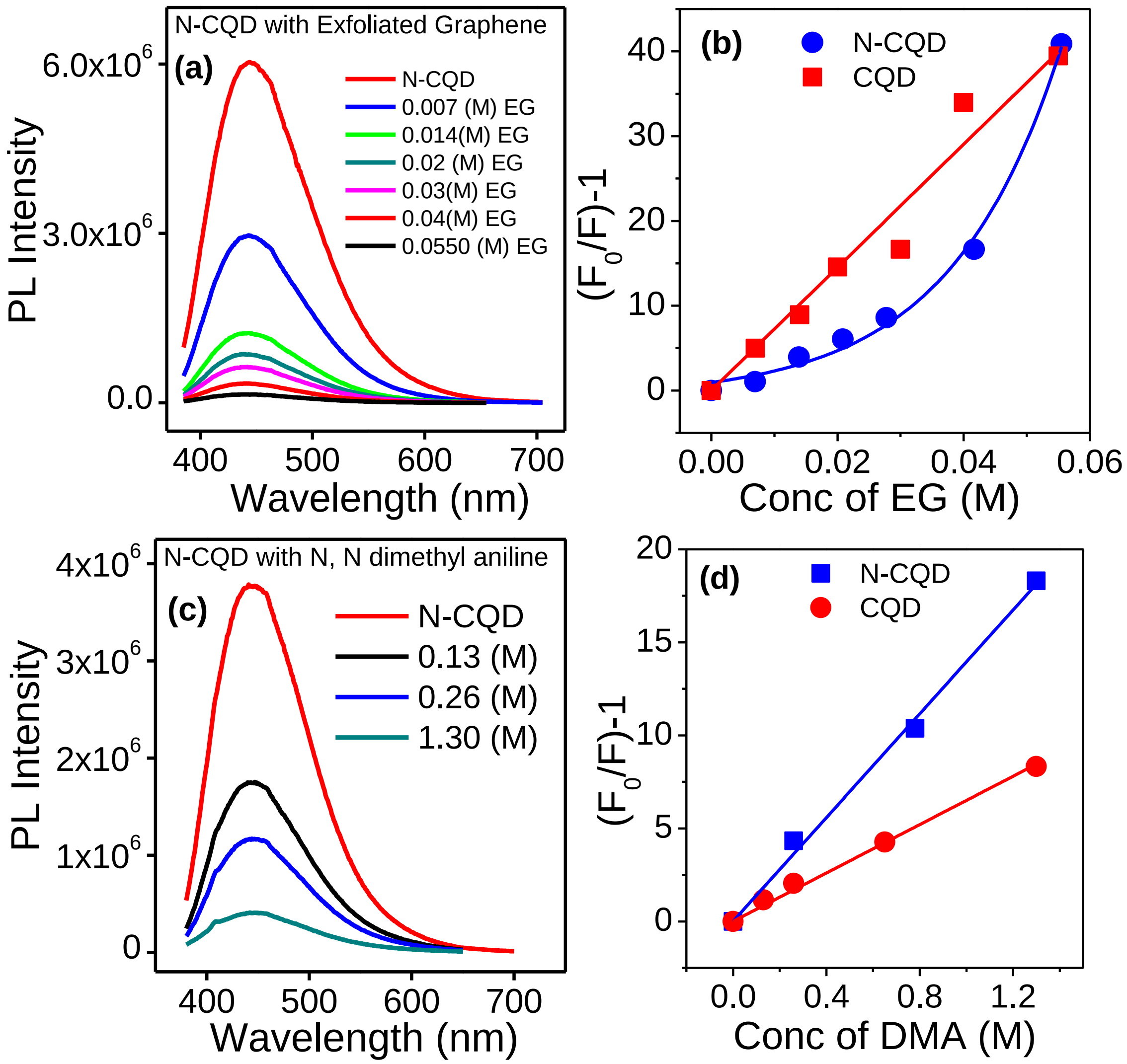

Figure 5. PL emission spectra (365 nm excitation) and Stern-Volmer plots for the quenching of luminescence of N-CQDs and undoped CQDs in ethanol in the presence of (a,b) exfoliated graphene and (c,d) N, N dimethyl aniline.

The quenching rate constants (k_q) for both CQDs and N-CQDs are similar (**Table 3**) as calculated using Stern-Volmer equation,

$$\frac{F_0}{F} = 1 + k_q \tau_0 [Q] - - - - - - - - (2)$$

Here F_0 and F is the emission intensity without and with quencher respectively. τ_0 is the lifetime of emissive excited state and [Q] is the conc. of quencher.

We have examined the quenching of photoluminescence of the CQDs in the presence of N,N-dimethyl aniline which is known to be an excellent fluorescence quencher (Figure 5). The k_q value obtained from the linear Stern-Volmer plots are in the range of 10^9 M^{-1} s^{-1} which agrees well with the literature reported values.[72] The exact mechanism of the interaction of all these quenchers with undoped and N-CQDs is not fully understood and needs further investigation.

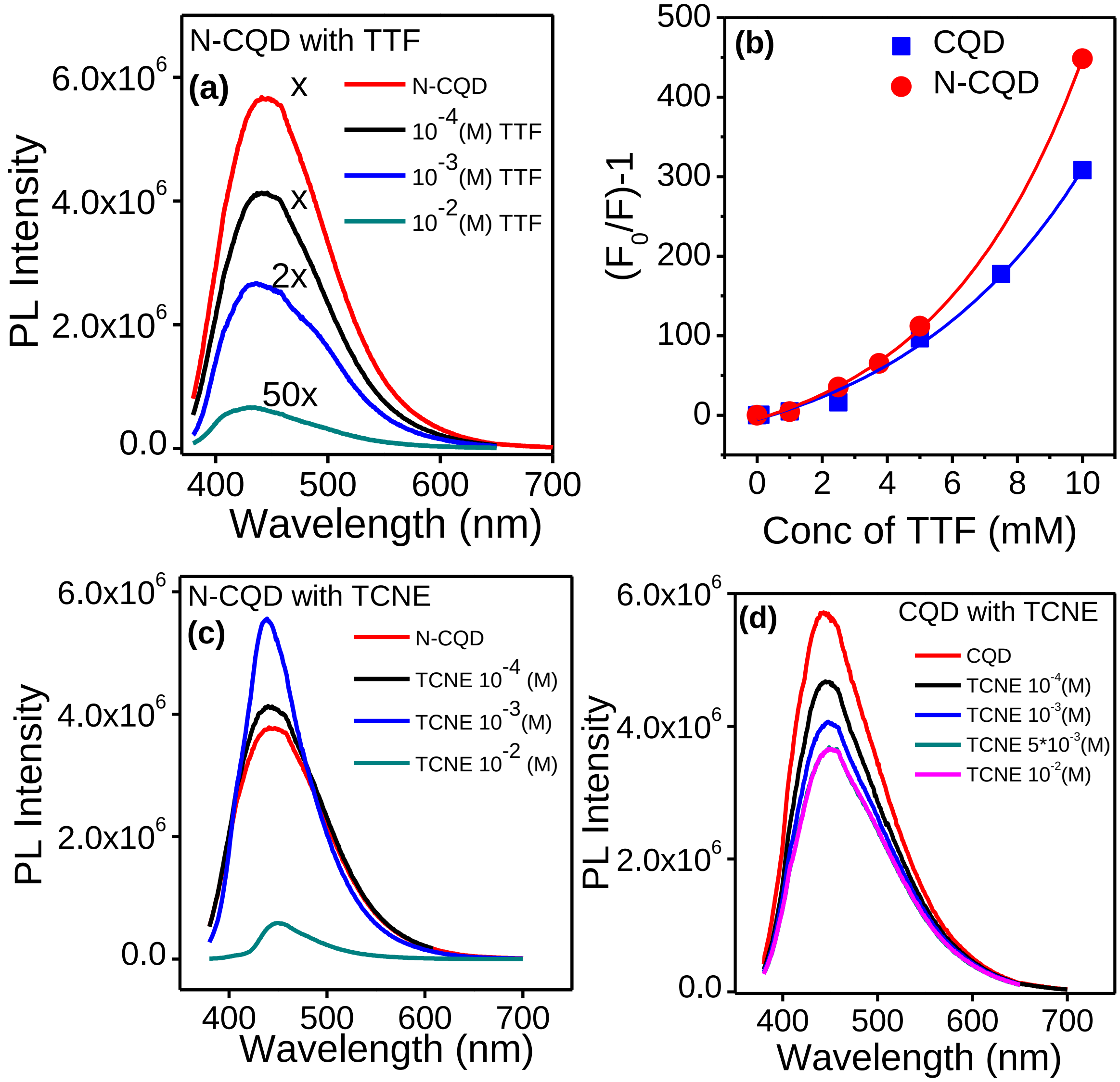

Figure 6. PL emission spectra (365 nm excitation) of N-CQDs in ethanol in the presence of (a) TTF and (c) TCNE and of (d) undoped CQDs in the presence of TCNE. (b) Stern-Volmer plots for the quenching of luminescence in the presence of TTF in ethanol.

Tetrathiafulvalene (TTF) and tetracyanoethylene (TCNE) are known for their charge transfer interaction with aromatics including graphene.[73, 74] In the case of undoped and N-doped CQDs, electron-donating TTF shows significant quenching of luminescence (**Figure 6a**). We observe a non-linear Stern-Volmer plot (Figure 6b) with a quenching constant of 6.1×10^{12} and 2.6×10^{12} M^{-1} s^{-1} for N-doped and undoped CQDs, respectively (Table 3). The high values of quenching constant indicate possible binding interaction between the fluorophore and the quencher.[75] Unlike TTF, electron accepting TCNE interacts differently with N-doped and undoped CQDs (Figures 6c and d). Undoped CQDs show a gradual decrease in luminescence on increasing the TCNE concentration, whereas N-doped CQDs show enhancement in the PL intensity up to a moderate concentration of TCNE (Figure 6c). A decrease in the full-width-half-maximum (FWHM) of the PL band occurs on addition of TCNE to N-CQDs.

Table 3. Calculation of Stern-Volmer quenching constant.

Quencher	**N-CQDs (M^{-1} s^{-1})**	**CQDs (M^{-1} s^{-1})**
TTF	6.11×10^{12}	2.58×10^{12}
Exfoliated graphene	1.14×10^{11}	2.8×10^{11}
N,Ndimethyl aniline	2.52×10^{9}	5.4×10^{9}

In order to understand this behavior, we have deconvoluted the broad PL emission spectrum into multiple Gaussian functions, which indicates the presence of more than one emissive site (**Figure 7**).[76] The initial addition of TCNE (1 mM) may quench surface-related emission (bands 2 and 3 in Figure **7**) of N-CQDs resulting in a decrease in the FWHM of PL the band (**Table 4**). The quenching of surface related emission increases the core related emission intensity. We speculate that the electron acceptor TCNE occupies some of the surface-emissive sites containing N-atoms in the CQD lattice. At high concentrations of

TCNE, sharp quenching in PL emission along with the red shift in PL suggest agglomeration of N-CQDs or chemical reaction. We note that specific interaction of TCNE with N-CQDs is to be expected since these CQDs can act as electron donors while TCNE is an electron acceptor.

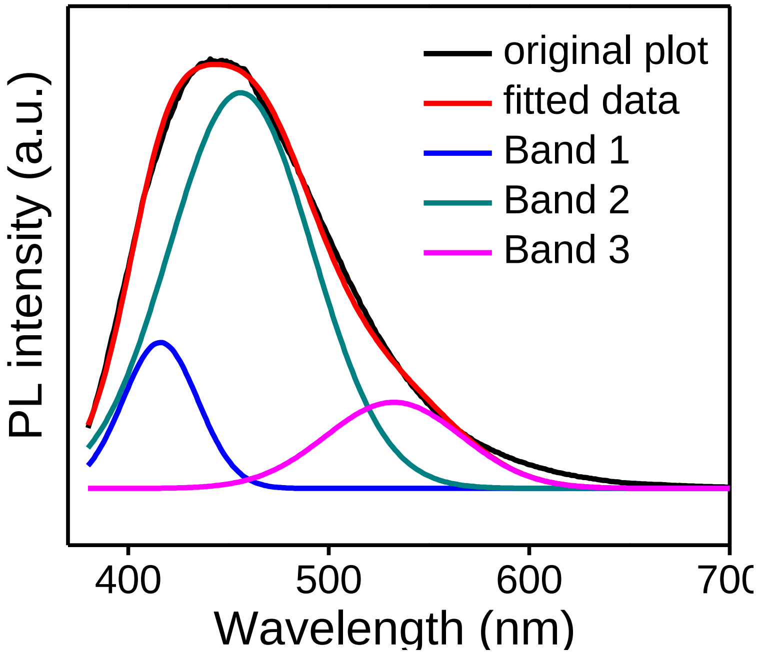

Figure 7. Fluorescence spectrum of N-CQDs deconvoluted in multiple Gaussian function, suggesting the presence of multiple emissive sites.

Table 4. Variation of luminescence (365 nm excitation) intensity, emission position and band width upon interaction of N-CQDs with TCNE.

Conc. of TCNE (mM)	PL Intensity (counts)	PL position (λ_{max} in nm)	FWHM
0	3.7×10^6	445	117
0.1	4.1×10^6	441	113
1	5.5×10^6	438	82
10	5.8×10^5	450	61

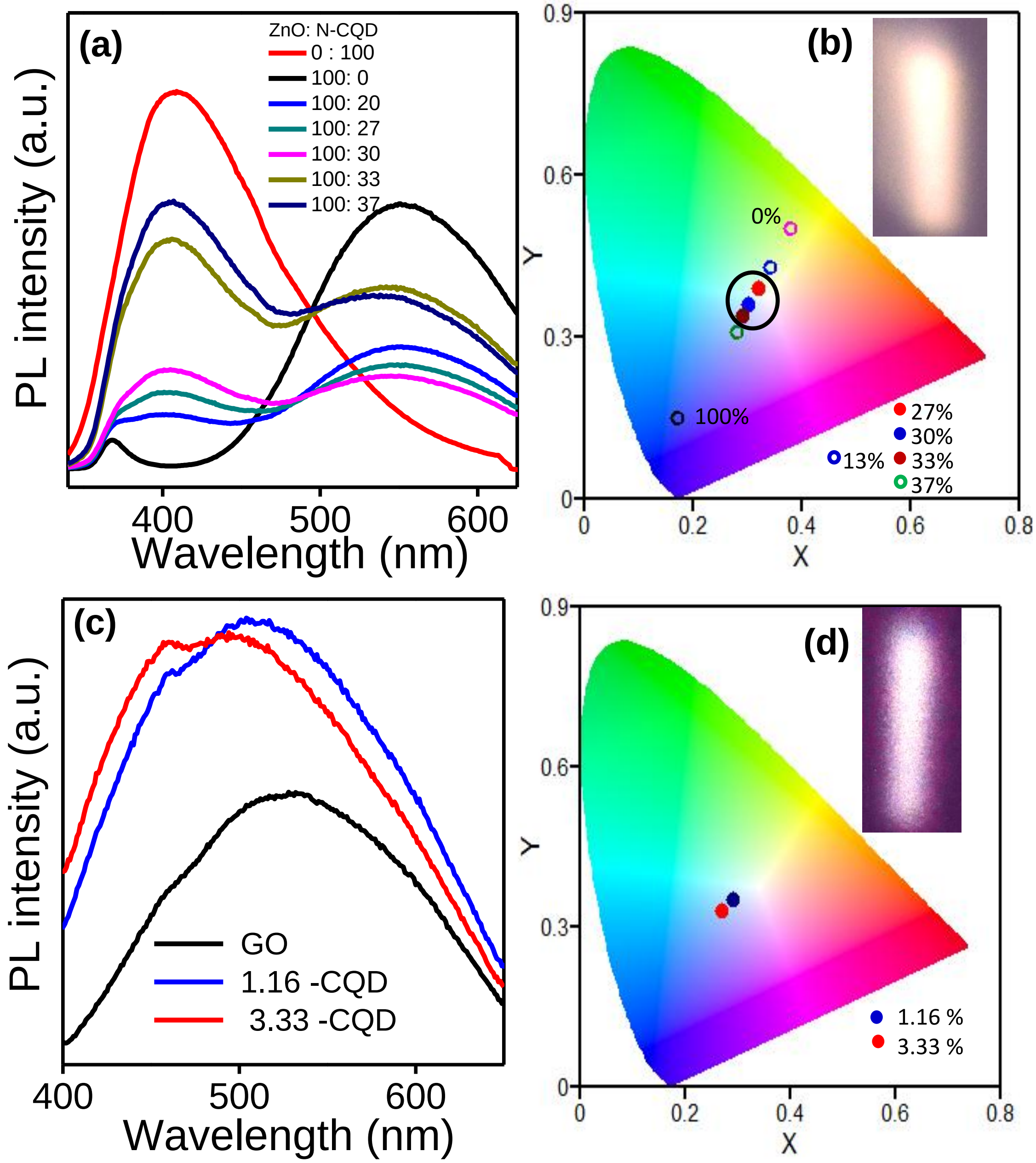

Figure 8. PL spectra of (a) ZnO + N-CQDs mixture and (c) Graphene oxide + N-CQDs mixture in water (excitation 325 nm and 350 nm respectively). CIE 1931 colour diagrams for the admixture of N-CQDs with (b) ZnO and (d) GO. Filled dots indicate the compositions close to white light emission. Inset shows the photograph of the white light emitted.

Defects in ZnO give rise to a characteristic broad emission in the green-yellow region. Combination of blue light emitting materials with ZnO or graphene oxide (GO) to generate white light is reported in literature.[77-79] There are reports where CQDs or N-CQDs have been used as colour converters to emit white light from blue LEDs.[57, 80] We find that admixing N-CQDs with ZnO in proper proportions give rise to white light emission (**Figure 8**). In figure 8a, we show typical PL spectra of ZnO with different amount of N-CQDs. ZnO shows a broad defect-related emission in the visible region centered around 550 nm. As the amount of N-CQDs increases, the PL emission spectrum covers the entire visible region. The PL spectra corresponding to 27%, 30% and 33% of N-CQDs mixed with ZnO (v/v) have CIE (Commission Internationale de L'Eclairaged) coordinates of (0.32, 0.39), (0.30, 0.36) and (0.29, 0.34) respectively which are in the white region of the CIE 1931 diagram (Figure 8b, excitation 325 nm). In figure 8c we show how proper admixture of yellow emitting filled balls marked by circle).[81] In the inset of figure 8b we have presented the photograph of emitted white graphene oxide (GO) with blue-emitting N-CQDs also gives white light emission (inset of Figure 8(c)) with CIE coordinates of (0.29, 0.35) and (0.27, 0.33) (Figure 8d).

We have studied the catalytic activity of the CQDs for the photodegradation of methylene blue (MB) under visible light irradiation (**Figure 9**). We have calculated the percentage degradation of MB (fig 6b) as a function of irradiation time using the following equation,

$$\%\ \mathrm{degradation} = \frac{\mathrm{A_0} - \mathrm{A_t}}{\mathrm{A_t}} \times 100 - - - - - (3)$$

where, $\mathrm{A_0}$ is the absorbance at time t = 0 min and $\mathrm{A_t}$ is the absorbance at given time interval t.

The kinetics of photo degradation reaction of MB dye in presence of both N-CQDs and CQD is following pseudo first order kinetics at very low dye concentration. We have fitted our data according to the following equation,

$$\ln\frac{C_0}{C_t} = kt - - - - - - - - (4)$$

Here, C_0 and C_t are the absorbance of MB at 666 nm recorded at time 0 min and t min. k is the apparent rate constant.

Figure 9a shows the time-dependent changes in the absorbance of MB under visible light irradiation. We observe that in the presence of N-CQDs almost complete degradation (~88%)

of MB is achieved upon irradiation for 30 mins (Figure 9b), whereas in the presence of pristine CQD, MB degrades only up to 32 % (Figure 9b). MB undergoes negligible self-degradation (24%) under visible light (control experiment). The rate constants (*k*) of

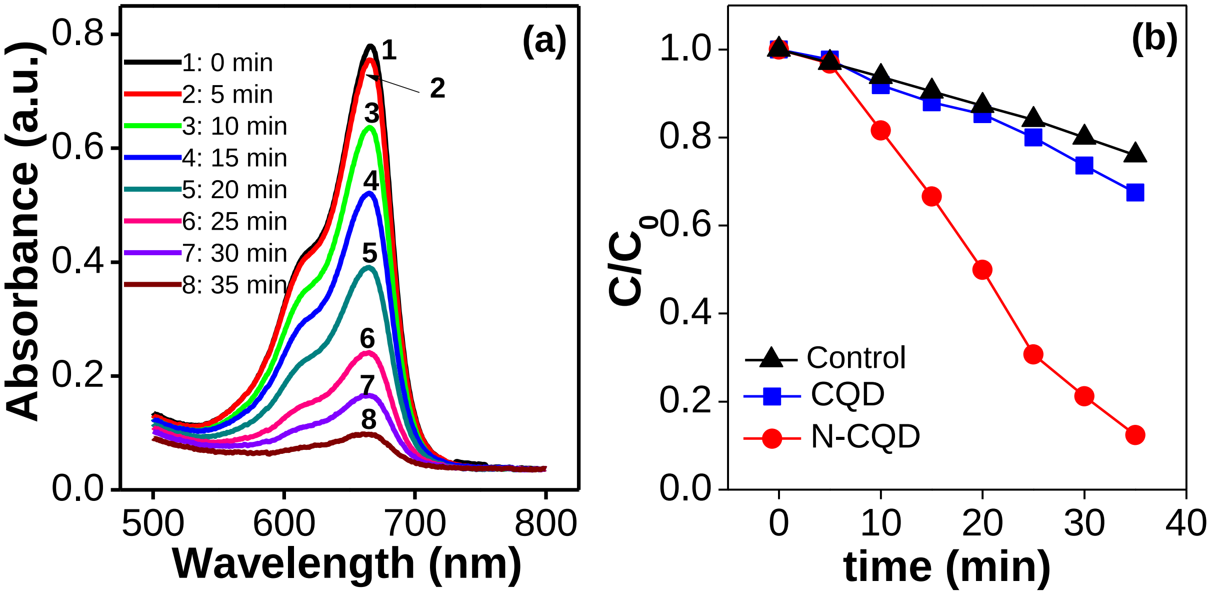

Figure 9. (a) Absorption spectra methylene blue on interaction with N-CQDs at different irradiation times. (b) Photocatalytic degradation of MB (normalized concentration) with the irradiation time in presence of undoped and N-CQD.

degradation of MB in the presence of N-CQDs and undoped CQD were calculated using the Langmuir-Hinshelwood rate equation. The values of *k* for N-doped and undoped CQD are 0.048 min^{-1} and 0.009 min^{-1} respectively. Clearly N-CQDs are more effective in the photodegradation of MB than undoped CQDs. Such superior performance in the photodegradation of methyl orange has been noted in the case of N-CQDs.[21] N-doping can generate local disordered structure and can affect the local electronic structure of CQDs which favors the formation of transient intermediates by enhancing the binding of ions present in solution, results in the formation of active OH•, which is responsible for photodegredation of dye.[18, 82-84]

Photocatlytic H_2O splitting has been performed utilizing N-CQDs as an electron channel which takes up the electron from the dye and guides electron to Pt, the site of H_2 evolution as shown in the plausible mechanism in **Figure 10**.

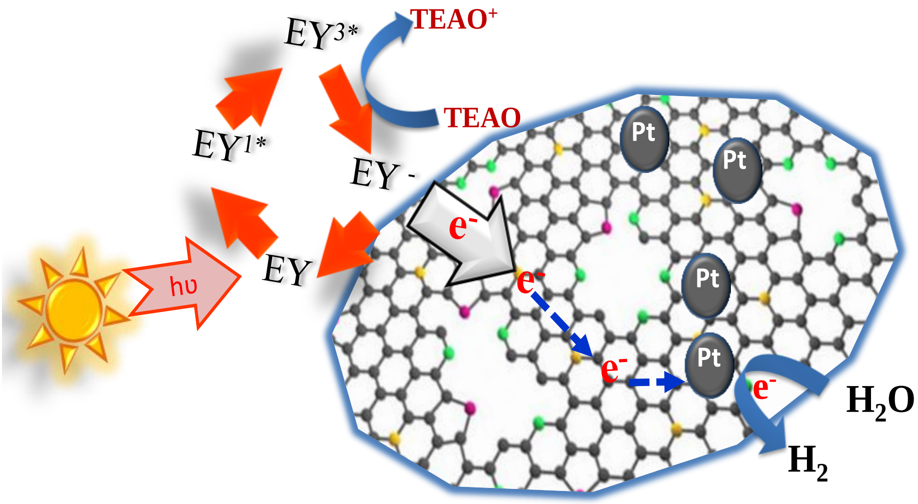

Figure 10. Schematic of photocatalytic H_2O splitting using N-CQDs-Pt composite.

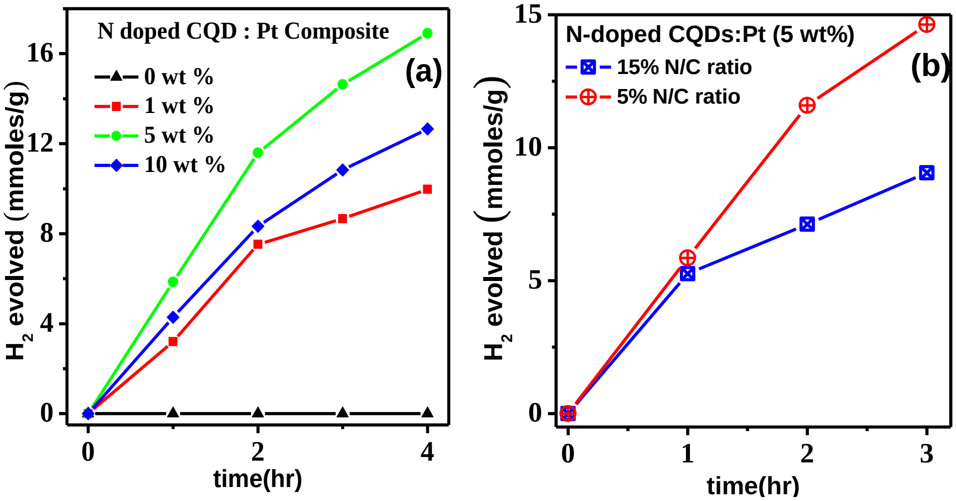

Figure 11. Photocatalytic H_2 evolution rate of various N-CQD-Pt composite. Variation of (a) weight % of Pt and (b) N/C ratio is shown.

The H_2 evolution was not observed in the absence of Pt particles. The hole left behind on Eosin-Y surface get consumed by triethnaolamine (sacrificial donor). The N-CQDs (%N/C= 5%) sample was grafted with different weight percent of Pt (1, 5 and, 10 wt %). H_2 evolution for 1, 5 and 10 wt % Pt composite was 3.1, 5.8 and 4.2 mmole h^{-1} g^{-1} respectively (**Figure 11a**). The lower activity at 1 wt% Pt grafting, could be due to lesser availability of H_2

evolution site and increases till an optimum amount is reached. At higher wt % of Pt activity decreases and reason can be due to the decrease in availability of free carbon dot sites.[85]

Table 5. Comparison of activity of N-CQDs/Pt composite with other CQD based system.

Serial No.	Catalyst	Activity (mmole h^{-1} g^{-1})	Reaction Conditions	Reference
1	Dye/N-CQDs/Pt (5 wt %)	5.80	10 mg of catalyst; 0.014 mM EY^-, 15 v/v % aqueous solution; 100 W halogen lamp	Present work
2	CQDs (2 wt%)/ TiO_2	0.05	50 mg of catalyst; 25% v/v methanol aqueous solution; 500 W xenon lamp (λ>450 nm)	43
3	CQDs/Ni-bis-(diphosphine)	0.40	0.5 mg in 30 nmol of NiP in aqueous EDTA (01.M) in $100mW/cm^2$, with UV-cut-off	86
4	G-CQDs/g-C_3N_4	0.10	80 mg of catalyst; water; 300 W xenon lamp (λ>450 nm)	45
5	N,S GQDs (1.24 wt%)/TiO_2/ (1 wt %) Pt	0.09	50 mg of catalyst; 25% v/v methanol aqueous solution; 300 W xenon lamp (λ>420 nm)	44

In order to understand the role of nitrogen doping in N-CQDs we have further synthesized 15 % N/C and compared it with 5 % N/C sample. 15 % N/C sample shows activity of 2.9 mmol h^{-1} g^{-1} while that of 5 % N/C evolves 5.8 mmole h^{-1} g^{-1} of H_2 with 5 wt % Pt. N-CQDs plays acts as an electron channel only, probably excess doping increases number of defects thereby, lowers the activity of 15% N/C sample due to more charge recombination sites. To the best of our knowledge there are few reports which show the activity of carbon dots in H_2 evolution reaction (HER). We have presented a comparative study of present sample with the literature reports in **Table 5**. Dye-sensitized HER using N-CQDs is found to be more efficient compared to semiconductor based system.

3.4.2

Luminescence properties of boron and nitrogen doped graphene quantum dots

3.4.2. Luminescence properties of boron and nitrogen doped graphene quantum dots

B- and N- doped graphene were prepared by using boron powder or diborane vapor as the boron source and NH_3 as the source of nitrogen (Step 1, **Figure 1**). In the preparation of B-doped graphene, B_2H_6 vapor was carried to the arc chamber by a mixture of H_2 and He gases. Under the arcing conditions, boron atoms generated from B_2H_6 or B-powder, substitute some of the carbon atoms of graphene produced from the arcing of graphite electrodes. Free nitrogen atoms were generated from NH_3 during arcing, which got incorporated in graphene

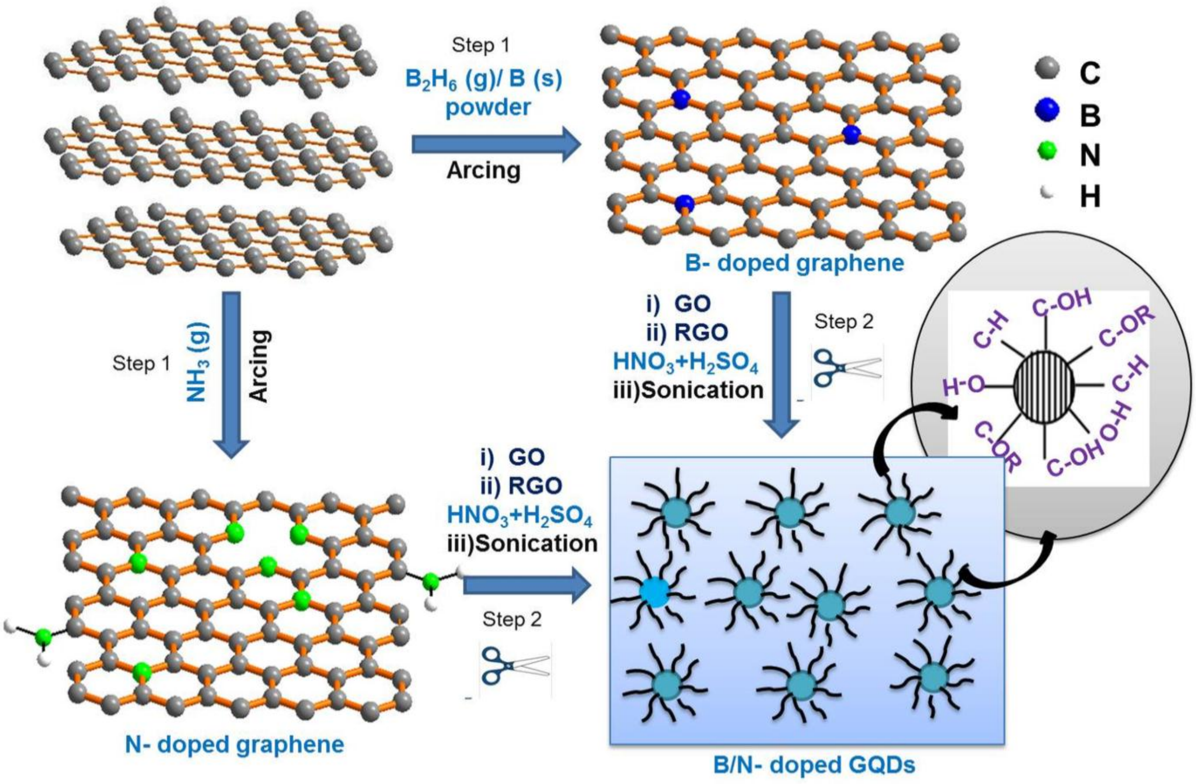

Figure 1. Synthetic strategy of B/N doped GQDs; step 1 describes the synthesis of doped graphene by arcing and step 2 describes the chemical scissoring of graphene sheets by acid treatment.

matrix to produce N-doped graphene. GQDs, B-GQDs and N-GQDs were produced by converting these graphene to graphene oxide followed by its reduction and finally cutting under the prolonged acid treatment (Step 2, Figure 1).

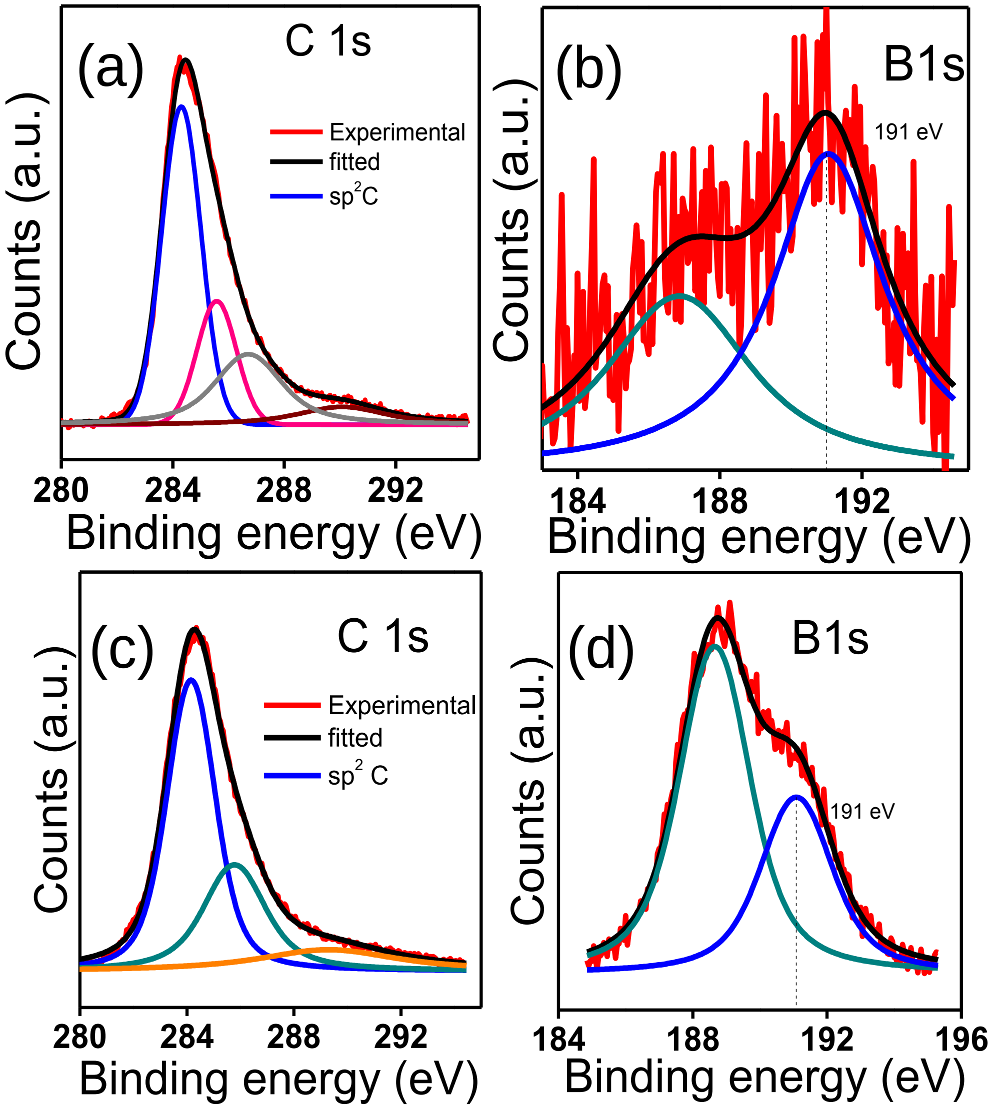

Figure 2. X-ray photoelectron spectra of B-doped graphenes. (a) C1s spectra and (b) B1s spectra of B-doped graphene prepared using boron powder route; (c) C1s spectra and (d) B1s spectra of B-doped graphene prepared using diborane route.

XPS measurements were carried out to establish the elemental compositions of B- and N - doped graphenes as well as B- and N-GQDs. The B/C atomic ratios were calculated to be ~2.5 and ~5 % in B-doped graphene quantum dots synthesized using boron powder (BGQD-

1) and B_2H_6 vapor (BGQD-2), respectively. Doping of B in the precursor graphene samples is confirmed by the B1s signal centered at 191.0 eV **(Figure 2)**, assigned to B atoms in the sp^2 carbon networks.

The predominant presence of carbon in both BGQD-1 and BGQD-2 are confirmed by the C1s spectra in **Figures 3a and b**, respectively. The high resolution C1s spectra show signals due to C=C, C-OH and C-O-C. The high resolution B1s spectrum of GQDs prepared with boron powder route shows peaks at 190.4 eV (**Figure 4a**), corresponding to the binding of boron atom with carbon. GQDs synthesized by diborane route show XPS peaks at 187.85 eV (B1s as in B_4C) and 191.2 eV (B 1s as in BCO_2) which confirm the presence of B in the GQDs (Figure 4b).

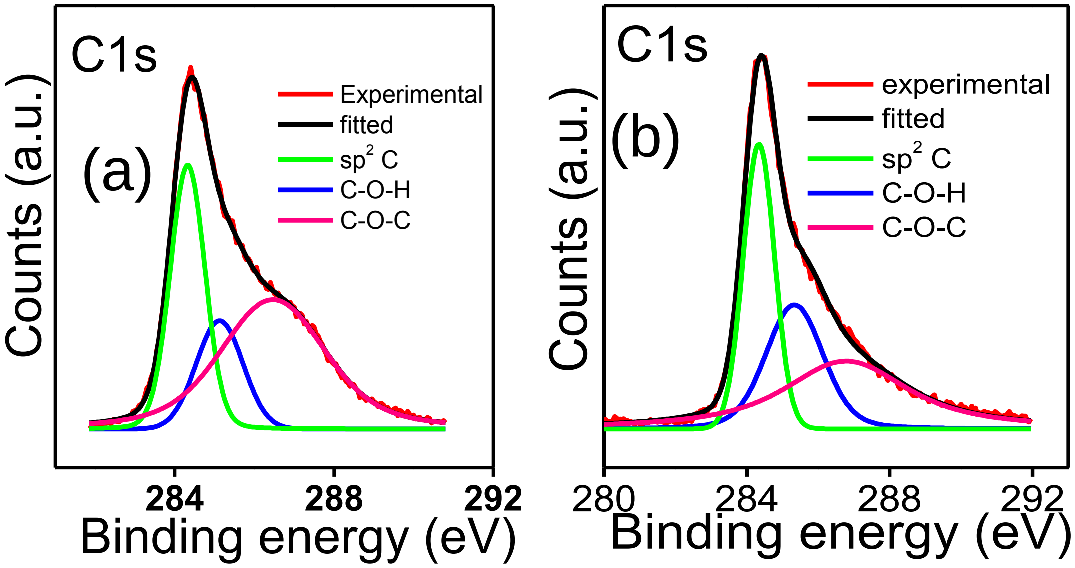

Figure 3. X-ray photoelectron spectra of B-doped GQDs. C1s spectra of B-GQDs prepared using (a) boron powder and (b) diborane route.

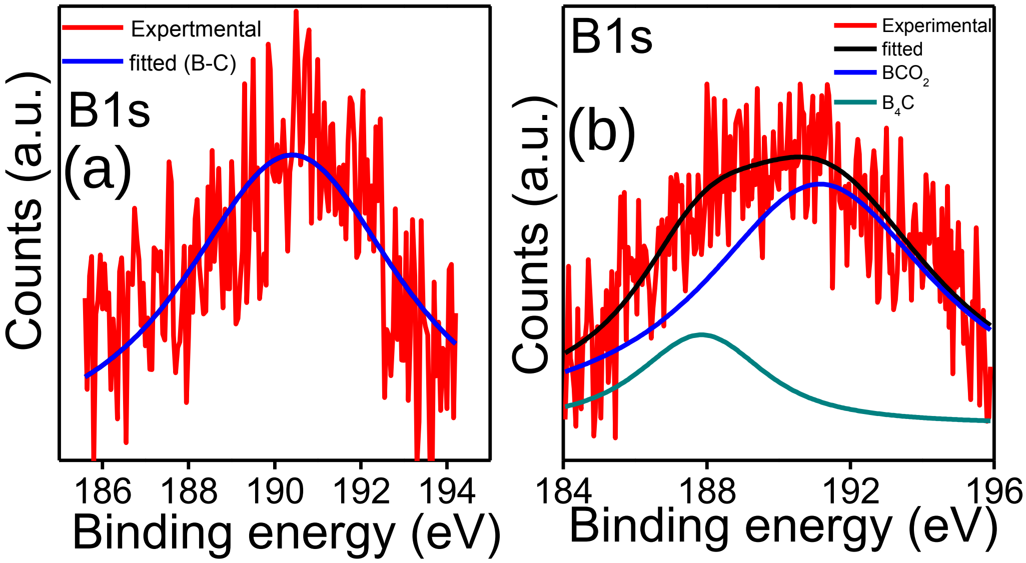

Figure 4. X-ray photoelectron spectra of B-doped GQDs. B1s spectra of B-GQDs prepared using (a) boron powder and (b) diborane route.

Presence of N in GQDs was confirmed by N1s spectrum (**Figure 5**). The deconvoluted N1s spectra consist of peaks at 399.6 eV and 400.7 eV characteristic of pyrrolic N and N in graphene sheet respectively, % of N being 2.2%.

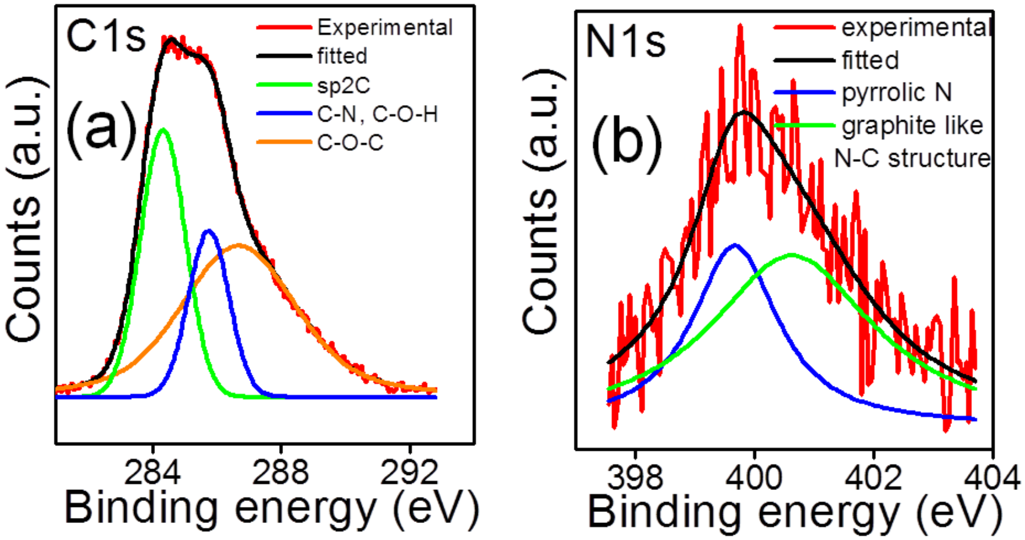

Figure 5. X-ray photoelectron spectra of N-doped GQDs. (a) C1s spectra and (b) N1s spectra of N-GQDs prepared using ammonium route**.**

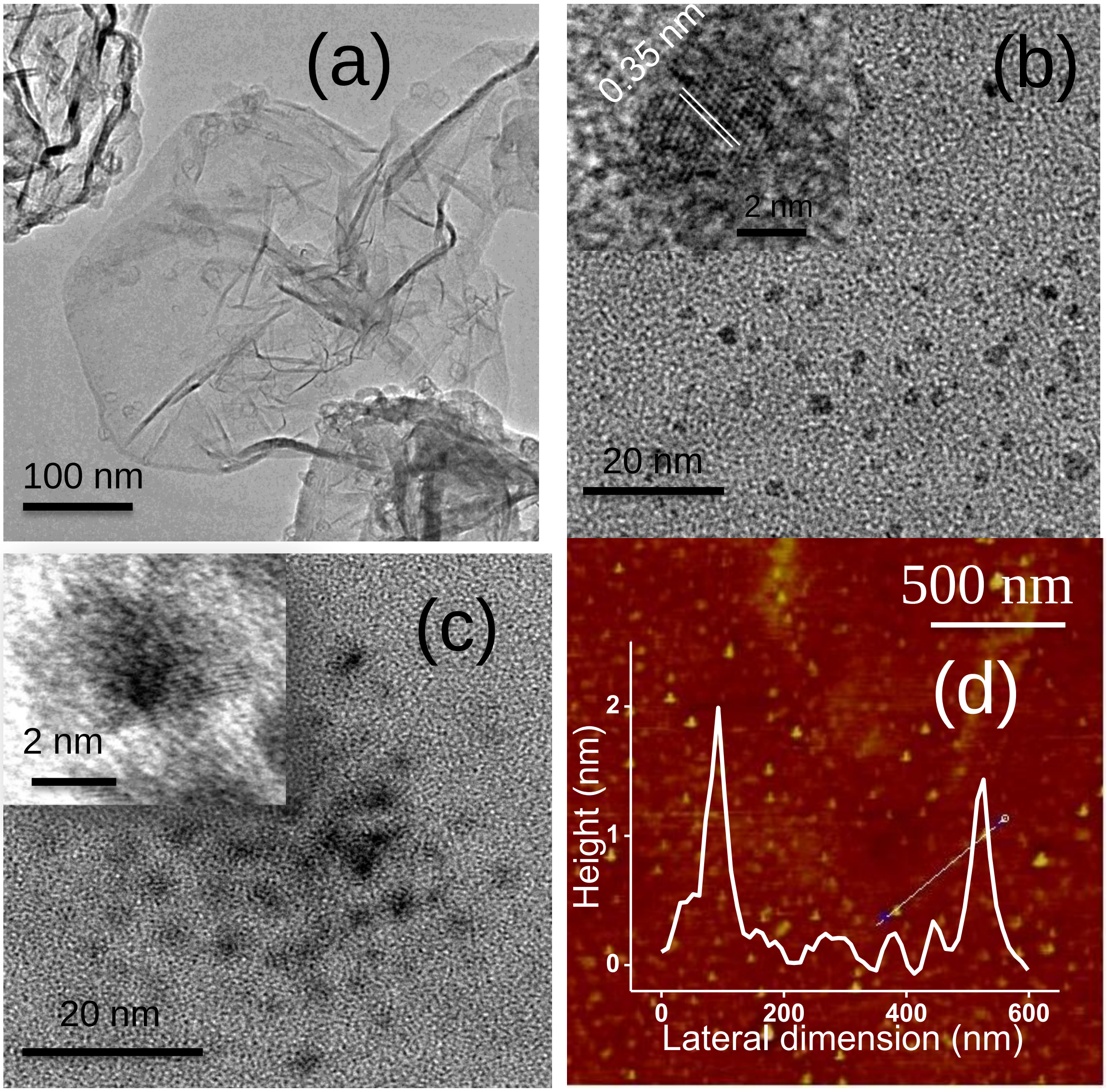

Figure 6. TEM images of (a) boron doped graphene and of GQDs prepared by using (b) boron powder and (c) diborane as B precursors. Inset shows the HRTEM images of the same (b, c). (d) AFM images of B-doped GQDs prepared by boron powder route.

In **Figure 6**, we show a TEM image of the arc-discharged B-doped graphene used as the precursor to prepare B-GQDs. TEM images of BGQD-1 and BGQD-2 indicate quantum dots to be narrow size range of 4-6 nm, respectively. The high resolution TEM (HRTEM) images of BGQD-1 and BGQD-2 (insets in Figures 6b and 6c) show an interlayer spacing of ~0.35 nm, indicating their graphitic nature and high crystallinity. TEM and HRTEM images of N-GQDs indicate the particle size to be ~6 nm. The atomic force microscope (AFM) image of

BGQD-1 demonstrates the topographic height distribution to be in the range 1-2 nm, corresponding to 2-3 graphene layers (Figure 6d).

UV-Vis spectra of the B/N doped GQDs and pristine GQD show a broad absorption edge ~325 nm, characteristic of a polycyclic aromatic π system (**Figure 7**).[61] We have measured the photoluminescence (PL) spectra of B/N-GQDs and of pristine GQD. GQD is known to show excitation wavelength-dependent PL emission in the 300-500 nm range,[40, 62, 87] but interestingly we observe excitation wavelength-independent PL emission (~400 nm) in the case of GQDs, B-GQDs and N-GQDs (Figure 7). Although the exact origin of the intense PL emission and the mechanism behind the excitation wavelength dependent emission is not fully understood, the luminescence is suggested to arise from a π-π* transition, due to emissive traps or free zigzag sites and/or edge states. Recent theoretical calculations reveal the relationship between PL and cluster size, suggesting a dependence of HOMO- LUMO gap on the size of graphene fragments.[41,88, 89] A recent experimental report points out that PL emission wavelengths can be varied in the whole visible region by gradual variation in size of graphite fragment.[7] It is likely that the narrow size distribution as well as highly crystallinity of the GQDs, B-GQDs and N-GQDs prepared in the present synthesis is responsible for excitation wavelength independent PL emission. Since we have synthesized GQDs from graphene, generated at high temperatures by gas phase arc-discharge reaction, there is highly crystallinity and low defect concentration in the GQDs. A few literature reports point out that the uniformity of size of GQDs could be behind the excitation wavelength independent emission.[51, 42, 17]

We observe PL emissions centered at 405 nm, 425 nm, 423 nm and 400 nm for GQD (Figure 7a), BGQD-1 (Figure 7b), BGQD-2 (Figure 7c), and N-GQD (Figure 7d), respectively. Increase in the PL emission wavelength in the case of B-GQDs compared to pristine GQDs may arise from the formation of trap states in the π-π* gap. The small blue-shift in the PL emission of N-GQDs compared to pristine GQDs can arise from the strong electron affinity of N compared to C in the N-GQDs.[19, 90, 91]

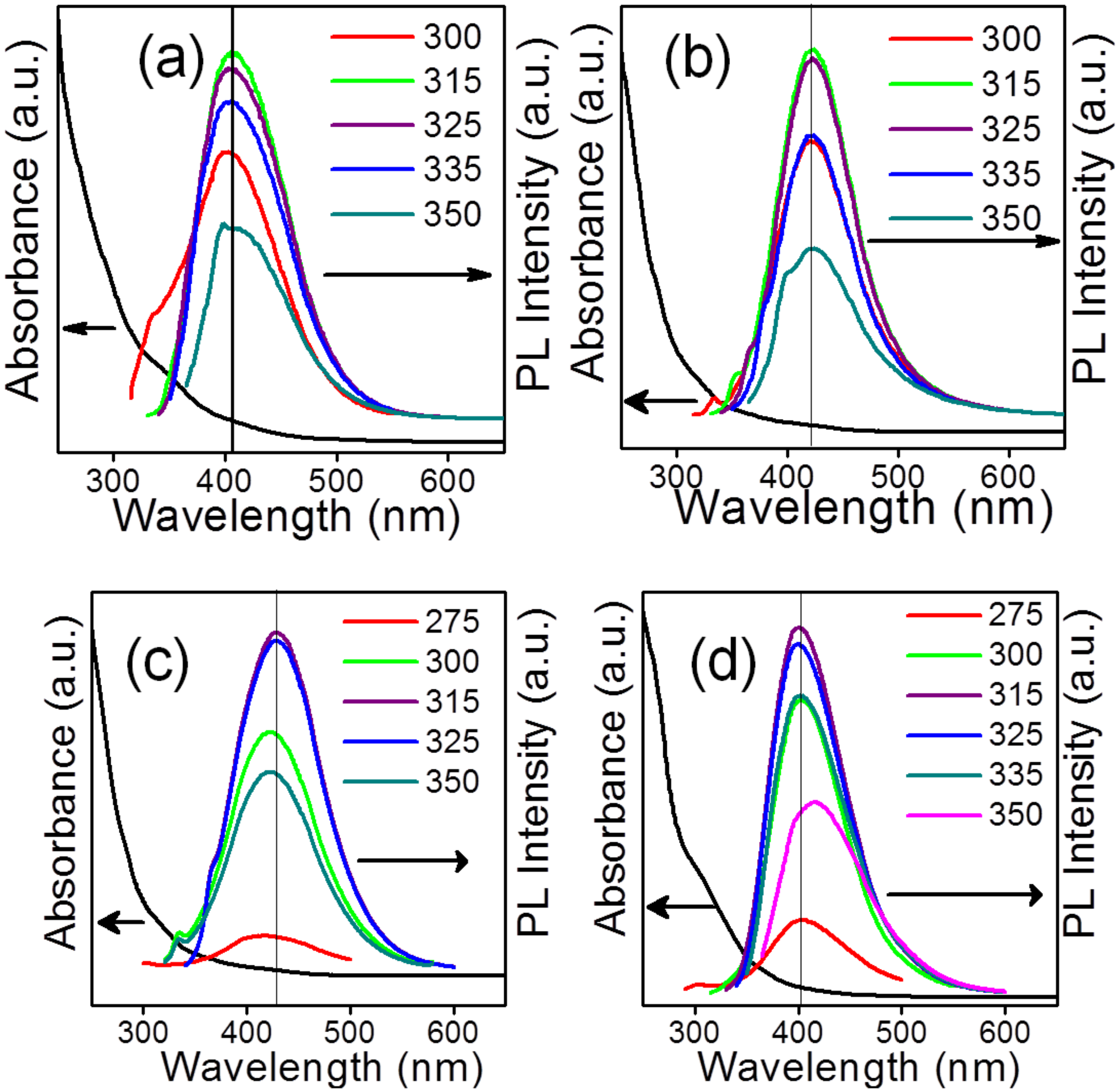

Figure 7. UV-vis and PL spectra (recorded at different excitation wavelengths) of (a) pristine GQD and B/N doped GQDs prepared under(b) boron powder (c) diborane (d) ammonium route.

The PL excitation (PLE) spectrum for the strongest luminescence of BGQD-2 indicates the presence of two bands centered at 273 nm and 317 nm (**Figure 8**). The two electronic transitions at 273 nm (4.5 eV) and 317 nm (3.9 eV) can be due to transitions from σ and π (HOMO) to π* (LUMO) of the GQDs, respectively.[90] The PL quantum yield

(PLQY) of GQDs, N-GQDs, BGQD-1 and BGQD-2 are 6.5, 8.7, 2.3 and 2.5 % respectively (**Table 1**).

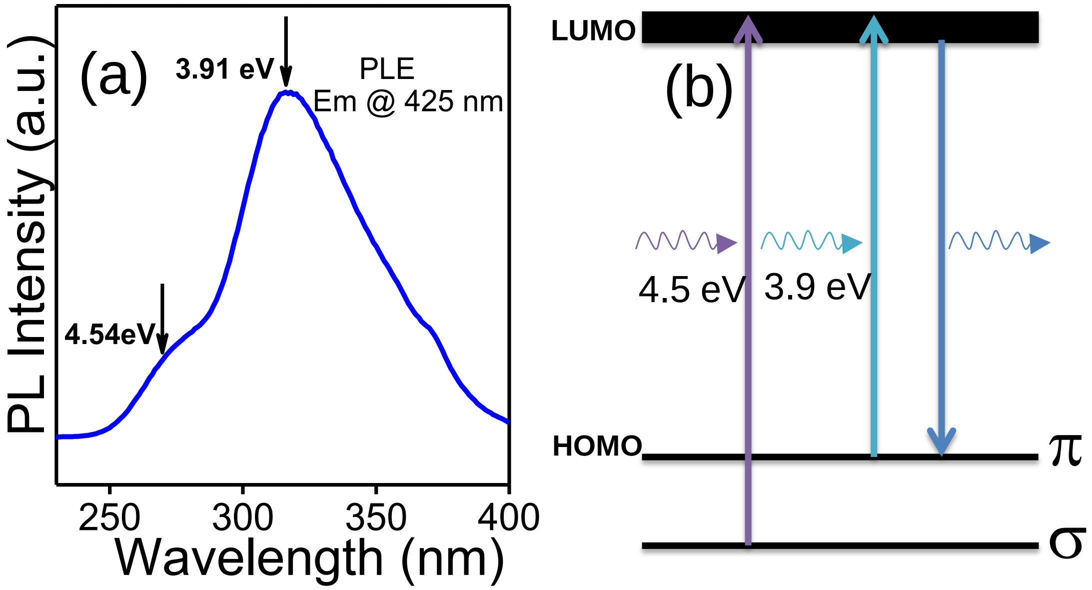

Figure 8. (a) PLE of BGQD-2 (prepared by diborane route) with the emission wavelength 425 nm (b) Electronic transition diagram of the spectrum (a).

Table 1. Quantum yields of GQDs

Material	Integrated Emission intensity (I)	Absorbance at 350 nm (A)	Quantum yield (φ)
Quinine sulphate in 0.1(M) H_2SO_4	3.8× 10^6	0.0037	57.7%
GQD	1.66× 10^6	0.025	6.56%
B-GQD(Boron powder)	2.2× 10^6	0.095	2.27%
B-GQD (Diborane)	2.35× 10^6	0.091	2.53%
N-GQD	6.6× 10^6	0.074	8.74%

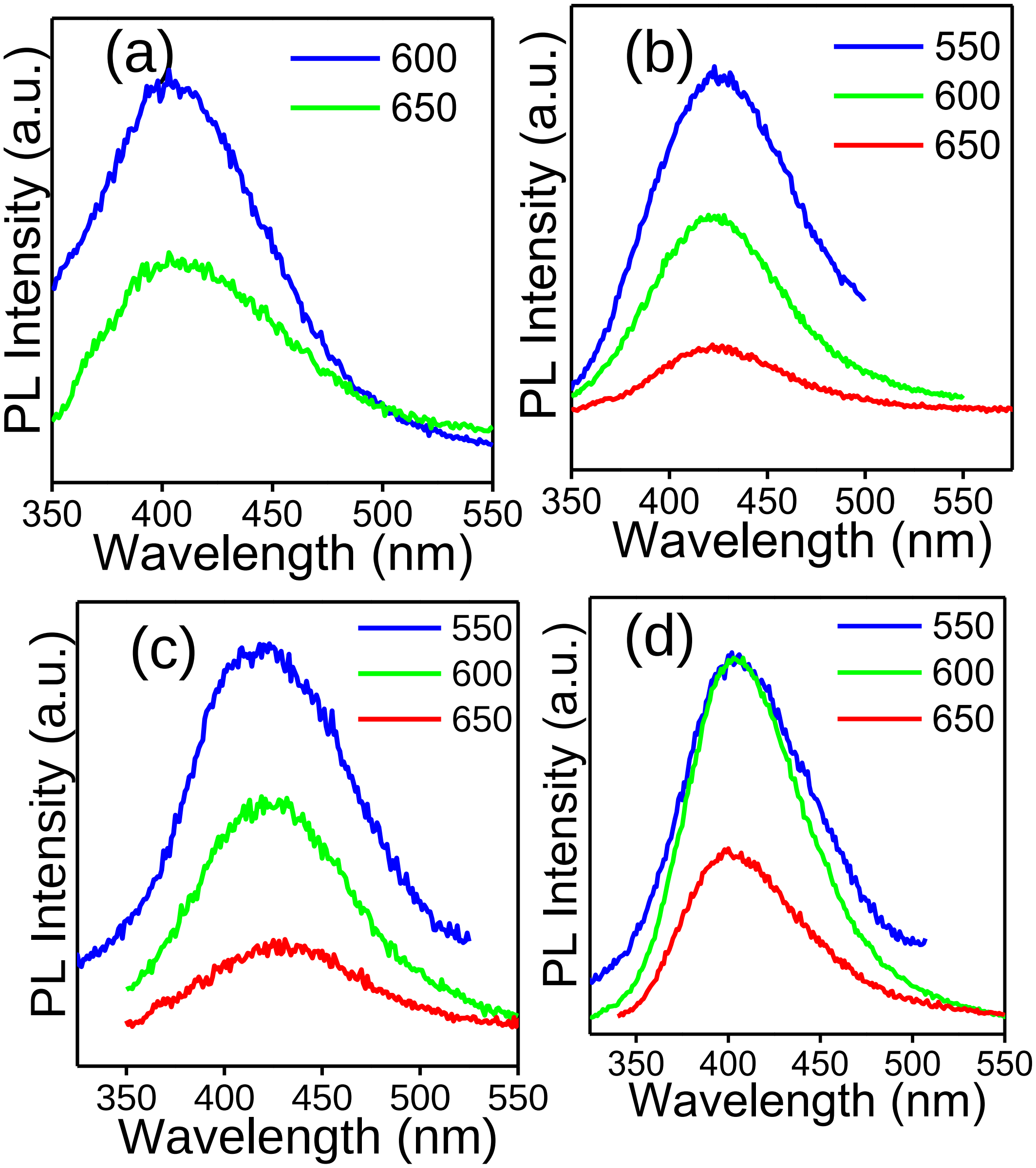

Figure 9. Upconverted PL spectrum of (a) pristine GQD and B/N doped GQDs prepared under(b) boron powder (c) diborane (d) ammonium route (excited at different wavelengths).

Apart from strong blue PL emission, pristine and doped GQDs show excellent upconversion photoluminescence (UCPL) emission, with excitation wavelength independent emission (**Figure 9**). We observe a red shift of ~25 nm in the UCPL emission of BGQD-1(Figure 9a) and BGQD-2 (Figure 9b) compared to the undoped GQDs, whereas we observe no significant change in the case of N-GQDs. Strong UCPL emission is observed when the excitation wavelength is 550 nm in the case of B and N doped GQDs. We have measured upconverted photoluminescence excitation (UCPLE) spectra with the strongest emission in case of the doped GQDs. The BGQDs show a strong and broad UCPLE feature centred at ~530 nm at a monitoring wavelength of 425 nm (**Figure 10**). NGQDs show a strong broad UCPLE feature centred at ~575 nm at a monitoring wavelength of 400 nm (Figure 10).

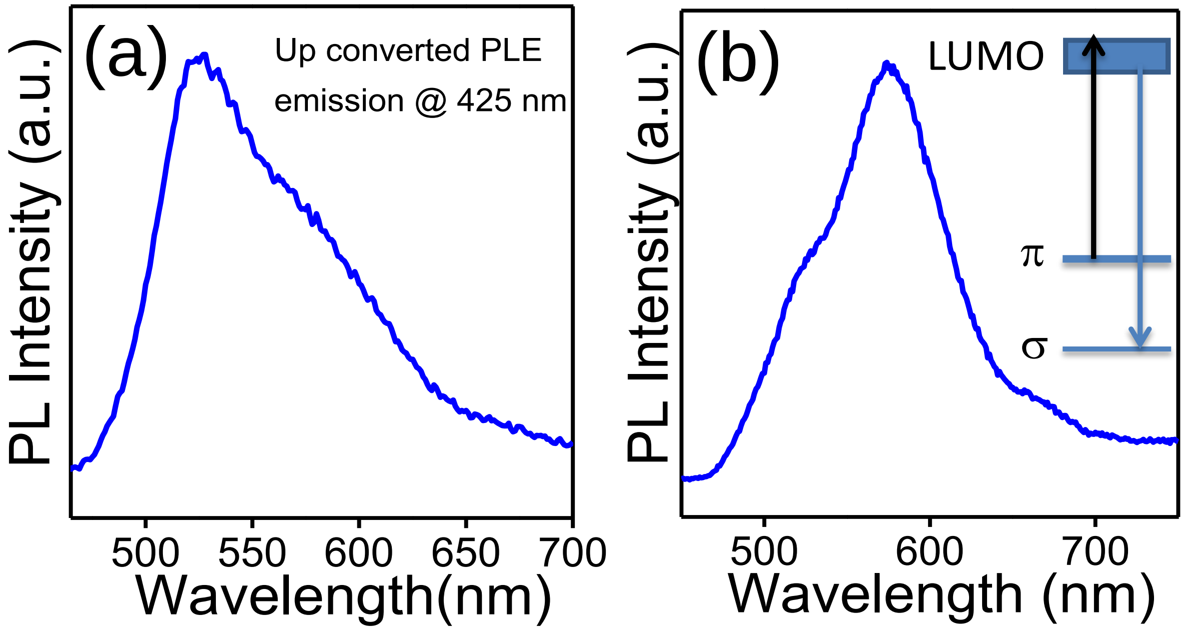

Figure 10. Unconverted PLE spectra of (a) B-GQDs (diborane route) and (b) N-GQDs with the emission wavelength 400 nm. Inset shows schematic probable mechanism of unconverted PL emission.

The upconverted PL spectra can be explained as arising from anti-Stokes transitions. In this process, π (HOMO) electrons of GQDs are excited to π* (LUMO), and the electron then goes back to low-energy σ orbital resulting in UCPL.[13, 92] We have estimated the energy difference (δE) between the σ and π orbitals of B-GQDs to be 0.56 eV, which is less compared to that in pristine GQDs (~0.85eV). The δE for N-GQDs is similar to that of pristine GQDs. Similar δE value for N-GQDs has been reported by Li et al.[90] The decrease in δE in B-GQDs compared to pristine GQDs is may be due to the increase in the band gap on B doping. The UCPL mechanism in GQDs is still not entirely understood and other processes such as multi photon excitation may also be responsible for the observation.[12, 93]

3.5. Conclusions

In conclusion, we have synthesized N-CQDs of 2-5 nm diameter and high N content by hydrothermal reaction as well as by MW irradiation of glucose in the presence of urea. Here, glucose acts the carbon source while urea decomposes to release NH_3. Besides comparing the photoluminescence property of N-CQDs with that of that of pristine CQDs, we have investigated the quenching of photoluminescence by graphene, with non-linear Stern-Volmer plots which suggest that the quenching process involves both static and dynamic energy transfer. Unlike electron-donating tetrathiafulvalene, electron-withdrawing tetracyanoethylene (TCNE) interacts differently with N-CQDs. This is likely because the N-doped quantum dots are n-type conductors. N-CQDs also exhibit enhanced activity for the photodegradation of methylene blue dye. It is noteworthy that white light emission can be obtained by mixing the blue-light emitting CQDs with yellow light emitters such as ZnO nanoparticles or graphene oxide.

We have synthesized B-and N- doped graphene quantum dots of average diameter 5-6 nm by a two-step chemical route. In the first step, B and N doped graphenes was prepared by the gas phase arc discharge in the presence of a B/N source. The second step involves chemical scissoring of B/N doped graphene to yield B/N-GQDs. We have observed strong blue PL emission in the GQDs as well as B/N-GQDs. We observe excitation wavelength-independent PL emission in the case of GQDs, B-GQDs and N-GQDs, which may be due to the narrow size distribution as well as highly crystallinity of the GQDs. Upconverted PL emission is also observed in B/N doped and undoped GQDs under visible light excitation and this may be find applications in energy technologies.

3.6. References

1 X. Xu, R. Ray, Y. Gu, H. J. Ploehn, L. Gearheart, K. Raker and W. A. Scrivens, *J. Am. Chem. Soc.*, 2004, **126**, 12736-12737.

2 L. A. Ponomarenko, F. Schedin, M. I. Katsnelson, R. Yang, E. W. Hill, K. S. Novoselov and A. K. Geim, *Science*, 2008, **320**, 356-358.

3 Y. Du and S. Guo, *Nanoscale*, 2016, **8**, 2532-2543.

4 S. Zhu, Y. Song, X. Zhao, J. Shao, J. Zhang and B. Yang, *Nano Res.*, 2015, **8**, 355-381.

5 J.-L. Li, K. N. Kudin, M. J. McAllister, R. K. Prud'homme, I. A. Aksay and R. Car, *Phys. Rev. Lett.*, 2006, **96**, 176101.

6 Z. Li, W. Zhang, Y. Luo, J. Yang and J. G. Hou, *J. Am. Chem. Soc.*, 2009, **131**, 6320-6321.

7 Y. Dong, J. Shao, C. Chen, H. Li, R. Wang, Y. Chi, X. Lin and G. Chen, *Carbon*, 2012, **50**, 4738-4743.

8 W. S. Hummers Jr and R. E. Offeman, *J. Am. Chem.Soc.*, 1958, **80**, 1339-1339.

9 D. Pan, J. Zhang, Z. Li and M. Wu, *Adv. Mater.*, 2010, **22**, 734-738.

10 Z. Lin, G. Waller, Y. Liu, M. Liu and C. P. Wong, *Adv. Energy Mater.*, 2012, **2**, 884-888.

11 H. Peng and J. Travas-Sejdic, *Chem. Mater.*, 2009, **21**, 5563-5565.

12 L. Cao, X. Wang, M. J. Meziani, F. Lu, H. Wang, P. G. Luo, Y. Lin, B. A. Harruff, L. M. Veca and D. Murray, *J. Am. Chem. Soc.*, 2007, **129**, 11318-11319.

13 J. Shen, Y. Zhu, C. Chen, X. Yang and C. Li, *Chem. Commun.*, 2011, **47**, 2580-2582.

14 X. Wang, X. Li, L. Zhang, Y. Yoon, P. K. Weber, H. Wang, J. Guo and H. Dai, *Science*, 2009, **324**, 768-771.

15 J. Peng, W. Gao, B. K. Gupta, Z. Liu, R. Romero-Aburto, L. Ge, L. Song, L. B. Alemany, X. Zhan and G. Gao, *Nano Lett.*, 2012, **12**, 844-849.

16 D. Pan, L. Guo, J. Zhang, C. Xi, Q. Xue, H. Huang, J. Li, Z. Zhang, W. Yu and Z. Chen, *J. Mater. Chem.*, 2012, **22**, 3314-3318.

17 M. Zhang, L. Bai, W. Shang, W. Xie, H. Ma, Y. Fu, D. Fang, H. Sun, L. Fan and M. Han, *J. Mater. Chem.*, 2012, **22**, 7461-7467.

18 Y. Li, Y. Zhao, H. Cheng, Y. Hu, G. Shi, L. Dai and L. Qu, *J. Am. Chem. Soc.*, 2011, **134**, 15-18.

19 Q. Li, S. Zhang, L. Dai and L.-s. Li, *J. Am. Chem. Soc.*, 2012, **134**, 18932-18935.

20 C. Hu, Y. Liu, Y. Yang, J. Cui, Z. Huang, Y. Wang, L. Yang, H. Wang, Y. Xiao and J. Rong, *J. Mater. Chem. B.* , 2013, **1**, 39-42.

21 Z. Ma, H. Ming, H. Huang, Y. Liu and Z. Kang, *New J.Chem.*, 2012, **36**, 861-864.

22 X. Zhai, P. Zhang, C. Liu, T. Bai, W. Li, L. Dai and W. Liu, *Chem. Commun.*, 2012, **48**, 7955-7957.

23 Y. Xu, M. Wu, Y. Liu, X. Z. Feng, X. B. Yin, X. W. He and Y. K. Zhang, *Chem. Eur. J.*, 2013, **19**, 2276-2283.

24 Q. Feng, Q. Cao, M. Li, F. Liu, N. Tang and Y. Du, *Appl. Phys. Lett.*, 2013, **102**, 013111.

25 S. Chandra, P. Patra, S. H. Pathan, S. Roy, S. Mitra, A. Layek, R. Bhar, P. Pramanik and A. Goswami, *J. Mater. Chem. B*, 2013, **1**, 2375-2382.

26 Y. Dong, H. Pang, H. B. Yang, C. Guo, J. Shao, Y. Chi, C. M. Li and T. Yu, *Angew. Chem. Int. Ed*, 2013, **52**, 7800-7804.

27 Y.-Q. Zhang, D.-K. Ma, Y. Zhuang, X. Zhang, W. Chen, L.-L. Hong, Q.-X. Yan, K. Yu and S.-M. Huang, *J. Mater. Chem.* , 2012, **22**, 16714-16718.

28 H. K. Sadhanala and K. K. Nanda, *J. Phys. Chem. C*, 2015, **119**, 13138-13143.

29 Y. Han, D. Tang, Y. Yang, C. Li, W. Kong, H. Huang, Y. Liu and Z. Kang, *Nanoscale*, 2015, **7**, 5955-5962.

30 M. K. Barman, B. Jana, S. Bhattacharyya and A. Patra, *J. Phys. Chem. C*, 2014, **118**, 20034-20041.

31 Q. Ye, F. Yan, D. Shi, T. Zheng, Y. Wang, X. Zhou and L. Chen, *J. Photoch. Photobiol. B*, 2016, **162**, 1-13.

32 Z. Fan, Y. Li, X. Li, L. Fan, S. Zhou, D. Fang and S. Yang, *Carbon*, 2014, **70**, 149-156.

33 X. Shan, L. Chai, J. Ma, Z. Qian, J. Chen and H. Feng, *Analyst*, 2014, **139**, 2322-2325.

34 L. Zhang, Z.-Y. Zhang, R.-P. Liang, Y.-H. Li and J.-D. Qiu, *Anal. Chem.*, 2014, **86**, 4423-4430.

35 A. B. Bourlinos, G. Trivizas, M. A. Karakassides, M. Baikousi, A. Kouloumpis, D. Gournis, A. Bakandritsos, K. Hola, O. Kozak and R. Zboril, *Carbon*, 2015, **83**, 173-179.

36 S. Jahan, F. Mansoor, S. Naz, J. Lei and S. Kanwal, *Anal. Chem.*, 2013, **85**, 10232-10239.

37 Y.-H. Li, L. Zhang, J. Huang, R.-P. Liang and J.-D. Qiu, *Chem. Commun.*, 2013, **49**, 5180-5182.

38 Z.B. Qu, X. Zhou, L. Gu, R. Lan, D. Sun, D. Yu and G. Shi, *Chem. Commun.*, 2013, **49**, 9830-9832.

39 H. Fei, R. Ye, G. Ye, Y. Gong, Z. Peng, X. Fan, E. L. G. Samuel, P. M. Ajayan and J. M. Tour, *ACS Nano*, 2014, **8**, 10837-10843.

40 H. Li, Z. Kang, Y. Liu and S.-T. Lee, *J. Mater. Chem.*, 2012, **22**, 24230-24253.

41 H. Li, X. He, Z. Kang, H. Huang, Y. Liu, J. Liu, S. Lian, C. H. A. Tsang, X. Yang and S.-T. Lee, *Angew. Chem.*, 2010, **49**, 4430-4434.

42 S. Zhuo, M. Shao and S.-T. Lee, *ACS Nano*, 2012, **6**, 1059-1064.

43 H. Yu, Y. Zhao, C. Zhou, L. Shang, Y. Peng, Y. Cao, L.-Z. Wu, C.-H. Tung and T. Zhang, *J. Mater. Chem. A*, 2014, **2**, 3344-3351.

44 D. Qu, Z. Sun, M. Zheng, J. Li, Y. Zhang, G. Zhang, H. Zhao, X. Liu and Z. Xie, *Adv. Opt. Mater.* , 2015, **3**, 360-367.

45 J. Liu, Y. Liu, N. Liu, Y. Han, X. Zhang, H. Huang, Y. Lifshitz, S.-T. Lee, J. Zhong and Z. Kang, *Science*, 2015, **347**, 970-974.

46 T.-F. Yeh, C.-Y. Teng, S.-J. Chen and H. Teng, *Adv. Mater.*, 2014, **26**, 3297-3303.

47 K. Sardar and C. N. R. Rao, *Adv. Mater.*, 2004, **16**, 425-429.

48 K. Biswas, K. Sardar and C. N. R. Rao, *Appl. Phys. Lett.*, 2006, **89**, 132503.

49 A. Gomathi and C. N. R. Rao, *Mater. Res. Bull.* , 2006, **41**, 941-947.

50 K. Gopalakrishnan, A. Govindaraj and C. N. R. Rao, *J. Mater. Chem. A*, 2013, **1**, 7563-7565.

51 L. S. Panchakarla, K. S. Subrahmanyam, S. K. Saha, A. Govindaraj, H. R. Krishnamurthy, U. V. Waghmare and C. N. R. Rao, *Adv. Mater.*, 2009, **21**, 4726-4730.

52 K. S. Subrahmanyam, L. S. Panchakarla, A. Govindaraj and C. N. R. Rao, *J. Phys. Chem. C*, 2009, **113**, 4257-4259.

53 Z.-H. Sheng, H.-L. Gao, W.-J. Bao, F.-B. Wang and X.-H. Xia, *J. Mater. Chem.*, 2012, **22**, 390-395.

54 X. Wang, K. Qu, B. Xu, J. Ren and X. Qu, *J. Mater. Chem.* , 2011, **21**, 2445-2450.

55 C. Pacholski, A. Kornowski and H. Weller, *Angew. Chem. Int. Ed.* , 2002, **41**, 1188-1191.

56 L. Sun, L. Wang, C. Tian, T. Tan, Y. Xie, K. Shi, M. Li and H. Fu, *RSC Adv.*, 2012, **2**, 4498-4506.

57 R. I. Walton, *Chem. Soc. Rev.*, 2002, **31**, 230-238.

58 L. Tang, R. Ji, X. Cao, J. Lin, H. Jiang, X. Li, K. S. Teng, C. M. Luk, S. Zeng and J. Hao, *ACS Nano*, 2012, **6**, 5102-5110.

59 B. De and N. Karak, *RSC Adv.*, 2013, **3**, 8286-8290.

60 S.-H. Yu, X. Cui, L. L. Li, K. Li, B. Yu, M. Antonietti and H. Colfen, *Adv. Mater.*, 2004, **16**, 1636-1640.

61 S.-Y. Xie, R.-B. Huang and L.-S. Zheng, *J. Chromatogr. A*, 1999, **864**, 173-177.

62 S. N. Baker and G. A. Baker, *Angew. Chem. Int. Ed.*, 2010, **49**, 6726-6744.

63 L. Cao, M. J. Meziani, S. Sahu and Y.-P. Sun, *Acc. Chem. Res.*, 2012, **46**, 171-180.

64 Z.-A. Qiao, Y. Wang, Y. Gao, H. Li, T. Dai, Y. Liu and Q. Huo, *Chem. Commun.*, 2010, **46**, 8812-8814.

65 H. Liu, T. Ye and C. Mao, *Angew. Chem. Int. Ed.*, 2007, **46**, 6473-6475.

66 Z. Chen, S. Berciaud, C. Nuckolls, T. F. Heinz and L. E. Brus, *ACS Nano*, 2010, **4**, 2964-2968.

67 Z. Liu, Q. Liu, Y. Huang, Y. Ma, S. Yin, X. Zhang, W. Sun and Y. Chen, *Adv. Mater.*, 2008, **20**, 3924-3930.

68 H. Dong, W. Gao, F. Yan, H. Ji and H. Ju, *Anal. Chem.*, 2010, **82**, 5511-5517.

69 H. S. S. R. Matte, K. S. Subrahmanyam, K. V. Rao, S. J. George and C. N. R. Rao, *Chem. Phys. Lett.*, 2011, **506**, 260-264.

70 W. Wei, C. Xu, J. Ren, B. Xu and X. Qu, *Chem. Commun.*, 2012, **48**, 1284-1286.

71 A. Airinei, R. I. Tigoianu, E. Rusu and D. O. Dorohoi, *Digest J. Nanomater. Biostruct.*, 2011, **6**, 1265-1272.

72 J. R. Lakowicz, Springer, 2009, p. 281.

73 X. Wang, L. Cao, F. Lu, M. J. Meziani, H. Li, G. Qi, B. Zhou, B. A. Harruff, F. Kermarrec and Y.-P. Sun, *Chem. Commun.*, 2009, 3774-3776.

74 R. Voggu, B. Das, C. S. Rout and C. N. R. Rao, *J. Phys. Condens. Matter.*, 2008, **20**, 472204.

75 C. N. R. Rao and R. Voggu, *Mater. today*, 2010, **13**, 34-40.

76 P. Yu, X. Wen, Y.-R. Toh and J. Tang, *J. Phys. Chem. C*, 2012, **116**, 25552-25557.

77 P. Kumar, L. S. Panchakarla, S. V. Bhat, U. Maitra, K. S. Subrahmanyam and C. N. R. Rao, *Nanotechnology*, 2010, **21**, 385701.

78 K. S. Subrahmanyam, P. Kumar, A. Nag and C. N. R. Rao, *Solid State Commun.*, 2010, **150**, 1774-1777.

79 D. I. Son, B. W. Kwon, D. H. Park, W.-S. Seo, Y. Yi, B. Angadi, C.-L. Lee and W. K. Choi, *Nat. Nanotechnol.*, 2012, **7**, 465-471.

80 W. Kwon, S. Do, J. Lee, S. Hwang, J. K. Kim and S.-W. Rhee, *Chem. Mater.*, 2013, **25**, 1893-1899.

81 http://hyperphysics.phy-astr.gsu.edu/hbase/vision/cie.html.

82 A. Houas, H. Lachheb, M. Ksibi, E. Elaloui, C. Guillard and J.-M. Herrmann, *Appl. Catal. B: Environ.*, 2001, **31**, 145-157.

83 R. I. Jafri, N. Rajalakshmi and S. Ramaprabhu, *J. Mater. Chem.*, 2010, **20**, 7114-7117.

84 V. F. Lapko, I. P. Gerasimyuk and Y. A. Tarasenko, *Russ. J. Phys. Chem. A*, 2010, **84**, 934-940.

85 U. Gupta, B. S. Naidu and C. N. R. Rao, *Dalton Trans.*, 2015, **44**, 472-474.

86 B. C. M. Martindale, G. A. M. Hutton, C. A. Caputo and E. Reisner, *J. Am. Chem. Soc.*, 2015, **137**, 6018-6025.

87 L. Li, G. Wu, G. Yang, J. Peng, J. Zhao and J.-J. Zhu, *Nanoscale*, 2013, **5**, 4015-4039.

88 X. Yan, X. Cui and L.-s. Li, *J. Am. Chem. Soc.*, 2010, **132**, 5944-5945.

89 X. Yan, B. Li, X. Cui, Q. Wei, K. Tajima and L.-s. Li, *J. Phys. Chem. Lett.*, 2011, **2**, 1119-1124.

90 M. Li, W. Wu, W. Ren, H.-M. Cheng, N. Tang, W. Zhong and Y. Du, *Appl. Phys. Lett.*, 2012, **101**, 103107.

91 K. Gong, F. Du, Z. Xia, M. Durstock and L. Dai, *Science*, 2009, **323**, 760-764.

92 S. Zhu, J. Zhang, X. Liu, B. Li, X. Wang, S. Tang, Q. Meng, Y. Li, C. Shi and R. Hu, *RSC Adv.*, 2012, **2**, 2717-2720.

93 Z. Gan, X. Wu, G. Zhou, J. Shen and P. K. Chu, *Adv. Opt. Mater.*, 2013, **1**, 554-558.

Part 4

Interaction of electron donor and acceptor molecules with inorganic nanostructures

Part 4

Interaction of electron donor and acceptor molecules with inorganic nanostructures*

Summary

Interaction of CdSe and ZnO nanocrystals with electron-donating tetrathiafulvalene (TTF) and electron-withdrawing tetracyanoethylene (TCNE) has been investigated. Isothermal calorimetry shows CdSe nanocrystals interact more strongly with TCNE than TTF. Interaction of larger CdSe nanocrystals with TCNE causes a red-shift in the band-edge emission because of agglomeration, while the smaller CdSe nanocrystals, exhibiting stronger interaction with TCNE modify the optical gap of the nanocrystal. Luminescence of CdSe gets quenched sharply after addition of both TTF and TCNE. ZnO nanocrystals also exhibit luminescence quenching to lesser extent. Defect-emission of ZnO nanocrystals gets red or blue-shifted after interaction with TTF or TCNE respectively.

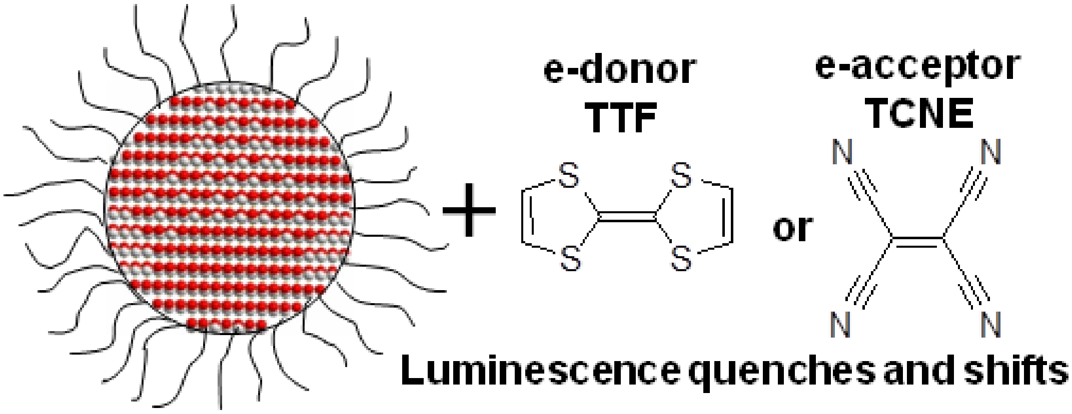

We were interested to explore the interaction of electron donor and acceptor molecules with a two-dimensional layered material such as MoS_2 to explore the occurrence of charge-transfer if any. With this purpose, we have studied the interaction of few-layer MoS_2 with TTF and TCNE. It is to be noted that MoS_2 layers consist of Mo atoms sandwiched between two layers of chalcogen atoms, where the adjacent sheets are stacked by van der Waals interactions. We have observed the occurrence of charge-transfer of few-layer MoS_2 material with TTF, but not with TCNE. Electronic absorption spectroscopic measurements indicate the formation of TTF radical cation by the interaction of TTF with few-layer MoS_2 material, accompanied by the stiffening of the A_{1g} mode of MoS_2 in the Raman spectrum. This shift in the Raman A_{1g} mode is opposite to that found in electrochemical doping. We have carried out detailed first principle calculations to understand the results.

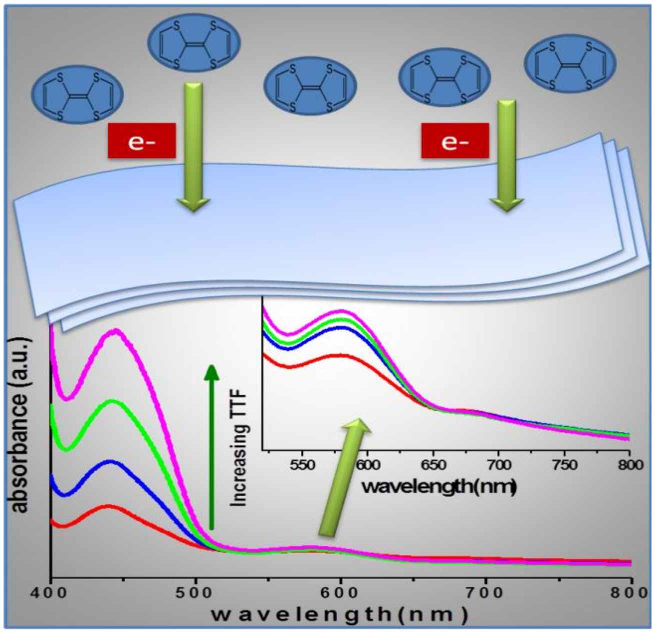

∗Papers based on this part of the thesis have been published in ***Chem. Phys. Lett. (2013) and Chem. Asian J. (2013).***

4.1. Introduction

Electron transfer in and out of nanocrystals is a subject of interest for many years, mostly in the context of photochemistry and photovoltaics. This can be realized either by applying electric field, with a gate voltage, or functionalization or through physical adsorption of electron donor/acceptor molecules. For instance, in the case of graphene based devices, a practical issue is to manipulate the carrier concentration by shifting the Fermi level of the graphene above or below the Dirac point. Chemical doping is also an effective method of tailoring the electrical properties of graphene which controls the hole or electron concentrations. The key parameter that should control the p-type doping is the energy difference between the lowest unoccupied molecular orbital (LUMO) and the work function of the material. In the same spirit, in case of n-type doping mechanism, the key parameter that controls the charge transfer is the energy difference between the highest occupied molecular orbital (HOMO) i.e. the ionization potential of the molecule and the work function of the material.

4.1.1. Interaction of semiconductor nanocrystals with e-donors and e-acceptors

Colloidal semiconductor nanocrystals are being investigated widely due to their interesting size-dependent optical, electronic and other properties.[1-4] An important feature of nanocrystals is the large surface to volume ratio, where ions in the surface are under-coordinated as compared to that in the core of nanocrystals. The under-coordinated surface sites can be passivated with organic ligands thereby stabilizing the nanocrystals in a given solvent. Optical properties of semiconductor nanocrystals (NCs) are affected by the nanocrystal-molecule interface.[5-7] Photo-generated electron-hole pairs can recombine radiatively or non-radiatively depending upon the energy levels of the nanocrystal-molecule interface and thereby influence the luminescence efficiency.[5] A red-shift in the excitonic absorption has been observed when phenyldithiocarbamate binds to the CdSe nanocrystal surface since the HOMO of the molecule has the appropriate energy and symmetry to interact with the valence states of the nanocrystal.[5]

Charge-transfer across the semiconductor nanocrystal-organic molecule interface plays a vital role, and affects the optical properties of the nanocrystals. Study of charge-transfer phenomenon is critical since the optical properties, specially the luminescence of nanocrystals, find useful applications in biology and optoelectronic devices. Electrons and holes can be injected to semiconductor nanocrystal films by applying bias voltages and the resulting optical properties examined.[8-11] Gooding et. al[8] observed the changes in the PL spectra of 2D monolayers of CdSe/CdS/ZnS semiconductor nanocrystals (NCs) deposited on gold substrates as a function of applied potential under atmospheres of both nitrogen and air. It has been observed that applying a positive potential to the film quenches the PL intensity irreversibly. This phenomana has observed irrespective of whether the sample is placed under an inert atmosphere or exposed to water vapor or air. But the application of negative potential gives two completely different results which are reversible in nature. Under nitrogen environment PL intesity quenches but under air PL intesity increases by a factor of more than 2 and undergoes photobrightening. These results surmises that photobrightening and charge carrier injection are coupled with each other.

An extra charge in the nanocrystal can facilitate non-radiative Auger recombination and reduce the luminescence efficiency.[8] It can also cause emission related to positively or negatively charged excitons[11] and enhance the luminescence efficiency by reducing the surface- related mid-gap trap states.[10]

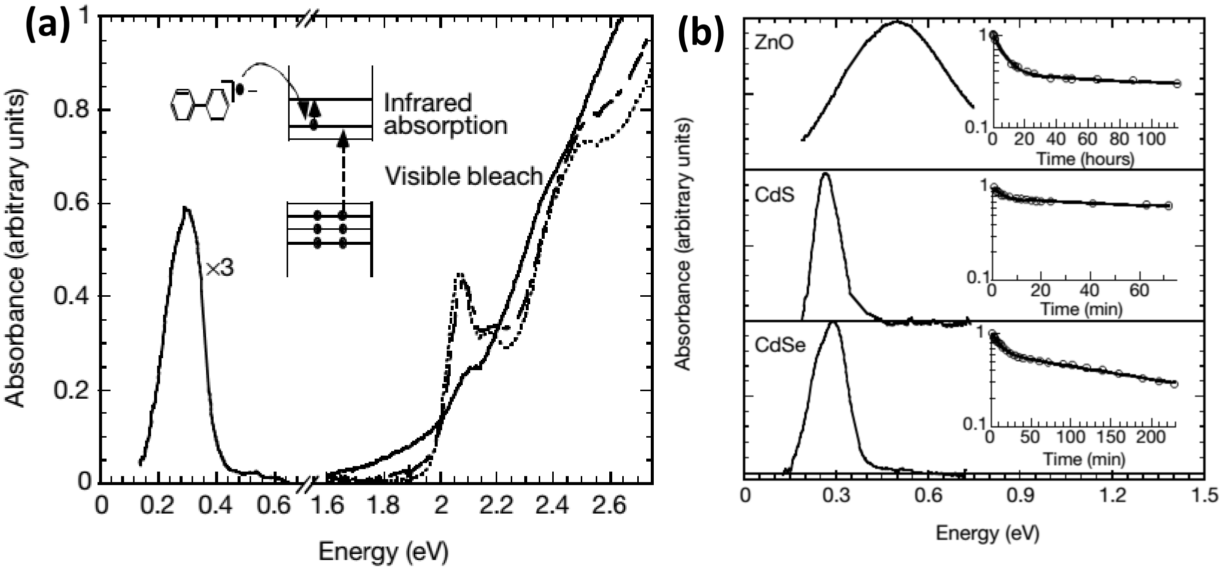

Figure 1. (a) Absorption spectra of CdSe nanocrystals before (dotted line), immediately after (solid line) and 27 hours after (dashed line) after injecting electron with the addition of sodium biphenyl. The solid line shows the appearance of IR spectra with the optical bleaching of visible absorption bands. (b) Infrared absorption spectra of ZnO, CdS and CdSe nanocrystals of specific size range. Inset shows the evolution of IR band with time (normailized) where the x axis is in hours. Reproduced by permission of Nature Publishing Group from Ref.[12].

Understanding the effect of injection of electrons and holes in colloidal semiconductor nanocrystals is of importance. In this context, Guyot-Sionnest et al.[12, 13] have utilized the combination of infrared and optical spectroscopy as a diagnosis tool of the n-type character of the nanocrystals. More specifically infrared spectroscopy of the $1S_e$–$1P_e$ intraband transition has been used to ascertain that the electrons are injected in the Lowest Unoccupied Quantum-Confined Orbital (LUQCO) of the nanocrystals, instead of merely charging them by occupation of surface states.

As shown in **Figure 1a**, that the injection of an electron in the conduction band of a semiconductor nanocrystal ($1S_e$), gives rise to an intra-conduction-band allowed infrared transition to the next higher state ($1P_e$) and at the same time bleaches the inter-band excitonic transitions, quenches the luminescence. The infrared absorption spectra of n-type ZnO, CdS and CdSe nanocrystals prepared by the electron injection method is shown in Figure 1b. It has been reported that at room temperature, ~30% of the infrared absorption is observed even after 5 days in case of n-type ZnO nanocrystals, whereas it completely decays in less than 2 days for both CdS and CdSe nanocrystals and is explained based on the relative reduction potentials of the semiconductotor and of the constituent elements.

Weiss et al.[6] have varied the electron donor capability of para-substituted aniline (R-aniline) ligand and studied the modification of optical properties of colloidal CdSe nanocrystals caused by the ligand. This modification depends on two factors: (a) the binding affinity of R-aniline depending on the R group and (b) electronic interactions depending the oxidation potential of these R-aniline ligands after they are bound with CdSe NCs. Quenching of the nanocrystal luminescence occurred with all the R-Aniline ligands, but the quenching behavior varied depending upon the electron-donating or electron-withdrawing nature of the R group as shown in **Figure 2**. The predominant mechanism of PL quenching is the passivation of uncoordinated Cd^{2+} surface sites through electron withdrawing substituents like R= H, Br, OCF_3, and reductive quenching through photo induced hole transfer for R = MeO, $(Me)_2N$.

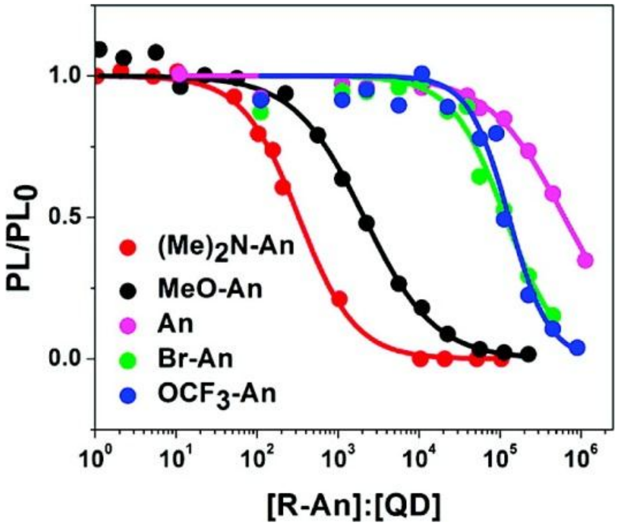

Figure 2. The ratio of PL intensity of CdSe NCs after and before addition of para-substituted aniline (R-aniline) ligands. Different R groups used in the experiment are given inside the figure. Reproduced by permission of American Chemical Society from Ref.[6].

4.1.2. Interaction of graphene with e-donor and e-acceptor

Several electron donor and electron acceptor molecules have been studied for doping of graphene or single-walled carbon nanotubes and substantial experimental have been conducted to understand changes in their electronic structures and for further property modifications. Doping molecules such as TCNQ, TTF, TCNE, and F_4-TCNQ has been employed to investigate the interactions with carbon nanostructures.[14-17] Graphene has emerged to be a material of great interest because of its unique electronic structure and properties associated with its two-dimensional structure.[18, 19] Graphene exhibits significant changes in electronic structure and properties on introduction of electrons or holes by electrochemical means.[20] Such doping is reported to stiffen the Raman G band (frequency of Raman band increases). Electron and hole doping can also be achieved by molecular charge transfer through non-covalent interaction with electron donor and acceptor molecules respectively. Molecular charge-transfer with graphene has been investigated in detail by using Raman spectroscopy and other techniques.[15, 16] Charge-transfer interaction with an electron donor molecule like tetrathiafulvalene (TTF) softens the G band of graphene whereas stiffening occurs upon interaction with an electron acceptor like tetracyanoethylene (TCNE). These changes in the Raman G band are different from those found with electrochemical doping.[20]

Graphene possesses a high mobility of up to 10^6 $cm^2/V.$ s,[21, 22] but the absence of a band gap limits its application in electronic or optoelectronic devices. Alternatively, molybdenum disulfide (MoS_2) is one of the widely studied semiconducting layered materials which possess a thickness-dependent energy band gap.[23, 24] Because of this, MoS_2 has gained much attention as a promising channel material in next-generation nanoelectronics.

4.1.3. Interaction of MoS_2 with e-donor and e-acceptor

Doping in MoS_2 can be performed via three possible ways. One approach to effectively dope MoS_2 is to substitute S atom with halogen atoms or substitute Mo with transition metals.[25, 26] Although the structure of MoS_2 is inevitably disturbed by the substitutional doping. Another approach is to physically adsorb molecules on MoS_2. However, the physically absorbed molecules and chemical doping don't give a stable doped MoS_2 system. Chemical functionalization is the last possible route which generally involves tedious synthesis processes and often alters the initial structure evitably.[27, 28]

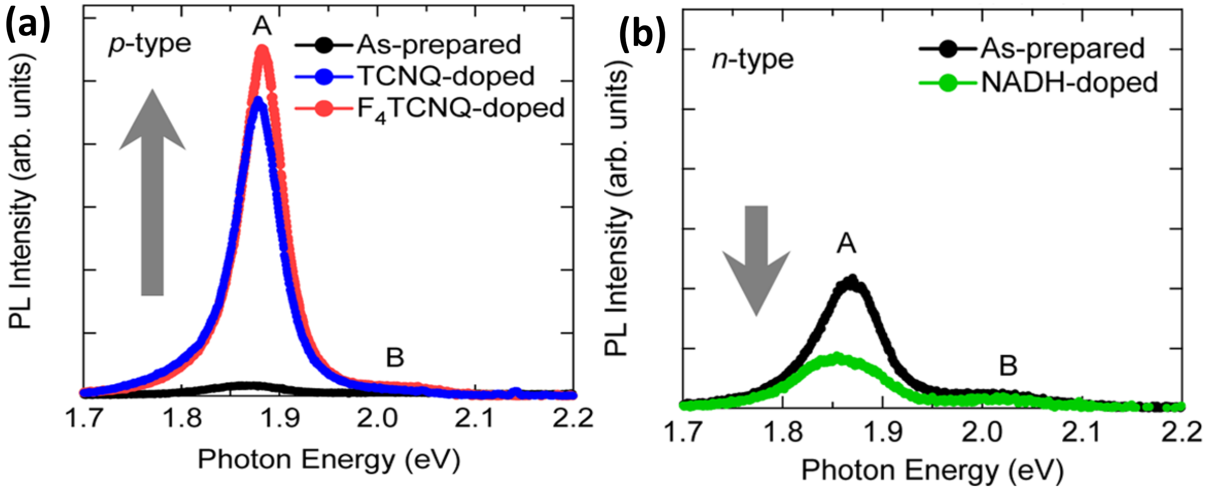

Figure 3. Change in photoluminescence intensity of Monolayer MoS_2 before and after electron (a) extraction to TCNQ, F_4TCNQ and (b) injection from NADH. Reproduced by permission of American Chemical Society from Ref.[26].

The PL intensity of Monolayer (ML) MoS_2 was drastically enhanced by the adsorption of p-type dopants like TCNQ and F_4-TCNQ with high electron affinity but reduced by the adsorption of n-type dopants such as NADH (**Figure 3**). This enhanced PL is found to be as a result of changing the dominant PL process from the recombination of the trion (negative) to the recombination of the exciton under extraction of excess electrons.[26] In contrast, the reduction in PL intensity of ML-MoS_2 is due to the suppression of exciton PL by the injection of excess electrons supplied by n-type dopants. Moreover the flat band potential of MoS_2 (−0.13 eV vs SHE) is reported to be lower than the reduction potentials of F_4TCNQ (0.84 eV vs SHE) and TCNQ (0.46 eV vs SHE) which act as a driving force of electron donation to these p-type dopants from MoS_2. In contrast, the oxidation potential of NADH (−0.32 eV vs SHE) lowers than MoS_2, which makes it an electron donor.

These observations by Mouri et. al[26] indicates that the optical properties in ML MoS_2 can be manipulated controllably by electron or hole doping. Recently n-type doping in ML MoS_2 is achieved with with K, blue violegen and Cs_2CO_3 doping.[29, 30 31] Cs_2CO_3, which is known as an efficient electron injecting material in OLEDs has been in situ deposited over ML MoS_2 and is found to increase the charge carrier concentrations by 9 times. The negative trion formation has been observed due to electron doping which in turn supperess the PL intesity with an increment in photocurrent.[29] Metal ion functionalization is also found to induce n- and p-type doping in MoS_2.[32] Metal ions with increasing work function are prone to act as p-type dopants such as Pt is found to be most active. n-type doping is obtained with Yttrium. However these doping effects are unstable and decay rapidly with increasing layer numbers of MoS_2.

Recently, intentionally created S- vacancy sites of MoS_2 has been functionalized with thiol terminating electron donating and accepting molecules. The amine and fluorine containing functionality is found to give n- and p-type doping respectively.[33] MoS_2 nanosheets decorated with optoelectronically active chromophore pthalocyanine results in an electronic heterostrusture which shows the charge transfer.[34] MoS_2 nanocrystals synthesized on DNA-host matrix has been reported to quench the PL intensity via fluorescence resonance energy transfer of dye donor (H258) molecules attached to DNA.[35] In addition there are few reports in literature about the p-type doping of few layer MoS_2. Phosphorus doping by plasma immersion ion implantation route is one of the feasible routes to perform the same.

4.1.4. Recent developments on interaction of MoS_2 with TTF

Theoretical calculations by Arkamita et. al [36, 37] and Jing et.al[38] have predicted the non-covalent interactions with considerable charge transfer from TTF based molecules to MoS_2. Signicant change of band gap of ML MoS_2 have been suggested due to the interaction with organic moieties. In 2016, Selhorst et.al[39] have studied interaction of 2H-MoS_2 with TTF and TTF-based polymers. The non-covalent interactions with TTF based moieties found to enhanced the solution stabilization of MoS_2 nanosheets. In addition, the TTF-based molecules have altered the electronic structure of MoS_2 by ground state charge transfer. First-principles DFT calculations have supported their observations further.[39]

4.2. Scope of the present investigations

Charge-transfer interaction of various semiconductor nanomaterials and carbon naomaterials with electron-donating and -accepting molecules are reported in literature.[15, 16, 40] Extraordinary changes in physical, optical as well as electronic properties have been observed as a result of these interactions find technological applications and are important from academic point of view as well. These interactions are generally accompanied by changes in band structure and surface structure of the host matrix. Among the routes available for injecting/extracting the electrons in/out of the nanomaterials, physical adsorption is the most simple one as it does not hamper the basic structure of the matrix. Various electron donor and acceptor molecules can be employed for this purpose including organic moieties and metallic nanoparticles. Recently chemical doping of graphene and SWCNT with electron donors such as TTF and electron acceptors such as TCNE has been found to alter the band gap and induce charge transfer band along with changes in the phonon modes. Motivated by these findings we have performed an investigation of the interaction of CdSe, ZnO nanocrystals and MoS_2 layers with the strong electron-donor and –acceptor organic molecules such as tetrathiafulvalene (TTF) and tetracyanoethylene (TCNE) respectively. MoS_2 is of interest as it has a band gap unlike graphene and can be important in nanoelectronics. UV, PL, Raman and spectroscopies were employed to examine the interaction. CdSe interacts with both TTF and TCNE irrespective of its size although the heat of interaction of smaller nanocrystals is found to be higher as reflected by isothermal titration calorimetry experiments. ZnO nanocrystals also exhibit luminescence quenching due to these interactions. We have observed the occurrence of charge-transfer of few-layer MoS_2 material with TTF, but not with TCNE. We observe the formation of the TTF radical cation accompanied by the stiffening of the A_{1g} mode of MoS_2.

4.3. Experimental Section

4.3.1. Synthesis

i) ZnO nanocrystals: For the synthesis of ZnO NCs, 0.5 g of Zn (acac) $_2$.xH_2O was mixed with 20 ml benzylamine, filled in 45 ml inner volume teflon cup in presence of inert atmosphere. The Teflon cup was slid into steel autoclave, sealed carefully and kept for heating at 200 ^oC for 2 days. The resulting milky suspension was centrifuged at speed of 5000 rpm for 5 min. Then the precipitate was thoroughly washed with ethanol followed by dichloromethane and dried in air at 60 ^oC for overnight.[41]

ii) CdSe nanocrystals: CdSe NCs were prepared by using cadmium oleate and solution of elemental selenium in trioctylphosphine (TOPSe) as precursors for cadmium and selenium respectively.[42] For the synthesis of Cd-oleate, CdO (0.3204 g), oleic acid (2.68 g) and octadecane (9 ml) were taken in a three necked round bottom flask. This mixture was heated at 80 ^oC for 1 hr under stirring and degassing. The flask was filled with argon gas and the temperature was increased to 300 ^oC. As soon as all CdO got dissolved, heating was stopped and the solution stored in a vial stoppered with rubber septa. TOPSe solution was prepared by mixing 5 ml trioctylphosphine (TOP) with 0.3952g of selenium. A mixture of 5 ml of octadecane and Cd-oleate (1.25 ml) was degassed for 1 hr at 80 ^oC, by purging with argon. The temperature of the solution was then set between 180 ^oC and 270 ^oC according to the desired size. When the desired temperature was reached, 0.25 ml of 1(M) TOPSe was added to the mixture. Methanol and octadecane were used for the separation as well as for purification. The extraction procedure was based on the principle that the solubility of unreacted cadmium precursor used in synthesis was greater in methanol at room temperature whereas the nanocrystals were insoluble. In octadecane, the nanocrystals are soluble. To improve the separation procedure, hexane and chloroform were used.

iii) Few layer MoS_2: Few layer MoS_2 was synthesized by the procedure in literature.[43] Molybdic acid was ground with an excess of thiourea of molar ratio 1:48 and heated at 773 K for 3 hrs under inert atmosphere). Then the sample was cooled to room temperature under inert gas flow atmosphere and ground for further use.

4.3.2. Characterizations

UV-Vis absorption spectra were recorded using a Perkin Elmer lambda 650(UV/VIS/NIR spectrometer) and PL measurements were carried with a Horiba Jobin Yvon Spectrometer (iHR 320). Electronic absorption and fluorescence spectroscopic measurements were carried out at room temperature. TEM investigations were carried out with JEOL microscope operating with an accelerating voltage of 300 kV. Dynamic light scattering measurements were carried out at 25 °C with Zetasizer Nano ZS (Malvern Instruments). Raman spectra were recorded with a 514 nm Ar laser and with a 632 nm He-Ne laser in a Jobin Yvon LabRam HR Spectrometer. The number of layers in the as synthesized MoS_2 was examined by atomic force microscopy (AFM) with a Vecco digital instrument.

4.3.3. Interaction with TCNE and TTF molecules

i) Spectroscopic methods:

To study the interaction of the nanocrystals with e-donor and e-acceptor molecules using optical spectroscopy, different concentrations of TTF and TCNE in the range of 0.1 to 10 mM were prepared in toluene (HPLC grade). 0.1 ml of CdSe solution was mixed with 2.9 ml solution of TTF or TCNE solution. The mixture was sonicated for 1 hr. To study the interaction with ZnO nanocrystals, TTF and TCNE solutions were prepared in acetonitrile (HPLC grade). 1 mg of ZnO nanoparticles was dispersed in 3 ml of TTF/ TCNE solution under continuous ultrasonication. To investigate the interaction of TTF (Sigma aldrich) and TCNE (Sigma aldrich) with MoS_2, different concentrations of TTF and TCNE in the range of 0.1 to 10 mM solutions were prepared in ethanol. Few layer MoS_2 was dispersed in ethanol for 15 minutes with sonication. 1ml of this dispersed solution was added to various concentration of TTF or TCNE solution to achieve the final desired composition. The mixture was sonicated for 20 min and the spectra recorded. For recording Raman spectra the solution of pristine MoS_2 and the mixture of MoS_2 +TTF / MoS_2+ TCNE were filtered through an anodisc membrane, dried and measured.

ii) Isothermal titration calorimetry:

Isothermal titration calorimetry (ITC) was carried out using a MicroCal VP-ITC unit. For this purpose CdSe nanocrystals solution was prepared in toluene and ZnO nanocrystals was dispersed in acetonitrile. Sample solutions were filled in the sample cell and the reference cell filled with toluene and acetonitrile for CdSe and ZnO, respectively. 10 mM solutions of TCNE and TTF were used as titrating reagents. In each experiment, 4 µL of the 10 mM solution was injected from a syringe to the sample cell in equal intervals of 3 min and the heat changes were measured after each injection. All the ITC experiments were conducted at 30 °C. The heat of dilution was obtained by titrating the respective solvents against TCNE and TTF keeping all other experimental condition same. The heat of interaction was obtained by subtracting this heat of dilution from the experimental value. It may be noted that ITC measurements provide relative interaction energies and not absolute values.

4.3.4. Computation details

First-principles calculations are based on density functional theory (DFT) as implemented in the Quantum ESPRESSO code.[44] We have employed the Generalized Gradient Approximation with PW91 functional for exchange correlation energy.[45] Interactions between ionic cores and valence electrons are represented by ultrasoft pseudopotentials.[46] Interaction between the periodic images of the sheets was made negligible with an inclusion of vacuum of 10 Å in the z direction. An energy cut-off 30 Ry was used for the plane wave basis in representing wavefunctions and a grid with a cut-off of 180 Ry in representing the density. The structures were relaxed till the magnitude of Hellman-Feynman forces on the ions were smaller than 0.02 eV/Å.

4.4. Results and discussion

4.4.1

Interaction of CdSe and ZnO nanocrystals with electron–donor and –acceptor molecules

4.4.1. Interaction of CdSe and ZnO nanocrystals with electron–donor and –acceptor molecules

Interaction of CdSe nanocrystals with electron-donor (TTF) and acceptor (TCNE) molecules was investigated. Two different sizes of CdSe nanocrystals were prepared by literature reported method.[42] TEM and UV-vis absorption spectra shows average nanocrystal diameters are 2.5 nm and 4.5 nm. **Figure 1** shows the PL spectra of 4.5 nm CdSe nanocrystals after interaction with different concentrations of TTF (0, 0.1, 1 and 10 mM). We observe little shift or change in the position of band-edge emission of CdSe at 600 nm even on interaction with 10 mM TTF. The PL intensity however, decreases sharply with increasing concentration of TTF. Figure 1b shows sharp monotonic decay of the relative PL intensity ($I_{CdSe}/I_{(CdSe + TTF)}$) with increasing concentration of TTF. PL measurements with 2.5 nm CdSe nanocrystals did not show any significant shift in the position of band-edge emission as well.

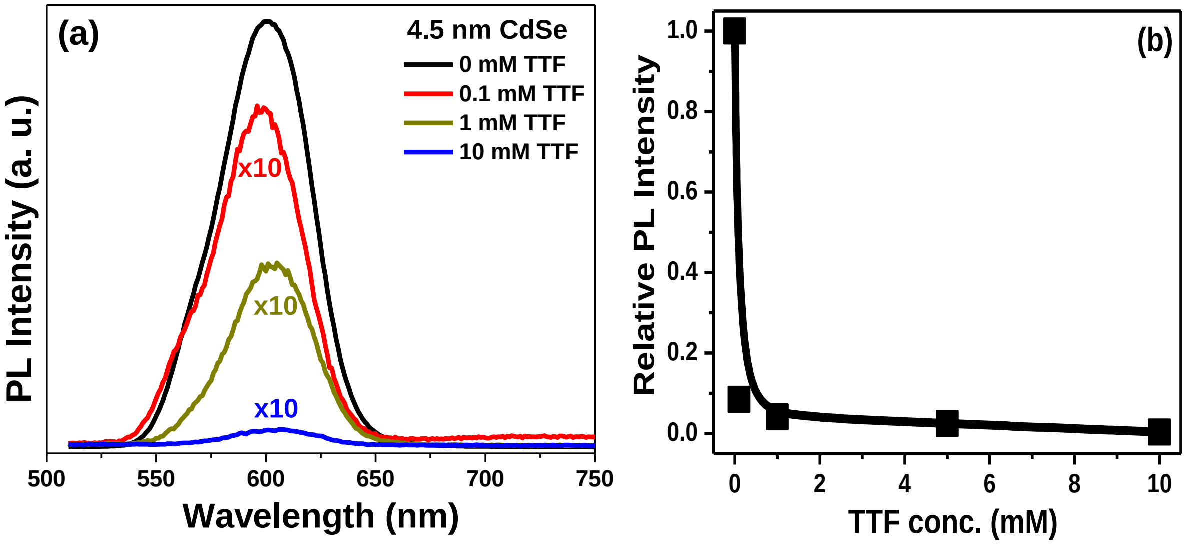

Figure 1. (a) PL spectra of CdSe nanocrystals of 4.5 nm after interaction with various concentrations of TTF. The excitation wavelength was 450 nm for all the samples. In panel (a), intensities of spectra for 0.1, 1 and 10 mM TTF are multiplied by 10 for a better presentation. (b) The decrease in the relative intensity (area under the PL spectrum, $I_{CdSe}/I(_{CdSe+TTF})$) as a function of increasing TTF concentration.

Figure 2 we show PL spectra of 2.5 nm CdSe nanocrystals after interaction with varying concentrations of TTF. Similar to the 4.5 nm nanocrystals, the PL intensity of 2.5 nm CdSe nanocrystals decreases sharply with increasing concentrations of TTF, as shown in the Figure 2b. The decrease in PL intensity can arise from multiple causes. For example charge and/or energy transfer from the luminescent CdSe nanocrystals to non-luminescent TTF molecules would quench the photoluminescence.

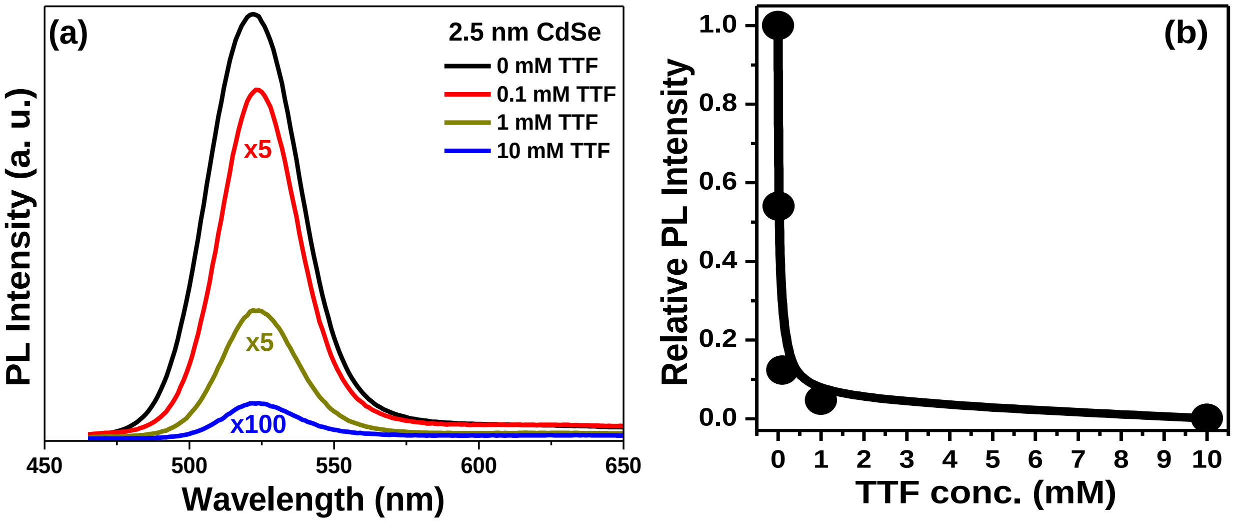

Figure 2. PL spectra of CdSe nanocrystals of 2.5 nm, after interaction with various concentrations of TTF. The excitation wavelength was 450 nm for all the samples. In panel (a), intensities of these spectra for 0.1 and 1 mM TTF are multiplied by 5, whereas, spectrum for 10 mM TTF is multiplied by 100. (b) The decrease in the relative intensity (area under the PL spectrum, $I_{CdSe}/I_{(CdSe+TTF)}$) as a function of increasing TTF concentration.

We carried out isothermal calorimetry to study the relative binding interaction of TTF with the CdSe NCs. We found negligible heat change (within the noise limit) after addition of TTF to CdSe NCs in toluene, indicating poor or no binding of TTF to the nanocrystals, though the PL intensity is quenched substantially even at concentration of 0.1 mM of TTF (Figure 1). TEM images in **Figure 3** show that the CdSe nanocrystals remain unchanged after interaction with 0.1 mM TTF, suggesting no significant agglomeration or modification of the nanocrystal surface. The black patches seen in Figure 3b arises from the presence of TTF molecules. Thus, the poor binding of TTF molecules to the nanocrystal may be taken to imply that one of the dominant mechanisms of PL quenching (Figure 1) is the energy transfer from the nanocrystals to TTF, since charge transfer would require closer proximity between the donor and the acceptor species. However, other important mechanisms like charge transfer can occur via collision of NCs with the TTF molecules in solution. It is possible that modification of the single surface states of NCs by dislodging the native ligands and adsorption of TTF molecules the NC surface can significantly influence PL efficiency.

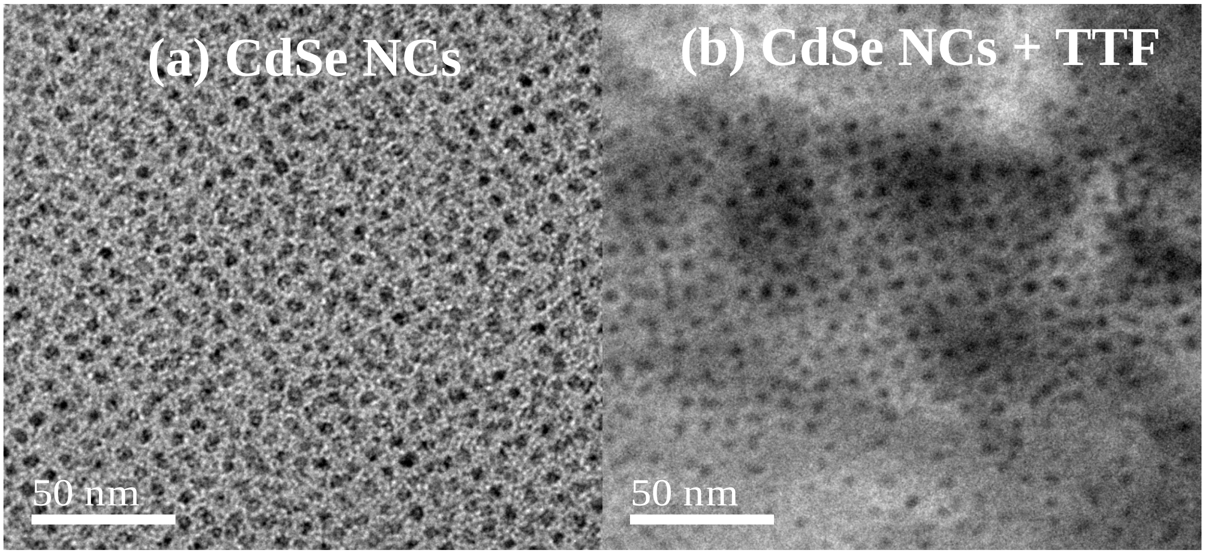

Figure 3. TEM images of 4.5 nm CdSe nanocrystals (b) before and (c) after interaction with 0.1 mM TTF.

We have examined the effect of interaction of electron withdrawing TCNE with CdSe nanocrystals. **Figure 4a** shows the UV-Vis absorption data obtained with the 4.5 nm CdSe nanocrystals dispersed in toluene before and after interaction with 0.1 mM and 1 mM of TCNE. The absorption features of CdSe nanocrystals remain identical, along with the appearance of an overlapping TCNE band at 1 mM concentration of TCNE. Interestingly, we observe signatures of scattering of longer wavelength (~700 to 800 nm) light after the addition of TCNE. A systematic increase in the scattering with increasing TCNE concentration is indicative of nanocrystal agglomeration and will be discussed further. Further increase in concentration of TCNE beyond 1 mM caused the TCNE band to dominate the absorption spectrum hiding the CdSe absorption band. The spectral overlap is greater for TTF with CdSe nanocrystals compared to TCNE. Thus even at a low concentration of TTF, it is difficult to distinguish spectral features of CdSe.

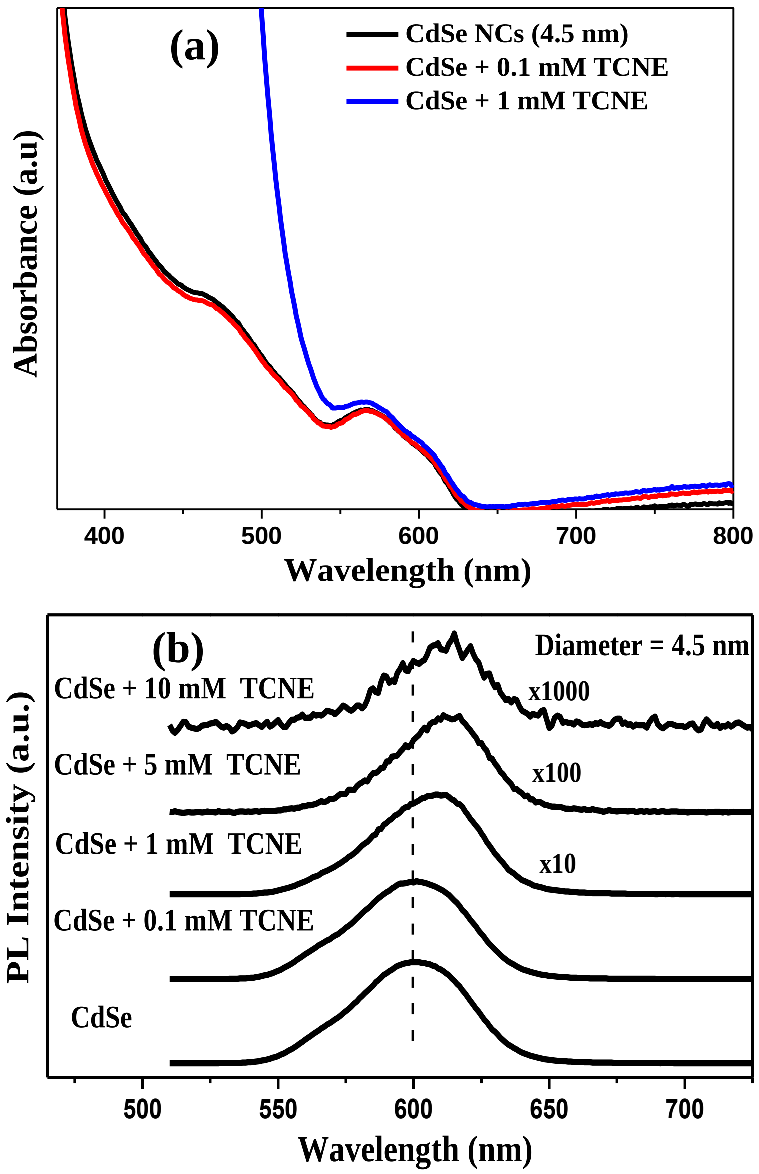

Figure 4. (a) UV-Vis absorption spectra and (b) PL spectra of 4.5 nm CdSe before and after interaction with TCNE molecules. All the PL spectra were obtained with an excitation wavelength of 500 nm. Polydispersity in nanocrystal size can blur some of the excitonic features in the absorption spectrum and broaden the PL spectrum of CdSe nanocrystals.

Figure 4b compares the PL spectra of 4.5 nm CdSe nanocrystals before and after addition of TCNE molecules of different concentrations. CdSe NCs exhibit band-edge emission around 600 nm. A significant red-shift (around 10 nm) of this band is observed on interaction of the nanocrystals with 1 mM TCNE. On interaction of the CdSe nanocrystals with higher concentrations, 5 and 10 mM of TCNE, we observe a systematic red-shift of the CdSe band-edge emission where in the band red-shifted to around 614 nm and 615 nm, respectively. This systematic red-shift in CdSe emission after interaction with TCNE was not observed with TTF.

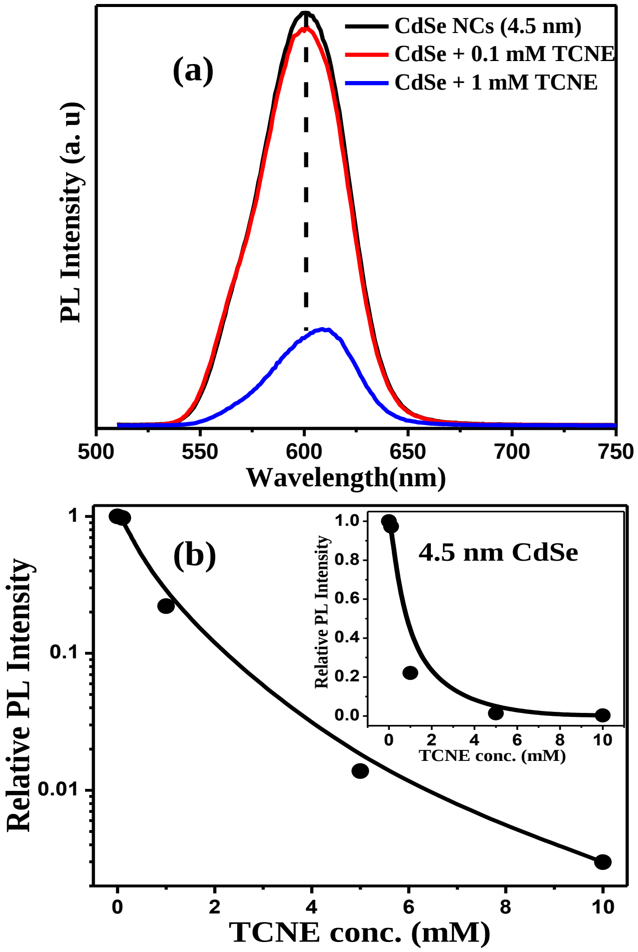

Figure 5. (a) Comparison of intensity of PL spectra of 4.5 nm CdSe nanocrystal after interacting with 0.1 and 1 mM TCNE molecules. (b) Relative PL intensity (area under the PL spectra, $I_{CdSe}/I_{(CdSe+TCNE)}$) as a function of TCNE concentrations; inset shows the same plot with linearly plotted Y-axis.

Figure 5a shows that the PL intensity of CdSe NCs also decreases after interaction with 0.1 and 1 mM TCNE molecules. This systematic decrease in the PL intensity with increasing TCNE concentration, shown in Figure 4b, is however similar to that found with TTF. **Figure 6a** shows the ITC data for the mixture of CdSe nanocrystal with TCNE in toluene. A clear release of heat (exothermic reaction) till about -2 Kcal is observed after the first injection of TCNE solution in to the nanocrystal solution. This heat change suggests a significant binding interaction of TCNE with the nanocrystal, unlike the case of TTF. After addition of a sufficient amount of TCNE, no more nanocrystal surface is available for interaction, and there is saturation in the heat of interaction.

Prompted by the observation of scattering in the UV-Vis spectra (Figure 4a) and a significant heat change (Figure 6a) after treating the CdSe nanocrystals with TCNE, we used dynamic light scattering (DLS) and TEM to study any morphological changes caused by the interaction of TCNE with the nanocrystals. The sizes of our CdSe nanocrystals and TCNE molecules were too small to achieve a strong enough DLS signal and we did not get any reliable DLS signal. However, a reproducible DLS signal appeared immediately after mixing nanocrystal solution with TCNE. DLS data after treating 4.5 nm CdSe nanocrystals with 0.1 and 1 mM TCNE in toluene is shown in **Figure 7**. A bi-modal distribution of particle size is observed for 0.1 mM TCNE, centering at ~20 and ~100 nm. This observation suggests extensive agglomeration of nanocrystals after addition of TCNE. The extent of agglomeration increases with increase in the TCNE concentration. The size becomes as large as ~400 nm after addition of 1mM TCNE. The hydrodynamic diameter of the organic ligand capped 4.5 nm CdSe nanocrystals is expected to be ~ 6 nm. Instead, we observe particles with size in terms of hundreds of nm, because of agglomeration. Clearly, agglomeration is caused by the addition of TCNE. TCNE molecules might replace some of the existing native organic ligands (mainly oleic acid) with long carbon chain, thus causing the agglomeration in non-polar toluene solvent. Interestingly, the agglomerated nanocrystals with hydrodynamic radius ~100 nm are quite stable in toluene, suggesting that the clusters of nanocrystals are porous enough to get solvated. The TEM image of the pure CdSe nanocrystals in Figure 3 does not show any signature of agglomeration. But TEM images of CdSe nanocrystal after treating with 0.1 mM TCNE (**Figure 8**) show a clear signature agglomeration. The size of these clusters varies. Here we observed a big cluster of ~80 nm along with smaller clusters around 20 nm. Such a bimodal distribution in cluster size along with large size-distribution in each size-range is in agreement with the DLS data. Further increase in TCNE concentration masks the nanocrystals on TEM grid hampering further microscopic study.

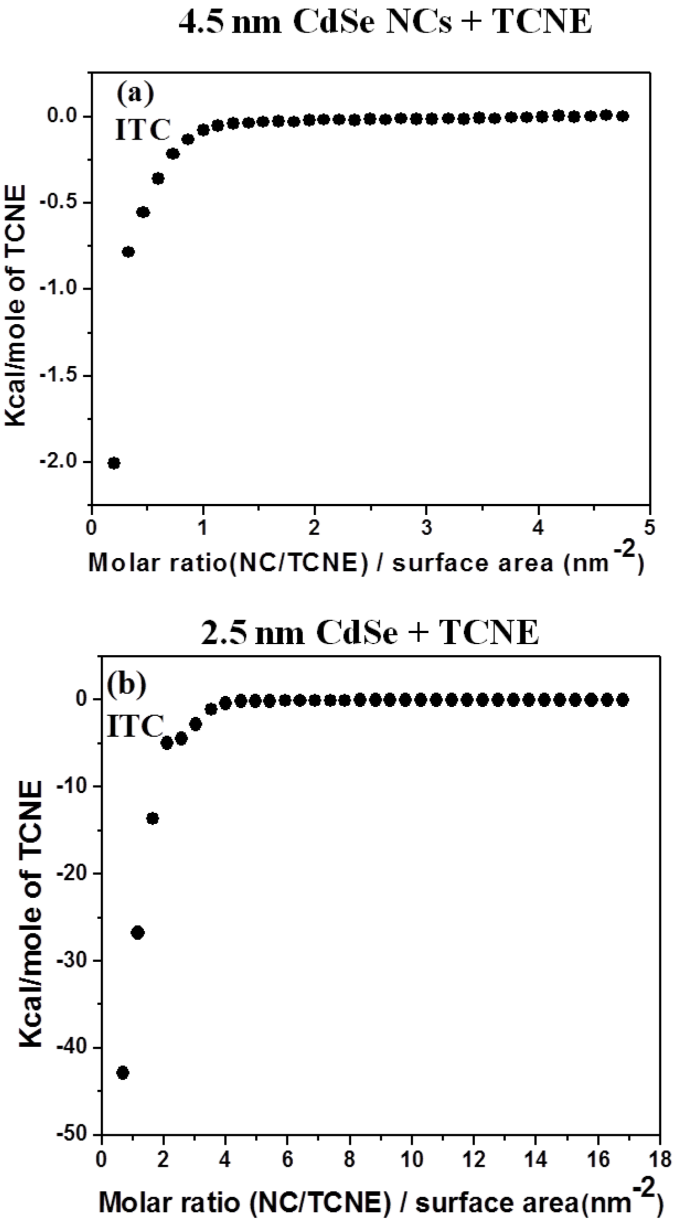

Figure 6. (a) ITC data showing the integrated heat of interaction of (a) 4.5 nm CdSe and (b) 2.5 nm CdSe nanocrystals at each injection of 10 mM TCNE.

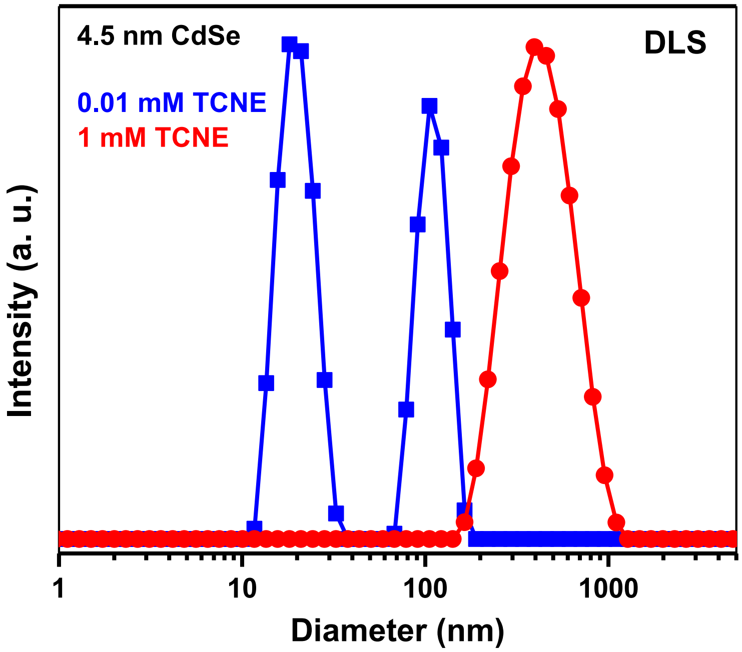

Figure 7. Dynamic light scattering (DLS) data shows the change in hydrodynamic diameter of CdSe with varying concentration of TCNE.

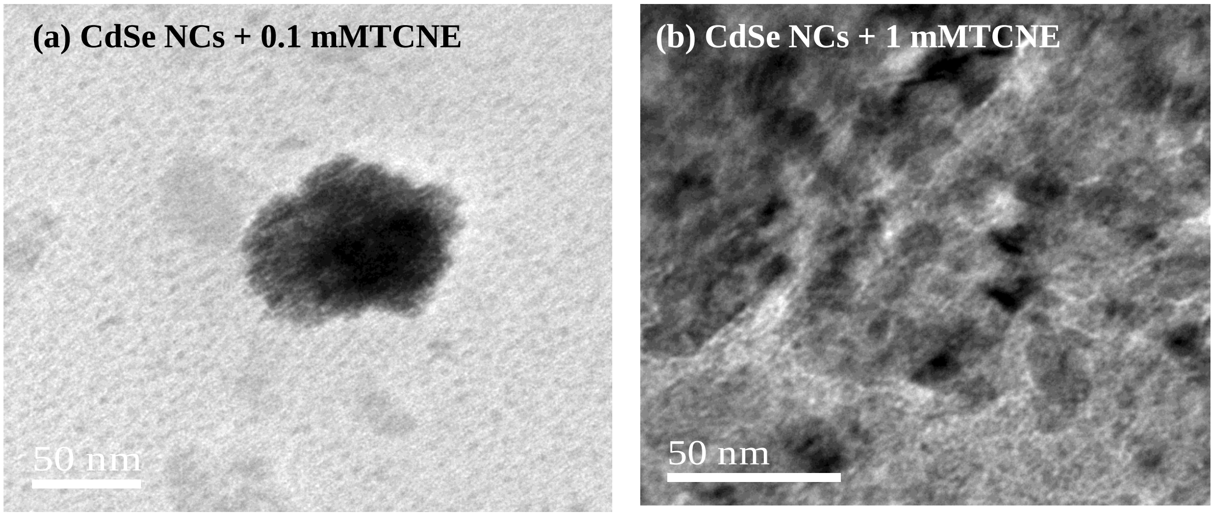

Figure 8. Transmission electron microscopy (TEM) images of 4.5 nm CdSe after interaction with (a) 0.1 mM and (b) 1 mM TCNE. Higher TCNE concentration (1 mM) masks the nanocrystals on TEM grid hampering microscopic study.

From the above discussion, we summaries that the addition of TCNE to CdSe nanocrystals causes, (i) no shift in the first excitonic absorption peak, but there is a red shift in the excitonic emission and (ii) there is significant agglomeration of nanocrystals. We, therefore, suggest that the red-shift in the excitonic emission is caused by resonance energy transfer from the smaller to larger nanocrystals in the ensemble,[47] and also probably because of self-absorption,[48] where the emitted light form smaller nanocrystals get re-absorbed by the larger nanocrystals. The quenching of PL can be due to other different causes. Strong binding of TCNE with the CdSe nanocrystals suggests the possibility of charge-transfer pathways between the nanocrystal and TCNE, thus introducing new nonradiative decay channels. Agglomeration of nanocrystals reduces the PL efficiency via energy transfer from brighter to darker nanocrystals in the vicinity. The possibility of charge transfer from CdSe nanocrystals to the surrounding TCNE molecules cannot be ignored.

To investigate whether the size of the nanocrystal plays a crucial role, we have performed experiments with smaller CdSe nanocrystals. For this purpose, we have used a dispersion of 2.5 nm CdSe nanocrystals in toluene, to which different concentrations of TCNE were added. The ITC data in Figure 6b shows strong interaction of the nanocrystals with TCNE. The exothermic heat change after the first injection of TCNE is -43 kcal and the heat of interaction saturates at a 4 nm^{-2} TCNE to nanocrystal molar ratio normalized by the nanocrystal surface area. Both these numbers are significantly larger than those (-2 kcal heat of interaction after first injection, and saturation at 1.1 nm^{-2}) obtained for the 4.5 nm CdSe nanocrystals. The greater interaction of smaller nanocrystals with TCNE cannot be explained on the basis of the larger surface to volume ratio of the smaller nanocrystals. Additional factors such as the larger surface curvature of the smaller nanocrystals could be important. A larger surface curvature reduces the steric hindrance between the surface binding molecules and provides a larger number of unsaturated dangling bonds on the nanocrystal surface. Both these factors are expected to favors the interaction of TCNE with the nanocrystal surface.

The band-edge PL emission of 2.5 nm CdSe nanocrystals gets blue-shifted at the TCNE concentrations greater than 1mM (**Figure 9a**). Such a blue shift can result from modification of CdSe nanocrystals band gap because of the strong binding interaction of the electron withdrawing TCNE molecules with the nanocrystals. Further increase in the TCNE concentration gives rise to the appearance of a new emission band around 534 nm.

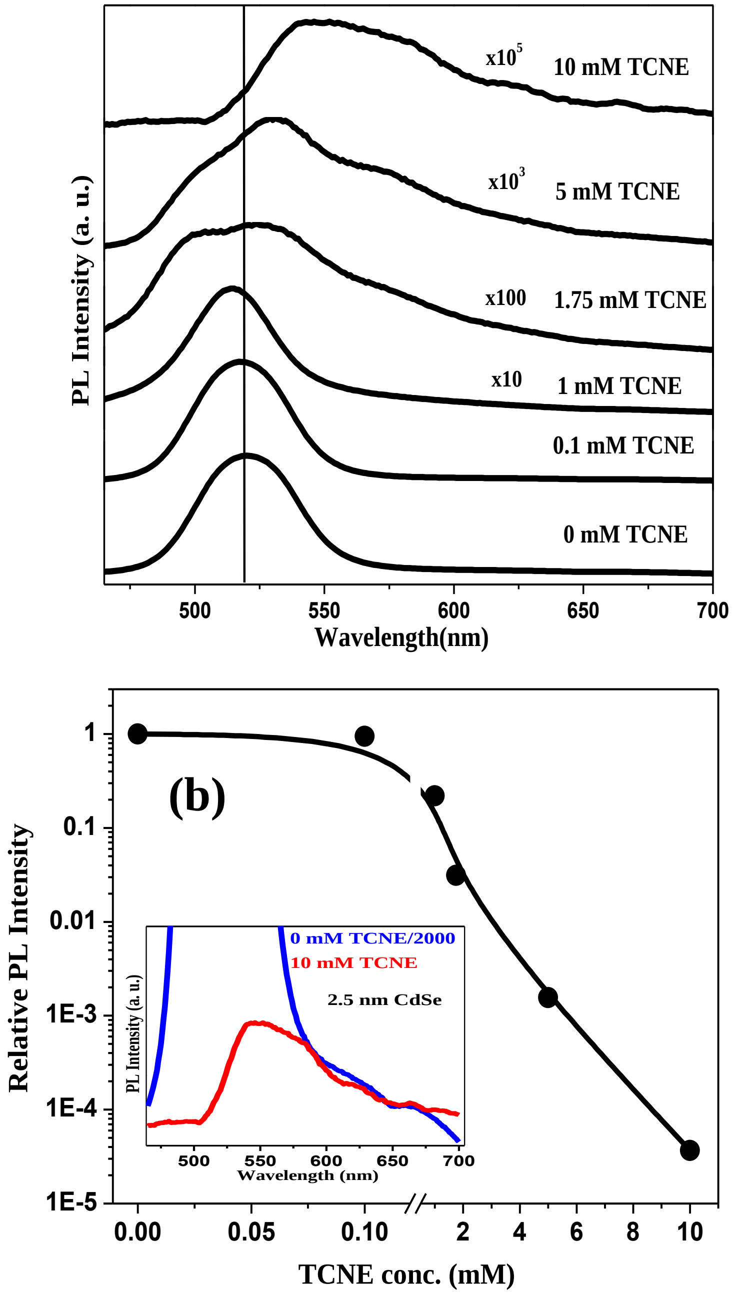

Figure 9. (a) PL spectra with different TCNE concentrations after interaction of 2.5 nm CdSe. (b) Relative PL intensity (area under the PL spectra, $I_{CdSe}/I_{(CdSe+TCNE)}$) as a function of TCNE concentrations. Inset compares the tail of PL spectrum for pure CdSe nanocrystals (after dividing the intensity by 2000) with the spectrum after addition of 10 mM TCNE.

To understand the origin of this new band, we first compare the intensity of this band. Figure 9b shows that the overall PL intensity decreases sharply on increasing the TCNE concentration. For example, the PL intensity of the sample after addition of 10 mM TCNE is about $3*10^4$ times smaller than that of pure CdSe nanocrystals (0 mM TCNE). The inset in Figure 9b compares the tail of PL spectrum of CdSe nanocrystals after dividing the intensity 2000 times with the spectrum after addition of 10 mM TCNE. It shows that the PL features at longer wavelengths are present in the tail of the emission spectrum of the pure CdSe nanocrystals. Thus, the addition of higher concentrations of TCNE completely quenches the band-edge emission, leaving behind insignificant longer wavelength emission features probably arising from defect-impurity-related emission. We also find from the DLS data occurrence of nanocrystal agglomeration at higher (>1 mM) TCNE concentrations, which might also contribute to the longer wavelength emission. These low intensity features become visible due to the large suppression of PL intensity at higher energies and also because of the highly magnified PL intensity scale in Figure 9a.

We have also studied the interaction of ZnO nanocrystals with an average diameter ~50 nm with TTF and TCNE. **Figure 10** shows the changes in PL spectrum of ZnO nanocrystals after addition of different concentration of TTF. The ZnO nanocrystals exhibit the band-edge emission at around 378 nm and defect-related emission band at 492 nm. On varying the TTF concentration, we observe a small blue-shift of the ZnO band-edge emission along with a significant red-shift in the defect-related emission. For a 10 mM TTF concentration, the ZnO defect-band at 492 nm shifts to 508 nm. Often quenching of defect-related emission enhances the intensity of band-edge emission, but in this case intensities of both the band-edge emission and the defect-related emission of ZnO nanocrystals are quenched significantly on interaction with increasing concentrations of TTF (Figure 7). However, the extent of quenching in the case of ZnO nanocrystals is significantly smaller than that found with CdSe nanocrystals. ITC data showed weak interaction of TTF with ZnO nanocrystals.

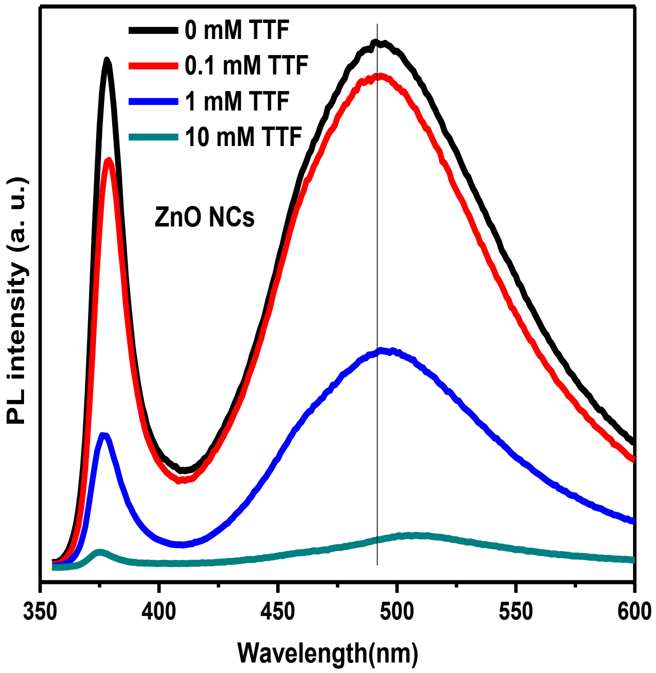

Figure 10. PL spectra of ZnO nanocrystals before and after interaction with TTF (excitation wavelength of 340 nm).

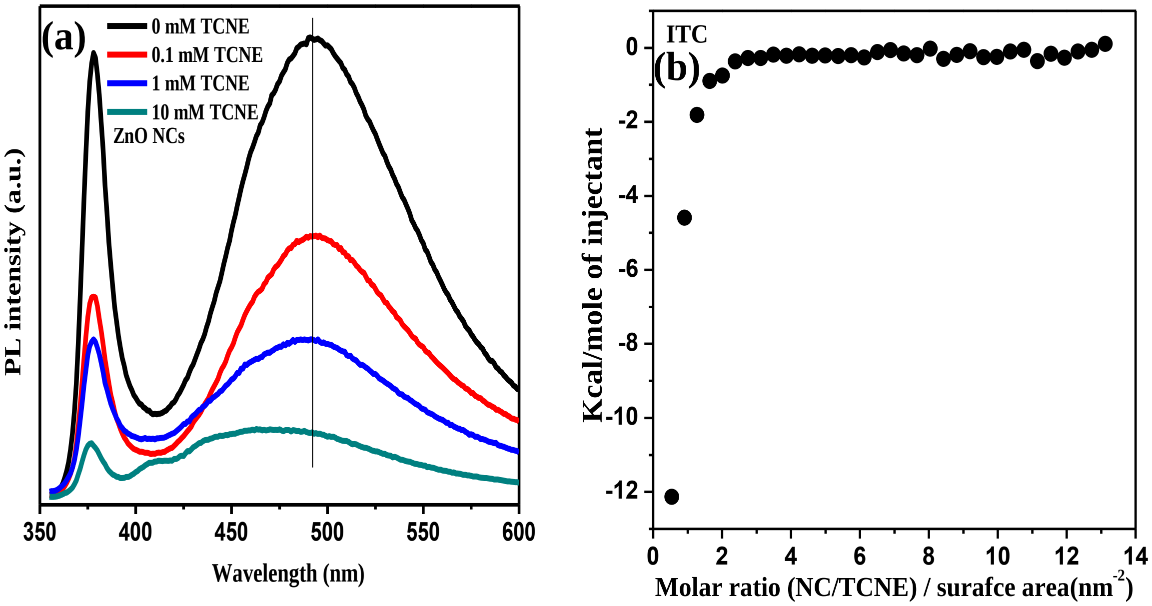

Figure 11. (a) PL spectra of ZnO nanocrystals before and after interaction with TCNE with excitation wavelength of 340 nm. (b) ITC data showing the integrated heat of interaction of ZnO at each injection of 10 mM of TCNE.

We have investigated the interaction of ZnO nanocrystals with electron-acceptor TCNE molecules. **Figure 11a** shows the PL spectra of ZnO nanocrystals after interaction with different concentrations of TCNE. There is hardly any shift in the position of band-edge emission of ZnO, but there is a systematic blue-shift of the defect-related emission. On interaction with 10 mM TCNE, we see a large blue-shift of the defect-related band from 492 nm to 474 nm as shown in Figure 11a. We note that the TTF molecules lead to a red-shift of the defect-related emission, while the TCNE causes blue-shift. Interaction of ZnO nanocrystals with TCNE also causes quenching of both the emission bands similar to TTF. Results from the ITC measurements in Figure 11b show strong binding interaction between TCNE and ZnO nanocrystals.

4.4.2

Charge-transfer interaction between few-layer MoS_2 and tetrathiafulvalene

4.4.2. Charge-transfer interaction between few-layer MoS_2 and tetrathiafulvalene

The XRD pattern of the few-layer MoS_2 used by us does not exhibit the (002) reflection, thus confirming the presence of only a few layers and the graphene-like nature of the material. The AFM images and the corresponding height profiles also confirm the presence of two to three layers with an average thickness of 2.44 nm. **Figure 1** shows the results obtained on the interaction of few-layer MoS_2 with TCNE. The absorption bands of both MoS_2 and TCNE remain unaffected by the interaction. We fail to observe any change in the Raman spectrum of MoS_2 as well. Unlike TCNE, electron donating TTF shows strong evidence of charge transfer interaction with few-layer MoS_2 material.

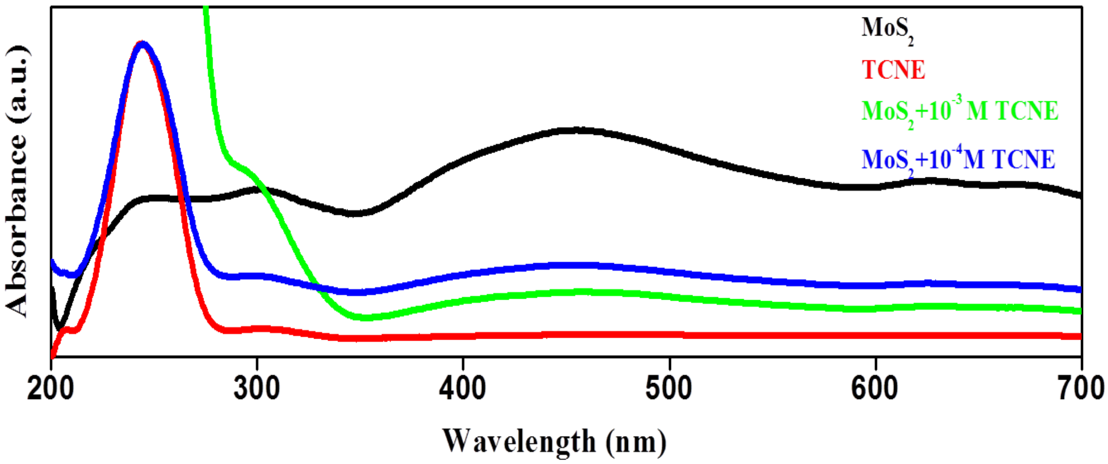

Figure 1. UV-Vis absorption spectra of few-layer MoS_2 before and after interaction with different concentrations of TCNE. Spectrum of pristine TCNE is also shown.

Figure 2(a) shows the UV-Vis spectra resulting from the interaction of a fixed concentration of TTF (5 mM) in ethanol with different concentrations of few- layer MoS_2. Pristine TTF exhibits a band centered around 450 nm (inset of Figure 2a). As a result of interaction with few layer MoS_2, two new bands appear at 440 nm and 580 nm accompanied by the disappearance of the 450 nm band. These two new bands can be readily assigned to the TTF free radical cation ($TTF^{+\cdot}$).[49, 50] The radical cation is formed by one-electron transfer from TTF to MoS_2. We have varied the TTF concentration keeping the MoS_2 concentration fixed and the results shown in Figure 2(b) are similar to those in Figure 2(a).

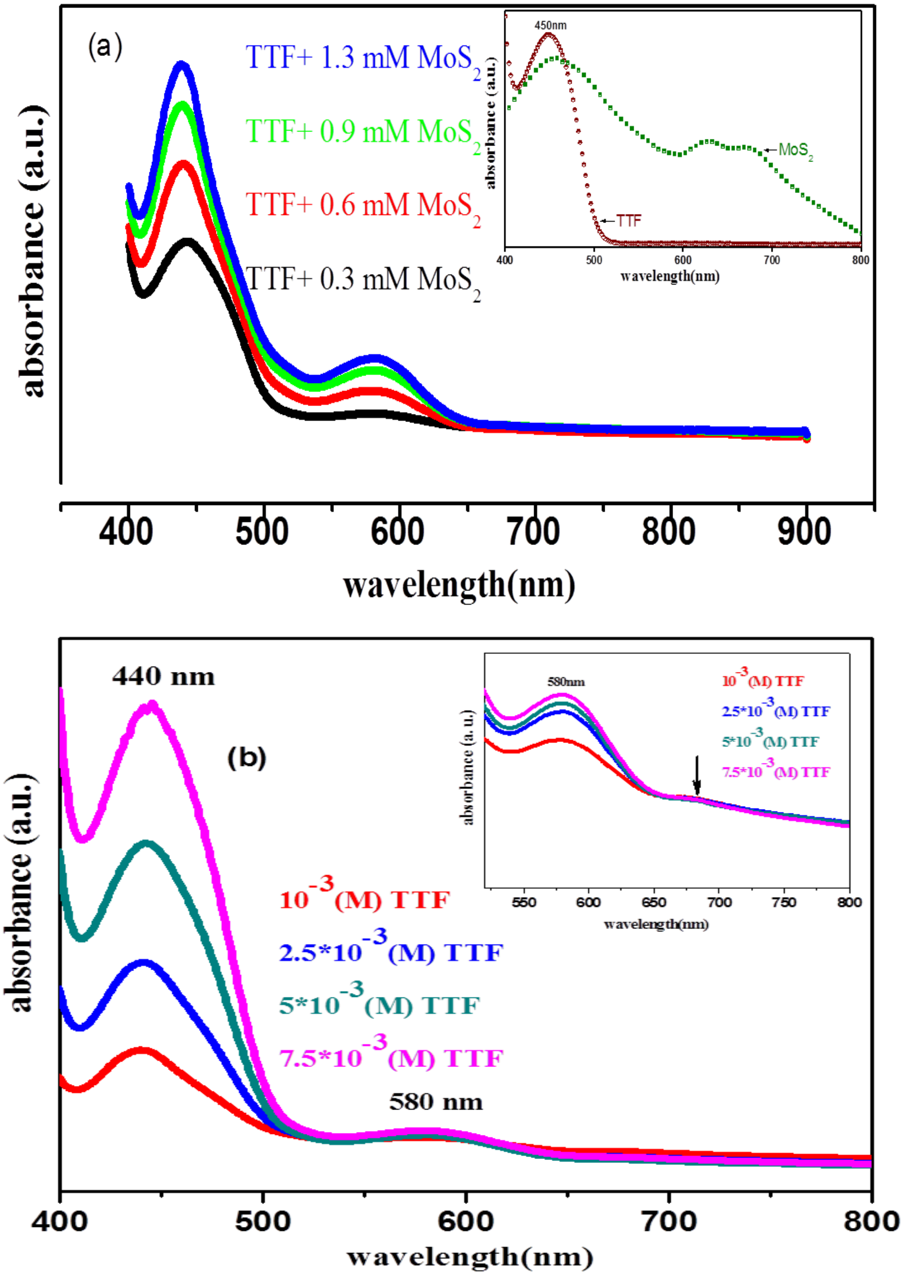

Figure 2. (a) UV-Vis absorption spectra of varying concentrations of few-layer MoS_2 after interaction with a fixed concentration of TTF (5 mM). Inset shows the spectra of pristine few-layer MoS_2 material and TTF. (b) UV-Vis absorption spectra of a fixed concentration of few-layer MoS_2 (0.7 mM) interacting with different concentrations of TTF. Inset shows changes in

the 580 nm band ; arrow indicates the band centered around 675 nm due to the direct excitonic transition of MoS_2.

Figure 3 shows the variation of the intensity of the 440 nm and 580 nm bands with the MoS_2 concentration. Similar variation in the intensity of the bands is seen when the TTF concentration was varied keeping MoS_2 concentration fixed. The absorbance of $TTF^{+\cdot}$ bands increase proportionally with MoS_2 or TTF concentration and approaches saturation at higher concentrations. We used Raman spectroscopy to examine the changes caused in MoS_2 by the interaction with TTF. Few-layer MoS_2 shows two first-order Raman active bands due to E^1_{2g} and A_{1g} modes centered around at 375 and 400 cm^{-1} respectively. In the region between 430 and 490 cm^{-1}, second order Raman bands are observed.[51] We observe changes in the position of A_{1g} and E^1_{2g} modes due to interaction with TTF (**Figure 4**). The A_{1g} band stiffens by 3 cm^{-1} upon interaction with TTF accompanied by band broadening of 5 cm^{-1} when using the 633 nm laser line. The E^1_{2g} mode shifts by 2 cm^{-1}.

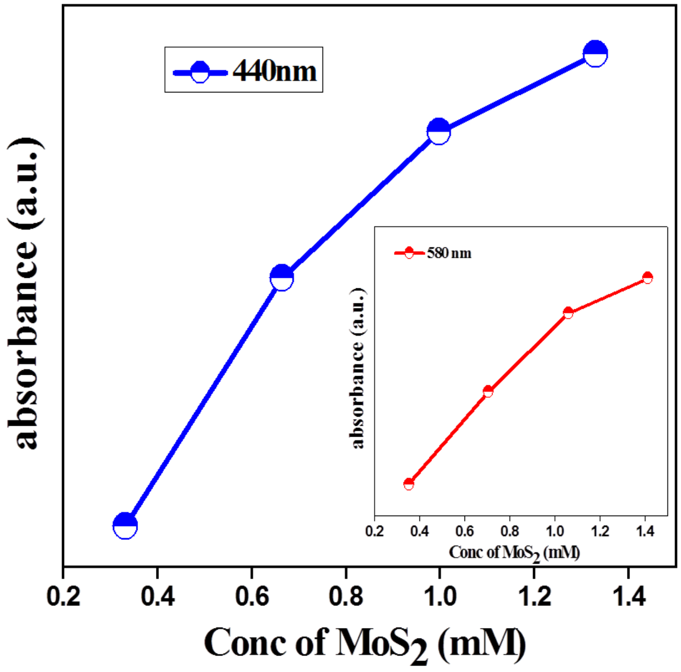

Figure 3. Variation of the absorption intensity of the 440 nm band with the concentration of few layer MoS_2 at a fixed concentration of TTF. Inset shows the variation of the intensity of the 580 nm band.

There is an increase in the relative intensity of second order Raman active mode of MoS_2 in the region of 430 - 480 cm^{-1} due to interaction with TTF. Electron doping of single layer

MoS_2 by electrochemical means can be achieved upto ~2×10^{13}/cm^2.[52] The A_{1g} band softens by electrochemical doping by 4 cm^{-1} along with a increase linewidth 6 cm^{-1} at maximum doping, while the E^1_{2g} mode is less sensitive to electrochemical doping. Such differences between electrochemical doping and charge-transfer doping have been observed in the case of graphene as well.[15, 16] The present results show that only electron doping of few-layer MoS_2 material is possible through charge transfer doping. Hole doping is not possible by electrochemical doping as well.[53] Furthermore, charge transfer doping which allows transfer of an electron transforms the electrical properties of MoS_2, making it metallic as seen from the charge-current (I-V) curves.

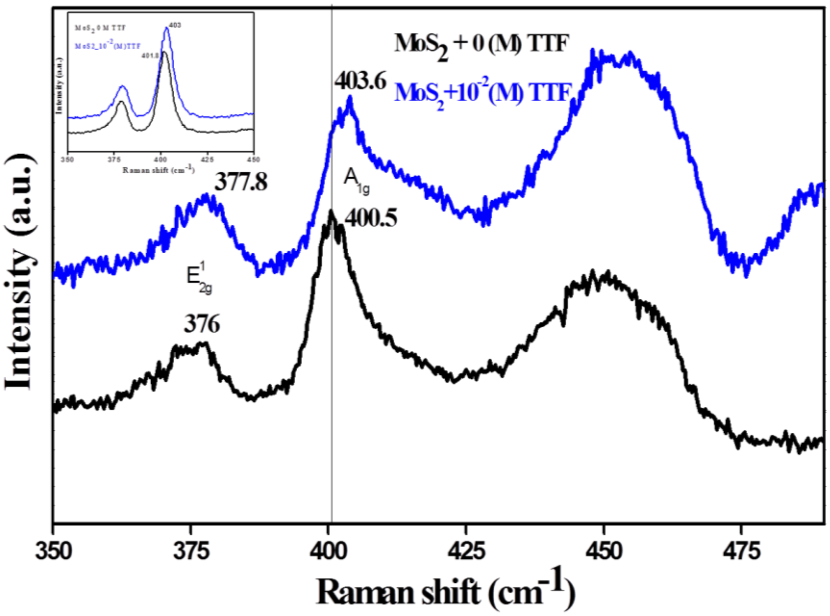

Figure 4. Raman spectrum of few layer MoS_2 before and after interaction with 10^{-2}(M) TTF using 633 nm laser irradiation.

We have carried out first-principles calculations on the interaction of TTF with MoS_2 sheets to understand the nature of charge transfer, by including semiempirical dispersive van der Waal (vdW) interactions using Grimme parametrization.[52] With one TTF molecule in the periodic cell, we varied the size of this supercell in MoS_2 plane to simulate variation in concentration of TTF, which decreases with increase supercell size. For the 6x6x1 and 3x3x1supercells, corresponding to 3.1×10^{13} cm^{-2} and 12.5×10^{13} cm^{-2} concentrations of TTF on MoS_2, Brillouin zone integrations were sampled with uniform 3x3x1 and 6x6x1 meshes of k-points, respectively.[54]

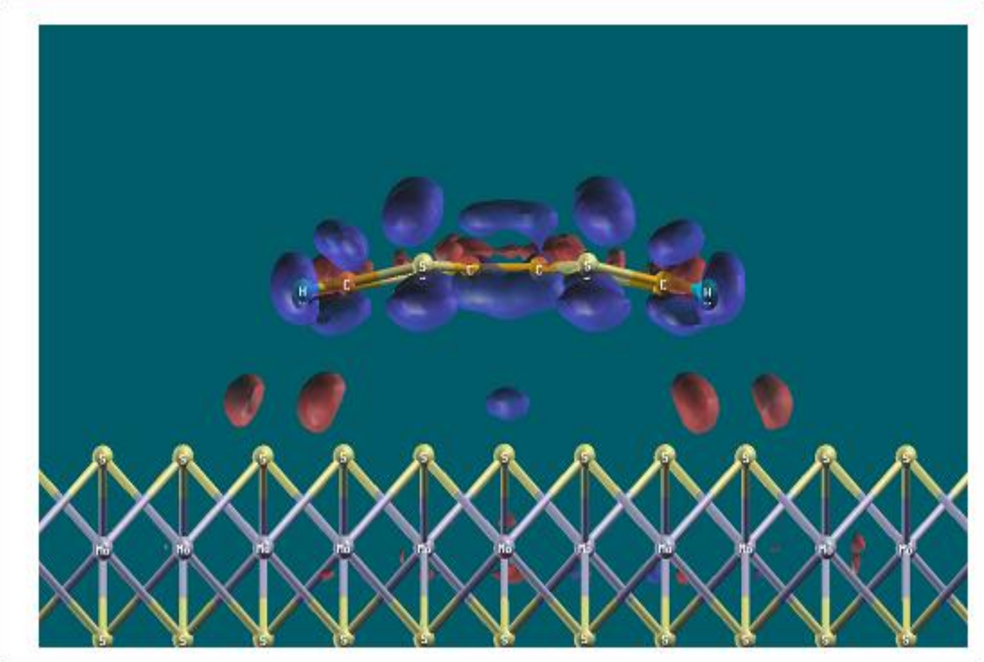

Figure 5. (Color online) Charge density iso-surface of the charge transfer from TTF to MoS_2 for $3.1x10^{13}cm^{-2}$ defect concentration. Red iso-surface denotes negative charge and blue denotes positive charge. Electrons are transferred from TTF (blue iso-surface) to MoS_2 (red iso-surface).

TTF $(H_2C_2S_2C)_2$ contains 14π electrons, 2 from each sulfur atom and 1 from each sp^2 hybridized carbon atom, and can be oxidized twice reversibly, with an electron from a sulfur atom removed per oxidation step. Since the electron is donated by a sulfur atom, we have considered two sites for adsorption of TTF on MoS_2: 1) S of TTF on Mo of MoS_2 (Mo-S) and 2) S of TTF on S of MoS_2 (S-S). For 3.1×10^{13} cm^{-2} concentration of TTF, we observe that adsorption energies of Mo-S and S-S are -98 kJ/mol and -88 kJ/mol, respectively. The distances of sulfur atoms of the TTF molecule with respect to sulfur layer of MoS_2 are about 3.2 Å (Mo-S configuration) and 3.6 Å (S-S configuration), considerably larger than the S-S bond length of ~2.05 Å. Thus, the binding between TTF and MoS_2 is primarily due to strong van der Waals interactions between MoS_2 and TTF. Since the adsorption in the Mo-S configuration is preferred over the S-S configuration, we consider only the Mo-S configuration in our analysis.

We observe that the extent of buckling of the TTF molecule (**Figure 5**) decreases with decreasing concentration. The out-of-plane deformation of the TTF molecule has contributions from the attractive coulomb interaction between TTF and MoS_2, and repulsive coulomb interaction between neighboring TTF molecules. As the concentration of TTF increases, the latter energy increases. As a result, TTF buckles to minimize the energy by reducing the repulsive interaction and enhancing the attractive interaction.

The amount of charge transfer from TTF to MoS_2 increases with decreasing concentration of TTF (**Table 1**), which can be understood from the electronic structure of the system. We now examine the electronic Density of States (DOS) of MoS_2 with and without the adsorbed TTF molecule (**Figure 6**), in which the contribution of the TTF molecule to the total DOS is projected out (see filled curve in Figure 6; we shift the energy such that the edges of valence and conduction bands of MoS_2 are aligned with similar band edges of TTF+MoS_2, with zero as the Fermi level of MoS_2). Since the size of the periodic supercell of MoS_2 is larger for smaller concentrations of TTF, the scales of the DOS of MoS_2 and MoS_2 + TTF are different in Figure 6a and Figure 6b. However, the scale of DOS of TTF is the same and directly comparable between Figures 6a and Figure 6b, and allows a systematic estimation of charge transfer. The highest occupied molecular orbital (HOMO) of the TTF molecule lies just below the conduction band (in the band gap) of MoS_2, reducing the apparent band gap of TTF+MoS_2 complex, from 1.66eV (pure MoS_2) to 0.23 eV and 0.33 eV for TTF concentrations of 3.1 x 10^{13} cm^{-2} and 12.5 x 10^{13} cm^{-2} respectively. The HOMO state of TTF may be regarded as a gap state of the TTF+MoS_2 complex. There is only a weak overlap or coupling between this state and the conduction band of MoS_2, and hence this gap may not be relevant to the absorption experiment. We observe that the HOMO of TTF shifts towards and almost merges with the conduction band of MoS_2 with decreasing concentration of TTF. Consequently, charge transfer from TTF to MoS_2 increases and binding between MoS_2 and TTF increases. The increase in the apparent band gap signals decoupling of the HOMO of the TTF from conduction band of MoS_2, which along with the distance between the molecule and MoS_2, is indicative of lower binding (Table1) between the two. The fractional charge transferred is 0.15 electrons per cell and 0.09 electrons per cell for TTF concentration of 3.1 x 10^{13} cm^{-2} and 12.5 x 10^{13} cm^{-2} respectively (Table 1 and Figure 5).

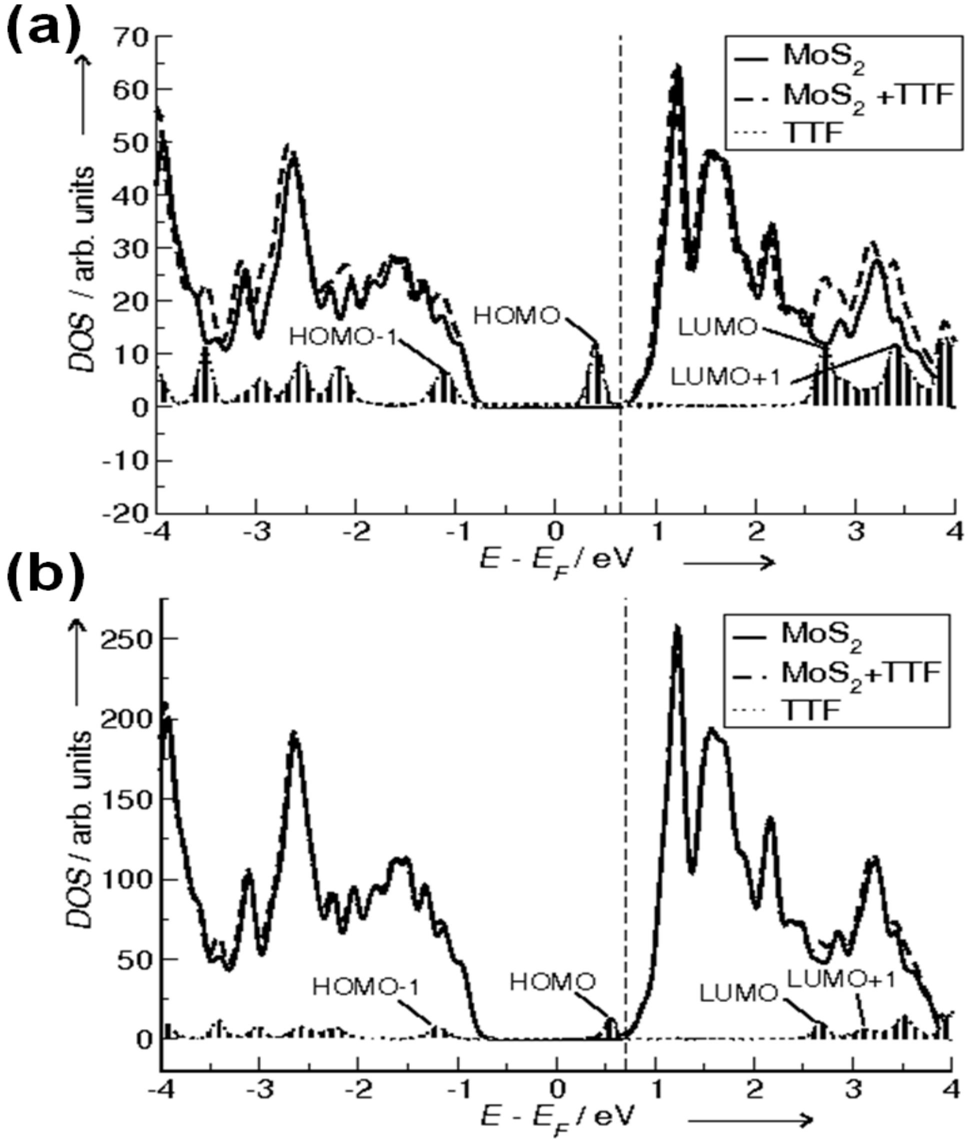

Figure 6. Electronic Density of States (DOS) plot for TTF concentration of a) 3.1x 10^{13}cm^{-2} and b) 12.5 x 10^{13} cm^{-2}. Solid curve denotes DOS of MoS_2 without TTF, dashed curve denotes the DOS of TTF+MoS_2, and filled curve is the projected DOS of TTF molecule on MoS_2. The energy was shifted such that the edges of valence and conduction bands of MoS_2 are aligned with similar band edges of TTF+MoS_2, with zero as the Fermi level of MoS_2. The vertical dashed line represents the Fermi level of TTF+MoS_2. The states of TTF molecule lie within the band gap of MoS_2. With decreasing concentration of TTF, the HOMO of TTF shifts further into the conduction band of TTF+MoS_2, and the amount of charge transferred from TTF to MoS_2 increases.

Table 1. Adsorption energy, charge transferred, band gap and distance (z) between TTF and MoS_2, for Mo-S configuration with varying TTF concentrations.

Concentration (10^{13} cm^{-2})	Adsorption Energy (kJ/mol)	Charge transferred (electrons/cell)	Band gap (eV)	z (Å)
3.1	-98	0.15	0.23	3.2
12.5	-83	0.09	0.33	3.5

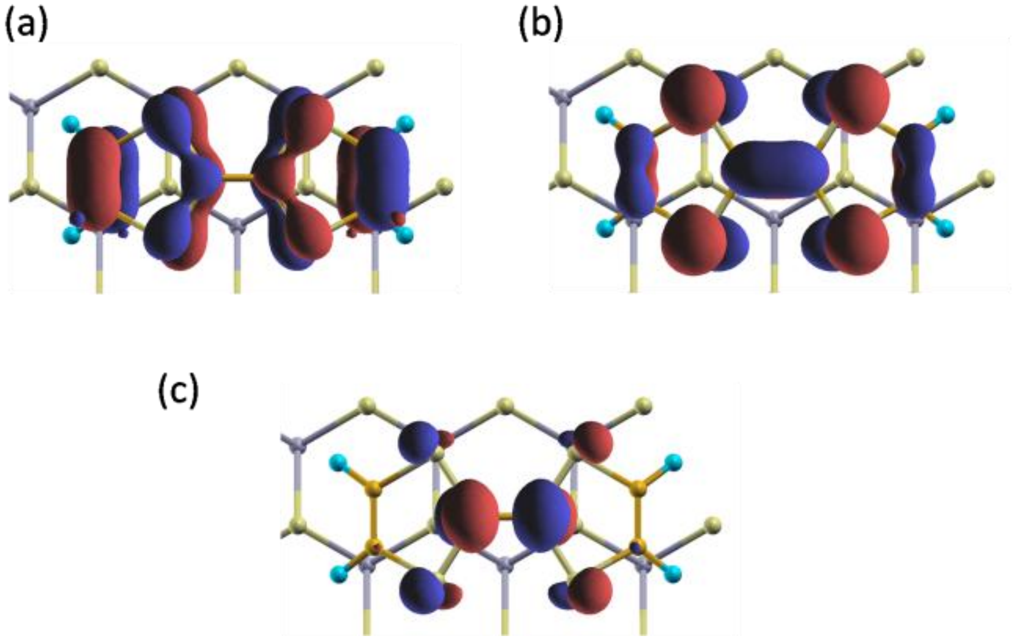

Figure 7. Charge density iso-surface of the states corresponding to a) HOMO-1, b) HOMO and c) LUMO+1 for a concentration of 12.5 x 10^{13} cm^{-2} of TTF on MoS_2.

Absorption bands at 580 nm (2.14 eV) and 440 nm (2.86 eV) for the TTF cationic radical arise from HOMO-1 to HOMO, and HOMO to LUMO+1 electronic transition, respectively.[55] Investigation of the HOMO-1, HOMO and LUMO+1 states of the TTF while adsorbed on MoS_2 with 12.5 x 10^{13} cm^{-2} concentration (**Figure 7**) reveals transition energies of 1.54 eV (HOMO-1 to HOMO) and 2.96 eV (HOMO to LUMO+1). The underestimation of the HOMO-1 to HOMO transition energy and overestimation of the HOMO to LUMO+1 transition energy is partly due to limitations of density functional theoretical (DFT) calculations and partly due to the partial charge transferred from TTF to MoS_2. As the concentration of TTF decreases, we expect the amount of transferred charge to increase and these transition energies to shift towards the experimental values.

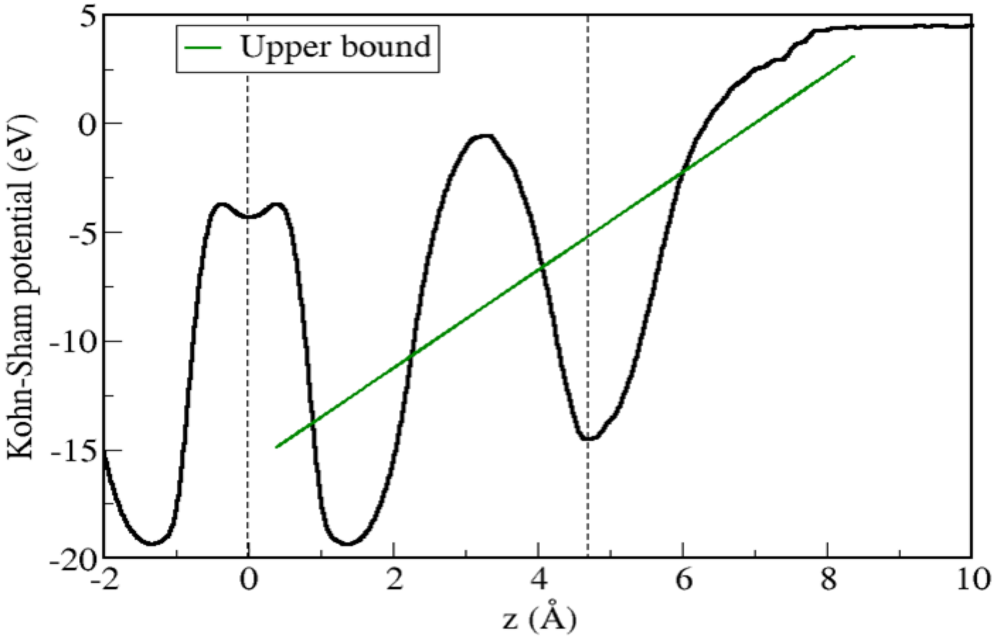

Figure 8. Spatial variation in the planar average of Kohn-Sham potential (eV) with distance (Å) for TTF concentration of 12.5 x 10^{13} cm^{-2}. The Mo and S planes are approximately at 0 Å and 4.7 Å (shown by dotted lines). The green line denotes the linear fit to the planar average, and the slope of the linear fit is directly proportional to the electric field (E). The estimate of the upper bound to the charge density from the plot is 40 x 10^{-6} C cm^{-2}.

We have estimated the upper bound on charge transferred from TTF to MoS_2, using the spatial variation in the planar average of Kohn-Sham potential between the TTF molecule and MoS_2 substrate (**Figure 8**). Due to subtlety in this analysis, we obtain the upper bound on the electric field (E) given by the slope of this potential. Approximating the MoS_2 surface as an uniformly charged plane, we estimate the charge density (σ), from the relation $E=\sigma/(2\varepsilon_o)$ (where ε_o is dielectric permittivity of vacuum). Our estimate of the upper bound on charge density is 40 x 10^{-6} C cm^{-2}, for 12.5 x 10^{13} cm^{-2} concentration of TTF on MoS_2.

With a fixed MoS_2 concentration, the number of TTF molecules per unit of area increases with increasing concentration of TTF and the total charge transfer also increases, as observed experimentally. For the same area (concentration) of MoS_2, calculated estimates of the charge transferred for 3.1 x 10^{13} cm^{-2} and 12.5 x 10^{13} cm^{-2} concentrations of TTF are 1.8 x 10^{-6} C cm^{-2} and 7.5 x 10^{-7} C cm^{-2} respectively. For a fixed concentration of TTF, the number of TTF molecules per supercell is the same (i.e. 1), but the supercell size increases, and hence the MoS_2 concentration increases, and the transferred charge increases (Table 1).

In our experiments on the adsorption of TCNE on few-layer MoS_2 material, no transfer of charge was observed. We corroborate this with first-principles analysis. For a concentration of 12.5 x 10^{13} cm^{-2} of TCNE on MoS_2, we find a negligible amount of charge (~0.01 electrons per cell) transferred from MoS_2 to TCNE. This result means that the interaction of MoS_2 with TCNE is an order of magnitude weaker than its interaction with TTF, and is also of the opposite type. This conclusion is consistent with experiments which suggest that MoS_2 can be electrochemically doped to introduce electrons (n-type) but not holes.[8] The top of the valence band of MoS_2 is narrow and comprise d-orbitals of Mo, indicating that these electrons are localized at Mo-sites and are tightly bound to the lattice. Thus, the removal of electrons from this band, and the consequent p-type doping, is not favorable.

4.5. Conclusions

From our study of the interaction of CdSe and ZnO nanoparticles with the electron donor (TTF) and –acceptor (TCNE) molecules we can draw the following conclusions. In the case of CdSe nanoparticles, interaction with TTF results in the quenching of the PL intensity. Interaction with TCNE also causes quenching of the PL intensity along with a red-shift of the PL band. 2.5 nm nanoparticles of CdSe show stronger interaction than the 4.5 nm nanoparticles. PL intensities of both the band-edge and defect-related emissions of ZnO nanocrystals undergo quenching after interaction with TCNE and TTF molecules. Calorimetric studies show stronger binding of TCNE with the surface of the nanocrystals compared to TTF.

Our experimental and theoretical studies of the interaction of few- layer MoS_2 with TTF and TCNE have shown that charge-transfer interaction occurs only with electron donating TTF and not with electron-withdrawing TCNE. Charge transfer from TTF to few-layer MoS_2 is substantial and is associated with the p-type nature of few- layer MoS_2. The decrease in the apparent band gap of the TTF+MoS_2 complex, corroborated by charge-current measurements, may be of practical use.

4.6. References

1 C. B. Murray, D. J. Norris and M. G. Bawendi, *J. Am. Chem. Soc.*, 1993, **115**, 8706-8715.

2 V. L. Colvin, M. C. Schlamp and A. P. Alivisatos, *Nature*, 1994, **370**, 354-357.

3 B. O. Dabbousi, M. G. Bawendi, O. Onitsuka and M. F. Rubner, *Appl. Phys. Lett.*, 1995, **66**, 1316-1318.

4 D. D. Sarma, A. Nag, P. K. Santra, A. Kumar, S. Sapra and P. Mahadevan, *J. Phys. Chem. Lett.*, 2010, **1**, 2149-2153.

5 M. T. Frederick, V. A. Amin, L. C. Cass and E. A. Weiss, *Nano Lett.*, 2011, **11**, 5455-5460.

6 K. E. Knowles, D. B. Tice, E. A. McArthur, G. C. Solomon and E. A. Weiss, *J. Am. Chem. Soc.*, 2010, **132**, 1041-1050.

7 K. E. Knowles, M. T. Frederick, D. B. Tice, A. J. Morris-Cohen and E. A. Weiss, *J. Phys. Chem. Lett.*, 2012, **3**, 18-26.

8 A. K. Gooding, D. E. Gomez and P. Mulvaney, *ACS Nano*, 2008, **2**, 669-676.

9 P. P. Jha and P. Guyot-Sionnest, *J. Phys. Chem. C*, 2007, **111**, 15440-15445.

10 A. L. Weaver and D. R. Gamelin, *J. Am. Chem. Soc.*, 2012, **134**, 6819-6825.

11 P. P. Jha and P. Guyot-Sionnest, *ACS Nano*, 2009, **3**, 1011-1015.

12 M. Shim and P. Guyot-Sionnest, *Nature*, 2000, **407**, 981-983.

13 C. Wang, M. Shim and P. Guyot-Sionnest, *Science*, 2001, **291**, 2390-2392.

14 N. Varghese, A. Ghosh, R. Voggu, S. Ghosh and C. N. R. Rao, *J. Phys. Chem. C*, 2009, **113**, 16855-16859.

15 V. Rakesh, D. Barun, R. Chandra Sekhar and C. N. R. Rao, *J. Phys. Condens. Matter*, 2008, **20**, 472204.

16 B. Das, R. Voggu, C. S. Rout and C. N. R. Rao, *Chem. Commun.*, 2008, 5155-5157.

17 W. Chen, S. Chen, D. C. Qi, X. Y. Gao and A. T. S. Wee, *J. Am. Chem. Soc.*, 2007, **129**, 10418-10422.

18 A. K. Geim and K. S. Novoselov, *Nat. Mater.*, 2007, **6**, 183-191.

19 M. I. Katsnelson, *Materials Today*, 2007, **10**, 20-27.

20 A. Das, S. Pisana, B. Chakraborty, S. Piscanec, S. K. Saha, U. V. Waghmare, K. S. Novoselov, H. R. Krishnamurthy, A. K. Geim, A. C. Ferrari and A. K. Sood, *Nat. Nanotech.*, 2008, **3**, 210-215.

21 K. M. Borysenko, J. T. Mullen, E. A. Barry, S. Paul, Y. G. Semenov, J. M. Zavada, M. B. Nardelli and K. W. Kim, *Phys. Rev. B*, 2010, **81**, 121412.

22 F. Schwierz, *Nat. Nanotech.*, 2010, **5**, 487-496.

23 K. K. Kam and B. A. Parkinson, *J. Phys. Chem. C*, 1982, **86**, 463-467.

24 K. F. Mak, C. Lee, J. Hone, J. Shan and T. F. Heinz, *Phys. Rev. Lett.*, 2010, **105**, 136805.

25 K. Dolui, I. Rungger, C. D. Pemmaraju and S. Sanvito, *Phys. Rev. B*, 2013, **88**, 075420.

26 S. Mouri, Y. Miyauchi and K. Matsuda, *Nano Lett.*, 2013, **13**, 5944-5948.

27 F. K. Perkins, A. L. Friedman, E. Cobas, P. M. Campbell, G. G. Jernigan and B. T. Jonker, *Nano Lett.*, 2013, **13**, 668-673.

28 Y. Du, H. Liu, A. T. Neal, M. Si and D. Y. Peide, *IEEE Electron Device Lett.*, 2013, **34**, 1328-1330.

29 J. D. Lin, C. Han, F. Wang, R. Wang, D. Xiang, S. Qin, X.-A. Zhang, L. Wang, H. Zhang and A. T. S. Wee, *ACS Nano*, 2014, **8**, 5323-5329.

30 H. Fang, M. Tosun, G. Seol, T. C. Chang, K. Takei, J. Guo and A. Javey, *Nano Lett.*, 2013, **13**, 1991-1995.

31 D. Kiriya, M. Tosun, P. Zhao, J. S. Kang and A. Javey, *J. Am. Chem. Soc.*, 2014, **136**, 7853-7856.

32 D. Sarkar, X. Xie, J. Kang, H. Zhang, W. Liu, J. Navarrete, M. Moskovits and K. Banerjee, *Nano Lett.*, 2015, **15**, 2852-2862.

33 D. M. Sim, M. Kim, S. Yim, M.-J. Choi, J. Choi, S. Yoo and Y. S. Jung, *ACS Nano*, 2015, **9**, 12115-12123.

34 E. Nguyen, B. Carey, C. J. Harrison, P. Atkin, K. J. Berean, E. Della Gaspera, J. Z. Ou, R. B. Kaner, K. Kalantar-zadeh and T. Daeneke, *Nanoscale*, 2016, **8**, 16276-16283.

35 N. Goswami, A. Giri and S. K. Pal, *Langmuir*, 2013, **29**, 11471-11478.

36 A. Bandyopadhyay and S. K. Pati, *Chem. Phys. Lett.*, 2015, **624**, 64-68.

37 B. Arkamita and K. P. Swapan, *Mater. Res. Exp.*, 2015, **2**, 085003.

38 Y. Jing, X. Tan, Z. Zhou and P. Shen, *J. Mater. Chem. A*, 2014, **2**, 16892-16897.

39 R. C. Selhorst, E. Puodziukynaite, J. A. Dewey, P. Wang, M. D. Barnes, A. Ramasubramaniam and T. Emrick, *Chem. Sci.*, 2016, **7**, 4698-4705.

40 D. Choudhury, B. Das, D. D. Sarma and C. N. R. Rao, *Chem. Phys. Lett.*, 2010, **497**, 66-69.

41 N. Pinna, G. Garnweitner, M. Antonietti and M. Niederberger, *J. Am. Chem. Soc.*, 2005, **127**, 5608-5612.

42 W. W. Yu, L. Qu, W. Guo and X. Peng, *Chem. Mater.*, 2003, **15**, 2854-2860.

43 H. S. S. Ramakrishna Matte, A. Gomathi, A. K. Manna, D. J. Late, R. Datta, S. K. Pati and C. N. R. Rao, *Angew. Chem.*, 2010, **122**, 4153-4156.

44 G. Paolo, B. Stefano, B. Nicola, C. Matteo, C. Roberto, C. Carlo, C. Davide, L. C. Guido, C. Matteo, D. Ismaila, C. Andrea Dal, G. Stefano de, F. Stefano, F. Guido, G. Ralph, G. Uwe, G. Christos, K. Anton, L. Michele, M.-S. Layla, M. Nicola, M. Francesco, M. Riccardo, P. Stefano, P. Alfredo, P. Lorenzo, S. Carlo, S. Sandro, S. Gabriele, P. S. Ari, S. Alexander, U. Paolo and M. W. Renata, *J. Phys. Condens. Matter*, 2009, **21**, 395502.

45 J. P. Perdew, J. A. Chevary, S. H. Vosko, K. A. Jackson, M. R. Pederson, D. J. Singh and C. Fiolhais, *Phys. Rev. B*, 1992, **46**, 6671-6687.

46 D. Vanderbilt, *Phys. Rev. B*, 1990, **41**, 7892-7895.

47 C. R. Kagan, C. B. Murray and M. G. Bawendi, *Phys. Rev. B*, 1996, **54**, 8633-8643.

48 A. Nag and D. D. Sarma, *J. Phys. Chem. C*, 2007, **111**, 13641-13644.

49 A. Y. Ziganshina, Y. H. Ko, W. S. Jeon and K. Kim, *Chem. Commun.*, 2004, 806-807.

50 A. J. Olaya, P. Ge, J. r. m. F. Gonthier, P. Pechy, C. m. Corminboeuf and H. H. Girault, *J. Am. Chem. Soc.*, 2011, **133**, 12115-12123.

51 G. L. Frey, R. Tenne, M. J. Matthews, M. S. Dresselhaus and G. Dresselhaus, *Phys. Rev. B*, 1999, **60**, 2883-2892.

52 S. Grimme, *J. Comput. Chem.*, 2006, **27**, 1787-1799.

53 B. Chakraborty, A. Bera, D. V. S. Muthu, S. Bhowmick, U. V. Waghmare and A. K. Sood, *Phys. Rev. B*, 2012, **85**, 161403.

54 H. J. Monkhorst and J. D. Pack, *Phys. Rev. B*, 1976, **13**, 5188-5192.

55 R. Andreu, J. Garin and J. Orduna, *Tetrahedron*, 2001, **57**, 7883-7892.